TIMING AND NATURE OF ALTERATION AND MINERALIZATION AT THE ÖKSÜT AU-CU DEPOSIT (KAYSERI, CENTRAL ANATOLIA)

A THESIS SUBMITTED TO
THE GRADUATE SCHOOL OF NATURAL AND APPLIED SCIENCES
OF
MIDDLE EAST TECHNICAL UNIVERSITY

BY

EMRECAN YURDAKUL

IN PARTIAL FULFILLMENT OF THE REQUIREMENTS
FOR
THE DEGREE OF MASTER OF SCIENCE
IN
GEOLOGICAL ENGINEERING

JUNE 2022

Approval of the thesis:

TIMING AND NATURE OF ALTERATION AND MINERALIZATION AT THE ÖKSÜT AU-CU DEPOSIT (KAYSERI, CENTRAL ANATOLIA)

submitted by **EMRECAN YURDAKUL** in partial fulfillment of the requirements for the degree of **Master of Science** i**n Geological Engineering, Middle East Technical University** by,

Prof. Dr. Halil Kalıpçılar
Dean, Graduate School of **Natural and Applied Sciences** _____

Prof. Dr. Erdin Bozkurt
Head of the Department, **Geological Engineering, METU** _____

Assist. Prof. Dr. Ali İmer
Supervisor, **Geological Engineering, METU** _____

Examining Committee Members:

Prof. Dr. Tolga Oyman
Geological Engineering, Dokuz Eylül University _____

Assist. Prof. Dr. Ali İmer
Geological Engineering, METU _____

Assoc. Prof. Dr. Kaan Sayıt
Geological Engineering, METU _____

Assoc. Prof. Dr. Fatma Toksoy Köksal
Geological Engineering, METU _____

Assist. Prof. Dr. Erkan Yılmazer
Geological Engineering, Aksaray University _____

Date: 29.06.2022

I hereby declare that all information in this document has been obtained and presented in accordance with academic rules and ethical conduct. I also declare that, as required by these rules and conduct, I have fully cited and referenced all material and results that are not original to this work.

Name Last name : Emrecan Yurdakul

Signature :

ABSTRACT

TIMING AND NATURE OF ALTERATION AND MINERALIZATION AT THE ÖKSÜT AU-CU DEPOSIT (KAYSERI, CENTRAL ANATOLIA)

Yurdakul, Emrecan
Master of Science, Geological Engineering
Supervisor: Assist. Prof. Dr. Ali İmer

June 2022, 208 pages

The Öksüt high-sulfidation epithermal gold-copper deposit is hosted within the late Miocene Develidağ Volcanic Complex (DVC) in south-central Anatolia. Mineralization mainly occurs in two domains, the Keltepe and Güneytepe orebodies, where steeply-dipping and pervasively supergene oxidized breccia zones exploited funnel-shaped diatreme conduits within andesite porphyry. Emplacement of these breccias was largely controlled by sub-vertical faults with dominant normal-slip components.

Mineralized breccias comprise a central zone of residual vuggy-massive silica alteration, laterally and vertically grading into zones of quartz-alunite and quartz-alunite- clay alteration. Silicified breccias contain relatively high gold grades, whereas significant mineralization was also encountered in quartz-alunite-clay alteration. In the oxide zone, gold occurs in native form, whereas in the hypogene zone it occurs both as native gold or within abundant pyrite accompanied by lesser enargite, marcasite, chalcopyrite, and tetrahedrite. In both mineralized domains mineralized breccias pass into barren argillic and then into biotite-magnetite-K-

feldspar-anhdyrite alteration, the latter typical of porphyry-type systems. Sporadic zones of calc-silicate alteration are also present to the west of the tenement area.

$^{40}Ar/^{39}Ar$ alunite and illite ages as well as U-Pb garnet ages range between 5.7 to 5.5 Ma and suggest that high-sulfidation epithermal alteration and mineralization developed contemporaneously with post-subduction magmatism at DVC, in relationship to regional E-W-directed extension. New age data also confirms Öksüt as the youngest known epithermal gold deposit in Anatolia, and possibly in the Western Tethyan metallogenic belt. The topographic prominence of the volcanic edifice combined with high permeability of the breccias favored deep supergene oxidation, thereby rendering Öksüt economically viable.

Keywords: Central Anatolia, Kayseri, Öksüt, High-Sulfidation Epithermal, Gold, Copper

ÖZ

ÖKSÜT AU-CU YATAĞININ (KAYSERİ, ORTA ANADOLU) ALTERASYON VE CEVHERLEŞME YAŞI VE ÖZELLİKLERİ

Yurdakul, Emrecan
Yüksek Lisans, Jeoloji Mühendisliği
Tez Yöneticisi: Dr. Öğr. Üyesi Ali İmer

Haziran 2022, 208 sayfa

Öksüt yüksek-sülfidasyon epitermal altın-bakır yatağı güney-orta Anadolu'da, Geç Miyosen yaşlı Develidağ Volkanik Kompleksi'nin (DVK) içerisinde yer almaktadır. Cevherleşme temel olarak Keltepe ve Güneytepe adlandırılmış iki bölgede, andezit porfiri ile bunu kesen, dik-açılı ve yukarı doğru genişleyen bir diyatrem içerisine yerleşmiş yoğun oksitli breş zonlarında gelişmiştir. Bu breşlerin yerleşimi genelde normal atımın baskın olduğu, dike yakın açılı faylar tarafından kontrol edilmiştir.

Cevherli breşlerin merkezinde kalıntı boşuklu-masif silika alterasyonu yer almakta, bu alterasyon yanal ve düşey olarak önce kuvars-alunit, sonrasında kuvars-alunit-kil alterasyonuna geçiş yapmaktadır. Silisli breşler görece yüksek altın tenörleri içerirken kayda değer cevherleşme ayrıca kuvars-alunit-kil alterasyonu içerisinde de gözlenmiştir. Oksitli zonda altın nabit formdadır. Hipojen cevherleşme zonunda ise altın hem nabit halde hem de yoğun miktarda pirit içerisindedir. Bunlara ayrıca daha az miktarda enarjit, markazit, kalkopirit ve tetrahedrit eşlik etmektedir. İki cevherli bölgede de cevherli breşler önce cevhersiz arjilik alterasyon sonrasında ise tipik olarak porfiri sistemlerde gözlemlenen biyotit-manyetit-K-feldspat-anhidrit

alterasyonuyla çevrelenmiştir. Ruhsat sahasının batısında ise yer yer kalk-silikat alterasyonu bulunmaktadır.

$^{40}Ar/^{39}Ar$ alunit ve illit yaşları ile U-Pb granat yaşları 5.7 ila 5.5 Ma arasındadır. Buna göre yüksek-sülfidasyon epitermal alterasyon ve cevherleşme DVK'de çarpışma sonrası dönemde, bölgesel D-B yönlü gerilmeyle ilişkili gelişmiş magmatizmayla eş zamanlıdır. Yeni yaş bulgularına göre Öksüt Anadolu'da ve büyük olasılıkla Batı Tetis Metalojenik Kuşağı içerisinde bilinen en genç epitermal Au yatağıdır. Volkanik yapının yüksek topoğrafyası breş zonlarının ileri derecede geçirgen yapısıyla birlikte derinlere uzanan süperjen oksidasyona neden olmuş, buna göre Öksüt cevherleşmesi ekonomiklik kazanmıştır.

Anahtar Kelimeler: Orta Anadolu, Kayseri, Öksüt, Yüksek-Sülfidasyon Epitermal, Altın, Bakır

In memories of

My Brother and Prof. Dr. Jeremy Peter Richards

To my family, love, supervisor, and Malcolm Stallman

ACKNOWLEDGMENTS

I wish to express my deepest gratitude to my supervisor Assist. Prof. Dr. Ali İmer for his guidance, advice, criticism, encouragements, and insight throughout the research.

I would like to thank Centerra Gold Inc. for financial and logistical support.

Particular thanks to Malcolm Stallman - VP Exploration, for his suggestions, comments and overall support.

Thanks to Mustafa Cihan for his support, critics, and comments.

I am grateful to the following Centerra Madencilik A.Ş manager and colleagues starting from Tolga Tosun, and colleagues, Deniz Can Serçe, Semih Bekarslan, Simge Cavunt, Ayşegül Dağgez, Habil Dinçer for their fruitful discussions and help.

Special thanks to Assoc. Prof. Kaan Sayıt for his support.

I am deeply grateful to Assoc. Prof. Fatma Toksoy Köksal for her comments and critics about thesis, to Prof. Dr. Tolga Oyman and Assist. Prof. Dr. Erkan Yılmazer for all their support and constructive comments.

I would like to extend my thanks to Akın Çil for discussions about this study and support especially while I was in field.

TABLE OF CONTENTS

ABSTRACT v

ÖZ vii

ACKNOWLEDGMENTS x

TABLE OF CONTENTS xi

LIST OF TABLES xv

LIST OF FIGURES xvi

CHAPTERS

1 INTRODUCTION 1

1.1 Purpose and Scope 1

1.1.1 Objectives 8

1.1.2 Methodology 9

1.1.2.1 Field work 9

1.1.2.2 Petrography 9

1.1.2.3 Laser-ablation inductively-coupled mass-spectrometry (LA-ICP-MS) 10

1.1.2.4 $^{40}Ar/^{39}Ar$ and U-Pb geochronology 11

1.2 Epithermal Deposits 12

2 REGIONAL GEOLOGY 17

2.1 Geologic History of South-Central Anatolia 17

2.1.1 Mesozoic–Cenozoic tectonic development of south-central Anatolia 20

2.1.2 Geology of The Ecemiş Corridor 25

2.1.2.1 Structure 25
2.1.2.2 Stratigraphy 26
2.1.2.2.1 Erciyes Basin 28
2.1.2.2.1.1 Margin Rocks 29
2.1.2.2.1.2 Çukurbağ Formation 29
2.1.2.2.1.3 Ürgüp Group 29
2.1.2.2.2 Basin Fill 31
2.1.2.2.2.1 Sedimentary Infill 31
2.1.2.2.2.2 Volcanic Infill 31
3 DEPOSIT GEOLOGY 33
3.1 Introduction 33
3.2 Local Stratigraphy 35
3.2.1 Mesozoic carbonates 35
3.2.2 Develidağ Volcanic Complex (DVC) 37
3.2.2.1 Hornblende andesite porphyry (late Miocene) 40
3.2.2.2 Pyroxene andesite porphyry (late Miocene) 40
3.2.2.3 Diatreme breccia and maar-fill sediments (late Miocene) 41
3.2.2.4 Basaltic lava flows (early Pliocene) 45
3.3 Structure 46
4 DEPOSIT CHARACTERISTICS 49
4.1 Hydrothermal Alteration 49
4.1.1 Alteration facies 53
4.1.1.1 Silicification 53
4.1.1.2 Advanced Argillic Alteration 57

4.1.1.3 Argillic Alteration 63
4.1.1.4 Biotite-magnetite ± K-feldspar ± anhydrite alteration 66
4.1.1.5 Propylitic alteration 67
4.1.1.6 Calc-silicate alteration 69
4.1.2 Mineralization 71
4.1.2.1 Breccias 74
4.1.2.1.1 Silica-matrix breccia 75
4.1.2.1.2 Alunite-matrix breccia 77
4.1.2.1.3 Kaolinite-matrix breccia 78
4.1.2.1.4 Sulfide-matrix breccia 79
4.1.2.2 Hypogene mineralization 81
4.1.2.2.1 Pyrite chemistry 86
4.1.2.3 Supergene mineralization 90
4.2 Geochronology 100
4.2.1 U-Pb garnet dating 102
5 DISCUSSIONS AND CONCLUSIONS 107
5.1 Discussion 107
5.1.1 Constraints on formation of hypogene gold-copper mineralization 107
5.1.2 Geodynamic Setting of the Öksüt Au-Cu Deposit 108
5.1.3 Regional Significance and Relation to Late Cenozoic Central Anatolian Tectonism 111
5.1.4 Deep Oxidation of the Epithermal System 114
5.2 Conclusions 114
REFERENCES 119

APPENDICES

A. Collected and Studied Drillhole Samples. 155

B. XRD Sample List 169

C. XRD Analysis Results 171

D. Samples of SEM-EDX Analyzed Samples and Assay Results 173

E. SEM and EDX Analysis Results of Sample OD79832 175

F. SEM and EDX Analysis Results of Sample OD79899 177

G. SEM and EDX Analysis Results of Sample OD79948 179

H. SEM and EDX Analysis Results of Sample OD79838 181

I. SEM and EDX Analysis Results of Sample OD79955 183

J. SEM and EDX Analysis Results of Sample OD79845 185

K. SEM and EDX Analysis Results of Sample OD79929 187

L. LA-ICP-MS Analysis Spots in Pyrites of Sample CTR2711 189

M. LA-ICP-MS Analysis Spots in Pyrites of Sample CTC2713 191

N. Samples CTR2711 and CTR2713 Pyrites LA-ICP-MS Analysis Results in PPM 193

O. $^{40}Ar/^{39}Ar$ Analyses - Description and Procedures 197

P. $^{40}Ar/^{39}Ar$ Analyses Data 201

Q. U-Pb Data of Garnets in Samples CTC78859 and CTC78857 203

LIST OF TABLES

Table 4.1 Alteration types identified at Öksüt and their characteristic minerals. ...52
Table 4.2 Characteristics of common breccia types in Öksüt 75
Table 4.3 Summary of Biotite, Alunite and Illite Minerals $^{40}Ar/^{39}Ar$ and Garnet Minerals U-Pb Geochronological Data from Hydrothermal Alteration Minerals. 105
Table 5.1. Summary Characteristics of Late Cenozoic Gold Systems in South Central and Western Anatolia. 115

LIST OF FIGURES

Figure 1.1. Generalized cartoon showing ideal geological setting of porphyry and associated epithermal deposits in relation to subduction-related magmatism (from Winter, 2001; Richards, 2011; Rabayrol, 2018).....2
Figure 1.2. Schematic illustration showing distribution of magmatic-hydrothermal deposits that develop within volcano-plutonic settings (Sillitoe, 2010).....3
Figure 1.3. Possible tectonic environments of porphyry and epithermal deposits, A) during normal arc magmatism, B) during post-collisional thermal rebound, C) during subcontinental lithospheric mantle (SCLM) delamination and, D) during post-collisional extension leading to lower crustal melting of previously subduction modified lithosphere. Redrafted after Richards (2009).....6
Figure 1.4. Map showing late Cenozoic to Recent volcanics and regionally-important structures in south-central Anatolia (redrafted after Koçyiğit and Beyhan, 1998; Koçyiğit and Erol, 2001; MTA, 2002). Significant deposits and prospects mentioned in the text are also shown. Background digital elevation map retrieved from GeoMap App (https://geomapapp.org). Major tectonic units of Turkey, important metallogenic belts, late Cenozoic central-western Anatolian volcanic belt, and some major gold and copper deposits/prospects are shown in the inset map. Extent of the main map is indicated via black rectangular box in inset map. Abbreviations: AFZ = Akşehir fault zone, BP = Biga Peninsula, CAFZ = Central Anatolian fault zone, DVC = Develidağ Volcanic Complex, IAESZ = Izmir-Ankara-Erzincan suture zone, KVB = Konya volcanic belt, SF = Salanda fault.....7
Figure 2.1. Paleogeographic reconstructions showing northward migration of the Anatolide-Tauride Block (ATB) in the Mesozoic with respect to the opening and closure of the Northern and Southern Neotethys: A. 180 Ma, B. 114 Ma, C. 68 Ma, D. 20 Ma. E. 10 Ma, F. Present. Modified and redrafted after Barrier and Vrielynck (2008) and Rabayrol (2018). 19
Figure 2.2. Major tectonic units including major suture zones of Turkey. Bold lines with filled triangle are former subduction units and lines with triangles are active

suture zones and strike slip faults are represented with its movement arrows. After Okay and Tüysüz (1999) and Okay (2008)..... 19
Figure 2.3. Regional map showing magmatic and metamorphic domains of the southern part of the Central Anatolian Crystalline Complex including major structures, important volcanic provinces, and epithermal deposits and prospects. Modified after MTA (2002). 21
Figure 2.4. Demonstration of central Anatolia because of decoupled accreted blocks and their mantle. (A) middle to late Miocene: Because of roll back and delamination Anatolide-Tauride block and Kırşehir mantle lithosphere extensional exhumation in the Kırşehir block occurred. As a result of delamination, hot asthenosphere could up well, melt and came to the base of central Anatolia crust where ignimbritic volcanism was initiated because of these activities. B) Latest Miocene – Recent: continuation of the slab roll back caused to SW migration of the initiated ignimbritic volcanism. Subducted African lithosphere broke off started in late Miocene and due to the isostasy resulted from slab break central Taurus mountains uplift were initiated. Redrafted after Delph et al., 2017. Abbreviations, ITS: Inner Tauride Suture, ATB: Anatolide-Tauride block, CTMs: Central Taurus mountains, IAESZ: İzmir-Ankara-Erzincan suture zone, KB: Kırşehir block. 27
Figure 3.1. Simplified geologic map of the Ecemiş corridor and the Sultansazlığı pull-apart basin located between the Yeşilhisar and Develi segments of the Ecemiş Fault Zone (simplified from MTA, 2002)..... 35
Figure 3.2. A generalized view of the south of the deposit which includes Pliocene cover rocks and mineralized silica ledges. Öksüt village located in the center of the margin of the complex and Tauride mountains are in the far south. Abbreviations: DVC= Develidağ Volcanic Complex. 36
Figure 3.3. Generalized columnar section and stratigraphic sequence of the major lithological units in Öksüt. 37
Figure 3.4. (A) Recrystallized limestone fragment derived from carbonate basement rocks underlying the access road between Zile and Öksüt mine (38.299112N,

35.476197E), (B) strongly silica- and carbonate-altered iron skarn exposure adjacent to the recrystallized limestone blocks sampled in (A).....37
Figure 3.5. Geological map of the Öksüt deposit showing main outcropping lithologies, structures, and distribution of hydrothermal alteration facies (modified from Cihan et al., 2016). Approximate outlines of the Keltepe and Güneytepe pits and satellite prospects as well as locations of some of the key drill holes mentioned in the text are also shown. 38
Figure 3.6. Alteration map of the Keltepe pit.....39
Figure 3.7. Alteration map of Güneytepe pit.....39
Figure 3.8. View of the Keltepe N and NW prospects from the Boztepe prospect. Pyroxene andesite porphyry makes up the ridges on both sides of the road. Erciyes Stratovolcano and the Sultansazlığı pull-apart basin can be seen in the background. 41
Figure 3.9. (A) Drill core and (B) thin section photograph (transmitted, cross-polarized light) of least-altered pyroxene andesite porphyry (sample OD78863; ODD-337, 706.30–706.60 m). This sample contains phenocrystals of plagioclase and pyroxene together with magnetite microphenocrysts surrounded by a groundmass containing fine-grained plagioclase and pyroxene. 42
Figure 3.10. Angular, silica-altered clasts predominating the diatreme breccia cross-cutting the altered pyroxene andesite porphyry in the southern part of the Keltepe pit. 43
Figure 3.11. (A) Drill hole interval from the Keltepe pit (ODD-312, 289.00–292.00 m) containing variably-sized clasts in a matrix- to clast-supported diatreme breccia, (B) diatreme breccia from SW wall of the Keltepe pit, (C) intensely-altered, poorly-sorted, polymictic diatreme breccia exposed on the main wall of the Güneytepe pit. 44
Figure 3.12. Outcrop photograph of finely-stratified maar-fill sediments of volcanic origin from the Güneytepe pit. Sediments have been strongly silicified and oxidized. 44

Figure 3.13. Contact between the late Miocene pyroxene andesite porphyry and overlying Pliocene basalt-basaltic andesite flows in the north of the Keltepe pit (38.289173N, 35.512541E)..... 45
Figure 3.14. Fragment of Pliocene basalt from the western margin of the DVC. Altered plagioclase phenocrysts are abundant and are set in a dark colored groundmass. 46
Figure 3.15. (A) NE-trending, steeply-dipping oblique fault (left-lateral with normal component; marked with dashed line) exposed on the southwestern wall of the Keltepe pit. This structure sharply separates silica and quartz-alunite alteration zones from the quartz-kaolinite alteration zone, (B) Close-up view of the silicified and oxidized fault surface. 47
Figure 3.16. Fractured surface of a drill core sample (ODD-444, 680.00–680.20 m, Güneytepe pit) with a steeply-dipping slickensided pyrite infill indicating post-mineralization faulting. 48
Figure 4.1. Pre-open pit view of the Keltepe orebody. Ledges are encircled by quartz-alunite alteration which transitioning to argillic and propylitic alteration. At the top, Pliocene rocks cover all the other units. 50
A zoned alteration pattern is also present at Öksüt (Table 4.1), and lateral and vertical distribution of various alteration zones can be observed around mineralized breccia bodies, particularly within the Keltepe (Figure 4.2A) and Güneytepe pits (Figure 4.2B)..... 51
Figure 4.2. Distribution of altered and mineralized domains, as well as various breccia facies in (A) Keltepe and (B) Güneytepe pits. Abbreviations: KM-Bx = Kaolinite matrix breccia, SM Bx = Silica matrix breccia, AM Bx = Alunite matrix breccia. 51
Figure 4.3. Residual vuggy silica alteration of the igneous wall-rock from the Keltepe orebody. Vugs have been partially filled by late silica. Reddish-orangish color is due to supergene oxidation and presence of Fe-oxide minerals (sample OD79995; ODD-316, 159.70–159.75 m, 3.08 g/t Au). 53

Figure 4.4. Massive silica replacement of an intensely-oxidized breccia sample from the Keltepe orebody (sample OD79983; ODD-316, 104.80–104.90 m, 0.53 g/t Au). 54
Figure 4.5. Outcrop sample from the Güneytepe pit with a moderately-silicified groundmass. Open vugs formed due to acid leaching of biotite and hornblende, whereas quartz occurs as a stable relict phase. 54
Figure 4.6. Core samples of drill hole ODD-312 from the Keltepe orebody showing vertical zonation of hydrothermal alteration. (A) Massive silica breccia with hematite dominant matrix transitioning to quartz-alunite alteration (this interval has a highest grade of 0.97 g/t Au), (B) Brecciated and fault interval with quartz-kaolinite altered, limonitic matrix (this interval has a highest grade of 0.36 g/t Au), (C) Quartz-alunite-altered, chalcocite-rich breccia (highest grades encountered in this interval are 0.66 g/t Au and 0.34% Cu). 55
Figure 4.7. Patchy silica (sil) in alunite-kaolinite-altered andesite porphyry (sample OD79889; ODD-12; 149.00–149.10 m, Güneytepe), fractured silica patch in advance argillic alteration. 56
Figure 4.8. Vertical and lateral epithermal alteration zonation along the northeastern wall in the Güneytepe, where advance argillic alteration is dominant and its sub-zones (quartz-alunite and quartz-kaolinite) are present. Silica ledges are visible above the pit wall, whereas patches of secondary sulfides (gray areas) are present in deeper levels around the ledges. 58
Figure 4.9. (A) Drill core photograph and (B) microphotograph (transmitted, cross-polarized light) of quartz-alunite-altered andesite porphyry from the Güneytepe orebody (sample OD79801; ODD-210; 179.50–179.60 m). Pyroxene andesite porphyry in this sample has undergone intense quartz-alunite alteration with complete replacement of primary igneous minerals. Acicular crystals of alunite occur as clusters partially filling vugs, and some fine-grained alunite also occurs in the groundmass alongside quartz. Gray areas in (A) contain patches of sulfide minerals such as pyrite and Cu-sulfides. Abbreviations: Qtz = quartz, Alun = alunite. 59

Figure 4.10. (A) Drill core photograph and (B) microphotograph (transmitted, cross-polarized light) of quartz-alunite-altered breccia from the Keltepe orebody (sample OD79990; ODD-316; 142.00–142.10 m; 4.1 g/t Au). Quartz-alunite alteration is well-developed in this matrix-supported breccia, both in the igneous clasts and in the matrix. Some of the clasts have been silica-altered, and the orange color of the sample is due to supergene weathering and oxidation. Microphotograph in (B) shows fine-grained quartz-allunite replacement of clasts surrounded by quartz-alunite altered matrix Abbreviations: Alun = alunite, Qtz = quartz. 60
Figure 4.11. (A) Drill core photograph quartz-alunite-clay-altered andesite porphyry from the Keltepe N orebody (sample OD78962; ODD-333, 369.80–370.00 m). Groundmass in this sample has been completely replaced by quartz-alunite, whereas plagioclase phenocrysts show partial replacement into clays. Pyrophyllite veinlet cross-cuts the sample. X-ray diffractogram in (B) confirms presence of quartz, alunite, pyrophyllite, and pyrite. 61
Figure 4.12. Drill core photograph of quartz-kaolinite-altered andesite porphyry from Güneytepe (sample OD79897; ODD-33, 131.70–131.80 m). Quartz-kaolinite-altered sample has been cross-cut by an irregular silica vein. 62
Figure 4.13. Patchy silica alteration overprinting alunite- and kaolinite-rich groundmass in andesite porphyry in the Güneytepe pit. 63
Figure 4.14. Drill core interval of strongly kaolinized andesite porphyry from the Keltepe pit. Kaolinite-rich zones are distinguished by their soft, wad-like powdery texture. Red-orange coloring is due to supergene oxidation of Fe-sulfides. 64
Figure 4.15. (A) Drill core photograph and (B) microphotographs (transmitted, cross-polarized light in B of quartz-illite-kaolinite-altered andesite porphyry from Keltepe pit (sample OD79861; ODD-316, 430.70–430.80 m). Original porphyritic texture in this sample is largely preserved, but all igneous minerals have been replaced by quartz, illite, and kaolinite. Quartz-pyrite veinlets are visible in drill core (A). 65
Figure 4.16. Drill core photograph of magnetite-biotite-K-feldspar-anhydrite alteration in andesite porphyry from Güneytepe (ODD-444; 1001.00–1001.10m).

Quartz-magnetite-biotite vein has an alteration selvedge of K-feldspar and anhydrite. Late propylitic alteration resulted in epidote-chlorite overprint of feldspars and biotite, whereas pyrite has partially replaced magnetite. 66

Figure 4.17. (A) Drill core photograph and (B) microphotograph (transmitted, cross-polarized) of propylitized pyroxene andesite porphyry from Boztepe W (far west of Keltepe), (sample OD78863; ODD-337, 706.30–706.60 m). Early biotite-magnetite-K-feldspar-anhydrite alteration in this sample has been overprinted by propylitic alteration, which caused partial to complete replacement of ferro-magnesian minerals by chlorite, and plagioclase by epidote. Abundant secondary biotite is still preserved in the sample. Magnetite is present either as disseminations or along M-veinlets, but has also been partially replaced by pyrite during propylitization. Abbreviations: bt = biotite, mag = magnetite, Ksp = K-feldspar, anh = anhydrite, ep = epidote, chl = chlorite, pyx = pyroxene..... 68

Figure 4.18. (A) Drill core photograph (transmitted, cross-polarized) of calc-silicate-altered pyroxene andesite porphyry from far west of Keltepe (sample OD78855; ODD-337, 71.40–71.45 m). Calc-silicate minerals, mainly represented by garnet, occur as veins (A). (B) core sample OD78857 (ODD0337, 77.30–77.60m), fracture filling calc-silicate (grossularite-diopside-vesuvianite) alteration in pyroxene andesite porphyry. (C) plane polarized reflected light microscope image of Sample OD78855 (ODD0337, 71.40–71.80m), garnet-diopside-vesuvianite veinlet in pyroxene andesite porphyry. Sericite and pyrite replacement occurred due to retrograde overprint. Abbreviations: grt = garnet, , py = pyrite, cpx = clinopyroxene, ves = vesuvianite. 70

Figure 4.19. Schematic cross-sections of the Keltepe orebody, showing spatial relationship between various alteration and mineralization domains as well as gold-copper grade shells. Section lines are shown in Figure 3.5. Abbreviations: alun = alunite, anh = anhydrite, bt = biotite, cc = chalcocite, chl = chlorite, cov = covellite, en = enargite, goet = goethite, hem = hematite, ill = illite, kaol = kaolinite, Ksp = K-feldspar, lim = limonite, mag = magnetite, py = pyrite, qz = quartz, smec = smectite. 72

Figure 4.20. Schematic cross sections of Güneytepe orebody, showing spatial relationship between various alteration and mineralization domains as well as gold-copper grade shells. Section lines are shown in Figure 3.5. Abbreviations: alun = alunite, anh = anhydrite, bt = biotite, cc = chalcocite, chl = chlorite, cov = covellite, en = enargite, goet = goethite, hem = hematite, ill = illite, kaol = kaolinite, Ksp = K-feldspar, lim = limonite, mag = magnetite, py = pyrite, qz = quartz, smec = smectite. 73

Figure 4.21. (A) Drill core photograph and (B and C) microphotographs (transmitted, cross-polarized) of massive silica-residual silica-matrix breccia from Güneytepe (sample OD79872; ODD-12, 12.2–12.30 m, 3.47 g/t Au). This sample contains fine-grained quartz both in the matrix and in the clasts. A dense network of hematite- and/or goethite-fill fractures are common. Late alunite partially fills vugs. Abbreviations: Qtz = quartz, Alun = alunite..... 76

Figure 4.22. Quartz-alunite matrix, silica-massive silica and quartz-alunite clast-rich outcrop (A) in the Keltepe pit, and (B) in the Güneytepe pit and in contact with quartz-alunite-kaolinite matrix breccia. 77

Figure 4.23 Drill core sample of kaolinite-matrix breccia from the Yelibelen prospect consisting of silica-altered clasts and fracture-filling hematite. 78

Figure 4.24. (A) Drill core photograph and (B) microphotograph (reflected, plane-polarized light) of sulfide-matrix breccia from Keltepe (sample OD79934; ODD-316, 328.40–328.50 m). This sample comprises crudely laminated tabular clasts of silicified rock surrounded by fine-grained pyrite. Abbreviations: py = pyrite, sil = silica. 79

Figure 4.25. (A) Drill core photograph and (B) microphotograph (reflected, plane-polarized light) of sulfide-matrix breccia with chalcocite-rich matrix surrounding clasts dominated by quartz-alunite alteration from Yelibelen (sample OD79960; ODD-319, 138.40–138.60 m, 0.25 wt.% Cu). Hypogene pyrite and enargite have been partially replaced by chalcocite in (B)..... 80

Figure 4.26. Paragenetic sequence of the Öksüt Au-Cu deposit, line thicknesses represent relative abundances of minerals. Line thicknesses represent relative abundances of minerals. 81
Figure 4.27. (A) Drill core photograph and (B) microphotograph (reflected, plane-polarized light) of silica and quartz-kaolinite altered breccia from Güneytepe (sample OD79899; ODD-210, 174.10–174.25 m). Pyrite occurs both in clasts and in fractures and vugs. C) Back-scattered electron (BSE) image of pyrite within an aggregate of tabular prismatic alunite crystals. 83
Figure 4.28. Drill core sample of quartz-alunite altered breccia with abundant pyrite and enargite from Keltepe (sample OD79845; ODD-316, 255.30–255.40 m, 0.53 g/t Au, 5.7 wt.% Cu, >1 wt.% As). Minor chalcocite has replaced primary Cu-sufides. 83
Figure 4.29 (A) Drill core photograph and (B and C) microphotographs (reflected, plane-polarized light) silica altered andesite porphyry cut by quartz-sulfide veins porphyry from Keltepe (sample OD79948; ODD-316, 383.60–383.70 m, 0.2 wt.% Cu). Zoned, euhedral crystals of marcasite have been overgrown by enargite, which was in turn partially replaced by minor chalcocite. D) Reflected plane polarized light microphotographs (ODD-399, 33.49-33.64m, 30.5 g/t Au; 0.48 % wt. Cu), ~35μm size native gold and hypogene pyrite from Güneytepe. 84
Figure 4.30. Microphotographs of hypogene sulfides (reflected, plane-polarized light) in sample OD79898 from Güneytepe (ODD-33, 132.30–132.50 m, 0.32 g/t Au, 5.74 wt.%. Cu). (A and B) Intergrown chalcopyrite and pyrite, (B) chalcopyrite-pyrite replacement, (C) disseminations of pyrite, chalcopyrite, and tetrahedrite. Abbreviations: py = pyrite, cpy = chalcopyrite, tet = tetrahedrite. 85
Figure 4.31. Microphotograph (reflected, plane-polarized light) of sample CTS2711 from Güneytepe showing an isolated native gold grain (~30 μm) with pyrite and chalcopyrite (ODD-399, 33.50-33.65 m; 30.5 g/t Au, 0.48 % wt. Cu). 88
Figure 4.32. Microphotograph (reflected, plane-polarized light) of sample CTR2713 from Güneytepe showing an isolated native gold grain (~15 μm in size) alongside

aggregates of pyrite and minor chalcopyrite. Chalcopyrite has mostly been replaced by covellite (ODD-399, 36.30–36.45 m, 11.5 g/t Au, 1.2 % wt. Cu). 88
Figure 4.33. LA-ICP-MS trace of clean and inclusion rich pyrites in CTR2711-A5-2, CTR2711-A3-1 and CTR2711-A3-2 for selected trace elements. The diagram shows overall (A) low Au concentrations in clean pyrite and (B and C) high Au concentrations in inclusion rich pyrites. 89
Figure 4.34. A) Drill core photograph and (B) microphotograph (reflected, plane-polarized light) sample OD79874 from Güneytepe (ODD-12, 53.20-53.27m, 3.39 g/t Au), A) strongly oxidized silica-alunite matrix and clasts dominant breccia, B) native gold around silica with Fe-oxides. Abbreviations: Al = alunite, Sil = silica. 91
Figure 4.35. (A) Drill core photograph and (B-C) microphotographs (reflected, plane-polarized light) sample OD79849 from Keltepe N (ODD-333, 327.60-327.67m, 7.3% wt. Cu), (A) silica matrix breccia with vug and fracture filled native copper and chalcocite, (B) native copper and chalcocite intercalated with each other, (C) native copper replaced chalcocite. Abbreviations: cc = chalcocite. 92
Figure 4.36. A) Drill core photograph, (B) microphotograph (transmitted, plane-polarized light), (C) microphotograph (transmitted, cross-polarized light), (D) microphotograph (reflected, plane-polarized light) sample OD79802 from Güneytepe (ODD-210, 182.00-182.10m, 0.24 g/t Au, 0.6% wt. Cu), A) well crystalline visible needle like fracture filled alunite, B) vug and fracture filled alunite with quartz, C) alunite around vugs, D) chalcocite replaced sooty pyrite. Abbreviations: Qtz = quartz, Alun = alunite, py = pyrite, cc = chalcocite 93
Figure 4.37. (A) Drill core photograph, (B) microphotograph (transmitted, plane-polarized light), (C) microphotograph (reflected, plane-polarized light), sample OD79965 from Keltepe (ODD-316, 180.90-181.00m, 1.33 g/t Au, 1% wt. Cu), (A) strongly silicified and fracture filled malachite, (B) fracture filled malachite around quartz, (C) pyrites are replaced by covellite. Abbreviations: mal = malachite, Qtz = quartz, py = pyrite, cv = covellite. 94
Figure 4.38. (A) Drill core photograph, (B) microphotograph (reflected, plane-polarized light), sample 78952 from Keltepe N (ODD-333, 315.00-315.22m, 3.4 %

wt. Cu), (A) chalcocite-malachite replacement at the paleowater table level in supergene enrichment zone, (B) fracture filled chalcocite minerals. Abbreviations: cc = chalcocite. 95
Figure 4.39. A) Drill core photograph, (B) microphotograph (reflected, plane-polarized light), sample OD78961 from Keltepe N (ODD-333, 332.10-332.20m, 4.5% wt. Cu), A) residual silica with chalcocite veinlets as bandings, B) hypogene enargite and supergene chalcocite minerals. Abbreviations: En = enargite, cc = chalcocite. 96
Figure 4.40. A) Drill core photograph, (B) microphotograph (reflected, plane-polarized light)**,** sample OD79838 from Keltepe (ODD-313, 235.00-235.10m, 2.81 g/t Au, 42.6 % wt. Cu), A) silica altered sheeted pyrite-chalcocite veinlets, B) chalcocite replaced pyrite. Abbreviations: py = pyrite, cc = chalcocite. 97
Figure 4.41. (A) Drill core interval with semi-massive sulfide chalcocite-rich zone with secondary Cu oxides, Cu hydroxy-carbonates and native copper in alunite-matrix breccia from Keltepe N (ODD-333, 328.10–330.90 m). (B) Microphotograph showing (reflected, plane-polarized light) of sample OD79838 (ODD-313, 235.00-235.10m, 2.8 g/t Au, 4.3 wt.% Cu), intense chalcocite replacement and relict pyrite. Abbreviations: cc = chalcocite, mal = malachite, hem = hematite, cup = cuprite, py = pyrite. 98
Figure 4.42. (A) Drill core photograph, (B) microphotograph (reflected, plane-polarized light), (C) microphotograph (transmitted, cross-polarized light) sample OD79952 from Keltepe (ODD-81, 293-293.10m, 0.31 g/t Au, 1.1% wt. Cu), (A) quartz-alunite altered andesitic rock with covellite patches, (B) fracture-filling covellite, (C) fine-grained alunite. Abbreviations: cv = covellite. 99
Figure 4.43. Güneytepe pit wall outcrops, quartz-kaolinite alteration patchy silica transition, also where oxide-sulfide boundary and supergene enrichment zone represented with malachite and native sulfur. 100
Figure 4.44. 40Ar/39Ar spectra of alunite, illite, and secondary biotite from Öksüt. 102

Figure 4.45. A) Drill core photograph, (B-C) microphotograph (transmitted, cross polarized light), sample OD78857 from Boztepe West (far west of Keltepe)- (ODD-337, 77.30-77.40m, 5.858 Ma), A) calc silicate altered brecciated rock with garnet veins, B) zoning in garnet and C) pyroxene-plagioclase dominant clasts and matrix. Abbreviations: pyx = pyroxene, Plg = plagioclase. 104
Figure 4.46. Terra-Wasserburg Concordia plots of garnet U-Pb data for samples (A) OD78857 and (B) OD78859 from Öksüt..... 104
Figure 5.1. Cartoons showing simplified formation model of the Öksüt high-sulfidation epithermal deposit in relation to the DVC. Abbreviations: EFZ = Ecemiş Fault Zone, DF = Develi Fault. 117
Figure 5.2. Cartoon illustrating the temporal evolution of late Cenozoic (middle to late Miocene-early Pliocene) gold-copper mineral districts in south central and western Anatolia in relationship to regional tectonics. Abbreviations: CACC = Central Anatolian Crystalline Complex, EFZ = Ecemiş fault zone, TGFZ = Tuz Gölü fault zone. 118

CHAPTER 1

INTRODUCTION

1.1 Purpose and Scope

Magmatic-hydrothermal ore systems are spatially and temporally associated with igneous activity developed in active tectonic plate margins (e.g., subduction zones, rifted margins) as well as in relation to magmatism developed during or following collision in convergent margins (e.g., Sillitoe, 1972; Lowenstern and Hedenquist, 1994; Sillitoe and Hedenquist, 2003; Richards, 2009 and 2011; Fig. 1.1). Among such magmatic-hydrothermal deposits, porphyry, epithermal, and skarn deposits contribute to an important portion of global base and precious metals production. Porphyry- and skarn-type systems are generally sourced from and centered around sub-volcanic intrusions (Fig. 1.2; Lowenstern and Hedenquist, 1994; Meinert et al., 2005; Seedorff et al., 2005; Sillitoe, 2010). Epithermal deposits on the other hand form at shallow volcanic levels and may or may not be genetically associated with magmatic sources. Nevertheless, in some geological environments these three mineralization styles may occur in continuum with each other around upper crustal volcano-plutonic complexes (Fig. 1.2; Sillitoe, 1973 and 2010).

Formation environments of epithermal systems, as originally defined by Lindgren (1922), is shallow crustal depths (<1 km), where precious and base metal mineralization is generally hosted in altered volcanic or volcanosedimentary rocks. Lindgren (1922 and 1933) also inferred low formation temperatures of up to 200°C, but more recent work has shown that epithermal mineralization can occur within a wider temperature range of ~50–320°C (e.g., Buchanan, 1981; Hedenquist et al., 1996 and 2000; Cooke and Simmons, 2000; Simmons et al., 2005).

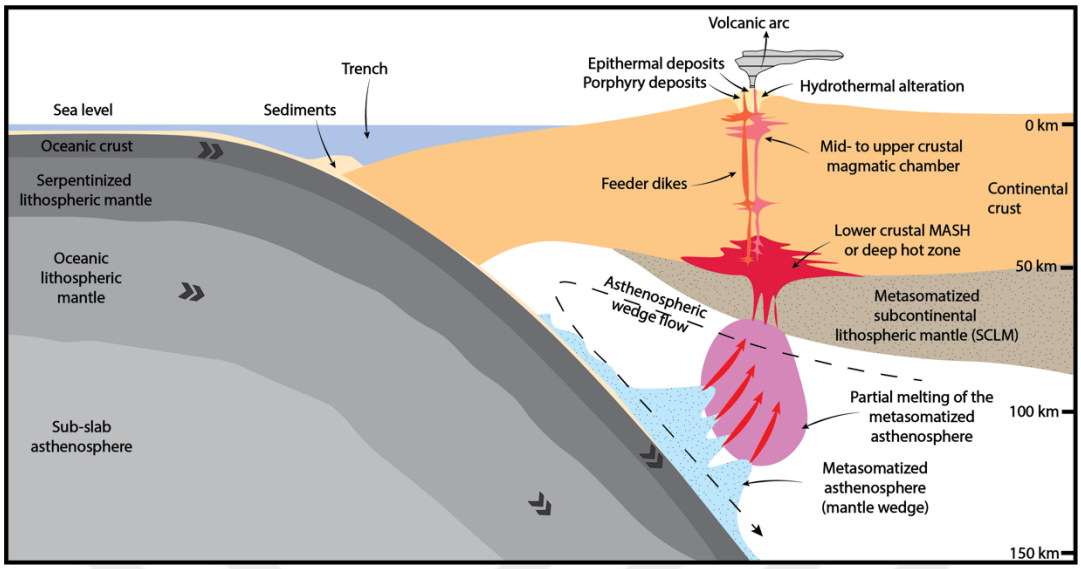


Figure 1.1. Generalized cartoon showing ideal geological setting of porphyry and associated epithermal deposits in relation to subduction-related magmatism (from Winter, 2001; Richards, 2011; Rabayrol, 2018).

Detailed studies on modern geothermal and volcanic-hydrothermal environments have shown that epithermal deposits are analogous to such systems. This connection allowed accurate determination of characteristics of fluids responsible from epithermal ore formation (e.g., Browne et al., 1971; Henley and Ellis, 1983; Hedenquist, 1986, 1990 and 1991; Reyes, 1990; Hedenquist et al., 1993 and 1994).

Based on their fluid characteristics and stability of ore and gangue mineral phases epithermal systems are divided into three groupings with two common end-member types: high-sulfidation and low-sulfidation epithermal deposits (Hedenquist et al., 2000; Sillitoe and Hedenquist, 2003). The former is associated with hydrothermal fluids emanating from shallowly sub-volcanic intrusions typically emplaced in andesitic-dacitic dome complexes in stratovolcanoes (Hedenquist et al., 2000), whereas the latter is found in extensional (rift-related) settings and associated bimodal volcanism (Hedenquist et al., 2000; John, 2001; John et al., 2003). There is a close genetic link between calc-alkaline magmatism developed in arc settings and porphyry Cu±Mo±Au and high-sulfidation epithermal Au mineralization (Sillitoe,

1972; Sillitoe and Hedenquist, 2003; Richards, 2009 and 2011; Figure 1.3A). The main reason behind this relationship is the relatively high oxidation states (Ballhaus, 1993; Brandon and Draper, 1996; Kelley and Cottrell, 2009) as well as water and volatile contents (e.g., S, Cl, F; Davidson, 1996; Noll et al., 1996 de Hoog et al., 2001; Wallace, 2005; Chiaradia, 2020) of subduction-related magmas.

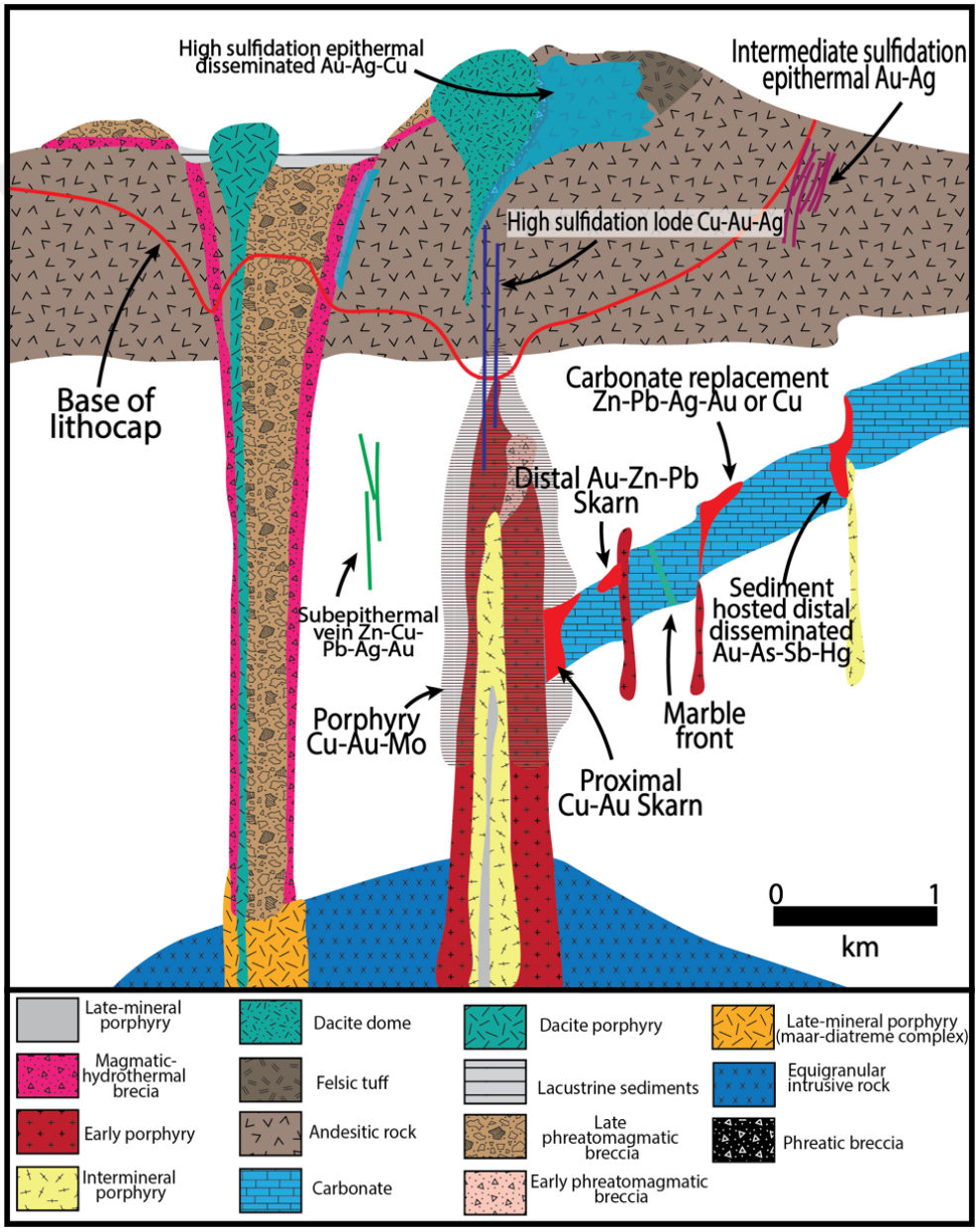


Figure 1.2. Schematic illustration showing distribution of magmatic-hydrothermal deposits that develop within volcano-plutonic settings (Sillitoe, 2010).

In particular, the high oxidation states of arc magmas have a crucial role in porphyry and high-sulfidation epithermal ore formation, since high magma fO_2 enable efficient transportation of chalcophile and siderophile metals (such as Fe, Cu, Au) from mantle depths to shallow crustal levels (Hamlyn et al., 1985; Richards, 2005, 2009 and 2011; Wilkinson, 2013; Park et al., 2021). High water contents, on the other hand, control magma differentiation and fluid exsolution processes leading to magmatic-hydrothermal mineralization (Candela and Holland, 1984; Candela, 1992; Richards, 2005, 2009, and 2011; Chiaradia et al., 2012; Chiaradia, 2020; Park et al., 2021).

Although early research on porphyry and associated epithermal mineralization emphasized their linkage to subduction zone magmatism, extensive work along the Tethyan Belt and in the western Pacific has shown that magmas with broadly similar chemistry and thus with porphyry-epithermal ore-forming potential can also be generated in back-arc, collisional, and post-collisional settings (e.g., Heinrich and Neubauer, 2002; Richards et al., 2012, Hou et al., 2009; Shafiei et al., 2009; Wang et al., 2014; Richards, 2015; Rabayrol et al., 2019). Productive high-K calc-alkaline to mildly alkaline magmas in post-subduction settings can be generated through remelting of previously subduction-modified sources by: 1) continent-continent collision and crustal thickening (Fig. 1.3B), 2) delamination of the lithospheric mantle (Fig. 1.3C), and 3) lithospheric extension following subduction (Fig. 1.3D; Richards, 2009 and 2011).

In both subduction and post-subduction tectonic settings, porphyry and high-sulfidation epithermal deposits form from magmatic fluids exsolving from sub-volcanic intrusions (Richards, 2003; Seedorff et al., 2005; Sillitoe, 2010). Porphyry Cu±Mo±Au mineralization is associated with high temperature (>350°C), high-salinity and near-neutral pH fluids, whereas acidic magmatic vapors with lower temperatures and salinities are responsible from formation of high-sulfidation epithermal Au deposits (Sheppard et al., 1971; Roedder, 1971; Reynolds and Beane, 1985; Cline and Bodnar, 1991; Hedenquist et al., 1998; Heinrich, 2005).

It is possible that within a given shallow crustal magmatic environment, both porphyry- and epithermal-style alteration and sometimes mineralization can develop through evolution of a single magmatic fluid (Hedenquist et al., 1998; Heinrich et al., 2004; Heinrich, 2005; Pudack et al., 2009; Reed et al., 2013). Many high-sulfidation epithermal deposits are underlain by zones of porphyry-style alteration, but districts with spatio-temporally-related and economic epithermal and porphyry mineralization are rare. In the Mankayan district in the Philippines, the Lepanto high-sulfidation epithermal Au deposit is associated with the deeper Far South East porphyry Cu-Au system (Arribas et al., 1995; Hedenquist et al., 1998). Similarly, the giant Yanacocha district in Peru contains several porphyry and epithermal deposits that developed as part of the same magmatic complex (Longo et al., 2010).

Located within the Tethyan Eurasian Metallogenic Belt (TEMB), Turkey hosts numerous epithermal systems as well as some important porphyry deposits. Most of these deposits, including some important examples from the Biga Peninsula, Central Anatolia, Eastern Pontides, and Eastern Anatolia, were formed following closure of the Neotethyan oceanic basins, and thus are regarded as post-subduction deposits (Yiğit, 2012; Richards, 2015; Imer et al., 2013 and 2015; Kuşcu et al., 2019; Rabayrol et al., 2019; Rabayrol and Hart, 2021).

In Anatolia, examples of economic post-subduction high-sulfidation epithermal Au deposits are mostly concentrated in the Biga Peninsula (Ağı Dağı, Kirazlı, Küçükdağ, and TV Tower deposits; Yiğit, 2012; Smith et al., 2014; Leroux, 2016). Additionally, recent exploration efforts by Stratex International plc. resulted in discovery of two important high-sulfidation deposits (İnlice and Öksüt) as well as several other prospects in south-central Anatolia (Tepeköy, Altunhisar, Doğanbey, Çukurağıl; Fig. 1.4). These deposits and prospects are hosted within stratovolcanoes and dome complexes of the regional Late Cenozoic volcanic belt between Kayseri in the east and Konya in the west (Fig. 1.4; Redwood, 2007; Yıldız et al., 2016 and 2017; Kuşcu et al., 2019; Rabayrol et al., 2019; Aluç et al., 2020; Terzi, 2020; Rabayrol and Hart, 2021; Yurdakul et al., 2021).

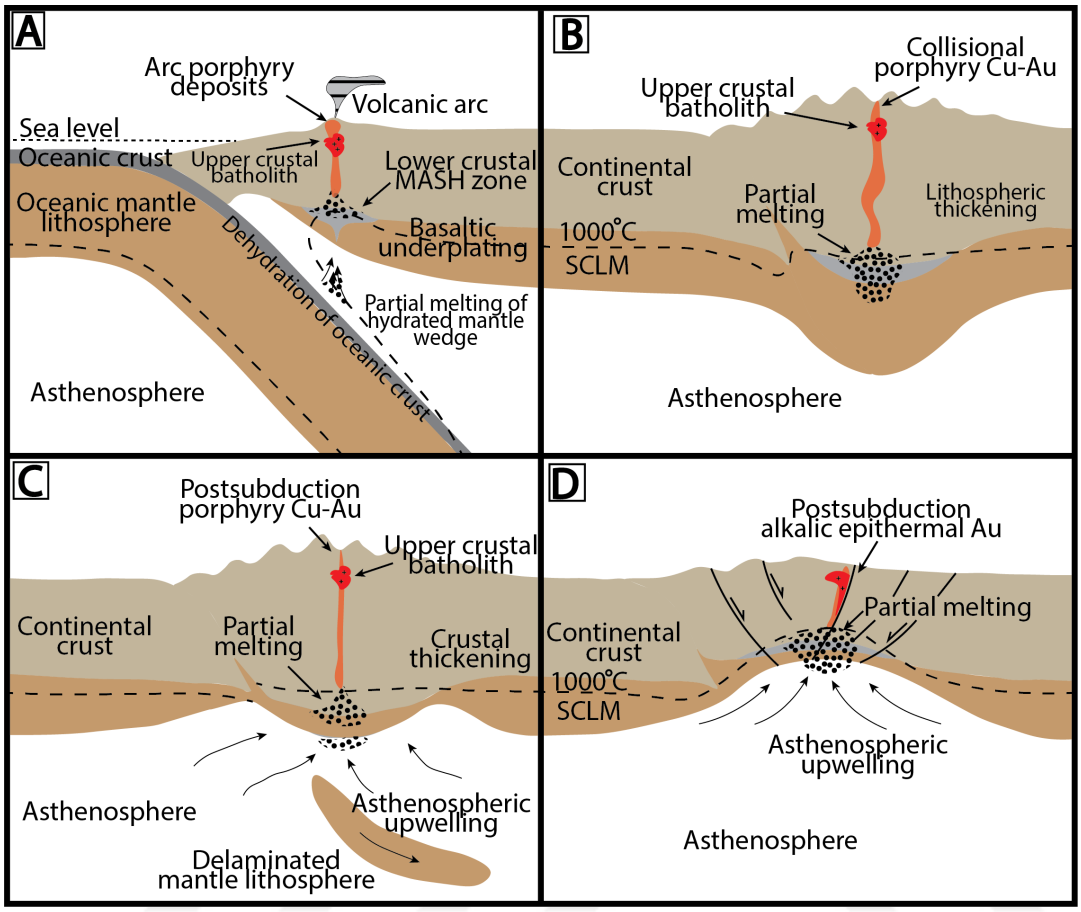


Figure 1.3. Possible tectonic environments of porphyry and epithermal deposits, A) during normal arc magmatism, B) during post-collisional thermal rebound, C) during subcontinental lithospheric mantle (SCLM) delamination and, D) during post-collisional extension leading to lower crustal melting of previously subduction modified lithosphere. Redrafted after Richards (2009).

The Öksüt gold-copper deposit is located near the town of Develi in Kayseri Province and is the most significant high-sulfidation mineralization in Central Anatolia (Figure 1.4). Öksüt was initially discovered by Stratex International plc. in 2007 and was later developed by Centerra Gold. In the tenement area, gold-copper mineralization occurs in a few domains, but to date economic ore was only highlighted in two areas known as the Keltepe and Güneytepe orebodies. Gold production at Öksüt commenced in early 2020 with total reserves of 1.14 Moz Au and an additional resource of 0.28 Moz Au as of late 2021. (https://www.centerragold.com/operations/oksut/resource-estimate).

Despite its regional significance, there are only a few studies in the literature on Öksüt mineralization. In a study that focused on the Late Cenozoic magmatic belt stretching between eastern and western Anatolia, Rabayrol et al. (2019) and Rabayrol and Hart (2021) focused on the regional tectonic and magmatic controls on porphyry and epithermal systems of Miocene age. Rabayrol et al. (2019) and Rabayrol and Hart (2021) reported U-Pb zircon ages and lithogeochemical data from the Develidağ Volcanic Complex (Fig. 1.4) that host the Öksüt high-sulfidation epithermal Au-Cu mineralization.

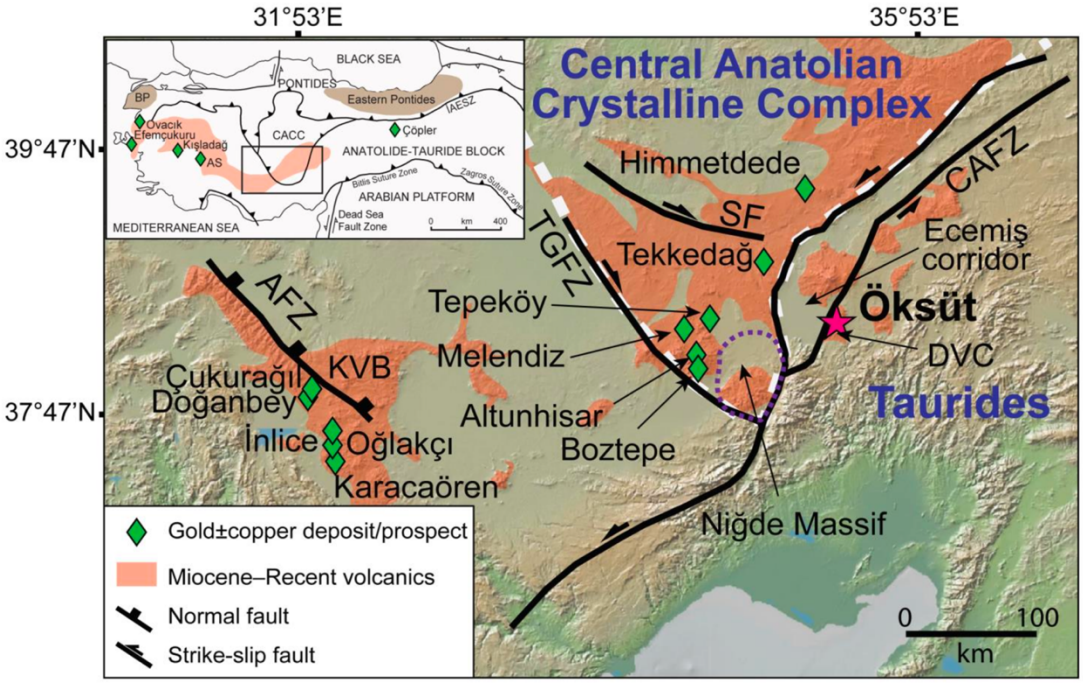


Figure 1.4. Map showing late Cenozoic to Recent volcanics and regionally-important structures in south-central Anatolia (redrafted after Koçyiğit and Beyhan, 1998; Koçyiğit and Erol, 2001; MTA, 2002). Significant deposits and prospects mentioned in the text are also shown. Background digital elevation map retrieved from GeoMap App (https://geomapapp.org). Major tectonic units of Turkey, important metallogenic belts, late Cenozoic central-western Anatolian volcanic belt, and some major gold and copper deposits/prospects are shown in the inset map. Extent of the main map is indicated via black rectangular box in inset map. Abbreviations: AFZ = Akşehir fault zone, BP = Biga Peninsula, CAFZ = Central Anatolian fault zone, DVC = Develidağ Volcanic Complex, IAESZ = Izmir-Ankara-Erzincan suture zone, KVB = Konya volcanic belt, SF = Salanda fault.

Aluç et al. (2020), on the other hand, conducted a more detailed study of the Öksüt deposit. All of these studies showed that high-sulfidation epithermal mineralization at Öksüt is spatially associated with Late Miocene (6–5.3 Ma) calc-alkaline andesitic magmatism developed following closure of the Southern Neotethys ocean basin. Aluç et al. (2020) further provided a brief account of ore paragenesis and hydrothermal alteration styles. In addition, sulfur, oxygen and hydrogen stable isotope analyses revealed a predominantly magmatic origin for the ore-forming fluids at Öksüt (Aluç et al., 2020).

1.1.1 Objectives

The main scientific problems of this thesis study are to understand mineralization characteristics of Öksüt in detail, to determine the timing of hydrothermal alteration at Öksüt, and to understand the relationship between Öksüt gold-copper mineralization and Late Cenozoic tectonomagmatism in south central Anatolia. The research questions identified to solve these problems are as follows:

- What are the ore and gangue mineral assemblages, and main hydrothermal alteration styles?

- How ore mineralization and alteration zones distributed in the deposit area?

- What is the timing of hydrothermal alteration that is related to gold-copper mineralization?

- What are the local and regional geological controls on high-sulfidation mineralization?

According to those questions, identified research objectives are:

- To date hydrothermal alteration minerals in the mineralized system and to determine the timing of hydrothermal alteration.

- To establish a detailed mineralogical framework of ore and gangue minerals through petrography, mineralogy as well as using available lithogeochemical and spectral data from least-altered and altered/mineralized rock samples.

- To demonstrate regional and local geology, volcanic stratigraphy, and tectonism in south central Anatolia.

1.1.2 Methodology

1.1.2.1 Field work

Field work was conducted with two main objectives: (1) for updating the geological maps of the Öksüt license area as prepared by Stratex plc. and Centerra Gold geologists, (2) sampling of drill core samples.

A total of 265 drill core samples were collected from 17 drill holes particularly from Keltepe and Güneytepe areas, as well as from five other satellite prospects (Appendix A). Sampled drill holes were selected on the basis of their representativeness of the altered and mineralized zones, and the magmatic system in the Öksüt property. Sampling was undertaken in three separate periods: initially in December 2018 and later in 2019 and 2020. Collected drill core samples were halved at the site and each sample was photographed for archiving purposes. In addition, drill core logging was carried out routinely during the 2018 and 2019 drilling programmes.

1.1.2.2 Petrography

A total of 140 polished thin sections were prepared from hydrothermally-altered and/or mineralized rock samples as well as from the least-altered igneous rock samples at the Geological Engineering Department of the Middle East Technical University. Polished thin sections were analyzed using a transmitted-reflected light

petrographic microscope for determination of mineral assemblages, textures, and for obtaining mineral paragenesis. Petrographic observations were supplemented by scanning electron microscopy (SEM) (Appendices D–K), X-ray diffraction (XRD) (Appendices B–C) and TerraSpec analyses, particularly for more accurate identification of alteration minerals (such as alunite and illite) selected for geochronological analyses.

1.1.2.3 Laser-ablation inductively-coupled mass-spectrometry (LA-ICP-MS)

Following petrographic examination, two gold mineralized samples representing hypogene mineralization at Öksüt were selected for LA-ICP-MS analyses. The purpose of LA-ICP-MS analyses was to determine trace element abundances in sulfide minerals, and particularly for understanding gold deportment, which was suspected to be largely in refractory form in pyrite at Öksüt.

LA-ICP-MS analyses were conducted at the Adelaide Microscopy Lab, Adelaide University (Australia). A resolution 193nm ArF excimer laser ablation system (Applied Spectra, USA) with a large volume S155 sample chamber (Laurin Technic, Australia) was coupled to an Agilent 7900x ICP-MS. Samples were ablated at a spot size of 30 μm, with a fluence at the sample of ~3 J/cm2 and a repetition rate of 5 Hz. Samples were ablated in a He atmosphere (flow rate 0.35 L/min) and the aerosol mixed with Ar carrier gas (flow rate 1.06 L/min) for transport to the ICP-MS. Each spot ablation and analysis were timed for ~70 seconds, being 30 seconds counting on background, 4 seconds wait time, and 36 seconds analysis on the pyrite grain. The STDGL3 standard (CODES, University of Tasmania) was used as the primary reference material for calibration and drift correction, and GSD-1G (United States Geological Survey) was used as a secondary standard. The two different standards were analyzed before, during and after analysis of the unknowns, for a total of 20 analyses of the standards.

1.1.2.4 $^{40}Ar/^{39}Ar$ and U-Pb geochronology

$^{40}Ar/^{39}Ar$ dating of K-bearing minerals and U-Pb dating of garnet were attempted to constrain the timing of hydrothermal activity at Öksüt. Biotite, alunite, and garnet were initially identified through petrography. Alunite-bearing samples were further analyzed through XRD and TerraSpec to distinguish between K- and Na-alunite. Same procedures were followed for confirmation of K-bearing illite in clay-altered rock samples.

Four samples (two alunite, one illite, and one biotite) selected for $^{40}Ar/^{39}Ar$ dating were sent to Nevada Isotope Geochronology Lab (NIGL) at the University of Nevada, Las Vegas (USA) for sample preparation and geochronological analyses. Following mineral separation, samples were wrapped in pure Al foil and irradiated in the TRIGA type reactor at the Nuclear Science Center of Texas A&M University. All samples yielded disturbed spectra, and, in this case, total fusion ages are considered to be more reliable. Full analytical procedures for $^{40}Ar/^{39}Ar$ geochronological analyses are provided in Appendices O–P.

Two garnet samples from calc-silicate alteration zones were dated through U-Pb geochronology at the Radiogenic Isotope Facility at the University of Queensland (Australia), (Appendix Q). U-Pb isotopic measurements were conducted on garnet grain mounts using a Nu Plasma II MC-ICP-MS or a Thermo iCap-RQ quadrupole ICP-MS (for cross-calibration of high-U garnet standards), equipped with an ASI resolution SE 193 nm ArF-excimer laser. The Nu Plasma II MC-ICP-MS consists of 15 Faraday cups and 5 secondary electron multipliers capable of static collection of all ^{238}U-^{232}Th-^{208}Pb-^{207}Pb-^{206}Pb-^{204}(Pb, Hg)-^{202}Hg ion beams. The $^{238}U/^{206}Pb$ ratios of garnets were calibrated with a matrix-matched reference material, the Taochong garnet (TC-13: 126.2 ± 2.3 Ma). Raw data reduction was completed using Iolite software_v3.64 (Paton et al., 2011). Garnet U-Pb ages were calculated with the online IsoplotR program (Vermeesch, 2018).

1.2 Epithermal Deposits

Epithermal deposits are a common sub-class of hydrothermal ore deposits that significantly contribute to global precious and base metal production. Epithermal systems were initially recognized by Emmons (1918) and Lindgren (1933) and were classified mainly on the basis of formation temperature and depth (<1 km depth, <250°C). Formation conditions of epithermal deposits were better constrained by improvement of analytical techniques (e.g., stable isotope and fluid inclusion studies) and these are now commonly accepted to form in the shallow crustal depths from low temperature (commonly <300°C), low salinity (typically <5 wt.% NaCl equiv.) fluids (Hedenquist et al., 2000; Sillitoe and Hedenquist, 2003; Simmons et al., 2005).

Later classification schemes of epithermal systems considered dominant ore/gangue mineralogy or fluid pH (acidic vs. alkaline; Sillitoe, 1977; Ashley, 1982; Hayba et al., 1985; Heald et al., 1987; Berger and Henley, 1989). Most recently, however, Hedenquist et al. (2000) and Sillitoe and Hedenquist (2003) used a sub-division based on the stable sulfur species in relation to oxygen and sulfur fugacities. Two end-member types defined by this classification scheme are high-sulfidation and low-sulfidation epithermal deposits. A third sub-type, the intermediate-sulfidation epithermal systems, share some characteristics of the former two sub-types.

High-sulfidation (HS) epithermal systems form within shallow levels of volcano-plutonic complexes, where they are spatially associated with calc-alkaline andesitic-dacitic dome complexes and stratovolcanoes (Hedenquist et al., 2000). Typical tectonic settings are convergent margins undergoing compression or transtension/transpression (Sillitoe and Hedenquist, 2003). In such geologic environments, magmatic vapors derived from shallowly crystallizing intrusions may be discharged to the surface or sub-surface environment (Hedenquist et al., 2000). Initially at the time of exsolution from sub-volcanic intrusions, these magmatic vapors are mainly in the form SO_2, which disproportionate into a mixture of H_2S and sulfuric acid (H_2SO_4) upon ascent (Hedenquist et al., 2000). Consequently, at

shallow levels the magmatic vapors become increasingly acidic and oxidized, leading to intense acid alteration and stabilization of sulfide minerals with high sulfidation states (Barton and Skinner, 1979; Hedenquist et al., 2000; Einaudi et al., 2003).

Alteration in HS epithermal deposits is typically zoned due to acid buffering, from an inner zone of residual/vuggy quartz through quartz-alunite-kaolinite-dickite and to quartz-illite-chlorite outwards (Stoffregen, 1987; Hedenquist and Taran, 2013; Hedenquist and Arribas, 2022). Main ore fluid causing hydrothermal alteration and mineralization is predominantly magmatic in origin, but this fluid may mix with cool meteoric waters at shallow depths (Rye, 1993; Mancano and Campbell, 1995). Hedenquist et al. (1998) and Muntean and Einaudi (2001) indicated that both epithermal and porphyry systems may form from a single phase magmatic fluid sourced by a magma chamber, but this magmatic volatile may separate into a liquid and a vapor phase upon ascent (Hedenquist et al., 1998; Heinrich et al., 2004; Heinrich, 2005), and while buoyant vapor may cause formation of an epithermal system, dense brine fluid tends to remain at depth leading to porphyry-style alteration and sometimes mineralization (Henley and McNabb, 1978; Sillitoe, 193; Heinrich et al., 1999). Hedenquist et al. (1998) stated that the initial magmatic vapor does not cause ore mineralization, but Heinrich et al. (1992) stated that vapor-rich inclusions in Mole Granite (Australia) contain high concentrations of copper.

Sulfide mineral abundances in HS epithermal systems vary between 5 and 90 vol.%., and ore mineral assemblage is represented by pyrite, enargite, covellite, digenite, famatinite, and luzonite (Hedenquist et al., 2000). Copper concentrations in HS epithermal deposits may be at economic levels, but silver is typically insignificant. Mineralization is generally in the form of breccias and disseminations, in close association with diatreme structures (Hedenquist et al., 2000). Formation depths are up to 700 m and ore fluids have temperatures in the range 150°–300°C, salinities between 0 to 6 wt.% NaCl equiv. and fluid pH is very low (e.g., Lindgren, 1933; Heald et al., 1987; Sillitoe, 1993 and 1999; White et al., 1995; Hedenquist et al., 2000).

The other end-member of the epithermal clan, the low-sulfidation (LS) epithermal systems, may not be necessarily related to volcanic activity in contrary to HS epithermal deposits. LS epithermal deposits are hosted in calc-alkaline andesitic to rhyolitic or tholeiitic bimodal (basaltic-rhyolitic) volcanic lithologies developed in extensional tectonic environments (Hedenquist et al., 2000). Fluids are dominated by meteoric waters that are convected by the heat of deeper intrusions (Hedenquist et al., 2000), with little to no magmatic contributions (Hedenquist et al., 2000). Consequently, hydrothermal fluids in LS epithermal deposits have relatively low oxygen and sulfur fugacities compared to the HS epithermal ore fluids (Hedenquist et al., 2000).

Due to the lower oxidation states and acidity of the fluids, alteration is caused by less corrosive fluids that have near neutral to slightly acidic pH (e.g., Hedenquist et al., 2000). Main alteration minerals are quartz-illite-chlorite ± adularia ± kaolinite ± carbonate, and barite and fluorite are common gangue minerals (e.g., Hedenquist et al., 2000). Sulfides are found in small concentrations (generally <2 vol.%) are represented by pyrite, marcasite, arsenopyrite, gold-silver sulfides/sulfosalts (Hedenquist et al., 2000). These minerals occur in sheeted to stockwork veins with banded textures (e.g., colloform, crustiform) as well as in hydrothermal breccia zones commonly emplaced along faults (Hedenquist et al., 2000). Mineralization in LS epithermal deposits may be restricted to shallower depths (from surface down to 400 m), and occurs from low temperature (100°–220°C), low salinity (0–6 wt.% NaCl equiv.) near neutral to slightly acidic fluids (e.g., Sillitoe, 1993 and 1999; White et al., 1995; John et al., 1999; Hedenquist et al., 2000).

Similar to HS epithermal deposits, intermediate-sulfidation (IS) epithermal deposits are also associated with andesitic calc-alkaline magmatism in extensional or compressional arc environments (Sillitoe and Hedenquist, 2003). IS and HS epithermal systems also resemble each other as both are sourced from magmatic fluids (Simmons, 1991; Albinson et al., 2001), and therefore it is also possible for IS epithermal systems to be spatially related to deeper porphyry systems (Hedenquist et al., 2000; Sillitoe and Hedenquist, 2003). On the other hand, hydrothermal fluids

in IS epithermal deposits have intermediate oxygen and sulfur fugacities, and as such fluid pH and alteration mineralogy is similar to LS epithermal deposits (Hedenquist et al., 2000). Main alteration minerals are quartz-illite ± adularia ± carbonate reflecting near neutral to slightly acidic nature of ore fluids. In contrary, however, to both HS and LS epithermal systems, base metal sulfide abundance in IS epithermal systems is often high (from 5 to >20 vol.%) with pyrite, gold-silver sulfides, chalcopyrite, sphalerite, galena, and tetrahedrite/tennantite as common sulfide mineral phases (Hedenquist et al., 2000 and Sillitoe, 1999). In addition, mineralization occurs in colloform/crustiform-banded veins, hydrothermal breccias over a relatively large depth range (down to 1000 m) from low temperature (135°–280°C) fluids with relatively high salinities (<10–23 wt.% NaCl equiv.; Hedenquist et al., 2000; Sillitoe and Hedenquist, 2003; Simmons et al., 2005).

CHAPTER 2

REGIONAL GEOLOGY

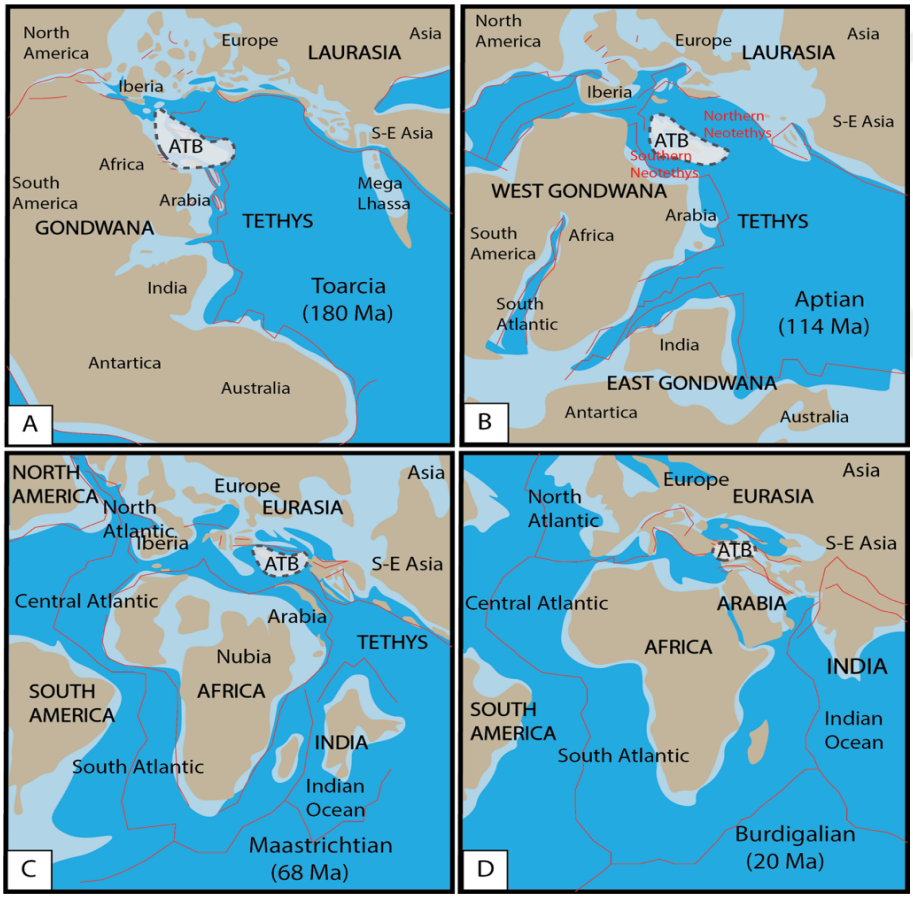
2.1 Geologic History of South-Central Anatolia

Geotectonic setting of Turkey is highly complex as it comprises Gondwana- and Laurasia-derived (Figure 2.1) tectonic fragments that have been juxtaposed against each other. Based on the early classification of Ketin (1966), Anatolia is sub-divided into four major tectonic entities: the Pontides, the Anatolides, the Taurides, and the Arabian Block, separated from each other by major suture zones represented by ophiolite belts (Şengör and Yilmaz, 1981; Okay and Tüysüz, 1999; Figure 2.2).

These fragments were once separated from each other by a long-lived oceanic system that is known as the Tethys Ocean. Rifting off of these fragments from Gondwanan and Laurasian margins and their subsequent amalgamation were developed in relation to the evolution of various Tethyan oceanic basins (e.g., Şengör and Yılmaz, 1981; Stampfli and Borel, 2002; Okay, 2008; Göncüoğlu, 2010; Figure 2.1).

Major Tethyan oceanic domains existed between Gondwana and Laurasia since at least the Paleozoic (Stampfli and Borel, 2002). Although the history of Paleotethys has been relatively poorly-understood, there is a general agreement that this ocean basin was largely diminished by the Late Triassic (Şengör, 1987; Stampfli and Borel, 2002 and 2004). The initiation of the younger Neotethys Ocean was contemporaneous with the closure of Paleotethys, and was a consequence of breaking up and northward drifting of a swath of continental fragments (known as Cimmerian fragments) from the northern margin of Gondwana (Şengör, 1979 and 1987; Stampfli et al., 1991). On the other hand, geochemical data obtained by Sayit et al. (2017) suggest that openning of the Neotethys should be lower Triassic or earlier. South-central Anatolia lies within the composite Anatolide-Tauride Block

(ATB), which is one of a number of continental blocks that form the Cimmerian fragments (Şengör, 1979; Figure 2.1). Anatolides represent the metamorphosed northern part of ATB and includes the Afyon and Tavşanlı Zones, as well as two metamorphic massifs, the Menderes Massif and the Kırşehir Massif (Central Anatolian Crystalline Complex; Figures 2.2 and Figure 2.3). Taurides, on the other hand, is mainly made up of Paleozoic–Mesozoic platformal carbonates (Moix et al., 2008), and share a similar Paleozoic stratigraphy with the Arabian Platform including Late Ordovician glacial deposits (Monod et al. 2003).



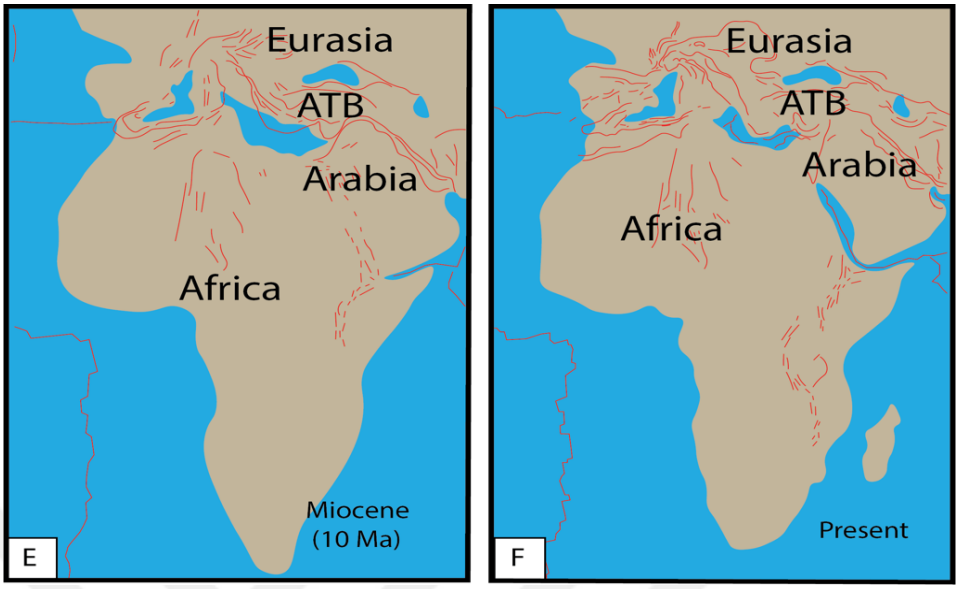


Figure 2.1. Paleogeographic reconstructions showing northward migration of the Anatolide-Tauride Block (ATB) in the Mesozoic with respect to the opening and closure of the Northern and Southern Neotethys: A. 180 Ma, B. 114 Ma, C. 68 Ma, D. 20 Ma. E. 10 Ma, F. Present. Modified and redrafted after Barrier and Vrielynck (2008) and Rabayrol (2018).

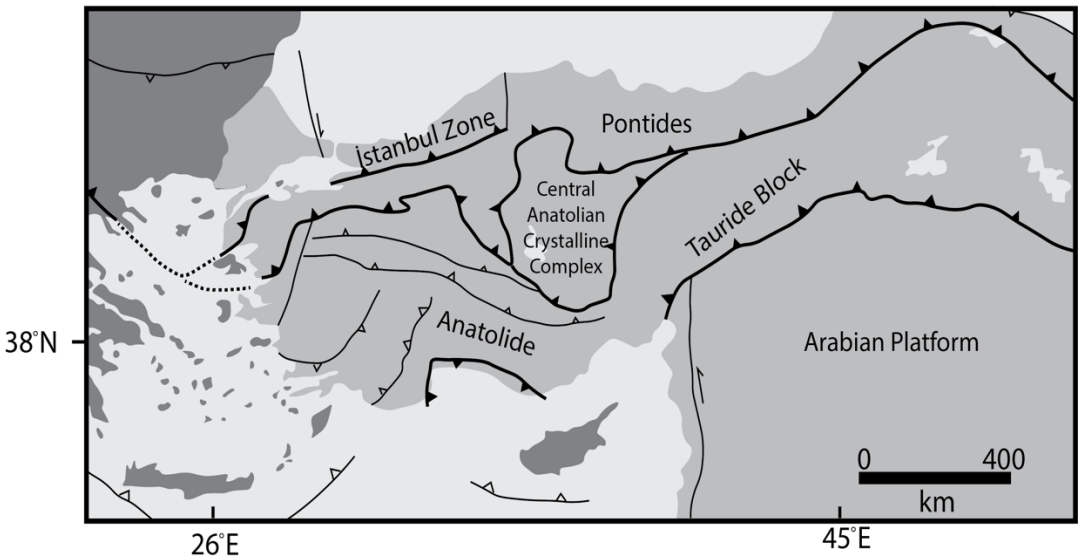


Figure 2.2. Major tectonic units including major suture zones of Turkey. Bold lines with filled triangle are former subduction units and lines with triangles are active suture zones and strike slip faults are represented with its movement arrows. After Okay and Tüysüz (1999) and Okay (2008).

2.1.1 Mesozoic–Cenozoic tectonic development of south-central Anatolia

The south-central part of Turkey between the Konya Province in the west and Kayseri Province in the east lies at the transition between two major tectonic entities; the Central Anatolian Crystalline Complex (CACC) and the Taurides (Figure 1.4).

The Central Anatolian Crystalline Complex (CACC or the Kırşehir Block; Göncüoğlu et al., 1991; Görür et al., 1984) is one of the two metamorphic massifs that comprise the Anatolides (Fig. 2.3); the other being the Menderes Massif. It is located between the İzmir-Ankara-Erzincan Suture Zone in the north and the Taurides in the south (Figure 2.3). Two major structural zones, the Ecemiş and Tuz Gölü Fault Zones, define the eastern and western boundaries of CACC, respectively (Figures 2.3 and 2.4). The origin of the CACC has been widely debated with some researchers considering it as the metamorphosed northern margin of the Anatolide-Tauride Block (Poisson et al., 1996; Yalınız et al., 2000; Köksal et al., 2013), whereas others proposed that it was a separate tectonic entity separated from the Taurides by the Inner Tauride Suture (Şengör and Yılmaz, 1981; Şengör et al., 1982; Görür et al., 1984; Okay, 1984; Gökten and Floyd, 1987; Gökten, 1993; Pourteau et al., 2010).

The CACC mainly comprises Paleozoic–Mesozoic metamorphic rocks, Late Cretaceous–Paleogene granitoids, and younger sedimentary and volcanic cover (Göncüoğlu et al., 1991). Collision between the Pontides and the CACC occurred in the Late Cretaceous–Paleocene (e.g., Göncüoğlu et al., 1997; Kaymakçı et al., 2009; Robertson et al., 2009; Meijers et al., 2010; Lefebvre et al., 2013; Espurt et al., 2014) eliminating the intervening Northern Neotethys basin. This resulted in obduction of ophiolitic blocks and mélange onto the northern margin of the CACC (Göncüoğlu et al., 1997; Yalınız et al., 1999; Toksoy-Köksal et al., 2009). Klippen of ophiolites and ophiolitic mélange can also be observed as overlying the metamorphic basement along the southern border of the CACC with the Taurides (Yalınız et al., 1996, 2000; Yalınız and Göncüoğlu, 1998; Göncüoğlu, 2010; Figure 2.4). However, the origin of the ophiolites is contentious. Some researchers interpreted these to have formed

within an oceanic basin ("Inner Tauride Ocean") located to the south of the CACC (Dilek et al., 1999; Özer et al., 2004; Parlak et al., 2013), whereas others suggested that the ophiolites were derived from a northerly basin (likely the Northern Neotethys Ocean) and were later swept southwards during unroofing of the CACC (Görür, 1981; Seymen, 2000; Moix et al., 2008; van Hinsbergen et al., 2016).

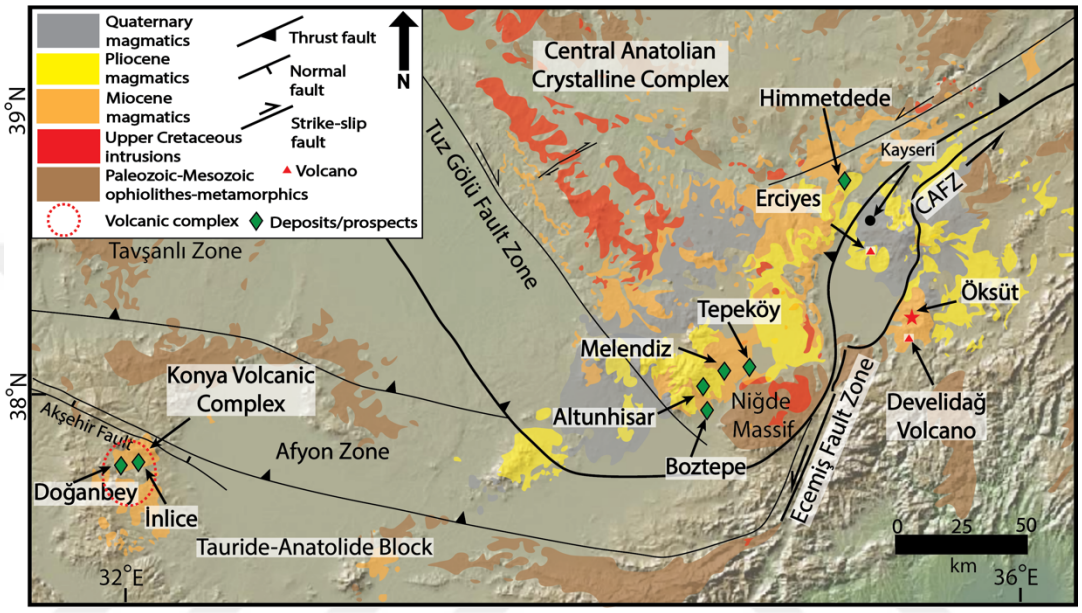


Figure 2.3. Regional map showing magmatic and metamorphic domains of the southern part of the Central Anatolian Crystalline Complex including major structures, important volcanic provinces, and epithermal deposits and prospects. Modified after MTA (2002).

There are three major metamorphic domains identified within the CACC as the Akdağ, Kırşehir and Niğde massifs. These were formed as a consequence of Alpine orogeny mainly during the Mesozoic (e.g., Vache, 1963; Göncüoğlu, 1977; Seymen, 1982; Göncüoğlu et al., 1991; Whitney et al., 2001). Following closure of the surrounding oceanic domains ophiolite obduction onto the CACC basement, widespread granitoid magmatism developed mainly between ~95 and 70 Ma (Göncüoğlu, 1986; Güleç, 1994; İlbeyli et al., 2004; Köksal et al., 2004 and 2012; Kadıoğlu et al., 2005 and 2006; Işık et al., 2008; Boztuğ et al., 2009; van Hinsbergen et al., 2016).

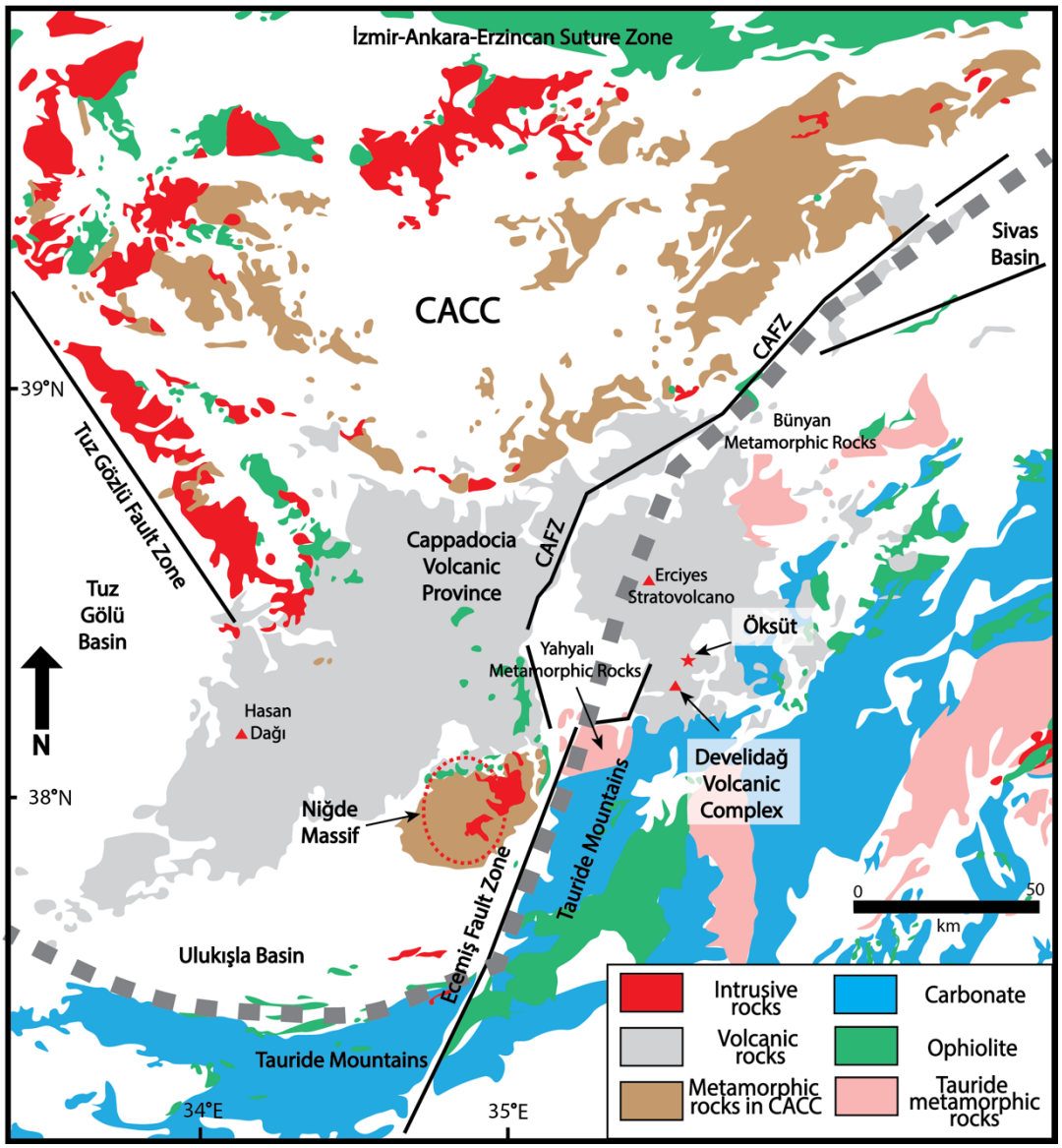


Figure 2.4. Simplified regional geological map of the Central Anatolian Crystalline Complex (CACC) and the Central Taurides. Inner Tauride suture (?) is demonstrated with grey dash line and fault zones are shown with bold lines. Modified after Umhoefer et al. (2020).

Emplaced plutons display a wide range of compositions but are predominantly represented by calc-alkaline to shoshonitic granites, quartz-monzonites and syenites with less common dioritic to gabbroic units (e.g., Göncüoğlu and Türeli, 1994; Erler and Göncüoğlu, 1996; İlbeyli et al., 2003; Kadıoğlu et al., 2005 and 2006; Toksoy-

Köksal, 2019). Tectonic settings proposed for granitoid emplacement include subduction-related to within-plate environments including post-collisional settings (İlbeyli et al., 2003; Köksal et al., 2004; Kadıoğlu et al., 2005 and 2006; Boztuğ et al., 2009, Toksoy-Köksal, 2019).

The southerly Taurides, on the other hand, is an E–W-elongated tectonic fragment that is mainly represented by extensive nappes of platformal carbonates (Ketin, 1966; Şengör and Yilmaz, 1981; Özgül, 1984). The Neoproterozoic Pan-African basement rocks (Hetzel and Reischmann, 1984; Kröner and Şengör, 1990; Gürsü et al., 2004; Gürsu and Göncüoğlu, 2006) are overlain by Cambrian red clastics (Erdoğan et al., 2004), which pass into a thick carbonate sequence starting from the Devonian and continuing into the Cretaceous (Demirtaşlı, 1984; Göncüoğlu and Turhan, 1984; Özgül, 1984).

The closure of the Southern Neotethyan basins resulted in nappe stacking and ophiolite obduction (Özgül, 1976 and 1984). These nappes, known as the Bozkır, Bolkardağ, Aladağ, Geyik, Antalya, and Alanya Units, display distinctive stratigraphic sequences (Özgül, 1976 and 1984). Thrusting of ophiolites and marginal sequences onto the Tauride belt likely initiated during the Cretaceous–early Eocene and nappes re-thrusted onto the late Tertiary cover in the middle Miocene (Göncüoğlu, 2010).

Despite the contradicting models on the relative positioning of the CACC and the Taurides, paleogeographic reconstructions agree that these were in contact with each other during the Paleogene (van Hinsbergen et al., 2016). Although the accretion of Taurides onto the southern margin of the CACC continued until the Eocene (van Hinsbergen et al., 2016), the latest Cretaceous to middle Eocene was a major period of crustal extension within the CACC (Delph et al., 2017). This resulted in development of several sedimentary basins (Ulukışla, Haymana, Sivas, and Tuz Gölü basins; Görür et al., 1984; Göncüoğlu et al., 1993; Cater et al., 1991; Koçyiğit, 1991; Clark and Robertson, 2002; Gülyüz et al., 2019). Another consequence of this extensional period at the lithospheric scale was asthenospheric upwelling leading to

high heat-flux, crustal melting, and a younger pulse of granitoid emplacement (Kadıoğlu and Dilek, 2010; Kuşcu et al., 2001). Eocene intrusive magmatism was less widespread compared to Late Cretaceous igneous activity and was mainly observed in the southern and southeastern margin of the CACC and partly along the northern margin of the Taurides (Gençalioğlu-Kuşcu et al, 2001; Kadıoğlu and Dilek, 2010; Parlak et al., 2013).

The Late Cretaceous to Eocene intrusive magmatism in the central and eastern Anatolide-Tauride Block was a product of northward subduction of the Southern Neotethys basin (Boztuğ et al., 2006; Kaygusuz et al., 2008; Ustaömer and Robertson, 2010). Closure of Southern Neotethys initiated during the Oligocene possibly by "soft-collision" between the Anatolide-Tauride Block and the Arabian Platform (Allen and Armstrong, 2008; Allen, 2009; Boulton, 2009; Ballato et al., 2011; McQuarrie and van Hinsbergen, 2013), but the terminal closure of this ocean basin did not occur until the middle Miocene (Dewey et al., 1986; Robertson et al., 2007; Hüsing et al., 2009; Okay et al., 2010). For much of the Oligocene, the Anatolide-Tauride Block underwent compressional deformation due to the initiation of "soft-collision" (e.g., Cater et al., 1991; Robertson et al., 2007; Hüsing et al., 2009).

A major episode of extensional deformation commenced throughout the entire Anatolide-Tauride Block during the late Oligocene–middle Miocene. A switch from compression to extension/transtension led to development of normal and strike-slip faults, a majority of which are still active today (Görür et al., 1984; Dirik and Göncüoğlu, 1996; Koçyiğit and Beyhan, 1998; Jaffey and Robertson, 2001; Koçyiğit and Erol, 2001; Jaffey et al., 2004; Özsayın et al., 2013). The Miocene to Recent Central Anatolian Volcanic Province between Nevşehir-Niğde-Kayseri (including the Develidağ Volcanic Complex hosting the Öksüt deposit) and other regional Late Cenozoic volcanic centers such as the Erenlerdağ Volcanic Complex (Konya) developed during this stage (Pasquare et al., 1988; Toprak and Göncüoğlu, 1993; Toprak, 1994; Temel et al., 1998; Tatar et al., 2002).

Late Miocene to Recent volcanism in south-central Anatolia is attributed to foundering of mantle lithosphere beneath central Anatolia (Bartol and Govers, 2014; Delph et al., 2017; Göğüş et al., 2017; Gal et al., 2021; Figure 2.5), which culminated in production of widespread ignimbrite deposits as well as numerous stratovolcanoes, monogenetic lava flows, dome complexes, and cone clusters (Innocenti et al., 1975; Pasquare et al., 1988; Figures 2.3 and 2.4). Volcanic products display varying compositions from basalt through andesite-dacite to rhyolite, which are predominantly calc-alkaline to mildly alkaline and show arc-like affinities (e.g., Gencalioglu-Kuscu and Geneli, 2010; Kürkçüoğlu, 2010; Reid et al., 2017), indicating a significant contribution from previous subduction-modified mantle lithosphere.

2.1.2 Geology of The Ecemiş Corridor

2.1.2.1 Structure

The Ecemiş corridor is represented by a roughly NNE-SSW-trending depression bounded by sub-parallel segments of the Ecemiş Fault Zone (Figures 2.3 and 2.4). The Ecemiş Fault Zone forms part of the lithospheric-scale Central Anatolian Fault Zone (CAFZ; Koçyiğit and Beyhan, 1998; Koçyiğit and Erol, 2001), where the NE-trending CAFZ makes a bend in the vicinity of the Erciyes Stratovolcano (Figures 2.3 and 2.4).

Although neotectonic activity of the Ecemiş Fault Zone is well-known and has been studied extensively, it is likely a paleotectonic feature initiated because of internal deformation of the Anatolide-Tauride Block during the Late Cretaceous–Eocene (Yetiş, 1978; Gül et al., 1984; Koçyiğit and Beyhan, 1998; Koçyiğit and Erol, 2001). The predominantly strike-slip movement along the Ecemiş Fault Zone is fault zone accommodated transtensional deformation in the Paleogene, but this switched into prominent transpression during the Eocene–Oligocene period (Umhoefer et al., 2020) and was later reactivated in the Miocene as an extensional structural system

(Gül et al., 1984; Koçyiğit and Erol, 2001; Jaffey et al., 2004; Umhoefer et al., 2020). The left-lateral displacement of the Ecemiş Fault Zone is estimated to be between 60 and 80 km (Koçyiğit and Beyhan, 1998; Jaffey and Robertson, 2001).

CAFZ's bend from its South with a 050N trend to a 005-010N trend that caused to sinistral releasing bend, which finally nucleated a large pull-apart basin called the Erciyes pull-apart basin. Morphologically this S-shaped basin is about 35 km-wide, 120 k-long, >1 km deep (Koçyiğit and Beyhan, 1998). The basaltic-andesitic Erciyes Stratovolcano occupies the central part of the basin (Koçyiğit and Beyhan, 1998).

Develi fault segment of the Ecemiş Fault Zone has a normal-slip component which located in east-southeast of the CAFZ and determines the boundary of the Erciyes basin. Also, the Dündarlı-Erciyes fault cuts the Erciyes Stratovolcano and caused to up to 70 m sinistral displacement (Koçyiğit and Beyhan, 1998). In detail, the 104 km-long Develi segment of the Ecemiş Fault Zone is an oblique-slip normal fault that dips west and has a NNE trend (Koçyiğit and Beyhan, 1998). It consists of several parallel to sub-parallel smaller faults that are closely spaced and have normal slip components (Koçyiğit and Beyhan, 1998). This group of faults caused a step-like westward facing morphotectonic pattern and a steep scarp with a relief of 925 m (Koçyiğit and Erol, 2001). Along the Develi Fault, the middle Miocene–early Pliocene volcanic rocks of the Develidağ and Koçdağ have been deformed (Koçyiğit and Beyhan, 1998).

2.1.2.2 Stratigraphy

Lithological units of the Develidağ area are related to middle Miocene–Quaternary volcanism in the Cappadocian volcanic plateau of the Central Anatolian Volcanic Province, and to Cenozoic sedimentary basin development in the vicinity of the Erciyes pull-apart basin along the Central Anatolian Fault Zone (Koçyiğit and Erol, 2001; Figures 2.3 and 2.4).

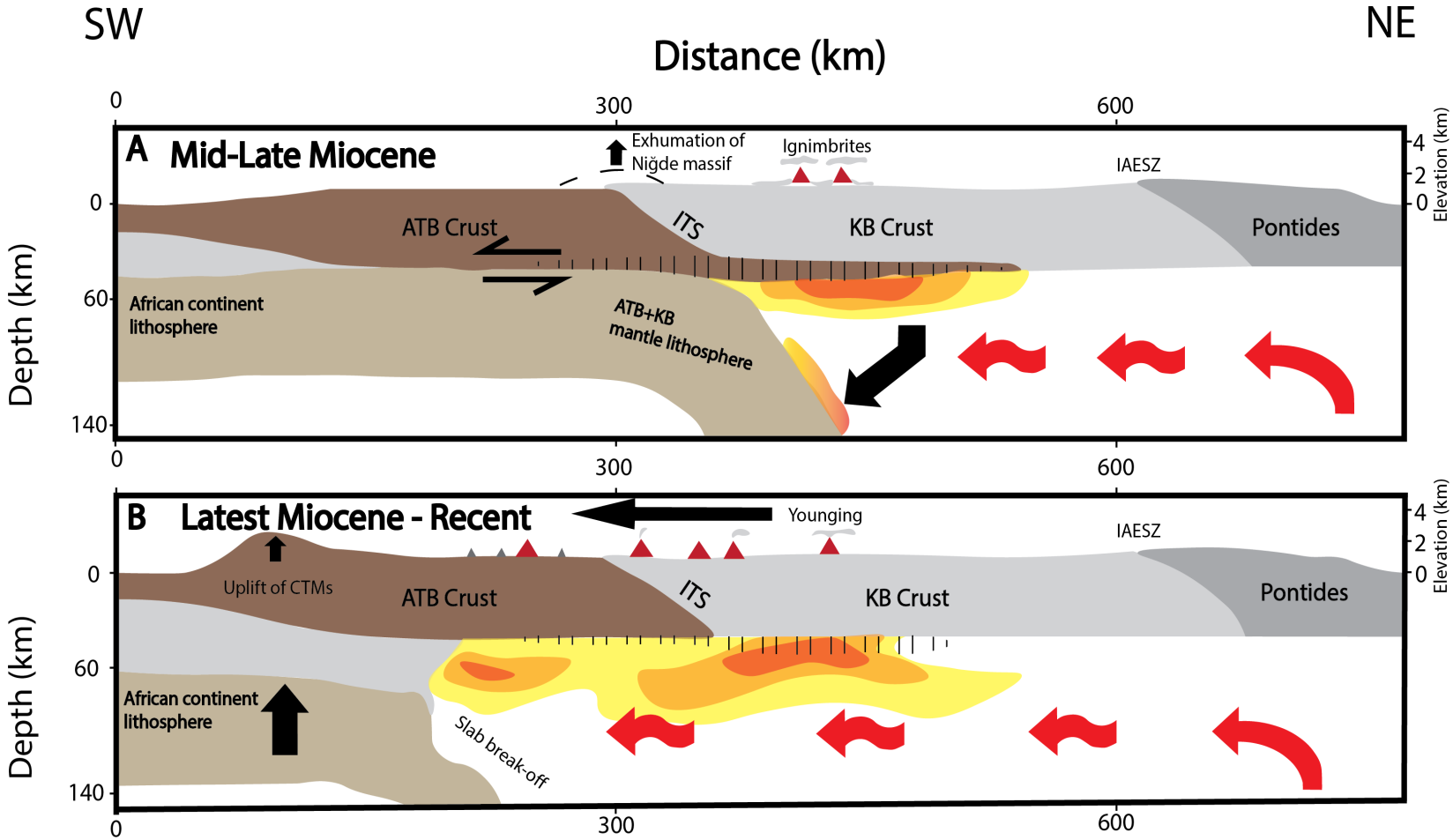


Figure 2.4. Demonstration of central Anatolia because of decoupled accreted blocks and their mantle. (A) middle to late Miocene: Because of roll back and delamination Anatolide-Tauride block and Kırşehir mantle lithosphere extensional exhumation in the Kırşehir block occurred. As a result of delamination, hot asthenosphere could up well, melt and came to the base of central Anatolia crust where ignimbritic volcanism was initiated because of these activities. B) Latest Miocene – Recent: continuation of the slab roll back caused to SW migration of the initiated ignimbritic volcanism. Subducted African lithosphere broke off started in late Miocene and due to the isostasy resulted from slab break central Taurus mountains uplift were initiated. Redrafted after Delph et al., 2017. Abbreviations, ITS: Inner Tauride Suture, ATB: Anatolide-Tauride block, CTMs: Central Taurus mountains, IAESZ: İzmir-Ankara-Erzincan suture zone, KB: Kırşehir block.

In detail, CAVP formed in an extensional continental setting and has a post-collisional timing. It is bounded by the high topography of the Tauride range in the southeast, the CACC in the northwest (Figure 2.4). The CAVP contains widespread pyroclastic deposits that are more than 2 km thick as well as fluvio-lacustrine deposits, volcanic units, and lava domes (Koçyiğit and Erol, 2001). Morphologically it has been shaped by numerous volcanoes, cinder cones and domes, including Erciyes and Hasandağ. The predominantly calc-alkaline volcanic and volcaniclastic rocks are middle Miocene to Quaternary in age (Innocenti et al.,1975; Ercan, 1986). NW-trending right-lateral strike slip faults cross-cut the CAVP and divided it into several blocks. The youngest structure that cross-cutting the CAVP is the NE-trending Ecemiş Fault Zone, that formed the NE-SW-trending Erciyes pull-apart basin (Koçyiğit and Erol, 2001).

2.1.2.2.1 Erciyes Basin

The Erciyes Basin is located in the eastern border of the CACC and is cut by the transcurrent Central Anatolian Fault Zone, which caused to up to 75 km sinistral displacement (Koçyiğit and Erol, 2001). The Erciyes pull-apart basin consists of the 3950 m high Erciyes Stratovolcano, which divides the Erciyes pull-apart basin into two sub-basins, the Sultansazlığı and Kayseri-Sarımsaklı depressions (Koçyiğit and Erol, 2001). According to Koçyiğit and Erol (2001), the Erciyes pull-apart basin and the Erciyes Stratovolcano developed contemporaneously. The, Erciyes Stratovolcano separates the northern and southern domains of the Erciyes pull-apart basins. The basement rocks of the CAVP are exposed along the basinward facing and steeply dipping basin margins. These units have been strongly tilted and folded and have been downthrown about 1.2 km by the border faults of the basin (Koçyiğit and Erol, 2001).

2.1.2.2.1.1 Margin Rocks

Oligocene-Miocene age Çukurbağ formation and middle Miocene–lower Pliocene Ürgüp group forming the margins rocks.

2.1.2.2.1.2 Çukurbağ Formation

Yetiş (1978) originally defined the Çukurbağ Formation and named it after its type locality in the vicinity of the Çukurbağ village located in the southern part of the study area.

The Çukurbağ Fm. is a fluviatile sequence, which unconformably overlain erosional surface of various metamorphic rocks, peridotites, a Late Cretaceous volcanosedimentary sequence and an Eocene nummulitic limestone (Koçyiğit and Erol, 2001). From bottom to top the sequence can be defined by reddish-brown, poorly-sorted, polygenetic conglomerate with sandy matrix and ferruginous calcite cement passing upwards into alternations of variably-colored sandstone-siltstone containing conglomerate lenses (Koçyiğit and Erol, 2001). The top of the fluviatile succession is represented by laminated siltstone-mudstone-shale rocks (Koçyiğit and Erol, 2001). Çukurbağ formation also contains Lutetian nummulitic limestone clasts that were derived from the basement (Koçyiğit and Erol, 2001). The entire sequence is unconformably overlain by the middle Miocene–Lower Pliocene Ürgüp Group and is also structurally separated from serpentinized peridotite through a thrust fault. According to these, the deposition age of the Çukurbağ Fm. was determined as Oligo-Miocene (Koçyiğit and Erol, 2001).

2.1.2.2.1.3 Ürgüp Group

The eastern and southern margins of the Erciyes basin are bordered by topographic highs comprising volcanic and volcanosedimentary rocks of the Ürgüp Group

including dome complexes, lava flows, and laterally-extensive ignimbrite deposits (Koçyiğit and Erol, 2001).

Pasquare (1968) named the Ürgüp Group and defined it as a regularly bedded fluvio-lacustrine sequence that includes pyroclastic and lava flow members. The Urgup Group unconformably overlies the Oligo-Miocene Çukurbağ Fm. and the pre-Maastrichtian ophiolites along the western margin of the basin and the folded and incipiently-metamorphosed Permo-Carboniferous carbonates and ophiolites along the eastern margin (Pasquare, 1968).

Ürgüp Group starts with basal conglomerate, followed by alternations of andesitic pyroclastics, andesitic dome complexes, basaltic lava flows and ignimbrites (Pasquare, 1968). At the top, the Valibaba ignimbrite, which is a 5–15 m-thick key horizon is present (Yetiş, 1978).

The Valibaba ignimbrite is well-exposed due to vertical displacement along basin margin faults, but does not crop out in the Erciyes basin (Koçyiğit and Erol, 2001). It is assumed that this ignimbritic unit is concealed beneath the Erciyes Stratovolcano, as confirmed by water wells drilled to depths of about 300 m around the margins of the Erciyes Stratovolcano (Koçyiğit and Erol, 2001).

Volcanic activity in the Erciyes basin began with the eruption of andesitic lava flows and pyroclastics, then continued with basaltic flows and was terminated by pyroclastic flows along basin margins (Koçyiğit and Erol, 2001).

Geochemical compositions of the margin rocks are calc-alkaline (Innocenti et al., 1975; Güner et al., 1984). In addition, K/Ar ages of lower andesitic lavas (absent in Erdemli formation) range between 13.7 and 5.5 Ma (Innocenti et al., 1975; Batum, 1978; Aluç et al., 2020; Yurdakul et al., 2021), on the other hand, radiometric ages of Valibaba ignimbrite, the uppermost unit, is around 2.8 Ma (Innocenti et al., 1975). Also, mammalian fauna in the rocks is referring ages between late middle Miocene to early Pliocene (Pasquare, 1968 and Becker-Platen et al., 1975). So, Ürgüp group age range is middle Miocene to early Pliocene (Koçyiğit and Erol, 2001)

2.1.2.2.2 Basin Fill

Sedimentary rocks and Erciyes stratovolcano complex filled the Erciyes depression (Koçyiğit and Erol, 2001).

2.1.2.2.2.1 Sedimentary Infill

Sedimentary infill within the Erciyes basin consist mainly of basin margin deposits such as conglomerates, mudstone, siltstone, marl, claystone and carbonates, often laterally and vertically grading (Altan, 1969; Oldaç, 1970; Koçyiğit and Erol, 2001). Basal conglomerate sits atop the erosional surface of the volcanosedimentary rocks that contain the Ürgüp Group and pre-middle Miocene basement rocks (Koçyiğit and Erol, 2001). Upwards it continues with various facies and is intercalated with volcanic rocks of the Erciyes basin with an overall thickness of around 300 m (Koçyiğit and Erol, 2001).

2.1.2.2.2.2 Volcanic Infill

Erupted products of the Erciyes Stratovolcano Volcanic Complex (ESVC) represent the volcanic infill of the Erciyes depression. The ESCV (3917 m a.s.l.) is in the central part of the depression and has an elevation of about 2842 m from the basin floor (Koçyiğit and Erol, 2001). The lowermost part of the sequence comprises basaltic and andesitic lavas, followed by dacitic-rhyodacitic lava domes, olivine basalt, hyalo-dacitic lava domes and finally pumiceous ash deposits (Pasquare, 1968). Also, general geochemical composition of the volcanic rocks of the ESVC is calc-alkaline (e.g., Kürkçüoğlu et al., 1998; Koçyiğit and Beyhan, 2001; Güçtekin and Köprübaşı, 2009).

Koçyiğit and Beyhan (1998) stated that pre and mid Pliocene age rocks are not only restricted in strike slip characteristic related basins or depressions, they were also observed in outside of the basins, there are significant structural and stratigraphical

controlling pattern differences between them and their cover rocks; which was commented that and count as clear proof of mid-Pliocene was the time that transition occurred from paleotectonic compressional characteristic to neotectonic strike slip characteristic. It has been resulted that a whole Central Anatolian Fault Zone may count as young neotectonic structure formed due to compensate high intracontinental strain, which was caused by convergence of plates, African-Anatolian and Arabian-Anatolian (Şengör and Yılmaz, 1981; Dewey et al., 1986; Hempton, 1987; Kelling et al., 1987; Karig and Kozlu, 1990; Robertson and Grasso, 1995). However, Ecemiş Corridor in Central Anatolian Fault Zone may have strike-slip characteristic which is represented by paleotectonic huge sinistral strike slip offset (Koçyiğit and Beyhan, 1998). This difference between Ecemiş Fault and other parts of the Central Anatolia Fault Zone can be explained by two distinct ways; Ecemiş Corridor could be a paleotectonic structure formed in Eocene to transfer motion as it was stated by Şengör and Yılmaz (1981); or it could be a tear fault formed in Late Cretaceous-pre-Oligocene period (Özgül, 1976; Koçyiğit, 1983; Gal et al., 1984; Demirtaşlı, 1984; Poisson et al., 1984). So, there is a big possibility that Ecemiş Corridor's strike slip motion occurred mostly in paleotectonic period, before mid-Pliocene; then, its activity was renewed along the zone of Inner Tauride Suture (Şengör and Yılmaz, 1981), weakness zone, which is striking Southwest and Northeast, finally, in the neotectonics time (after early Pliocene times), it converted to intracontinental transcurrent structure which is called as Central Anatolian Fault Zone (Koçyiğit and Beyhan, 1981)

Post Paleocene to pre-Lutetian age was stated by Yetiş (1978) for the age of Ecemiş Fault Zone, that was resulted by comparing stratigraphy of east and west blocks of the zone. On the other hand, Gül et al. (1984) assigned Late Eocene age for the fault zone, that was commented as a conclusion of stratigraphic similarity between Bolkardağ and Aladağlar. Finally, it was concluded that activation of the Ecemiş fault zone was in starting times of Early Miocene (Gül et al., 1984).

CHAPTER 3

DEPOSIT GEOLOGY

3.1 Introduction

The Öksüt high-sulfidation epithermal deposit is located in the Kayseri Province in Central Anatolia, about 11 km south of the town of Develi and 5 km southeast of the town of Zile (Figure 3.1). Mineralization is hosted within the late Miocene–Pliocene Develidağ Volcanic Complex, which was emplaced along the Ecemiş sector of the sinistral CAFZ (Koçyiğit and Beyhan, 1998; Figure 3.1). Here, the DVC and the Erciyes Stratovolcano lies along a N–S-extending topographic high that was bordered to the west by the Develi Fault (Figure 3.1). The Sultansazlığı pull-apart basin occupies the western side of the Develi Fault (Figure 3.1). Based on previously published $^{40}Ar/^{39}Ar$ and LA-ICP-MS, U-Pb zircon age data, emplacement of the DVC occurred during the latest Miocene (~6.3–5.4 Ma; Jaffey et al., 2004; Rabayrol et al., 2019; Aluç et al., 2020), coincident with the onset of east-west extension and associated normal faulting along the Ecemiş Fault Zone (Toprak and Göncüoğlu, 1993; Koçyiğit and Beyhan, 1998; Jaffey et al., 2004).

The DVC was partly collapsed and faulted down on the western flank for at least 300 m along the Develi fault, against the Plio-Quaternary volcanic infill of the Sultansazlığı pull-apart basin (Figure 3.1; Koçyiğit and Erol, 2001). The remaining part of the complex overlies the Permo-Carboniferous metacarbonates of the Tauride range and is dominated by Miocene-Pliocene volcanic and volcaniclastic lithologies with a surface extent of >300 km^2 (Figures 3.1 and 3.2). Thin sheets of ignimbrites regionally surround the lavas of the complex to the north and south. A simplified stratigraphic column showing the main lithologic units in the study area is shown in Figure 3.3.

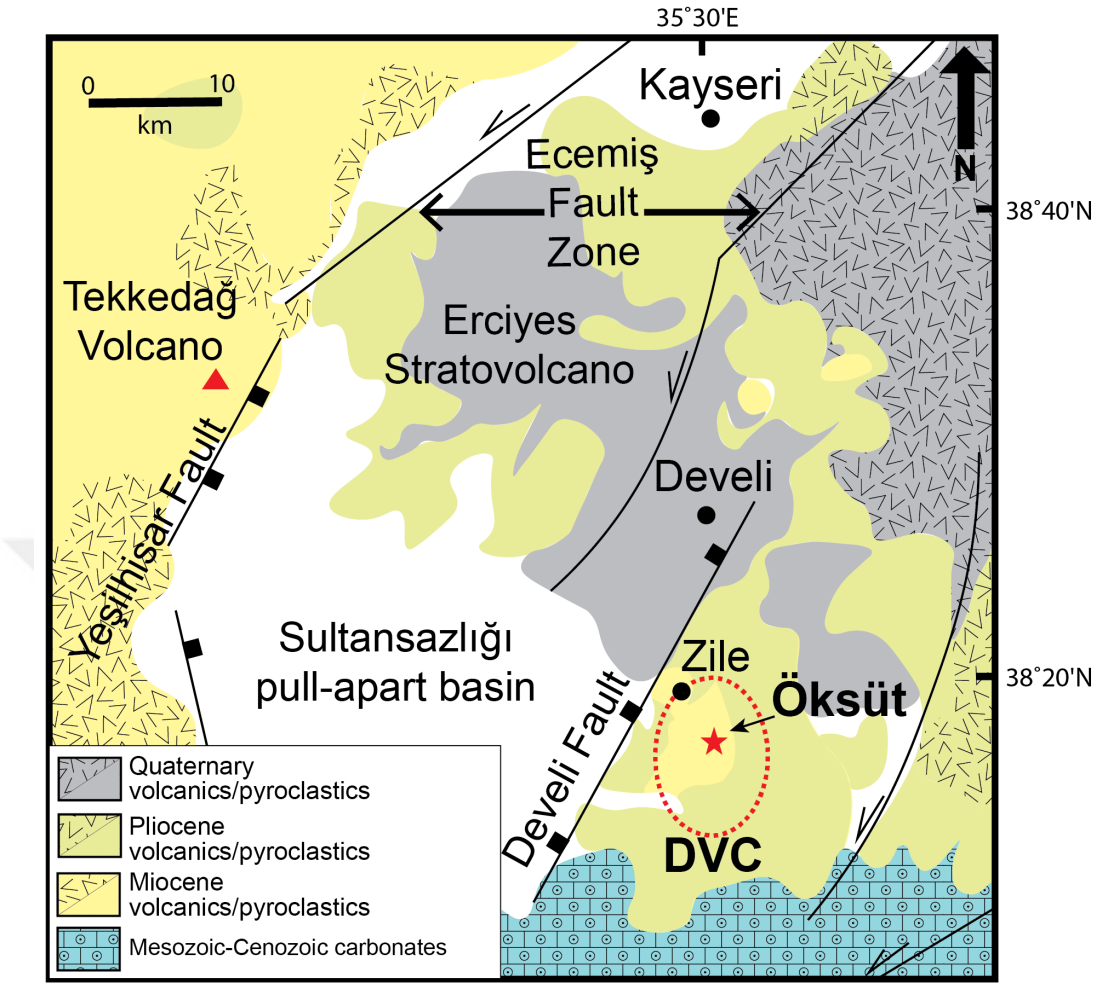


Figure 3.1. Simplified geologic map of the Ecemiş corridor and the Sultansazlığı pull-apart basin located between the Yeşilhisar and Develi segments of the Ecemiş Fault Zone (simplified from MTA, 2002).

3.2 Local Stratigraphy

3.2.1 Mesozoic carbonates

The Paleozoic–Mesozoic carbonates of the Tauride range represents the local basement in the study area into which the DVC was emplaced (Fig. 3.2). Although outcropping basement carbonate rocks are largely absent in the study area and were not intersected in the drill holes, fragments of gray colored, fine- to medium-grained recrystallized limestone were encountered along the access road between Zile and

Öksüt. This part of the Öksüt tenement lies within the collapsed western flank of the DVC, and hence it appears that the concealed basement rocks are likely to crop out on this part of the system (Figure 3.4A and B).

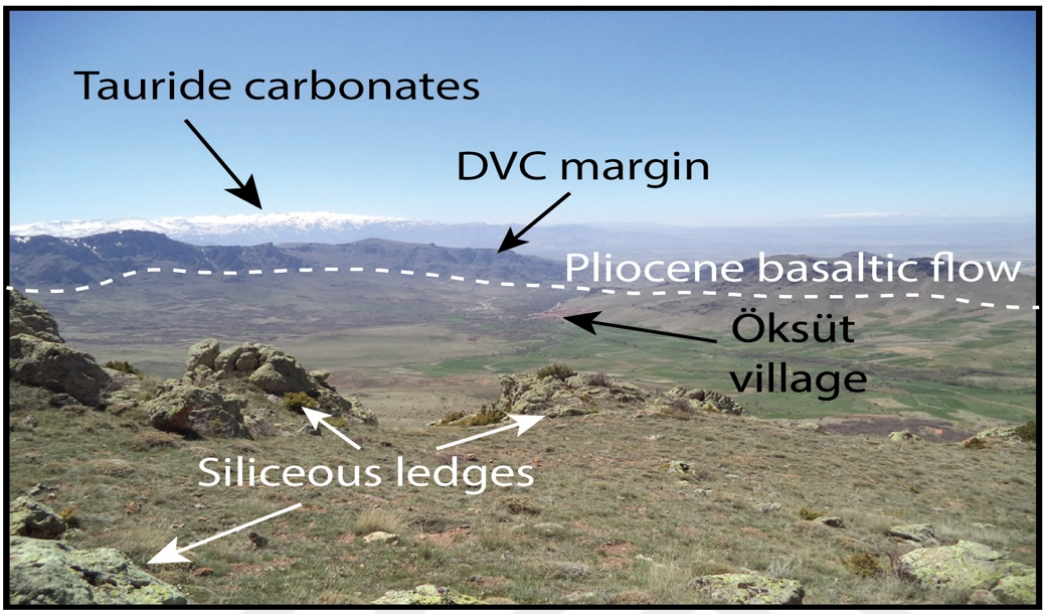


Figure 3.2. A generalized view of the south of the deposit which includes Pliocene cover rocks and mineralized silica ledges. Öksüt village located in the center of the margin of the complex and Tauride mountains are in the far south. Abbreviations: DVC= Develidağ Volcanic Complex.

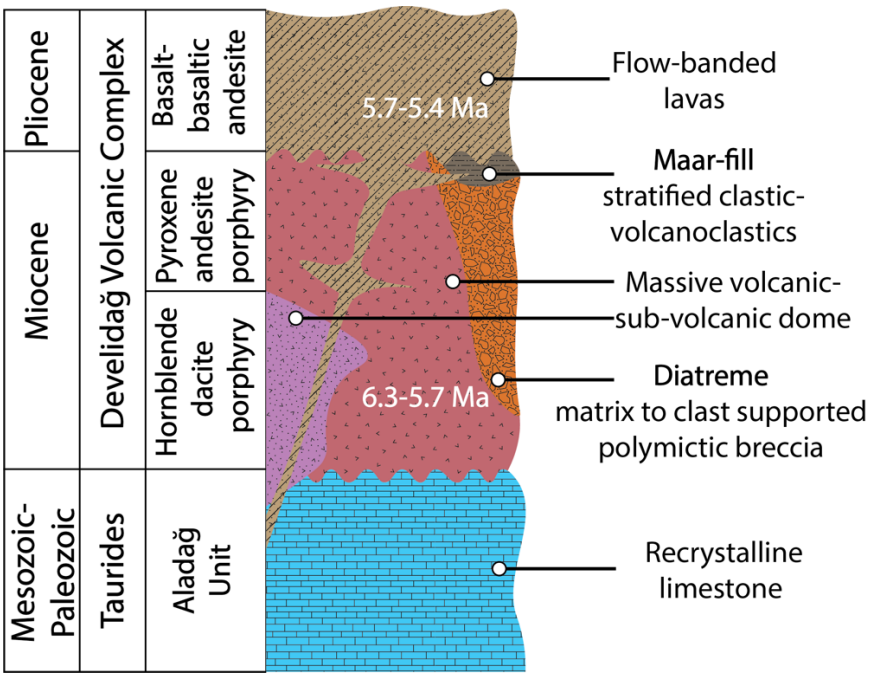


Figure 3.3. Generalized columnar section and stratigraphic sequence of the major lithological units in Öksüt.

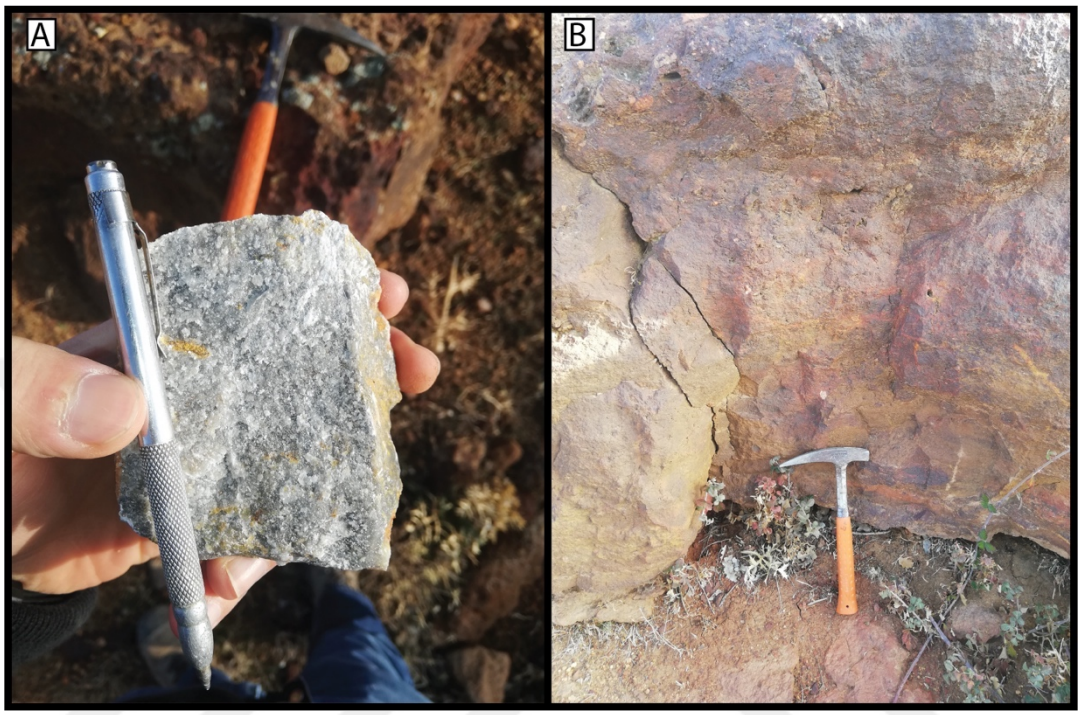


Figure 3.4. (A) Recrystallized limestone fragment derived from carbonate basement rocks underlying the access road between Zile and Öksüt mine (38.299112N, 35.476197E), (B) strongly silica- and carbonate-altered iron skarn exposure adjacent to the recrystallized limestone blocks sampled in (A).

3.2.2 Develidağ Volcanic Complex (DVC)

The DVC is a large, regionally-prominent stratovolcano that is mainly made up of late Miocene to Pliocene basaltic to andesitic volcanic and sub-volcanic lithologies, at least one main diatreme structure, and minor maar infill sediments (Figures 3.2 and 3.3), surrounded by thick deposits of ignimbrites along the rims of the volcanic complex(Figure 3.2). Its elevation reaches up to about 1950 m, but the Keltepe and Güneytepe orebodies are found at elevations close to 1800 m (Figures 3.5, 3.6 and 3.7).

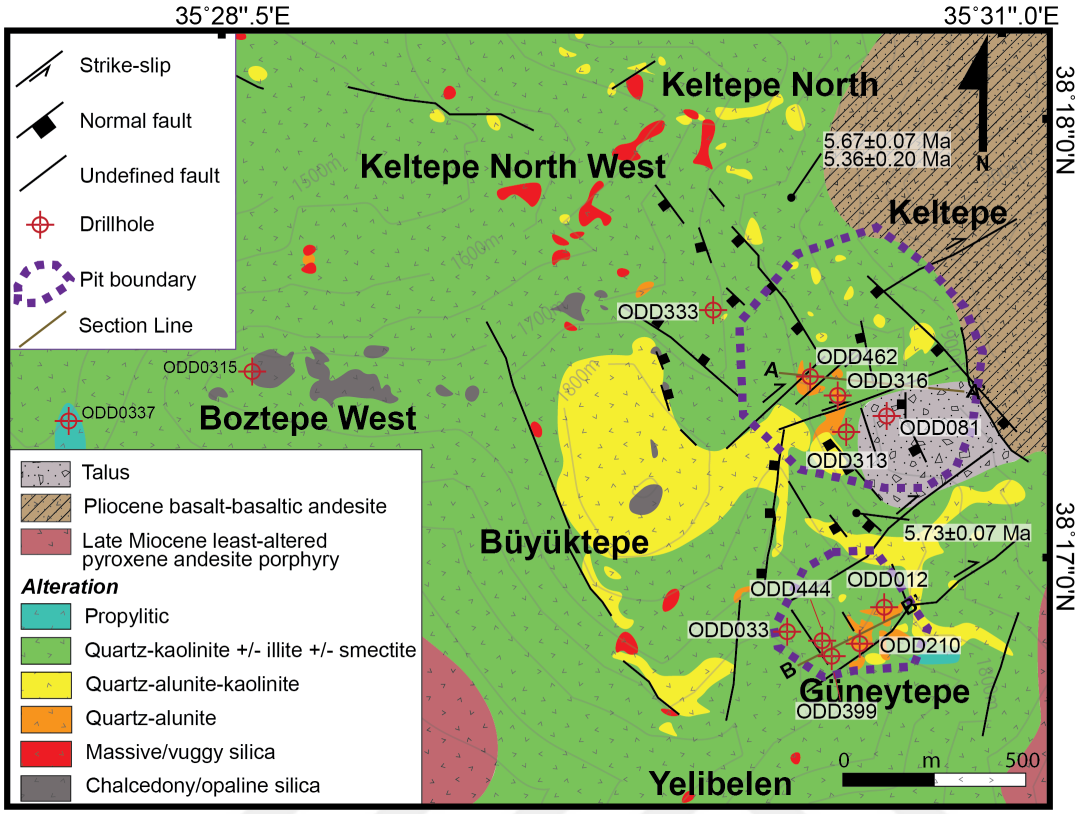


Figure 3.5. Geological map of the Öksüt deposit showing main outcropping lithologies, structures, and distribution of hydrothermal alteration facies (modified from Cihan et al., 2016). Approximate outlines of the Keltepe and Güneytepe pits and satellite prospects as well as locations of some of the key drill holes mentioned in the text are also shown.

In the immediate deposit area, most of the volcanic units have undergone extensive hydrothermal alteration, and therefore the original host rock is often difficult to distinguish in the shallow epithermal levels. The lower part of the volcanic stratigraphy comprises at least two distinct late Miocene andesitic to dacitic porphyries (Figure 3.3), which collectively represent an exogenous dome complex.

Miocene volcanic rocks are overlain by Pliocene basaltic andesite and basalt at higher elevations (Figure 3.3). All of these units are calc-alkaline in nature and display arc-like signatures (relatively enrichments in large ion lithophile elements, depletions in Nb, Ta, and Ti, and with downward sloping normalized rare earth element patterns; Kürkçüoğlu, 2010; Rabayrol et al., 2019; Aluç et al., 2020).

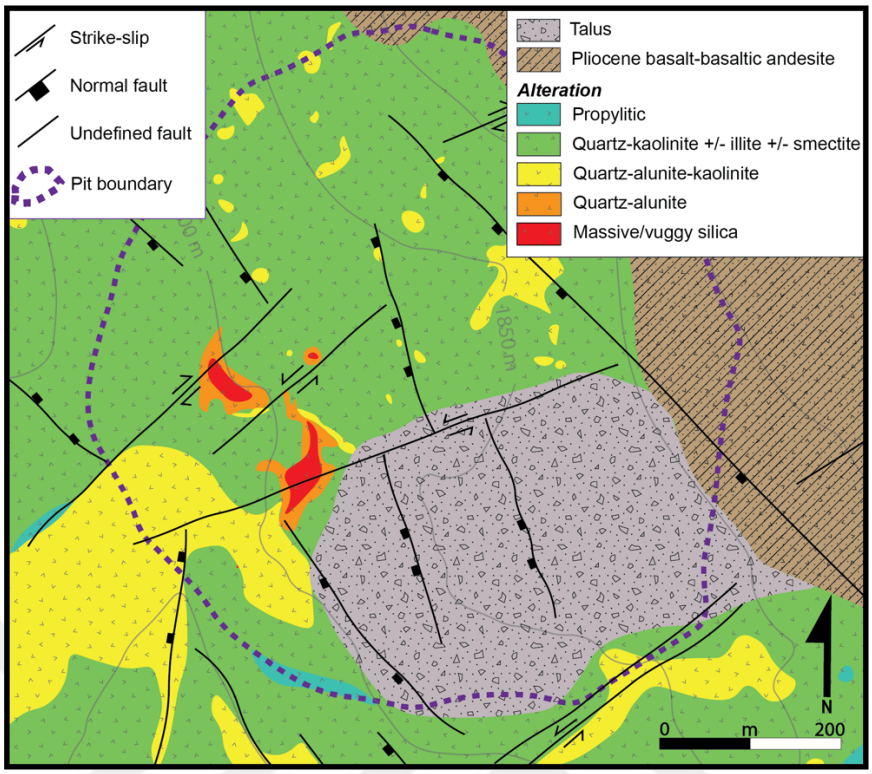


Figure 3.6. Alteration map of the Keltepe pit.

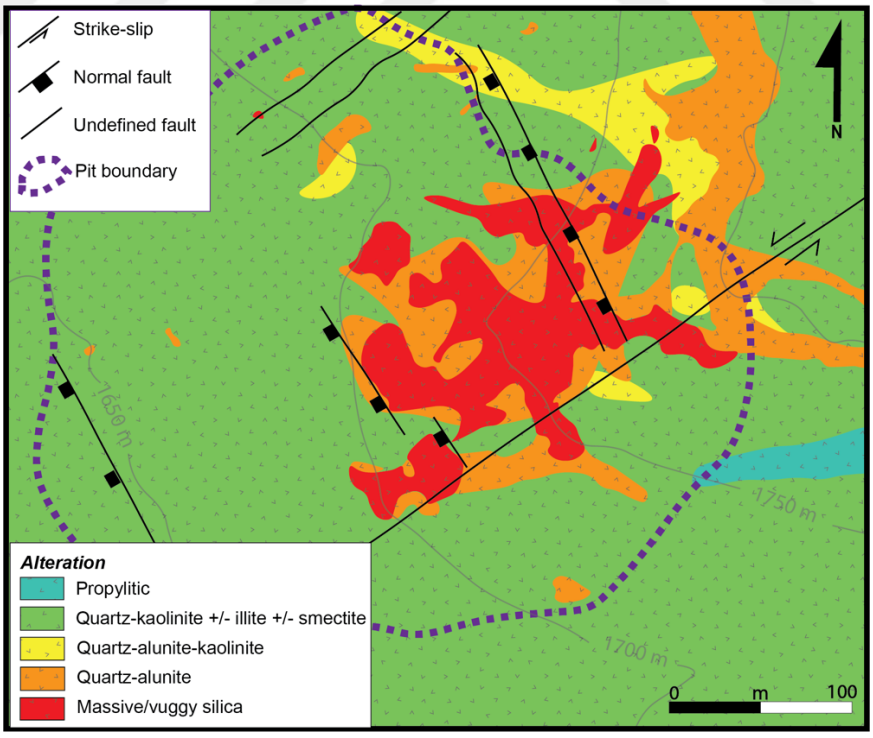


Figure 3.7. Alteration map of Güneytepe pit.

3.2.2.1 Hornblende andesite porphyry (late Miocene)

Hornblende andesite porphyry, as described by Aluç (2017) and Aluç et al. (2020), comprises the lower levels of the volcanic stratigraphy. This unit only locally crops out in the northern and western parts of the study area. It is represented by large phenocrysts of hornblende and plagioclase with plagioclase and magnetite microphenocrysts surrounded by a glassy groundmass. Hornblende andesite porphyry has not undergone extensive alteration and shows only minor sericite alteration within plagioclase phenocrysts. Aluç et al. (2020) reported U-Pb zircon ages of 5.78 ± 0.01 Ma and 5.73 ± 0.06 Ma from two samples of hornblende andesite porphyry, whereas Jaffey et al. (2004) reported $^{40}Ar/^{39}Ar$ fusion plagioclase ages of 6.29 ± 0.07 and 5.80 ± 0.11 Ma from samples obtained near Zile.

3.2.2.2 Pyroxene andesite porphyry (late Miocene)

Pyroxene andesite porphyry is the predominant magmatic unit at Öksüt and is the main wall rock to the gold-copper mineralization (Figure 3.3). In the study area it has been mostly altered, particularly in the shallow parts of the DVC (Figure 3.8). Nevertheless, least-altered samples observed in deeper levels of the magmatic system display a phenocryst dominant porphyritic texture (Fig 3.9A and B). Pyroxene andesite porphyry has a phenocryst assemblage of clinopyroxene and plagioclase with minor orthopyroxene and sparse biotite embedded in a groundmass containing plagioclase and magnetite microphenocrysts. In deeper drill holes to the west of the Keltepe pit (ODD-337), pyroxene andesite porphyry was encountered to depths of >700 m. Three samples of pyroxene andesite porphyry yielded U-Pb zircon ages of 5.70 ± 0.02, 5.67 ± 0.07, and 5.36 ± 0.02 Ma (Rabayrol et al., 2019; Aluç et al., 2020), indicating overlapping or slightly younger timing for this unit compared to hornblende andesite porphyry.

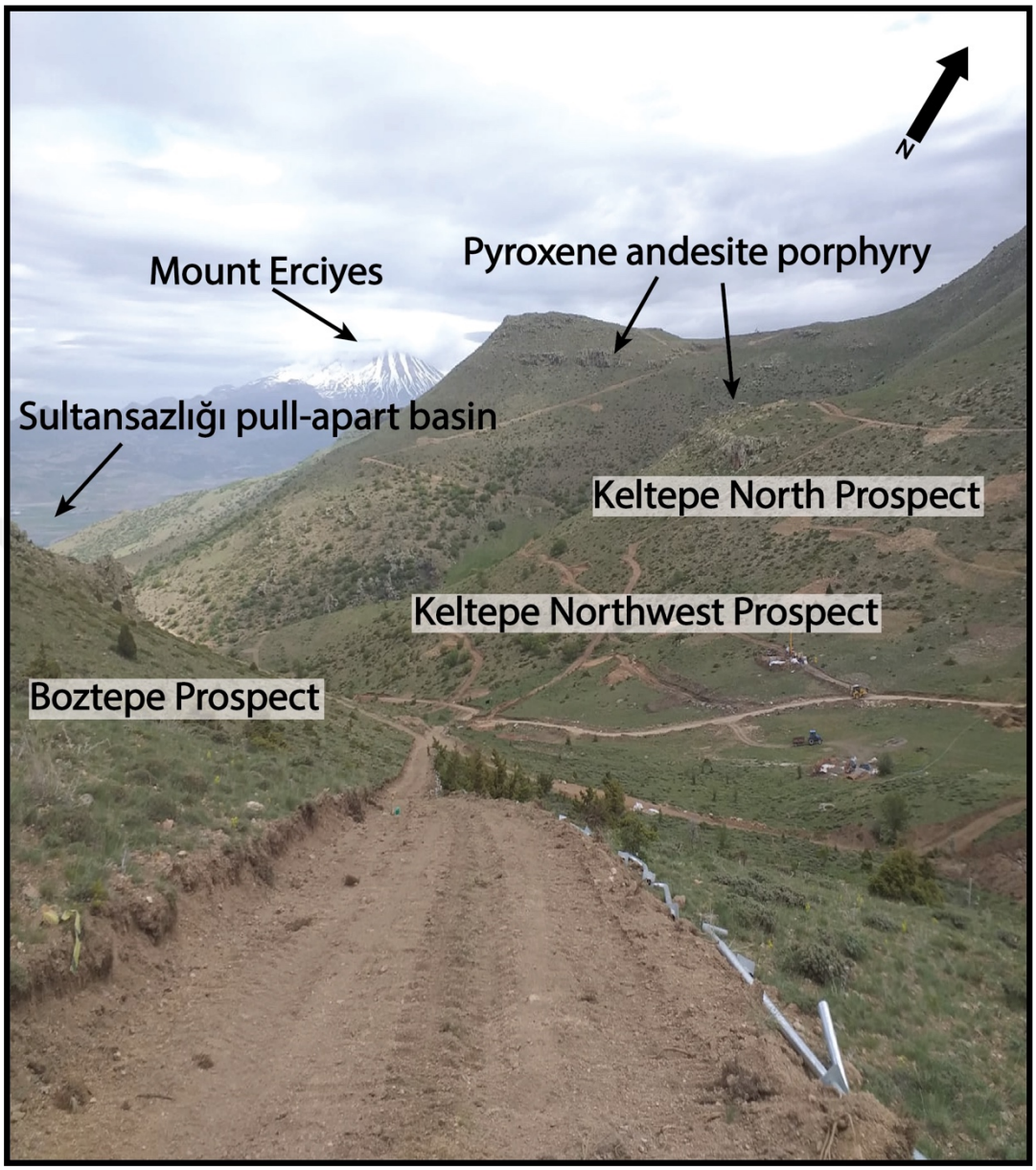


Figure 3.8. View of the Keltepe N and NW prospects from the Boztepe prospect. Pyroxene andesite porphyry makes up the ridges on both sides of the road. Erciyes Stratovolcano and the Sultansazlığı pull-apart basin can be seen in the background.

3.2.2.3 Diatreme breccia and maar-fill sediments (late Miocene)

A funnel-shaped and intensely-brecciated structure exists along the western wall of the Keltepe pit, which was interpreted to be a diatreme or sub-volcanic vent, developed within the andesitic dome complex (Figure 3.10). Diatreme breccia is a

matrix- to clast-supported polymict breccia that is made up of small to large (up to about 10 cm) sub-angular to sub-rounded fragments of altered andesite and silica set within a silica-altered matrix (Figure 3.11A-B-C).

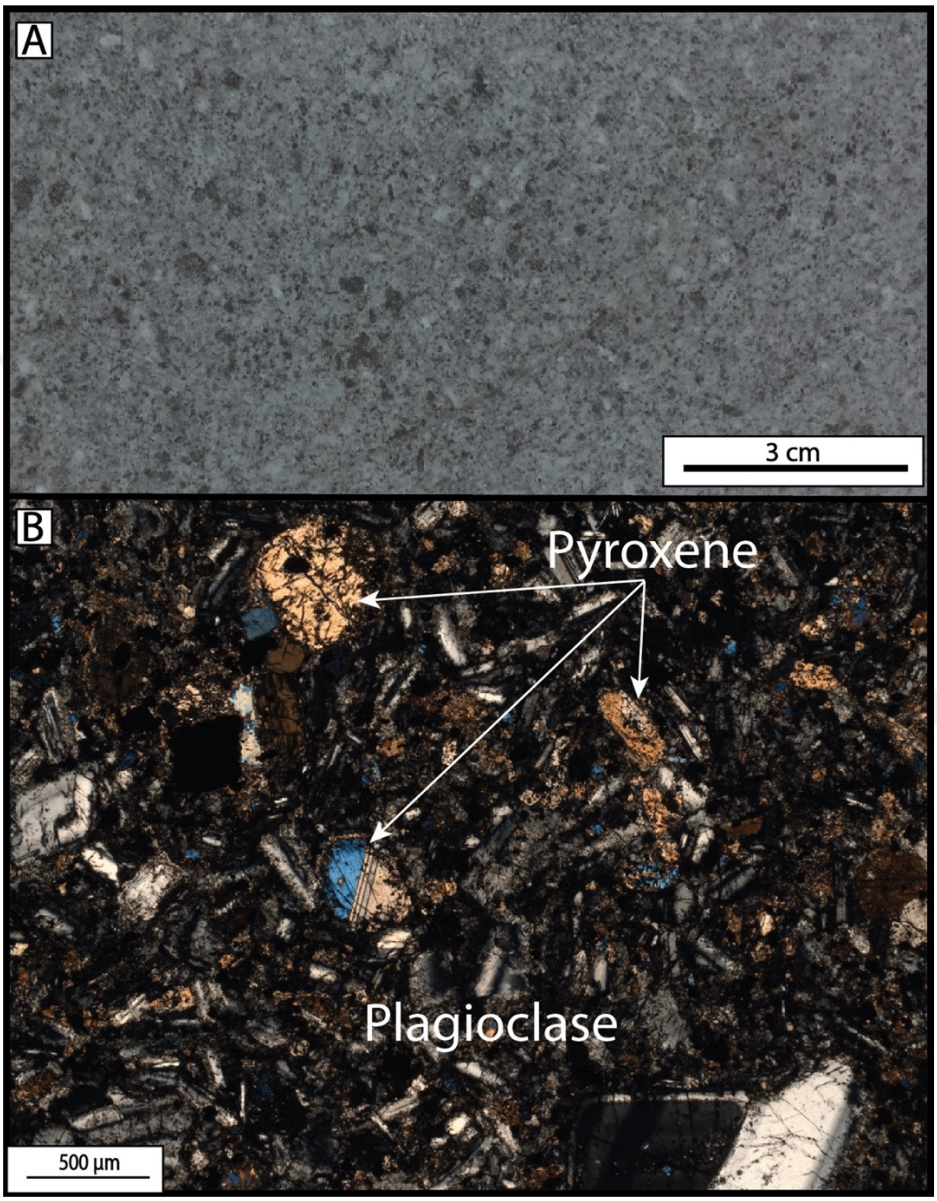


Figure 3.9. (A) Drill core and (B) thin section photograph (transmitted, cross-polarized light) of least-altered pyroxene andesite porphyry (sample OD78863; ODD-337, 706.30–706.60 m). This sample contains phenocrystals of plagioclase and pyroxene together with magnetite microphenocrysts surrounded by a groundmass containing fine-grained plagioclase and pyroxene.

Part of the Öksüt gold-copper minealization is hosted within the diatreme breccia as some of the ore fluids also utilized this structure. No basement carbonate rock fragments were identified within the diatreme, possibly due to low possibility of these fragments to survive the acidic alteration the diatreme has undergone. The diatreme has been capped by an up to 10 m-thick maar-fill consisting of stratified, fine- to medium-grained clastic material that is also highly silica altered and oxidized (Figure 3.12).

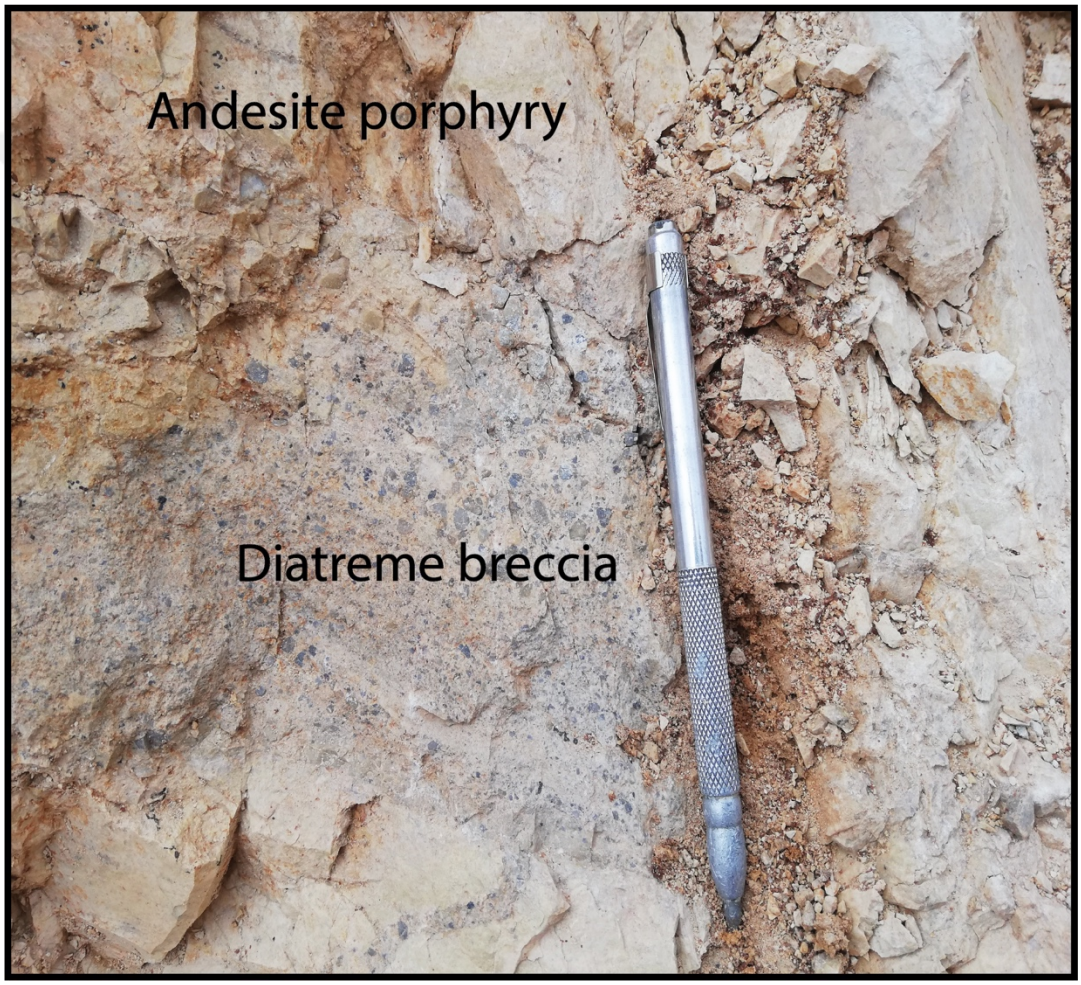


Figure 3.10. Angular, silica-altered clasts predominating the diatreme breccia cross-cutting the altered pyroxene andesite porphyry in the southern part of the Keltepe pit.

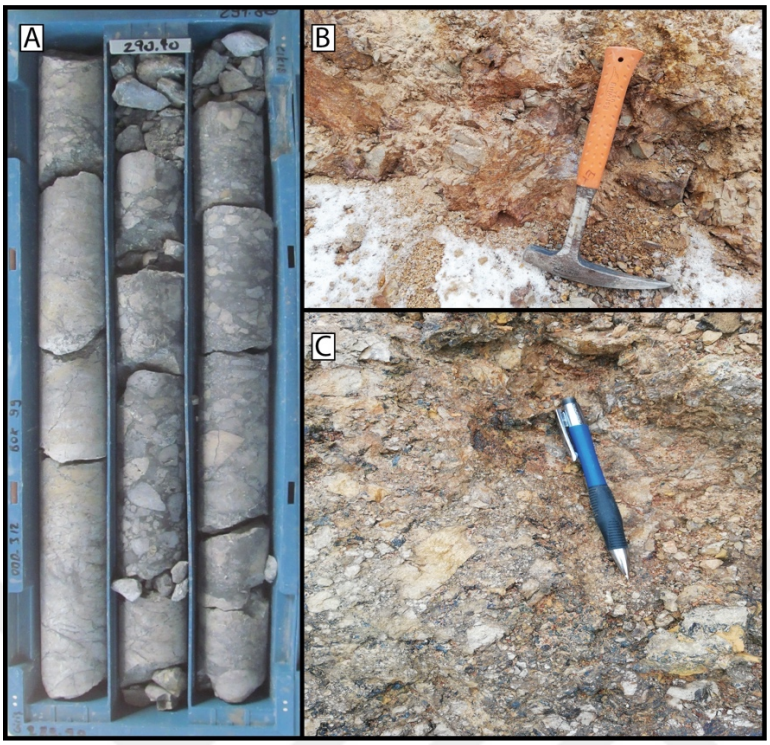


Figure 3.11. (A) Drill hole interval from the Keltepe pit (ODD-312, 289.00–292.00 m) containing variably-sized clasts in a matrix- to clast-supported diatreme breccia, (B) diatreme breccia from SW wall of the Keltepe pit, (C) intensely-altered, poorly-sorted, polymictic diatreme breccia exposed on the main wall of the Güneytepe pit.



Figure 3.12. Outcrop photograph of finely-stratified maar-fill sediments of volcanic origin from the Güneytepe pit. Sediments have been strongly silicified and oxidized.

3.2.2.4 Basaltic lava flows (early Pliocene)

Pliocene basalt-basaltic andesite flow-banded lavas form the younger volcanic cover throughout the eastern part of the volcanic complex at higher elevations (Fig. 3.5; Kürkçüoğlu, 2010), and also occur along the margins of the DVC (Fig. 3.2). These are distinguished from massive andesite to basaltic porphyries by their gently outward-dipping flow banding (Figure 3.13). This unit is neither altered nor mineralized and is characterized by olivine, pyroxene, and plagioclase both as phenocryst and as groundmass phases, alongside minor amounts of magnetite microphenocrysts (Figure 3.14). Dikes and sills of similar composition were also observed in drill core cross-cutting the pyroxene andesite porphyry, and these were considered as feeders to shallower basaltic lavas.

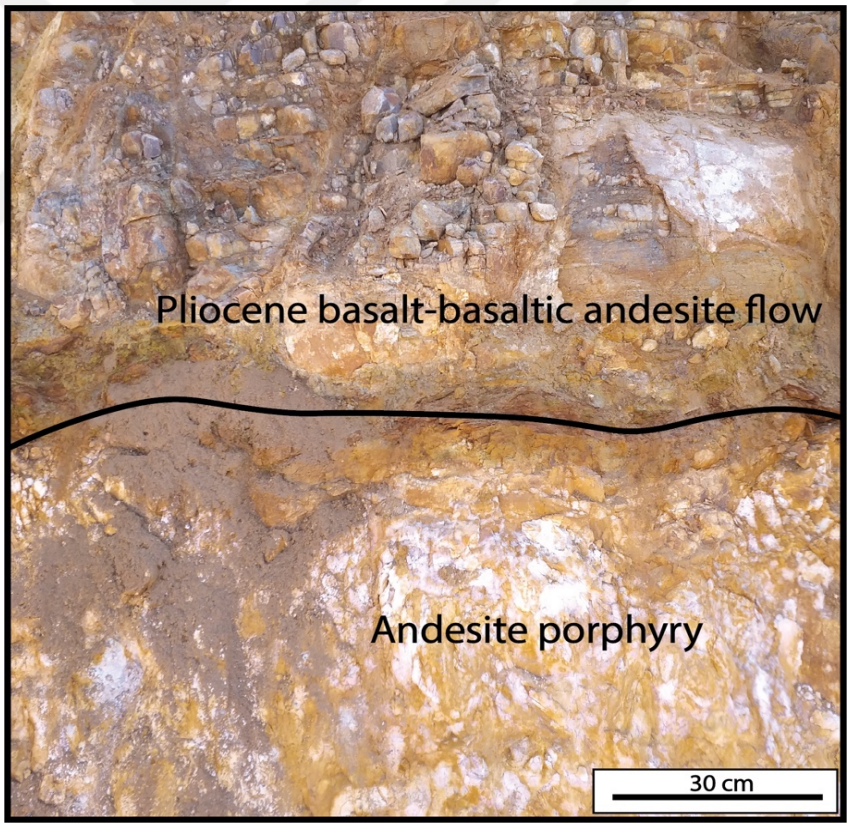


Figure 3.13. Contact between the late Miocene pyroxene andesite porphyry and overlying Pliocene basalt-basaltic andesite flows in the north of the Keltepe pit (38.289173N, 35.512541E).



Figure 3.14. Fragment of Pliocene basalt from the western margin of the DVC. Altered plagioclase phenocrysts are abundant and are set in a dark colored groundmass.

3.3 Structure

The Develidağ Volcanic Complex is cut by NNE-, NE-, and NW-trending, steeply dipping oblique faults that can be traced over several hundred meters along strike (Figure 3.15A, B). NNE-trending faults mainly display sinistral movement, whereas NE- and NW-trending faults are predominantly normal-slip with a minor strike-slip component. The structural blocks bounded by this latter group of faults have systematically stepped down to the southwest. Intermittent seismic activity of the

Ecemiş fault zone since the Miocene (Koçyiğit and Beyhan, 1998) resulted in widespread post-mineralization fault reactivation, and therefore it is difficult to resolve relative timing of different fault populations at Öksüt unequivocally. Nevertheless, both NW- and NNE-trending faults were consistently observed as crosscut by the NE-trending faults (Cihan et al., 2016). On the other hand, all three fault populations seem to have exerted structural control on localization and emplacement of sub-vertical breccia bodies and associated hydrothermal alteration (Figure 3.15 A and B). Silica ledges, in particular, developed at intersections of NW- and NE-trending faults. The latter host much of the gold mineralization at Güneytepe.

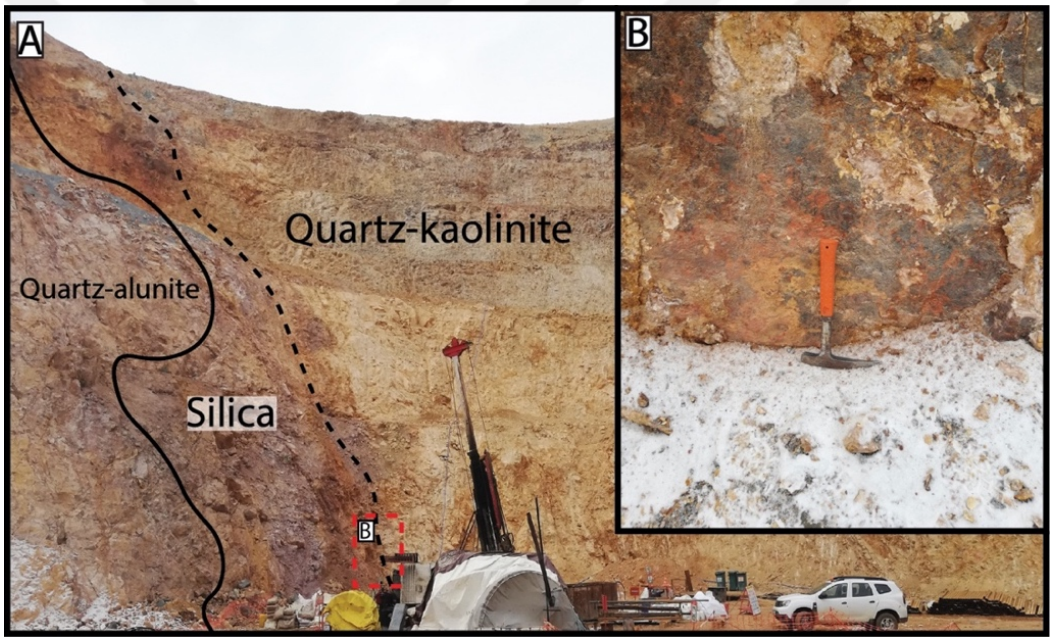


Figure 3.15. (A) NE-trending, steeply-dipping oblique fault (left-lateral with normal component; marked with dashed line) exposed on the southwestern wall of the Keltepe pit. This structure sharply separates silica and quartz-alunite alteration zones from the quartz-kaolinite alteration zone, (B) Close-up view of the silicified and oxidized fault surface.

The NW-trending faults also mark the contact between pyroxene andesite porphyry and Pliocene basaltic flows, now largely concealed underneath the landslide material

of Pliocene basaltic lava flows cover at the southeast border of the Keltepe pit (Figure 3.5). All three fault generations extend into this talus material as well as into the basaltic cover units (Figure 3.5), suggesting postmineralization fault reactivation. This is also supported by sulfide slickensides observed in drill core with dextral oblique-slip movement (Figure 3.16).

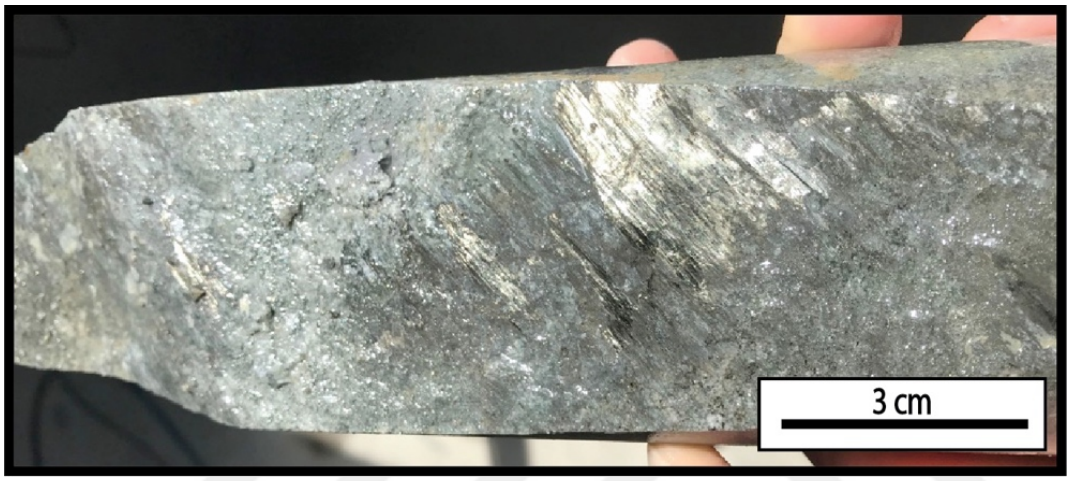


Figure 3.16. Fractured surface of a drill core sample (ODD-444, 680.00–680.20 m, Güneytepe pit) with a steeply-dipping slickensided pyrite infill indicating post-mineralization faulting.

CHAPTER 4

DEPOSIT CHARACTERISTICS

Gold-copper mineralization and related hydrothermal alteration at Öksüt is primarily associated with sub-vertical breccia bodies, that are referred as “ledges” by Yıldız et al. (2016) (Figure 4.1). There are two main mineralized domains identified at Öksüt by Yıldız et al. (2016, 2017), the Keltepe and Güneytepe orebodies, which are currently producing gold in two separate open pits. The Keltepe and Güneytepe orebodies are located 400 meters apart from each other in north-south direction (Figure 3.5). Keltepe and Güneytepe display broadly similar alteration and mineralization styles as well as overall gangue and ore mineralogy, primarily developed within structurally controlled upward-flaring breccia zones.

4.1 Hydrothermal Alteration

Hydrothermal deposits usually have distinct alteration zones developed around them due to variable degrees of buffering by fluid-wall-rock interaction. The passage of reactive hydrothermal fluids is facilitated by zones of permeability within the wall-rocks. In epithermal deposits permeable zones are generally represented by faults, fractures, diatremes or breccia pipes, and in the presence of volcaniclastic or sedimentary lithologies porosity may contribute to fluid flow and subsequent wall-rock alteration (e.g., Sillitoe, 1993; Arribas, 1995; Hedenquist et al., 2000; Rhys et al., 2020).

The innermost core of the alteration domain in high-sulfidation epithermal systems is occupied by a zone of massive or vuggy silica (e.g., Stoffregen, 1987; Hedenquist et al., 2000). Silica alteration is often separated from the surrounding advanced argillic alteration zone with a sharp boundary (Stoffregen, 1987; Arribas, 1995; Hedenquist et al., 2000). This zone is further enveloped by argillic alteration grading

outward into propylitic alteration, which represents the distal, outermost alteration halo (Stoffregen, 1987; Arribas, 1995; Hedenquist et al., 2000). Widths of these alteration zones may vary greatly; for example residual silica and advanced argillic alteration may range from <70 cm as vein selvages (Deen 1990) up to zones greater than >50 m lateral extent such as in Summitville or Lepanto (Arribas, 1995). Also through increasing depth, high sulfidation alteration generally grade from silicic alteration to advance argillic, argillic, phyllic zones (Arribas, 1995).

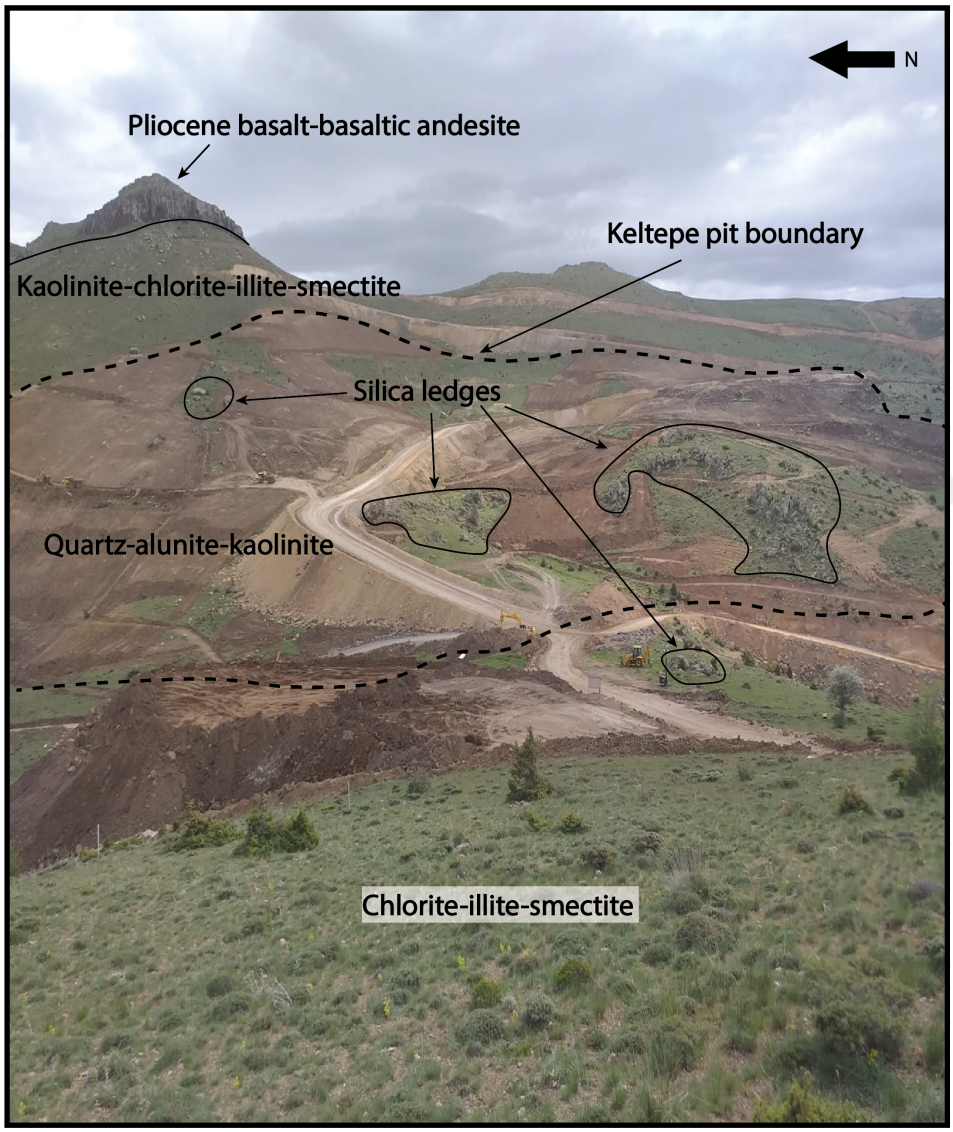


Figure 4.1. Pre-open pit view of the Keltepe orebody. Ledges are encircled by quartz-alunite alteration which transitioning to argillic and propylitic alteration. At the top, Pliocene rocks cover all the other units.

A zoned alteration pattern is also present at Öksüt (Table 4.1), and lateral and vertical distribution of various alteration zones can be observed around mineralized breccia bodies, particularly within the Keltepe (Figure 4.2A) and Güneytepe pits (Figure 4.2B).

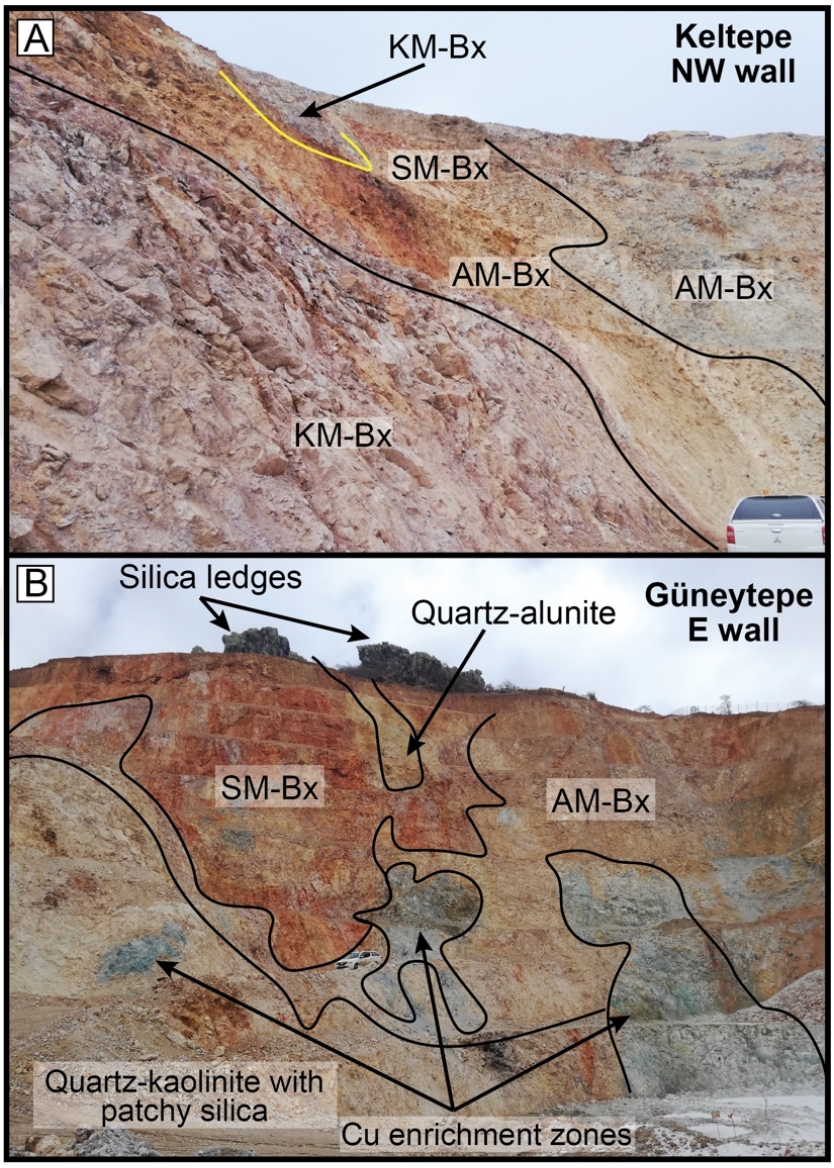


Figure 4.2. Distribution of altered and mineralized domains, as well as various breccia facies in (A) Keltepe and (B) Güneytepe pits. Abbreviations: KM-Bx = Kaolinite matrix breccia, SM Bx = Silica matrix breccia, AM Bx = Alunite matrix breccia.

Table 4.1 Alteration types identified at Öksüt and their characteristic minerals.

Observation method/ Alteration type	Petrography	TerraSpec	XRD
Silica	Quartz *Alunite, jarosite, clay*	Quartz *Jarosite*	not applied
Advance argillic 1	Alunite, quartz, jarosite *Alunite, pyrite, marcasite*	Quartz, pyrophyllite, natroalunite, k-alunite, jarosite *Dickite, gypsum, kaolinite, illite*	Quartz, alunite, natroalunite, jarosite, pyrophyllite, muscovite *Halloysite, pyrite, phlogopite, rutile, talc*
Advance argillic 2	Clay, quartz, jarosite *Clay, pyrite, marcasite, chlorite*	Kaolinite, illite, quartz *Alunite, gypsum, dickite*	Halloysite, kaolinite, quartz, phlogopite *Alunite, pyrite, pyrophyllite, talc, rutile, jarosite, muscovite, magnetite, hecrettite*
Argillic	Clay, quartz, chlorite *Pyrite, sericite, rutile, marcasite, alunite*	Montmorillonite, paragenotic illite, illite, phengite *Quartz, kaolinite, smectite, iron saponite, hematite, goethite*	Kaolinite, nacrite, clinochlore, quartz, halloysite, muscovite/illite, albite *Pyrite, rutile, sericite, alunite, marcasite, talc, phlogopite*
Patchy silica	Quartz, clay *Pyrite, chlorite*	Quartz, kaolinite *Alunite*	not applied
Propylitic	Epidote *Carbonate, pyrite, chlorite*	Iron-magnessium chlorite, diaspore, paragonite *Montmorillonite, epidote, dolomite*	Phlogopite, albite *Lanarkite*
Potassic	Biotite, magnetite *K-feldspar, anhydrite*	Biotite, hydrobiotite, tourmaline, hornblend *Dolomite, gypsum, epidote*	Sodian anorthite, talc, phlogopite *Quartz, amphibole, chlorite, pyrite, K-feldpsar*
Calc-silicate	Garnet, epidote, carbonate *Chlorite, sericite*	Garnet, calcite, clinozoisite *Brucite*	Halloysite, grossular garnet *Anorthite, muscovite*

4.1.1 Alteration facies

4.1.1.1 Silicification

Silicification is the earliest phase of hydrothermal alteration and is characterized by replacement of andesitic porphyry and breccias by variably-textured zones of residual vuggy and massive silica (Table 4.1).

Residual vuggy quartz formed by almost complete leaching and replacement of the matrix material in the breccias and the fine-grained groundmass in porphyritic rocks (Figures 4.3 and 4.4). Vuggy appearance of the rocks is due to dissolution of igneous phenocrysts (Figure 4.3). Some silica was also added to altered rocks as veinlets, hydrothermal breccias, and as vug fill (Figures 4.3, 4.4, and 4.5).

Silicified rocks occupy the central portions of the ledges and are widely distributed in the study area (Figure 4.2A and B). A number of silicified ledges are present at Öksüt, and some of these can be still seen as forming topographic highs outside the open pits (Figure 4.2B). The initial discovery of the Öksüt mineralization actually was based on anomalous gold concentrations obtained from the outcropping silica altered rocks (Cihan et al., 2016; Yıldız et al., 2016 and 2017).

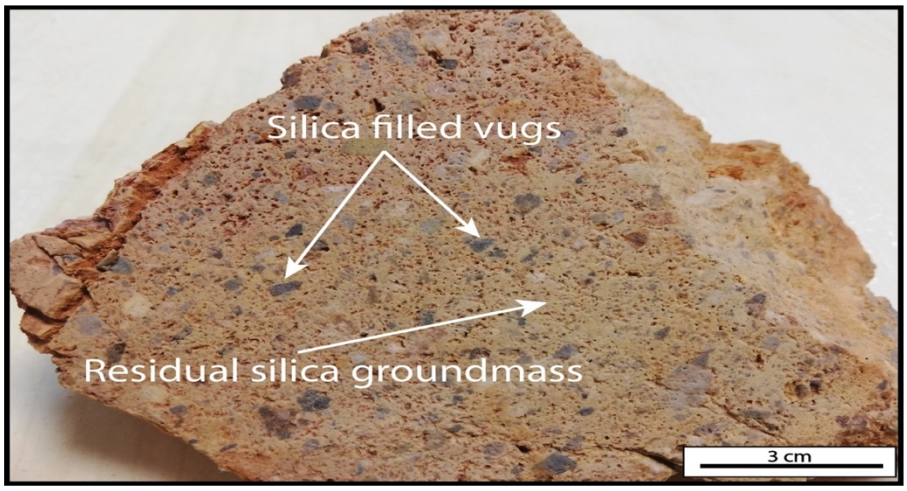


Figure 4.3. Residual vuggy silica alteration of the igneous wall-rock from the Keltepe orebody. Vugs have been partially filled by late silica. Reddish-orangish color is due to supergene oxidation and presence of Fe-oxide minerals (sample OD79995; ODD-316, 159.70–159.75 m, 3.08 g/t Au).

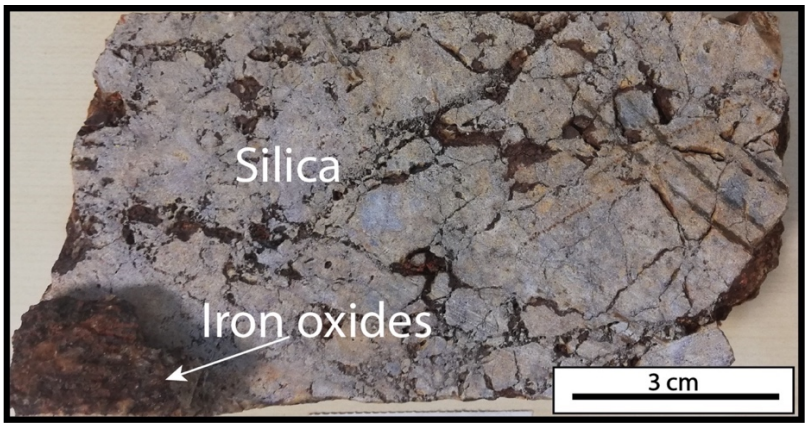


Figure 4.4. Massive silica replacement of an intensely-oxidized breccia sample from the Keltepe orebody (sample OD79983; ODD-316, 104.80–104.90 m, 0.53 g/t Au).

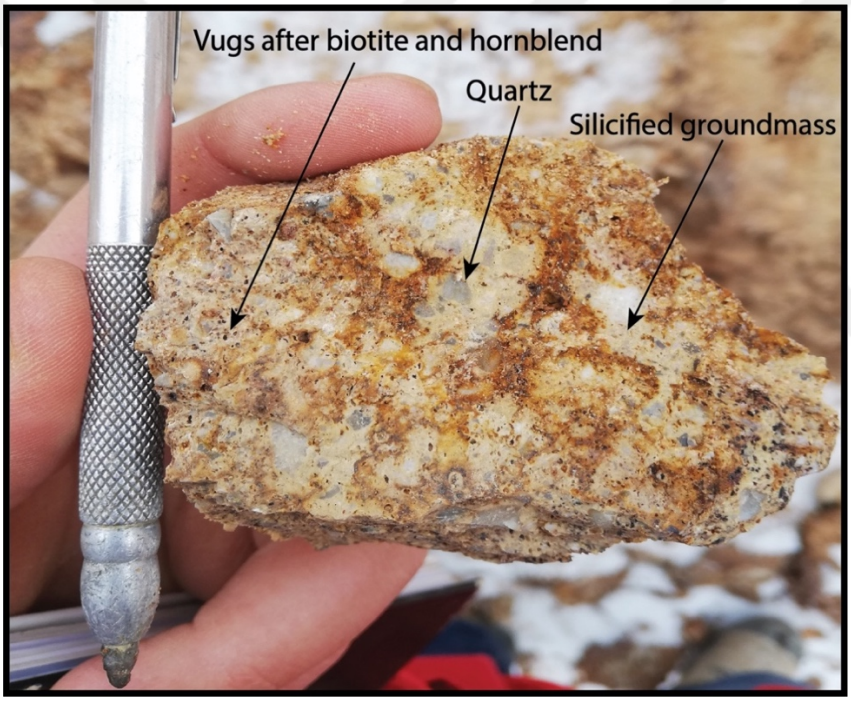


Figure 4.5. Outcrop sample from the Güneytepe pit with a moderately-silicified groundmass. Open vugs formed due to acid leaching of biotite and hornblende, whereas quartz occurs as a stable relict phase.

At shallow depths (typically down to 10–20 m), silicified rocks contain metastable silica phases of opaline silica and porcellaneous chalcedony instead of fine-grained quartz, likely due to low temperature conditions (<200°C; Browne, 1978; Henley and Ellis, 1983; Stoffregen, 1987; Reyes, 1990).

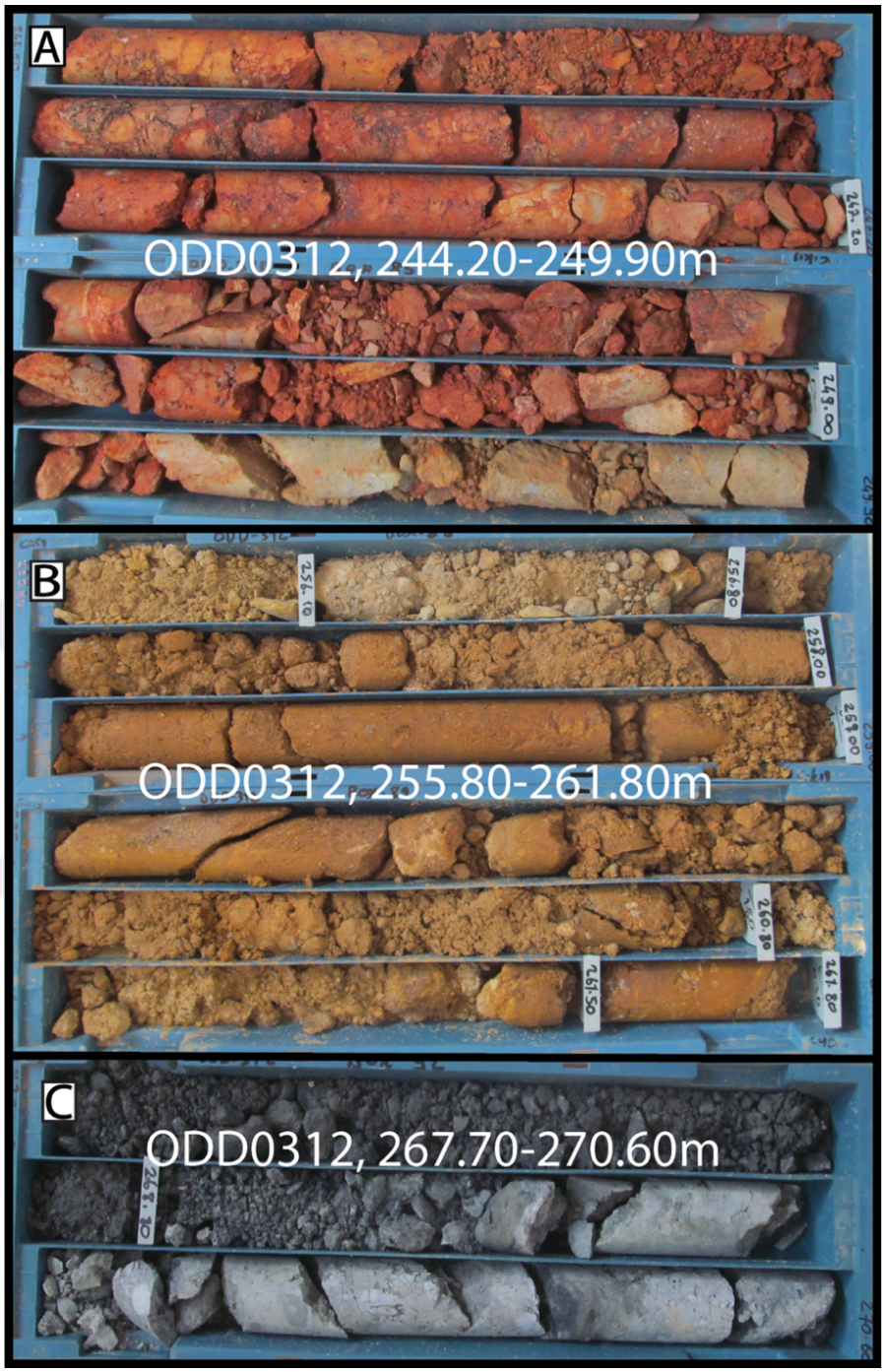


Figure 4.6. Core samples of drill hole ODD-312 from the Keltepe orebody showing vertical zonation of hydrothermal alteration. (A) Massive silica breccia with hematite dominant matrix transitioning to quartz-alunite alteration (this interval has a highest grade of 0.97 g/t Au), (B) Brecciated and fault interval with quartz-kaolinite altered, limonitic matrix (this interval has a highest grade of 0.36 g/t Au), (C) Quartz-alunite-altered, chalcocite-rich breccia (highest grades encountered in this interval are 0.66 g/t Au and 0.34% Cu).

In addition, sugary quartz is also present in this alteration zone and observed in both Keltepe and Güneytepe pits. Due to their intensely weathered and oxidized nature, silicified and brecciated rocks lack sulfide minerals, and these rather comprise Fe-oxide and Fe-hydroxide minerals. In the Keltepe pit, silicic alteration is generally restricted to the outcrops in the northern pit wall (Figure 4.2A). These can be traced up to 100 meters depth in the drill holes. However, a few of silicified domains were also observed in different parts of the Keltepe pit at various depths, such as in transitional zones where secondary Cu-enrichment blanket zones developed (Figures 4.6A–C). In the Güneytepe pit, silicification was observed in most of the outcropping ledge structures, generally as restricted to shallower depths (up to 50 meters depth; Figures 4.2B and 4.8).

In both Keltepe and Güneytepe deposits silicified zones may have widths exceeding >100 meters. However, instead of being present within the ledges, these rather occur in advanced argillic domains as silica patches (Figure 4.7).

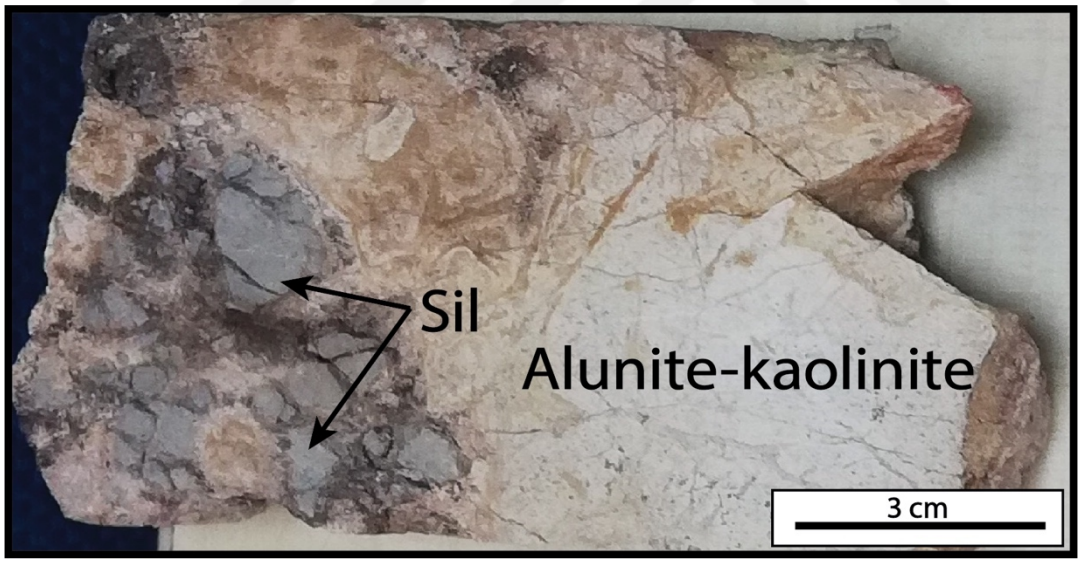


Figure 4.7. Patchy silica (sil) in alunite-kaolinite-altered andesite porphyry (sample OD79889; ODD-12; 149.00–149.10 m, Güneytepe), fractured silica patch in advance argillic alteration.

4.1.1.2 Advanced Argillic Alteration

Advanced argillic alteration, as originally defined by Meyer and Hemley (1967), is a common alteration style in many volcanic-hydrothermal systems and is characterized by an assemblage of variable amounts of quartz, alunite, kaolinite/dickite, pyrophyllite, diaspore, zunyite, and various other minerals (Hedenquist, 1994). Hedenquist and Arribas (2022) have recently shown that alteration styles including a general mineral assemblage of quartz-alunite-clay and are broadly categorized as “advanced argillic alteration” can develop under various conditions such as: (1) by ascending magmatic vapors derived from shallowly crystallizing intrusions, (2) by fumarolic activity leading to steam-heated alteration within the vadose zone above the water table, and (3) by supergene oxidation of sulfide phases mainly including pyrite.

At Öksüt, advanced argillic alteration resulted from ascending magmatic vapors that later condensed into shallow meteoric waters to form an extremely corrosive alteration product after the host porphyritic rocks. This alteration zone was observed both in mineralized breccias and in andesite porphyry wall-rocks (Figure 4.9A) and it commonly envelopes the silicified cores of mineralized ledges both laterally and also at depth (Figures 4.2A-B). The vertical extent of advanced argillic alteration can be traced down to 400 meters depth particularly within ledges located at the western part of the Keltepe pit. In the Güneytepe pit, however, this alteration terminates at much shallower levels, around 50-meters depth (Figure 4.8). In advanced argillic altered rocks, primary magmatic textures have been partially to completely obliterated. Based on the dominant alteration minerals, advanced argillic alteration has been sub-divided into two major domains as quartz-alunite and quartz-kaolinite alteration zones. Rocks that have undergone quartz-alunite alteration form large outcrops around silicified breccias and these grades outwards into the quartz-kaolinite zone (Figure 4.1). Quartz-alunite alteration is recognized in the outcrop as white to light pink colored, massive to brecciated rocks with porcellaneous appearance due to abundant alunite (Figure 4.10). This alteration is widespread in

the west of Keltepe pit, in the east of Güneytepe pit and within the area that lies in between these two mineralized domains (Figures 3.5, 4.2A-B and 4.8).

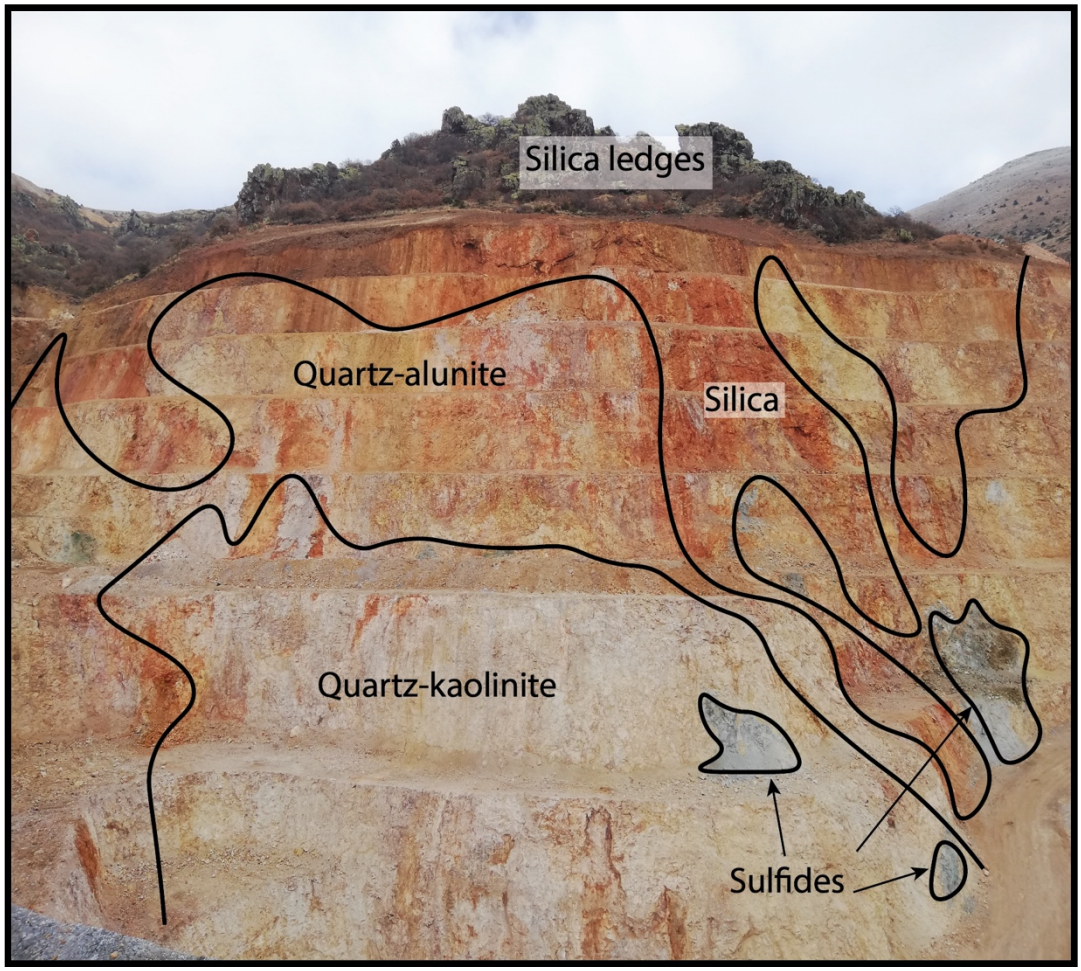


Figure 4.8. Vertical and lateral epithermal alteration zonation along the northeastern wall in the Güneytepe, where advance argillic alteration is dominant and its sub-zones (quartz-alunite and quartz-kaolinite) are present. Silica ledges are visible above the pit wall, whereas patches of secondary sulfides (gray areas) are present in deeper levels around the ledges.

Alunite is the predominant mineral alongside fine-grained quartz and makes up about 40 vol.% of the altered rocks (Figures 4.9A-B). Texturally two distinct varieties of alunite have been identified. Fine-grained alunite was observed as a common

replacement product in mineralized andesitic breccias both in the matrix as well as in the clasts (Figures 4.10A and B). Coarse-grained alunite is paragenetically later and was identified as clusters of acicular prismatic crystals (up to ~2 cm in length) generally in the matrices of breccias and in massive andesite porphyry, often as vug-fill (Figure 4.9A and B). XRD analyses and TerraSpec readings indicated presence of both K-alunite and Na-alunite (natro-alunite), but spatial distribution of these alunite varieties is not systematic at Öksüt (Table 4.1). K-alunite tends to be pinkish in the hand specimen, whereas Na-alunite is typically white colored (Figure 4.11A and B). In this alteration domain, quartz and alunite are accompanied by minor amounts of kaolinite and sulfide minerals.

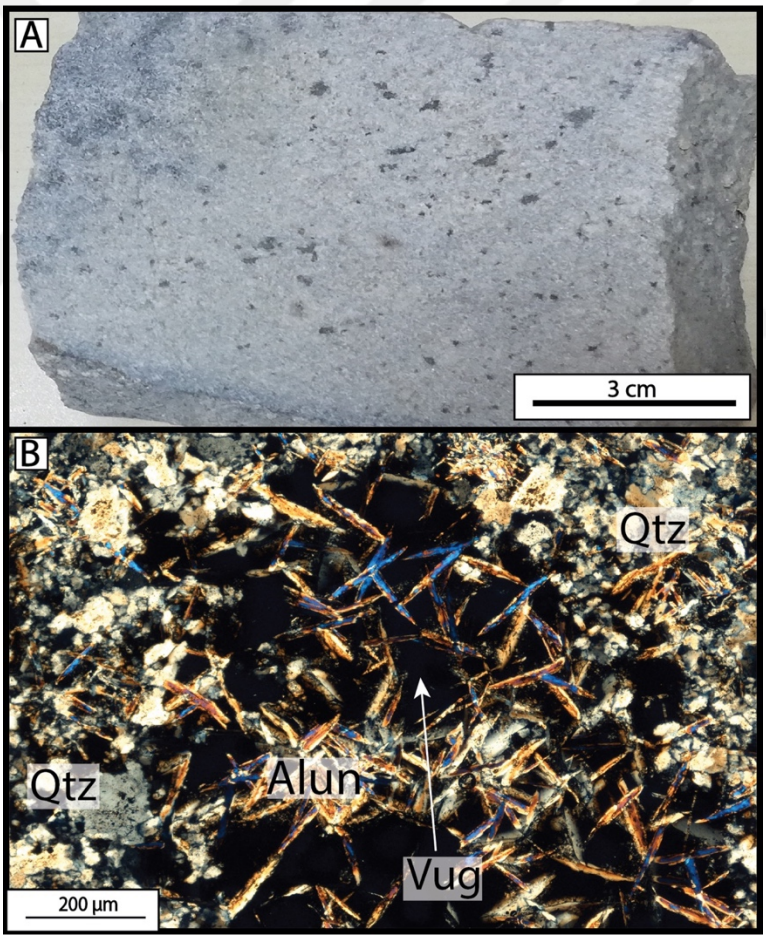


Figure 4.9. (A) Drill core photograph and (B) microphotograph (transmitted, cross-polarized light) of quartz-alunite-altered andesite porphyry from the Güneytepe orebody (sample OD79801; ODD-210; 179.50–179.60 m). Pyroxene andesite

porphyry in this sample has undergone intense quartz-alunite alteration with complete replacement of primary igneous minerals. Acicular crystals of alunite occur as clusters partially filling vugs, and some fine-grained alunite also occurs in the groundmass alongside quartz. Gray areas in (A) contain patches of sulfide minerals such as pyrite and Cu-sulfides. Abbreviations: Qtz = quartz, Alun = alunite.

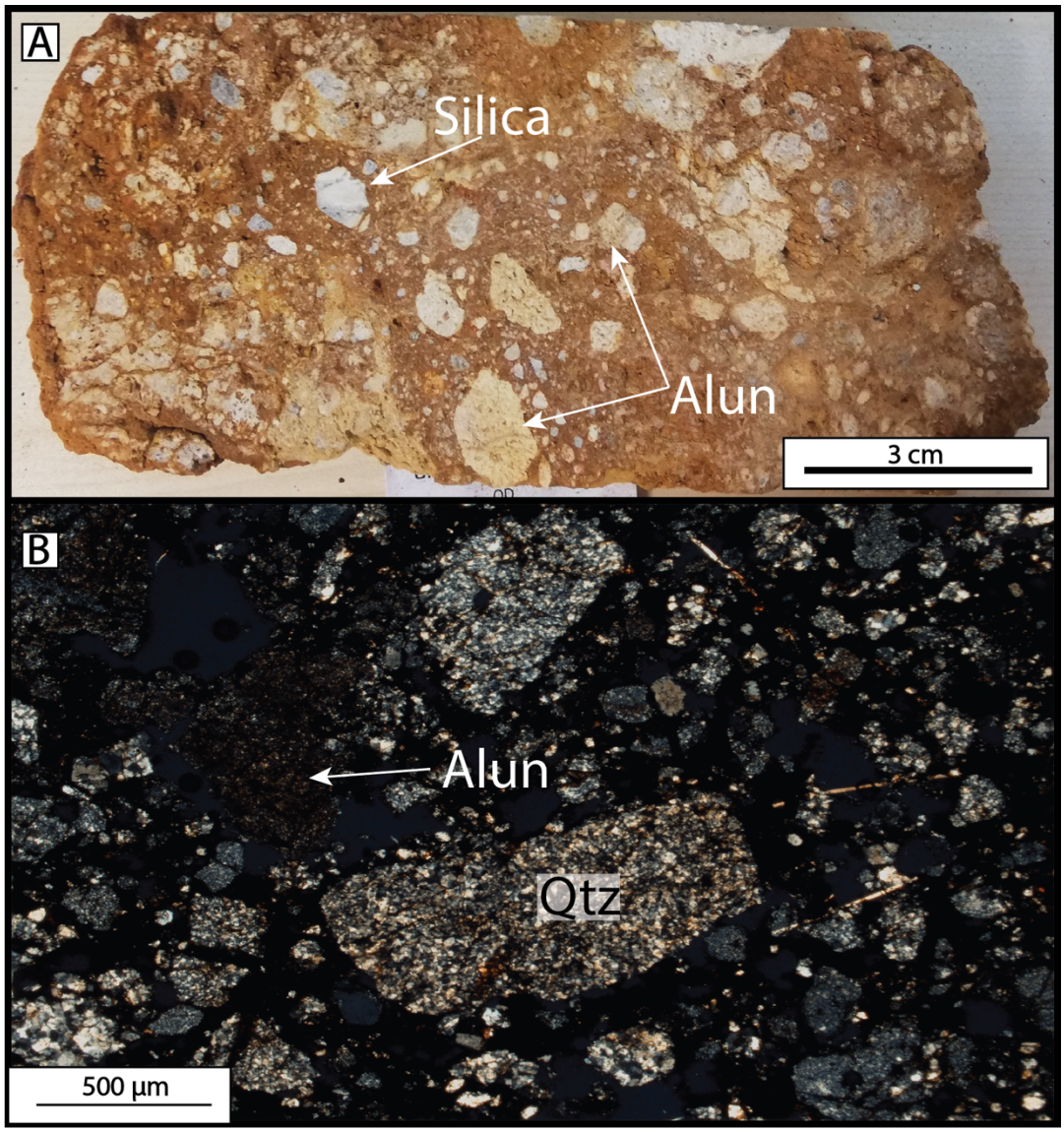


Figure 4.10. (A) Drill core photograph and (B) microphotograph (transmitted, cross-polarized light) of quartz-alunite-altered breccia from the Keltepe orebody (sample OD79990; ODD-316; 142.00–142.10 m; 4.1 g/t Au). Quartz-alunite alteration is well-developed in this matrix-supported breccia, both in the igneous clasts and in the matrix. Some of the clasts have been silica-altered, and the orange

color of the sample is due to supergene weathering and oxidation. Microphotograph in (B) shows fine-grained quartz-allunite replacement of clasts surrounded by quartz-alunite altered matrix Abbreviations: Alun = alunite, Qtz = quartz.

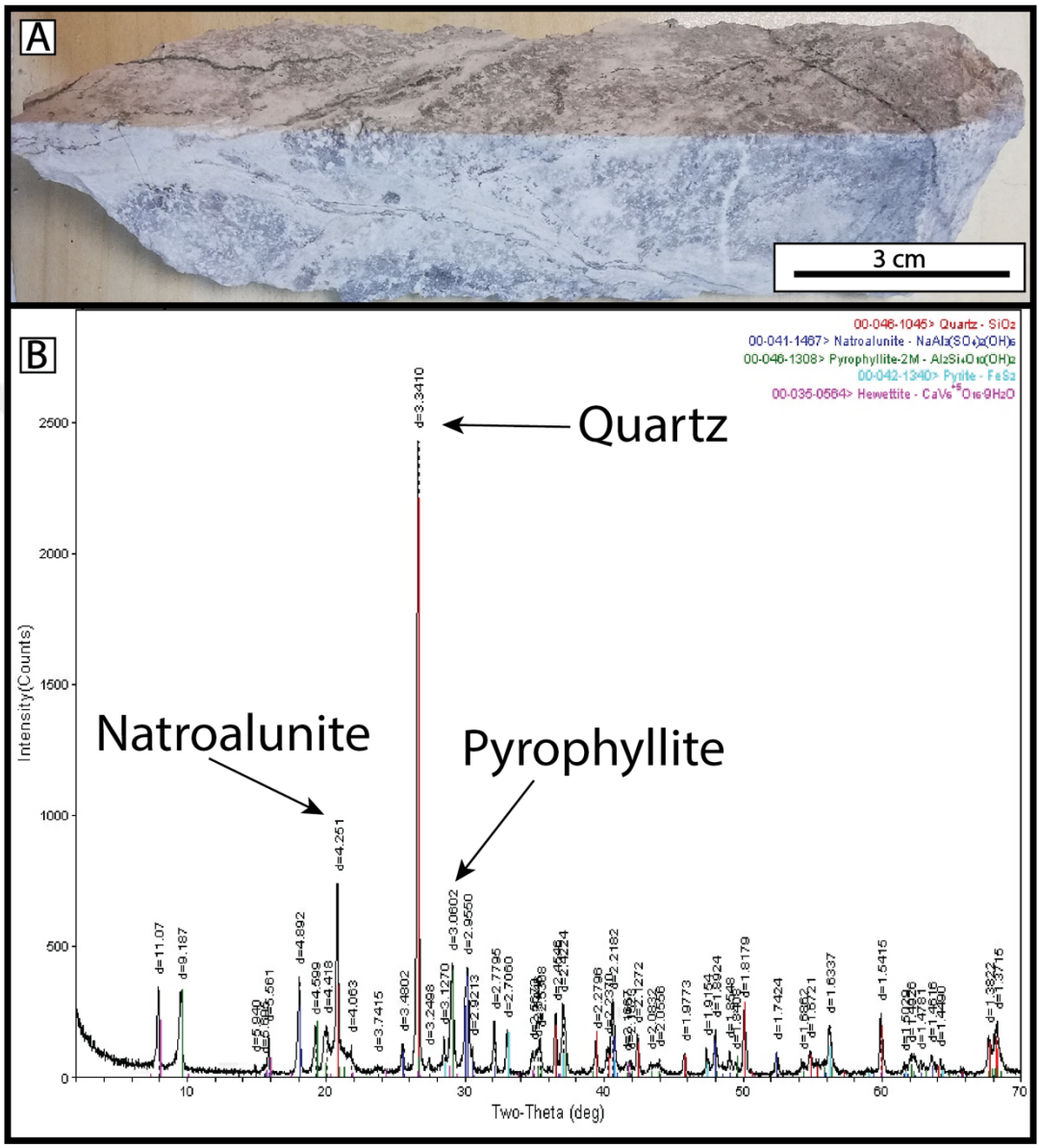


Figure 4.11. (A) Drill core photograph quartz-alunite-clay-altered andesite porphyry from the Keltepe N orebody (sample OD78962; ODD-333, 369.80–370.00 m). Groundmass in this sample has been completely replaced by quartz-alunite, whereas plagioclase phenocrysts show partial replacement into clays. Pyrophyllite veinlet cross-cuts the sample. X-ray diffractogram in (B) confirms presence of quartz, alunite, pyrophyllite, and pyrite.

Quartz-kaolinite alteration, on the other hand, is characterized by distinctly white rocks both in the outcrop and in drill core (Figure 4.8). Rocks that have undergone this alteration style appear soft and are much friable than their quartz-alunite-altered counterparts. In quartz-kaolinite alteration zones, much of the original igneous rocks have been replaced by fine-grained quartz and kaolinite, and these also contain relatively minor amounts of pyrophyllite, dickite, native sulfur, pyrite (Figure 4.12).

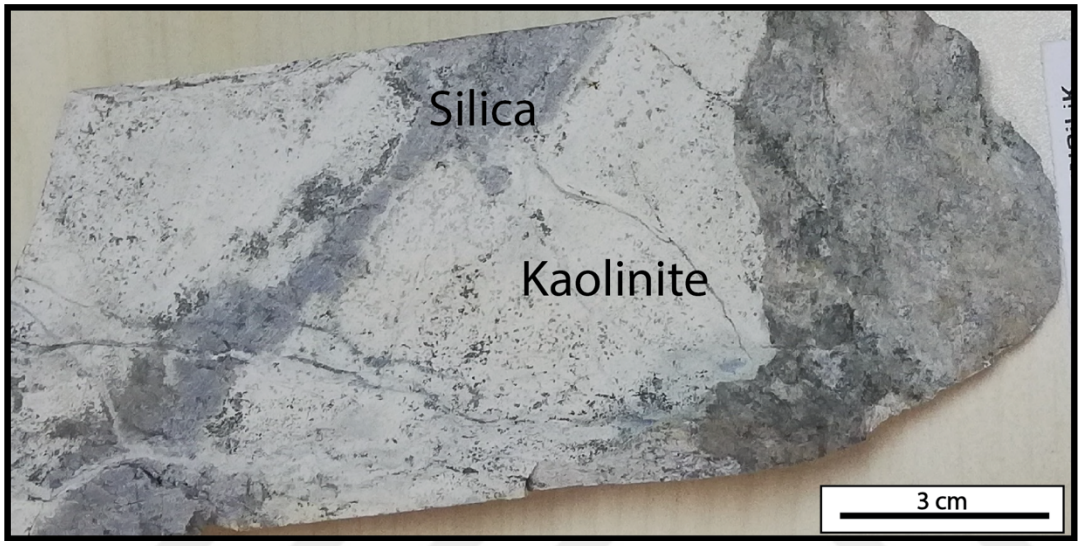


Figure 4.12. Drill core photograph of quartz-kaolinite-altered andesite porphyry from Güneytepe (sample OD79897; ODD-33, 131.70–131.80 m). Quartz-kaolinite-altered sample has been cross-cut by an irregular silica vein.

A texturally-distinct variety of quartz-kaolinite alteration was developed locally, at variable depth intervals within the Güneytepe orebody and at about 300 meters depth at Keltepe. This alteration, as commonly known as “patchy silica” alteration (Yıldız et al., 2017; Hedenquist and Arribas, 2022), is characterized at Öksüt by lobate patches of quartz surrounded by kaolinite±pyrophyllite (Figure 4.13). Patchy silica alteration was suggested to represent transition from advanced argillic alteration in high-sulfidation epithermal systems to deeper porphyry-style alteration such as potassic and phyllic alteration (Hedenquist and Arribas, 2022). Beneath the Keltepe pit, zones of patchy silica alteration are underlain by porphyry-style biotite-magnetite±K-feldspar±anhydrite alteration.

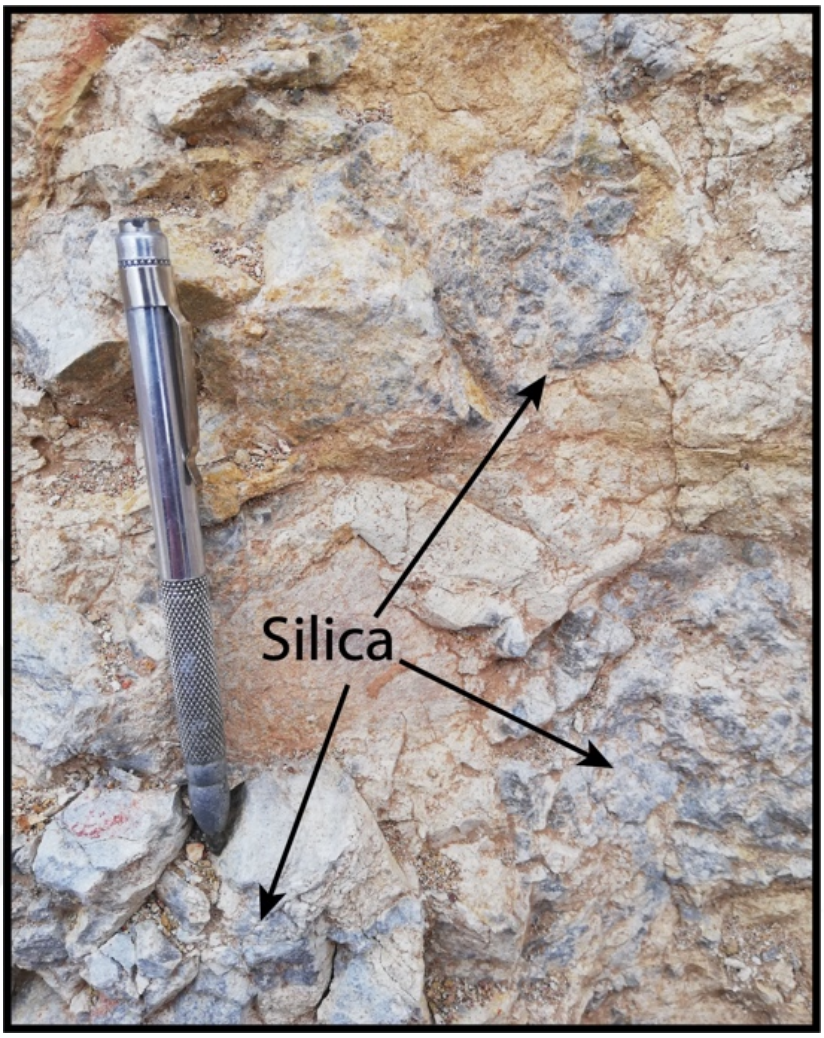


Figure 4.13. Patchy silica alteration overprinting alunite- and kaolinite-rich groundmass in andesite porphyry in the Güneytepe pit.

4.1.1.3 Argillic Alteration

Argillic alteration affected large areas around zones of advanced argillic alteration and is the most widespread alteration at Öksüt both at surface and at depth (Figure 4.14). This alteration envelopes the advanced argillic alteration and was generally encountered at depths >350 meters, marking the outer limit of altered and mineralized breccias. Argillic alteration also represents the transition between shallow epithermal-style alteration to deeper, high-temperature porphyry-style biotite-magnetite ± K-feldspar ± anhydrite alteration.

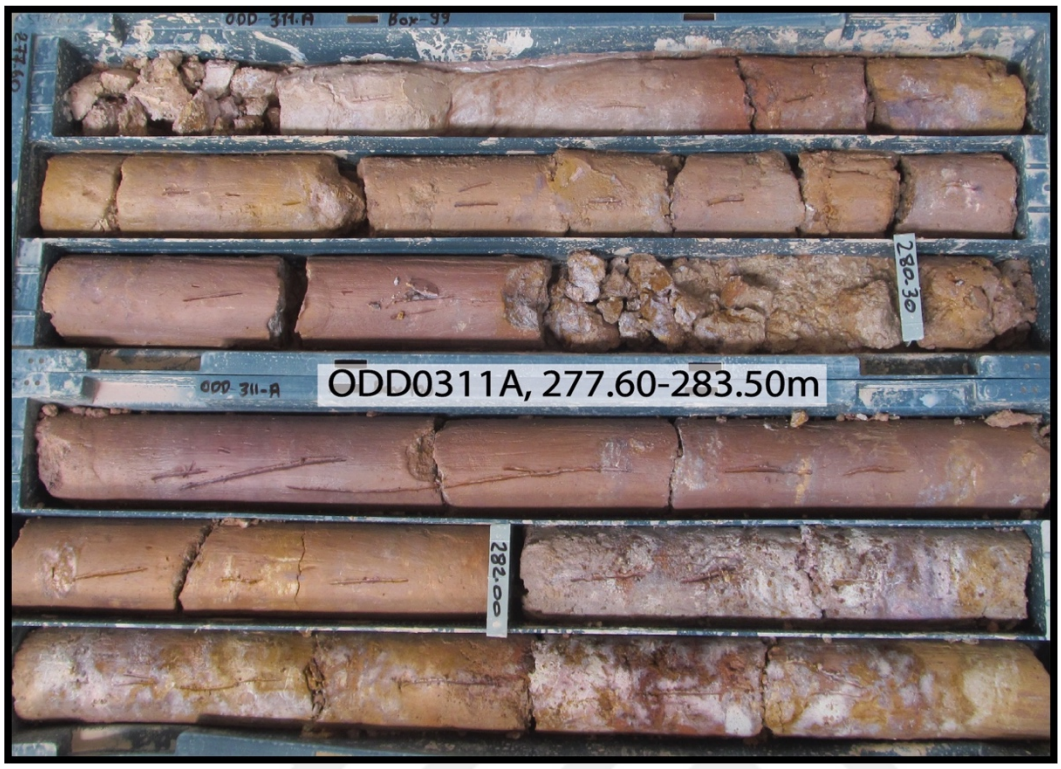


Figure 4.14. Drill core interval of strongly kaolinized andesite porphyry from the Keltepe pit. Kaolinite-rich zones are distinguished by their soft, wad-like powdery texture. Red-orange coloring is due to supergene oxidation of Fe-sulfides.

Argillic alteration is well-developed in the outcrop and is readily distinguished from texture-destructive silicification and advanced argillic alteration by preservation of primary igneous textures in andesite porphyry. Argillic altered rocks appear gray to beige in color. Predominant phyllosilicate phases characteristic of this alteration are illite and kaolinite, which are commonly observed together with fine-grained quartz and relatively minor smectite, chlorite, pyrite, marcasite, and rutile (Table 4.1). In andesite porphyry, pyroxene and biotite have been completely replaced by chlorite and clay mineral phases, whereas feldspars have been partially to completely replaced by clay minerals (Figure 4.15A-B). Stockworking quartz veins were commonly observed in argillic alteration zones with pyrite and marcasite as major sulfide vein infill (Figure 4.15A). Illite-kaolinite±smectite form mm- to cm-thick alteration haloes around quartz stockworks (Figure 4.15A).

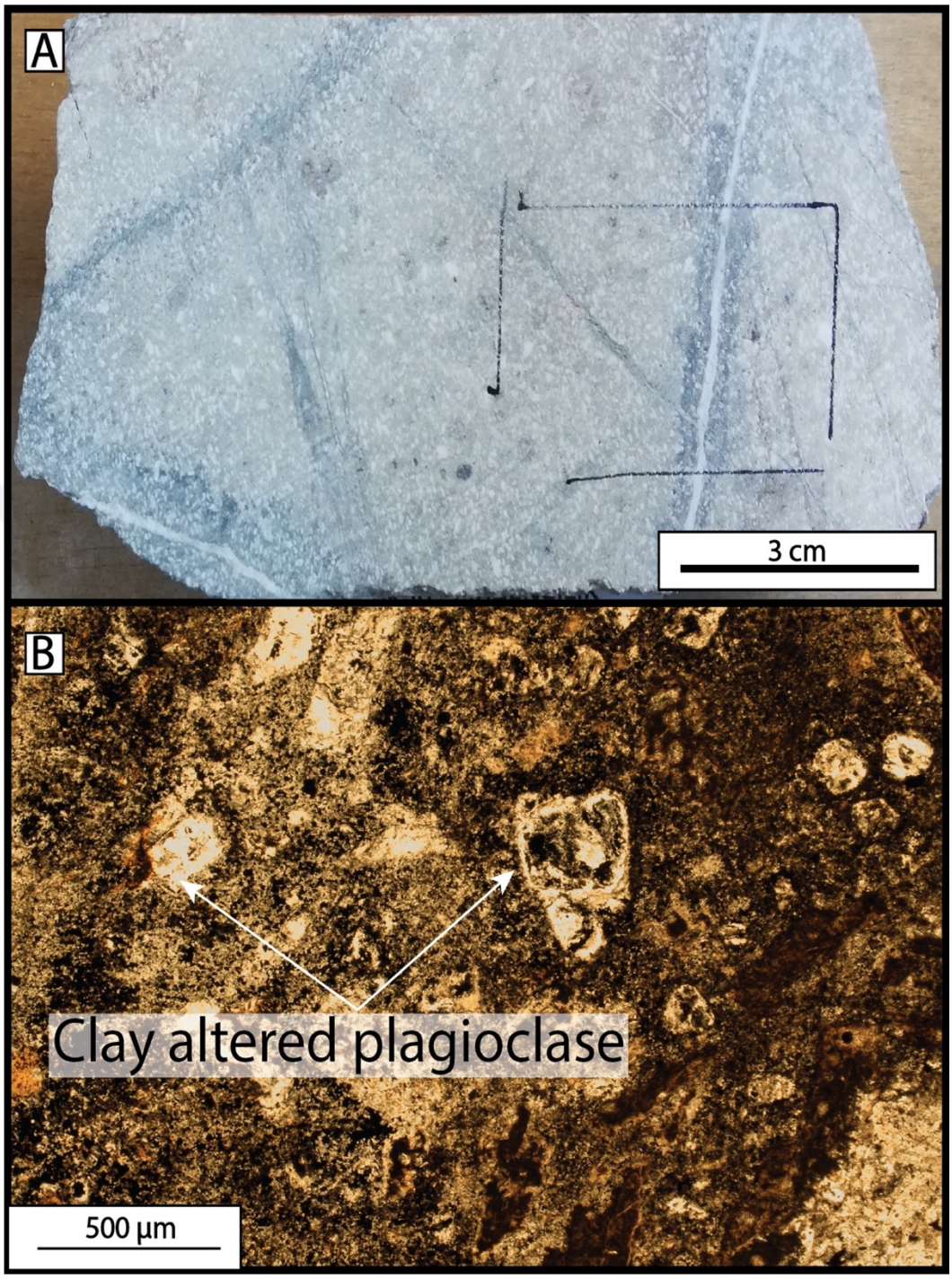


Figure 4.15. (A) Drill core photograph and (B) microphotographs (transmitted, cross-polarized light in B of quartz-illite-kaolinite-altered andesite porphyry from Keltepe pit (sample OD79861; ODD-316, 430.70–430.80 m). Original porphyritic texture in this sample is largely preserved, but all igneous minerals have been replaced by quartz, illite, and kaolinite. Quartz-pyrite veinlets are visible in drill core (A).

4.1.1.4 Biotite-magnetite ± K-feldspar ± anhydrite alteration

Biotite-magnetite± K-feldspar ± anhydrite alteration similar to K-silicate alteration observed within core zones of porphyry systems (e.g., Lowell and Guilbert, 1970; Seedorff et al., 2005; Sillitoe, 2010) represents the deepest levels of the hydrothermal system at Öksüt. In the Keltepe pit, this alteration appears at depths of 900 meters, whereas in Güneytepe it begins at around 350 meters depth and extends down to about 700 meters depth (Figure 4.16).

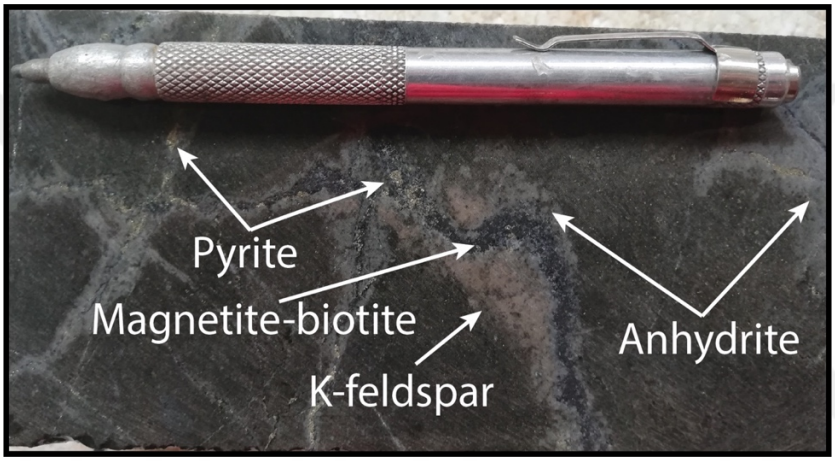


Figure 4.16. Drill core photograph of magnetite-biotite-K-feldspar-anhydrite alteration in andesite porphyry from Güneytepe (ODD-444; 1001.00–1001.10m). Quartz-magnetite-biotite vein has an alteration selvedge of K-feldspar and anhydrite. Late propylitic alteration resulted in epidote-chlorite overprint of feldspars and biotite, whereas pyrite has partially replaced magnetite.

Biotite-magnetite± K-feldspar ± anhydrite alteration is represented by abundant secondary biotite and hydrothermal magnetite with lesser K-feldspar and anhydrite. Secondary biotite is distinguished by its fine-grained, anhedral form, and was observed as aggregates at the sites of former pyroxene crystals. Some biotite also occurs as vein infill (Figure 4.16). XRD and TerraSpec analyses have shown that biotite is phlogopitic in composition (Table 4.1). Hydrothermal magnetite is fine- to medium-grained, and occurs either as disseminations or as vein infill in M-veinlets (sensu Arancibia and Clark, 1996). In addition, minor K-feldspar have partially

replaced plagioclase phenocrysts. Quartz veining and sulfide mineralization is generally absent in rocks that have undergone biotite-magnetite± K-feldspar ± anhydrite alteration (Figures 4.17A, B).

4.1.1.5 Propylitic alteration

Propylitic alteration is a common alteration style in many hydrothermal systems, and in gold-rich porphyry and high-sulfidation epithermal deposits it defines the outer halo of the mineralized system (Sillitoe, 2000). In porphyry systems this alteration is represented by chlorite-epidote-carbonate ± albite ± actinolite and may grade inwards into potassic alteration (Lowell and Guilbert, 1970; Seedorff et al., 2005; Sillitoe, 2000 and 2010). In high-sulfidation epithermal deposits, on the other hand, characteristic typical propylitic mineral assemblage of chlorite-illite-smectite-carbonate develops as the outermost halo following argillic alteration (e.g., Arribas, 1995; Hedenquist et al., 2000; Simmons et al., 2005).

At Öksüt, propylitic alteration is not widespread within the shallow epithermal system. However, it developed commonly as a late overprint in deeper levels, typically at depths >300 m. Propylitic alteration represents the peripheral zones of hydrothermal fluid upflow responsible from formation of mineralized ledges. It is represented by abundant epidote and carbonate with lesser carbonate and pyrite (Table 4.1). Epidote and chlorite have replaced ferromagnesian minerals in the precursor pyroxene andesite porphyry (Figure 4.17A). Propylitic alteration also developed as an overprint after paragenetically earlier high-temperature alteration minerals of biotite-magnetite± K-feldspar ± anhydrite and calc-silicate alteration. In propylitized rocks carbonate veinlets of up to 1–2 cm thickness are common.

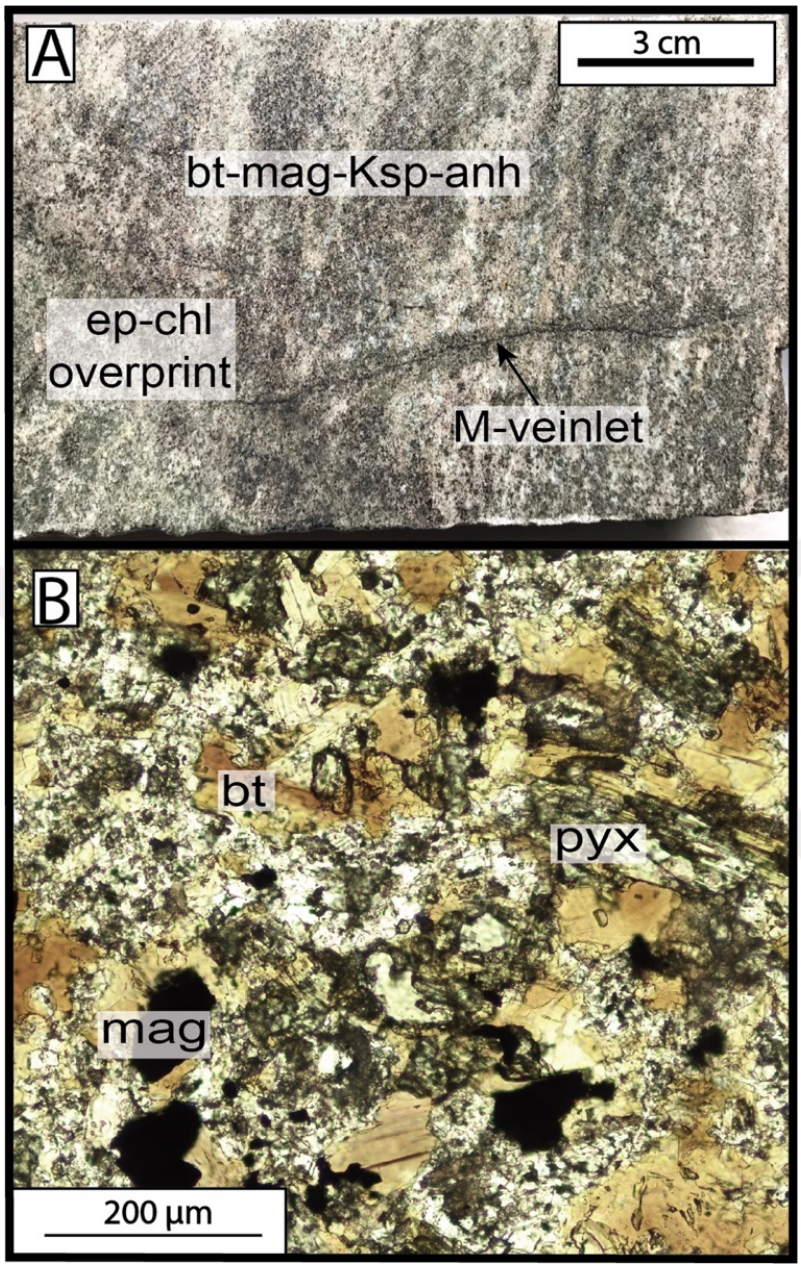


Figure 4.17. (A) Drill core photograph and (B) microphotograph (transmitted, cross-polarized) of propylitized pyroxene andesite porphyry from Boztepe W (far west of Keltepe), (sample OD78863; ODD-337, 706.30–706.60 m). Early biotite-magnetite-K-feldspar-anhydrite alteration in this sample has been overprinted by propylitic alteration, which caused partial to complete replacement of ferro-magnesian minerals by chlorite, and plagioclase by epidote. Abundant secondary biotite is still preserved in the sample. Magnetite is present either as disseminations or along M-veinlets, but has also been partially replaced by pyrite during propylitization. Abbreviations: bt = biotite, mag = magnetite, Ksp = K-feldspar, anh = anhydrite, ep = epidote, chl = chlorite, pyx = pyroxene.

4.1.1.6 Calc-silicate alteration

Calc-silicate minerals typical of skarn systems were only developed locally in Öksüt, mainly in the western sector of the license area, about a km west of the Keltepe pit. It occurs as irregular replacement bodies and as infill in non-planar fractures (1–3 cm thick) within host andesite porphyry.

Main calc-silicate minerals in this metasomatic alteration zone are grossularite, diopside, and vesuvianite. Grossularite is dark red to brown in color, and occurs as coarse-grained (locally >1 cm-long), euhedral crystals (Figure 4.18A). Under the microscope it displays well-developed compositional zoning. Grossularite is accompanied by euhedral prismatic crystals of vesuvianite and fine-grained, anhedral crystals of diopside, the latter commonly transformed into sericite due to propylitic overprint (Figure 4.18B, C; Table 3.1).

Although calc-silicate alteration is commonly regarded to be a product of metasomatic reaction between silicate magmas and surrounding carbonaceous rocks, carbonate lithologies were not mapped within or in the vicinity of the Öksüt property. Similarly, carbonate rocks were not intersected in any of the drill holes in the study area. On the other hand, areas of calc-silicate alteration are mainly present in the western part of the license area (Boztepe West prospect), near Zile (Figure 3.2), and concealed fragments of carbonate rocks were encountered along access roads in this region (Figure 3.4A-B). Therefore, the presence of this alteration to the west of Öksüt was interpreted to indicate proximity to the regional basement rocks of the Tauride platform, which were likely to be present at relatively shallower depths along the collapsed western flank of the Develidağ Volcanic Complex.

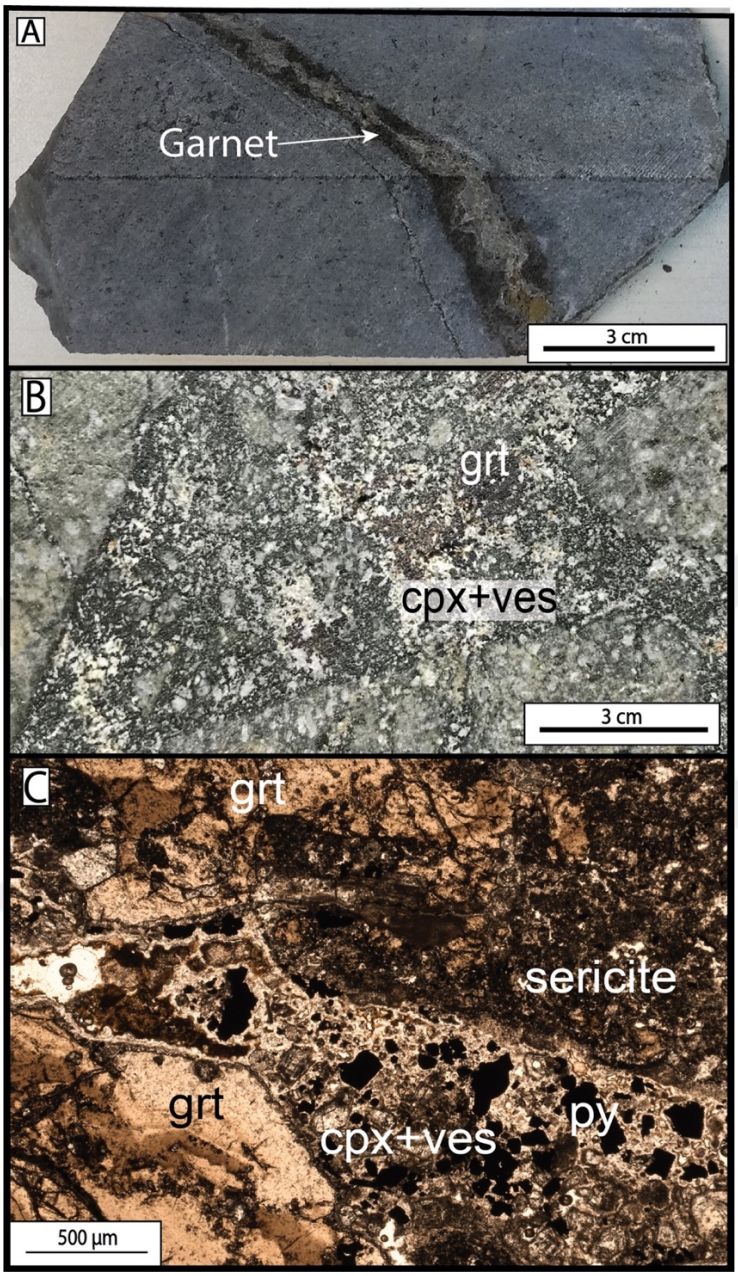


Figure 4.18. (A) Drill core photograph (transmitted, cross-polarized) of calc-silicate-altered pyroxene andesite porphyry from far west of Keltepe (sample OD78855; ODD-337, 71.40–71.45 m). Calc-silicate minerals, mainly represented by garnet, occur as veins (A). (B) core sample OD78857 (ODD0337, 77.30–77.60m), fracture filling calc-silicate (grossularite-diopside-vesuvianite) alteration in pyroxene andesite porphyry. (C) plane polarized reflected light microscope image of Sample OD78855 (ODD0337, 71.40–71.80m), garnet-diopside-vesuvianite veinlet in pyroxene andesite porphyry. Sericite and pyrite replacement occurred due to retrograde overprint. Abbreviations: grt = garnet, , py = pyrite, cpx = clinopyroxene, ves = vesuvianite.

4.1.2 Mineralization

Öksüt gold-copper mineralization is primarily associated with and is generally confined to breccia zones emplaced within vertical to sub-vertical ledges. Minor gold-copper mineralization also occurs outside of the ledges, as disseminations in the pyroxene (includes both clinopyroxene and orthopyroxene) andesite porphyry.

Ledges hosting altered and mineralized breccias have upward flaring forms – i.e., these are relatively narrow at depth and widen up towards shallower levels. In both Keltepe and Güneytepe sector gold is hosted by breccias and disseminated style mineralization.

Mineralized breccias in Keltepe are steeply-dipping (50° to 70°) to the SE, and these can be followed within a NNW-trending zone about 950 meters long and 500 meters wide. Their vertical extent reaches up to 350 meters and individual breccia bodies are often less than 60 meters wide (Figure 4.19). Silicic breccia ledges in Güneytepe are also steeply-dipping (75°) towards SE and have similar trends, but their strike lengths are relatively limited (<300 m) within a zone that is about 300 meters wide (Figure 4.20).

Disseminated mineralization, which was particularly better developed in andesite porphyry in Güneytepe, is vertically more limited (<100 m), but its lateral extent may locally reach up to about 250 meters (Figure 4.20). Despite this significant variability in orebody extents, all ledges and breccia zones are consistently controlled by steeply-dipping faults (Figures 4.19 and 4.20).

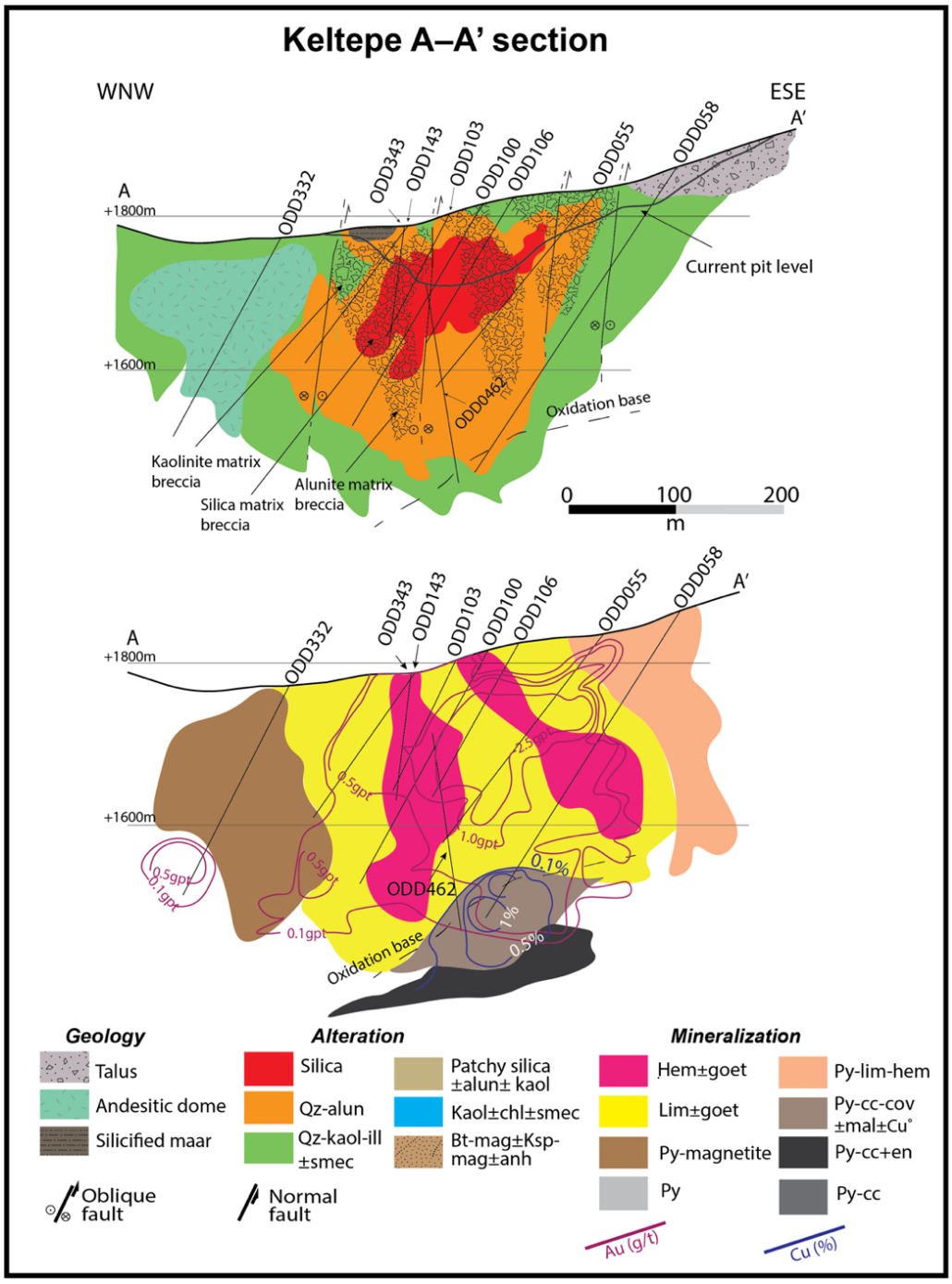


Figure 4.19. Schematic cross-sections of the Keltepe orebody, showing spatial relationship between various alteration and mineralization domains as well as gold-copper grade shells. Section lines are shown in Figure 3.5. Abbreviations: alun = alunite, anh = anhydrite, bt = biotite, cc = chalcocite, chl = chlorite, cov = covellite, en = enargite, goet = goethite, hem = hematite, ill = illite, kaol = kaolinite, Ksp = K-feldspar, lim = limonite, mag = magnetite, py = pyrite, qz = quartz, smec = smectite.

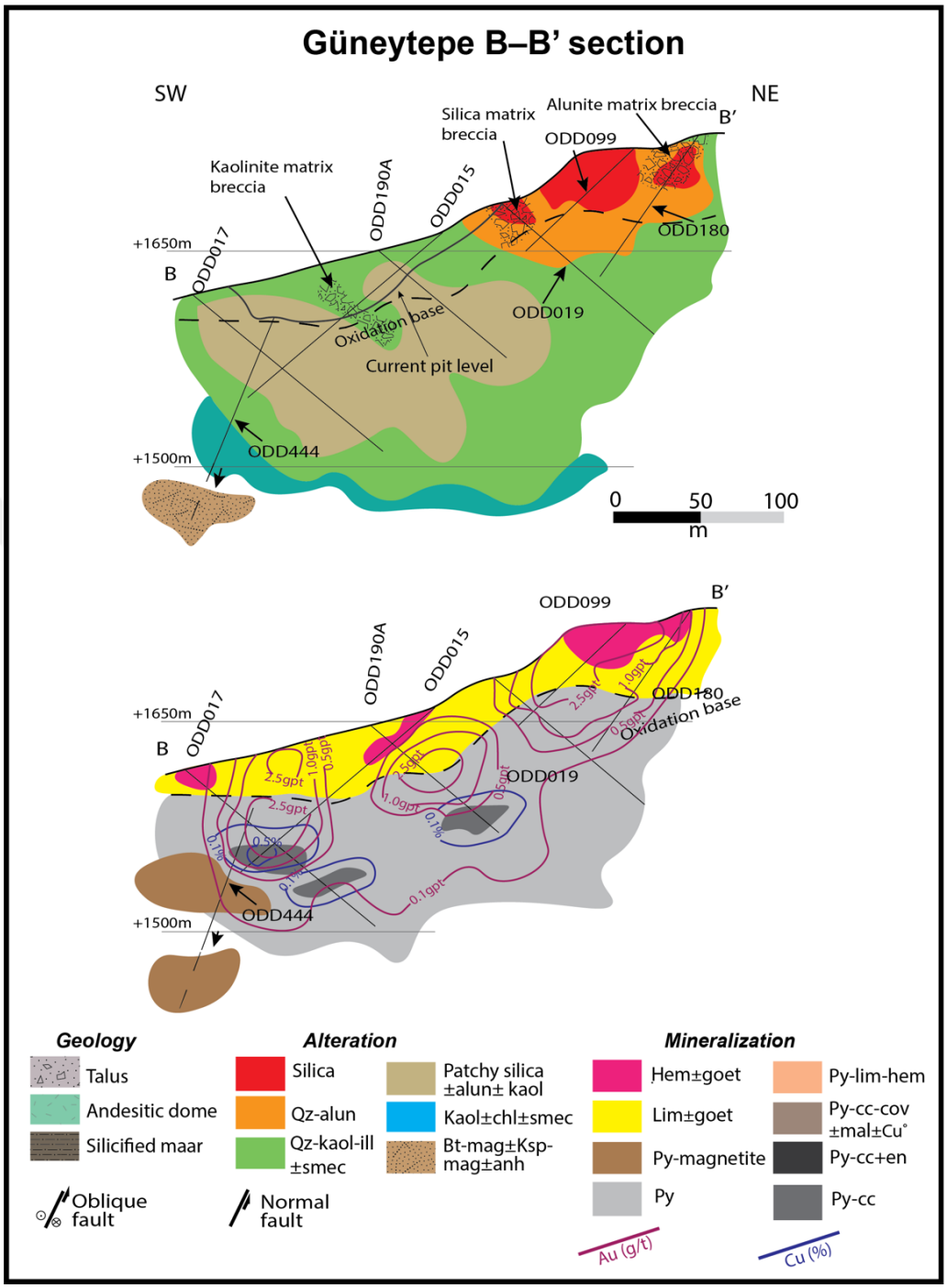


Figure 4.20. Schematic cross sections of Güneytepe orebody, showing spatial relationship between various alteration and mineralization domains as well as gold-copper grade shells. Section lines are shown in Figure 3.5. Abbreviations: alun = alunite, anh = anhydrite, bt = biotite, cc = chalcocite, chl = chlorite, cov = covellite, en = enargite, goet = goethite, hem = hematite, ill = illite, kaol = kaolinite, Ksp = K-feldspar, lim = limonite, mag = magnetite, py = pyrite, qz = quartz, smec = smectite.

4.1.2.1 Breccias

Öksüt breccias, the main host of gold-copper mineralization, were sub-grouped into four distinct types based on detailed core logging and petrography (Table 4.2). Within the mineralized zones, a large part of these breccias has undergone intense supergene oxidation, and therefore it is difficult to accurately ascribe a genetic origin for these. Still, a broad distinction was made between early breccia facies (silica-, alunite-, and kaolinite- matrix breccias) that display phreatomagmatic character and late-stage breccia facies with sulfide-rich matrices that rather have mixed hydrothermal-tectonic character (Reid et al., 2015; Yıldız et al., 2017; this study). The former group has been observed in both Keltepe and Güneytepe. These, in places, contain large (several centimeters across) angular fragments within rock-flour matrix, suggesting a diatreme origin (Yıldız et al., 2017).

Phreatomagmatic (or phreatic) breccias characterize the earliest phase of brecciation and these are likely to have formed during diatreme development. Based on their predominant alteration phreatomagmatic breccias are classified as silica-, alunite-, kaolinite-matrix breccias (Table 4.2). Both Keltepe and Güneytepe deposits contain these early phase breccias either within the ledges or in the enveloping alunitic and/or kaolinitic halos. In some places these breccias display strongly-destroyed texture (Reid et al., 2015) with several cm-length angular clasts on rock-flour matrix (Yıldız et al., 2017) and fall deposits nearby some of these breccias in the south pit wall of Keltepe deposit suggesting these are products of diatreme formation (Figures 3.8, 3.9A-C). On the other hand, hydrothermal-tectonic breccias are distinguished by their abundant pyrite- and/or chalcocite-rich matrices. Such breccia types were only encountered in drill holes from the Keltepe orebody.

4.1.2.1.1 Silica-matrix breccia

Silica-matrix breccias are commonly present in the center of the ledges and are distinguished by abundant silica in both its matrix and clasts with or without alunite. These are matrix- to clast-supported and contain crackled silica clasts with often angular to sub-angular geometry. Polymictic character is dominant and 80% of the clasts are made up of massive and residual vuggy silica, but these breccias may also contain quartz-alunite altered rock andesite porphyry fragments which form about 20% of the clasts. Alunite may also be present as vug fill (Figures 4.21A–C).

Table 4.2 Characteristics of common breccia types in Öksüt

Breccia type	Origin	Internal organization	Components		Alteration	Ore minerals
Silica matrix	Phreatomagmatic, diatreme	Matrix to clast supported, polymictic, grey-pale grey-porcelaneous white-red-brown	Clasts: Medium to coarse, massive and vuggy silica, alunite, rarely kaolinite, crackled and fractured clasts touch each other, rarely jigsaw, ameoboid, angular to subangular	Matrix: Fine grained silica, rarely vug and fracture filled alunite, both oxidized and sulfide matrix	Silica, alunite	Hematite, goethite, gold, pyrite, chalcocite, covellite
Alunite matrix	Phreatomagmatic	Matrix to clast supported, polymictic, white-pinkish-yellow-red-brown	Clasts: Medium, alunite, silica, and kaolinite, rarely fractured, ameoboid, angular to subangular	Matrix: Fine grained alunite with or without quartz, both oxide and sulfide	Alunite	Hematite, limonite, jarosite, goethite, pyrite, gold, chalcocite, malachite, covellite
Kaolinite matrix	Phreatomagmatic	Matrix to clast supported, monomictic-polymictic, white-red-brown	Clasts: Fine to medium, kaolinite, rarely alunite, and silica, subangular to subrounded	Matrix: Kaolinite, both oxide and sulfide matrix	Kaolinite	Hematite, limonite, pyrite
Sulfide matrix	Hydrothermal-magmatic	Clast supported, monomictic-polymictic, black-grey-pale grey	Clasts: Medium to coarse silica, alunite, crackled and fractured clasts touch each other, rarely jigsaw, subangular to lineated	Matrix: Sulfide, dominantly pyrite and/or chalcocite forming, lineated	Silica, alunite	Pyrite, chalcocite, gold

In the supergene oxidized levels fractures with hematite and/or goethite fill are commonly present imparting silica-matrix breccias a typical yellow to reddish brown color. Such zones return gold grades up to 4 g/t. On the other hand, at deeper levels massive silica-silica matrix breccias appear in darker colors due to the presence of

secondary copper sulfides, such as chalcocite and covellite together with fine-grained pyrite. Consequently, these are associated with significant gold (up to 2.7 g/t Au) and copper (up to 7 wt.% Cu) grades (Figure 4.41A and B).

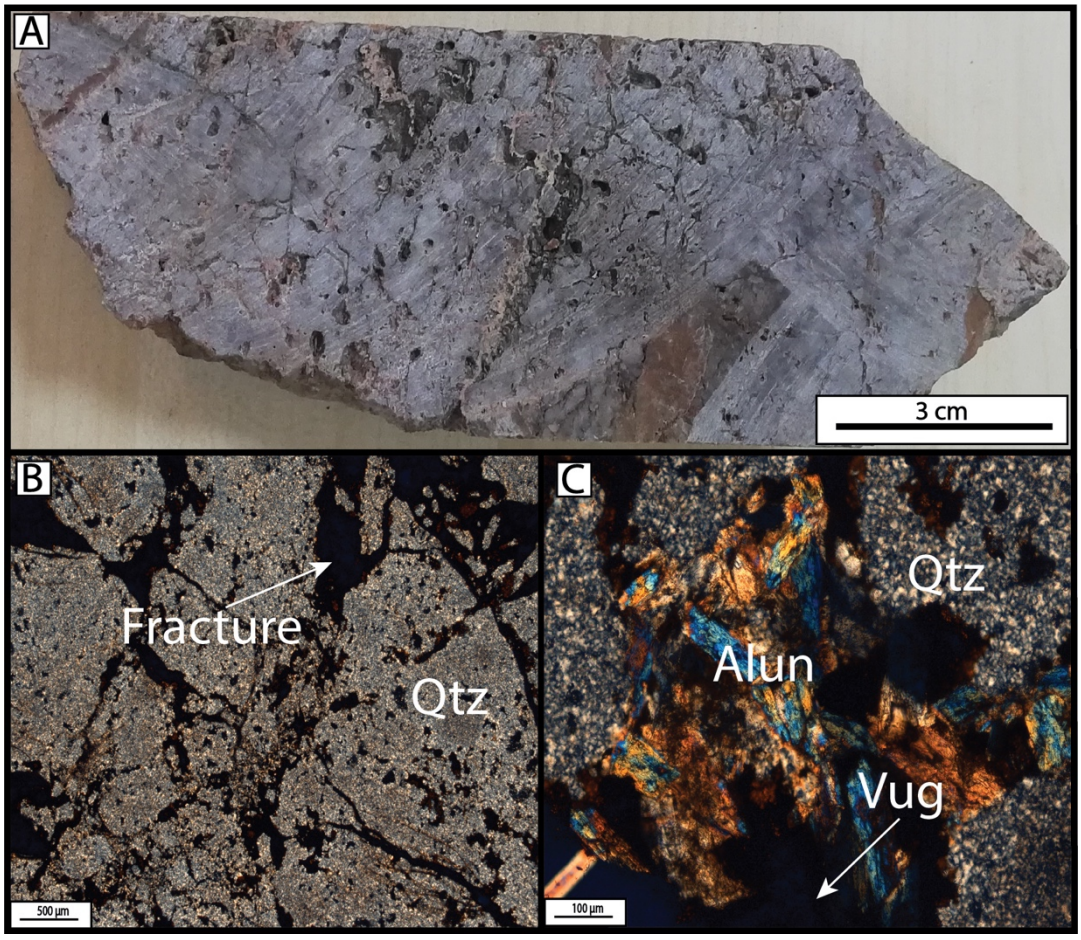


Figure 4.21. (A) Drill core photograph and (B and C) microphotographs (transmitted, cross-polarized) of massive silica-residual silica-matrix breccia from Güneytepe (sample OD79872; ODD-12, 12.2–12.30 m, 3.47 g/t Au). This sample contains fine-grained quartz both in the matrix and in the clasts. A dense network of hematite- and/or goethite-fill fractures are common. Late alunite partially fills vugs. Abbreviations: Qtz = quartz, Alun = alunite.

4.1.2.1.2 Alunite-matrix breccia

Alunite-matrix breccias encircled silica matrix breccias in ledges. These are polymictic, matrix- to clast-supported breccias comprising pervasively quartz-alunite-altered matrices (Figure 4.10A, Table 4.2). Poorly-sorted clasts are fine- to coarse-grained, angular to sub-angular and include massive to vuggy silica- and quartz-alunite-altered fragments (Figure 4.22A and B), with >60% of these showing quartz-alunite alteration. Altered juvenile fragments of andesite porphyry are also visible, and in places these have cuspate margins. Similar to silica-matrix breccias, alunite-matrix breccias are frequently cut by irregular fractures containing hematite, goethite, and limonite infill at shallow levels in the supergene oxide zone. Overall gold grades are lower than those observed in silica-matrix breccias, and grades of ~2 g/t Au and <0.2 wt.% Cu are generally associated with increased secondary oxide and hydroxide mineral abundance (Figure 4.10A).

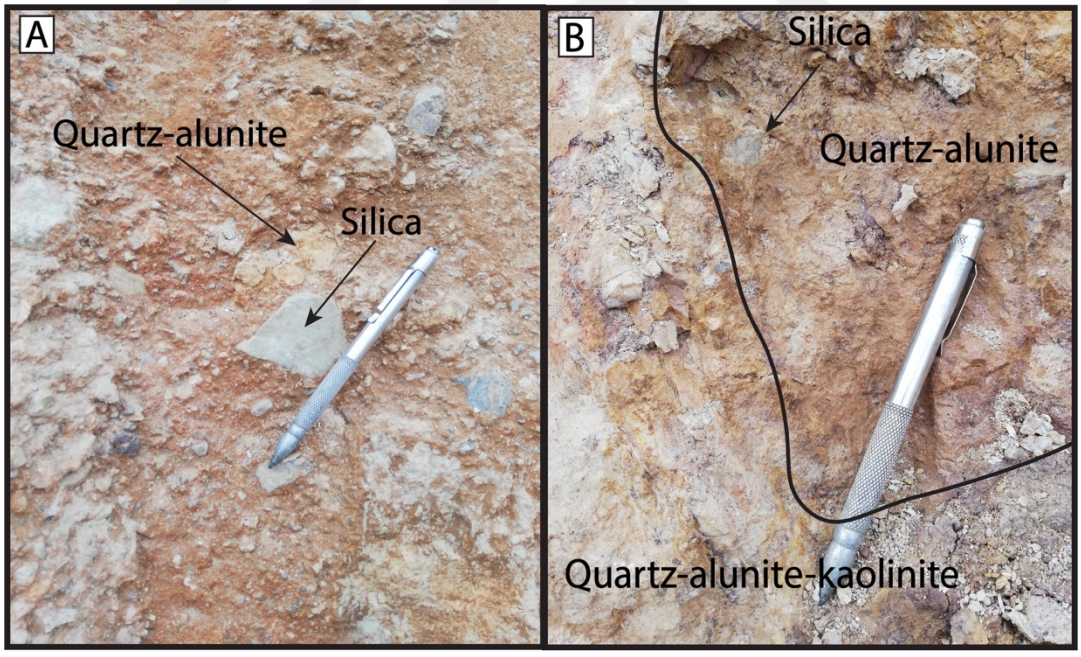


Figure 4.22. Quartz-alunite matrix, silica-massive silica and quartz-alunite clast-rich outcrop (A) in the Keltepe pit, and (B) in the Güneytepe pit and in contact with quartz-alunite-kaolinite matrix breccia.

4.1.2.1.3 Kaolinite-matrix breccia

These are rare breccias that generally lack gold-copper mineralization. Both clasts and matrix contain abundant clay, dominated by kaolinite (Figure 4.23, Table 4.2). Kaolinite-matrix breccias are polymict, matrix- to clast-supported, and composed of sub-angular to sub-rounded clasts. Altered juvenile andesite porphyry fragments have been mainly replaced by quartz-kaolinite, as well as by minor amounts of quartz-alunite- and silica-altered fragments (Figure 4.22B).

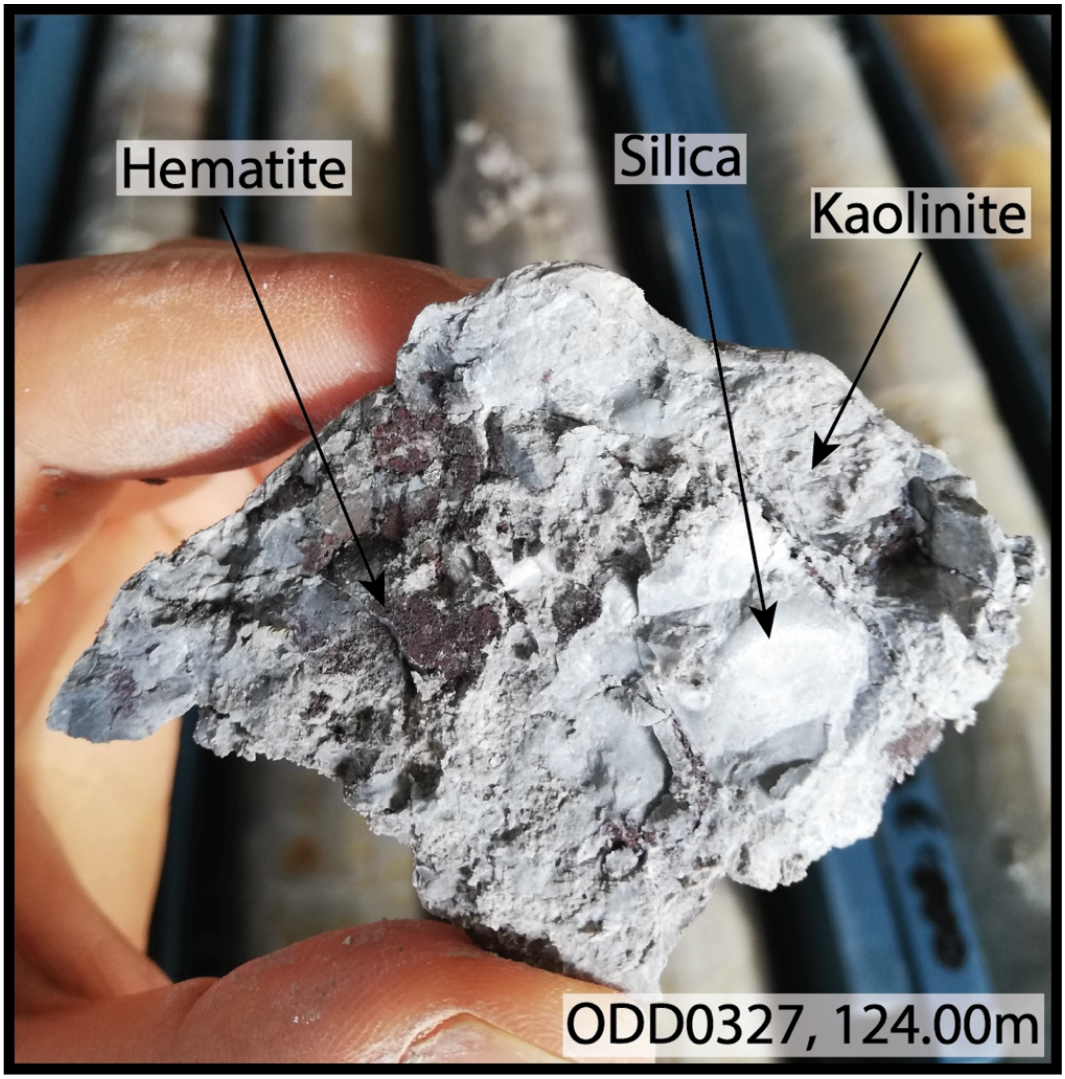


Figure 4.23 Drill core sample of kaolinite-matrix breccia from the Yelibelen prospect consisting of silica-altered clasts and fracture-filling hematite.

4.1.2.1.4 Sulfide-matrix breccia

Sulfide-matrix breccias were mainly observed in and to the west of Keltepe. These are monomict, clast- to matrix-supported breccias with clasts predominantly composed of quartz-kaolinite±alunite-altered andesite porphyry, and sometimes containing quartz-sulfide veinlets. Matrix, on the other hand, is characteristically made up of fine-grained sulfides, either dominated by pyrite or chalcocite (Figures 4.24A and B, 4.25A and B). Where pyrite dominates the matrix, these locally display crude layering with tabular-shaped fragments (Figure 4.24A and B, Table 4.2).

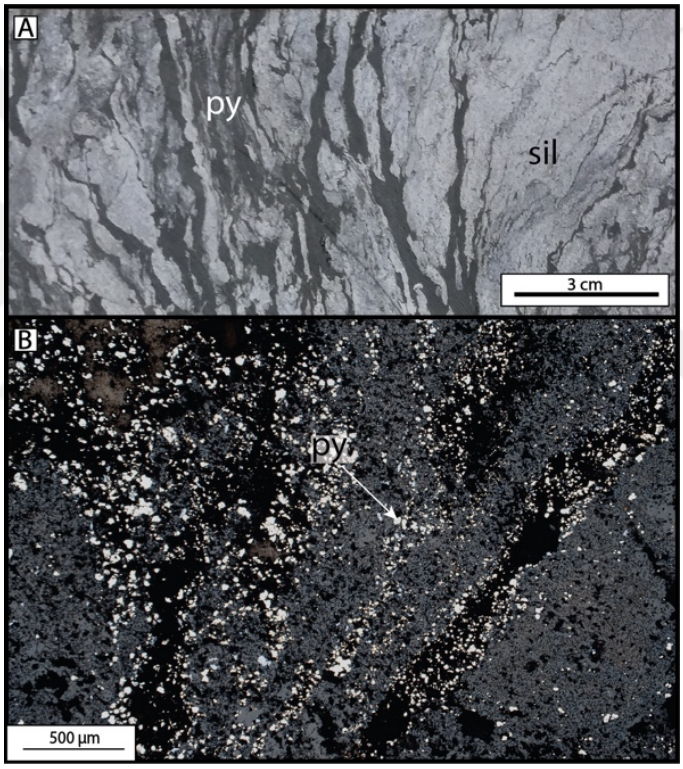


Figure 4.24. (A) Drill core photograph and (B) microphotograph (reflected, plane-polarized light) of sulfide-matrix breccia from Keltepe (sample OD79934; ODD-316, 328.40–328.50 m). This sample comprises crudely laminated tabular clasts of silicified rock surrounded by fine-grained pyrite. Abbreviations: py = pyrite, sil = silica.

Sulfide-matrix breccias are not always associated with significant gold and/or copper grades, but in places, grades as high as ~0.5 g/t Au and ~0.5 wt.% Cu. Chalcocite-rich sulfide- matrix breccias are usually jig-saw fit, clast-supported breccias (Figure

4.25 A and B), and as such, they are associated with elevated copper grades (several weight percent Cu).

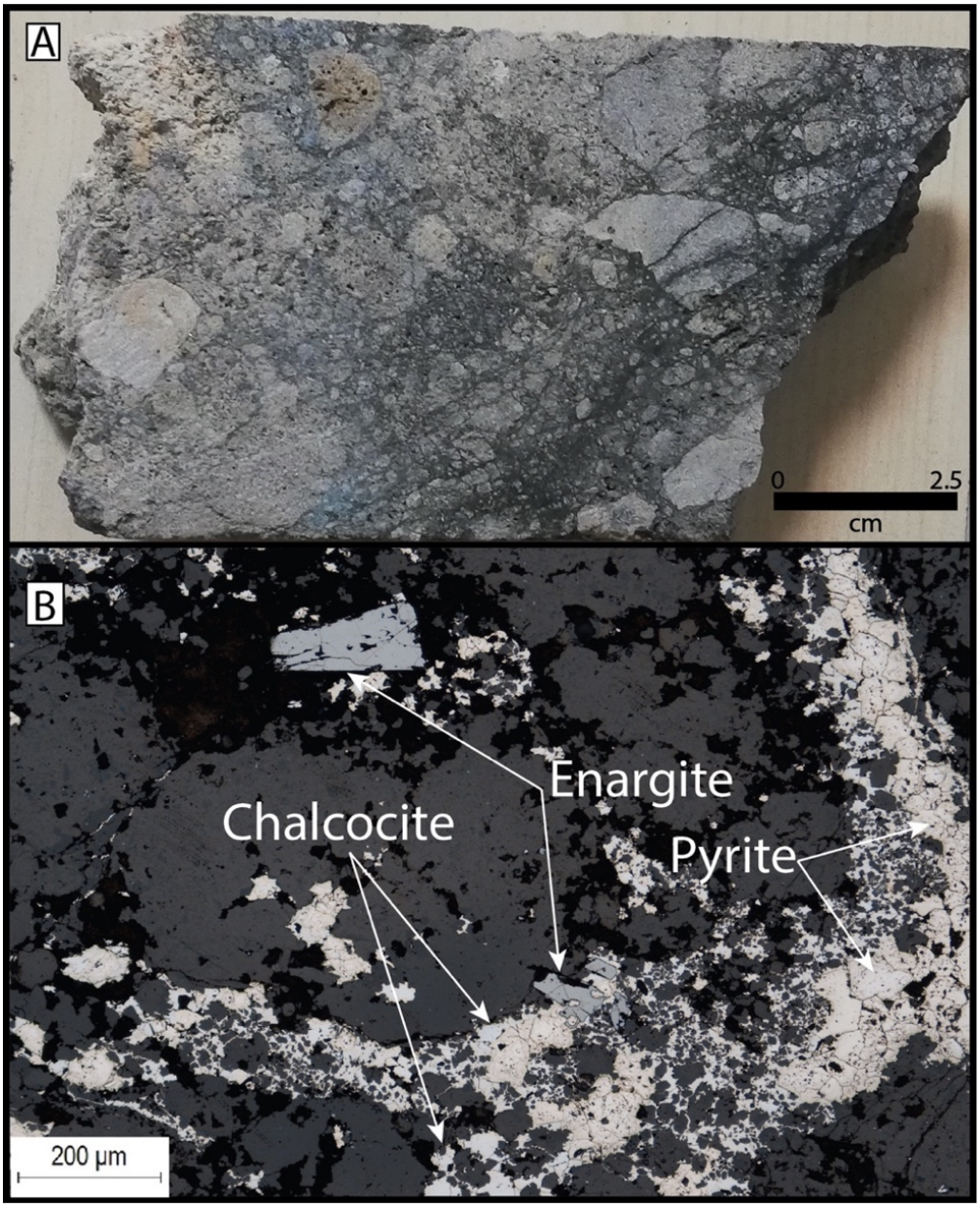


Figure 4.25. (A) Drill core photograph and (B) microphotograph (reflected, plane-polarized light) of sulfide-matrix breccia with chalcocite-rich matrix surrounding clasts dominated by quartz-alunite alteration from Yelibelen (sample OD79960; ODD-319, 138.40–138.60 m, 0.25 wt.% Cu). Hypogene pyrite and enargite have been partially replaced by chalcocite in (B).

4.1.2.2 Hypogene mineralization

Majority of breccia-hosted gold-copper mineralization occurs in intensely oxidized breccias at Öksüt. Hypogene mineralization is poorly-preserved in ledges, generally at depths >400 m. However, primary sulfides are relatively better preserved at shallow levels (as shallow as 30 meters) in the subjacent andesite porphyry. Relative timing of mineral assemblages representing different stages of hydrothermal activity were identified based on cross-cutting relationships as observed both in drill core and during petrographic studies, and were supplemented by geochronological data of various alteration minerals (Section 4.2). Obtained paragenetic sequence is provided in Figure 4.26.

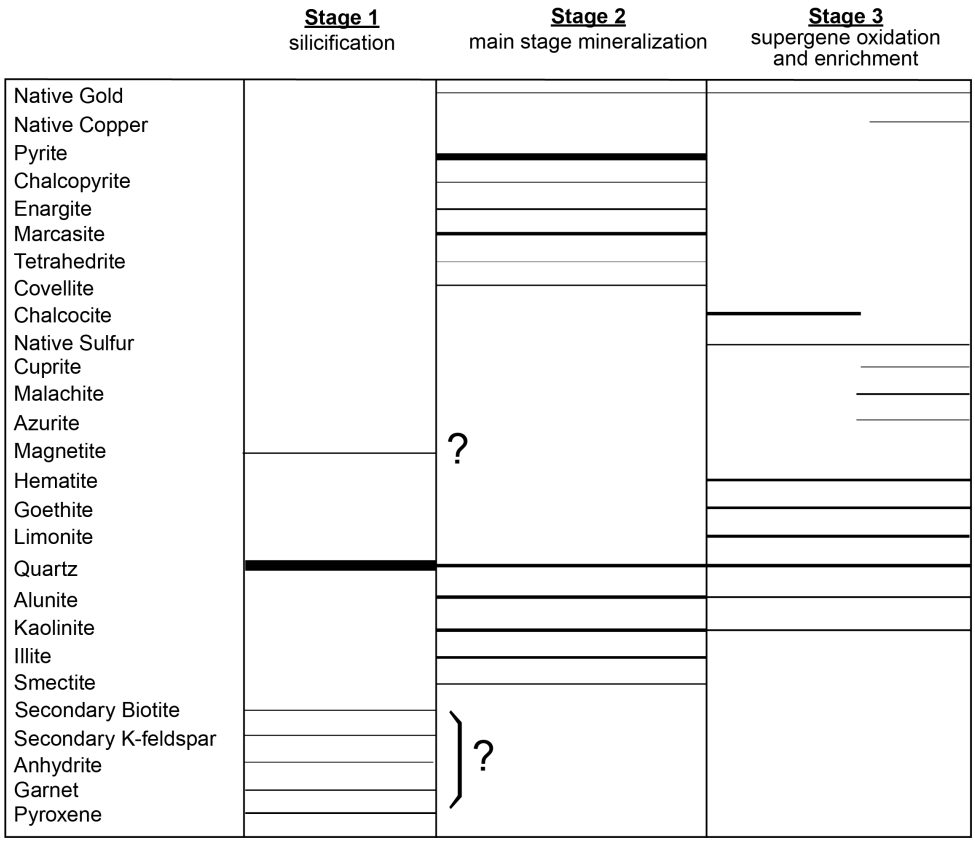


Figure 4.26. Paragenetic sequence of the Öksüt Au-Cu deposit, line thicknesses represent relative abundances of minerals. Line thicknesses represent relative abundances of minerals.

Although rarely preserved, drill core observations and petrographic investigation relatively unoxidized samples indicated presence of primary sulfide phases in close association with quartz-alunite ± kaolinite alteration both in breccias and in andesite porphyry (Figures 4.27A–C). Presence of similar mineralization is also suspected in residual vuggy quartz alteration, since these zones return relatively high gold grades. However, higher permeability in such zones, perhaps enhanced by dense fracturing (Figure 4.4), likely caused intense oxidation of primary sulfides in zones of silicification (Figure 4.4).

In unoxidized breccias, hypogene sulfides including pyrite, marcasite, and enargite primarily occur in the matrices, less commonly in clasts, and locally as vug fill (Figures 4.28, 4.29A-C). Outside the ledges, the same mineral assemblage as well as relatively minor amounts of chalcopyrite, tetrahedrite- tennantite, and sparse hypogene covellite are found as disseminations in pyroxene andesite porphyry (Figures 4.30A–C).

Two distinct pyrite varieties were noted in hypogene sulfide zones. Medium-grained, subhedral to anhedral granular pyrite is intergrown with marcasite and tabular prismatic, locally skeletal enargite. Early pyrite, marcasite, and enargite have been overgrown by anhedral, often porous looking, sooty pyrite. Gold in hypogene sulfide zones is mostly refractory and occurs as submicron inclusions in pyrite and enargite, and also in pyrite lattice. Microscopic gold is sparse and is generally fine grained (<15 μm; largest observed ~30 μm; Figures 4.29D, 4.31 and 4.32).

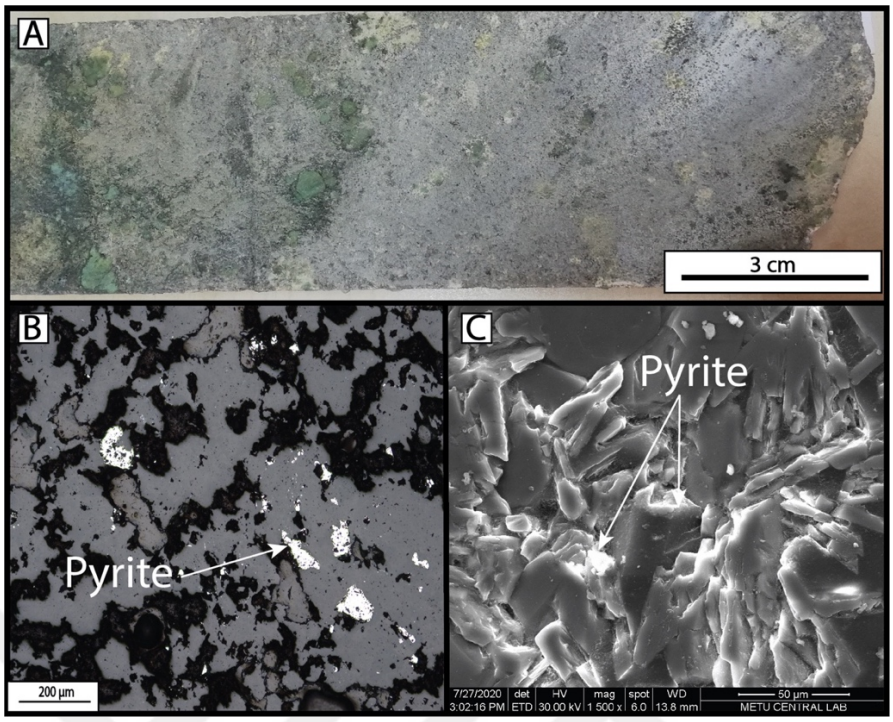


Figure 4.27. (A) Drill core photograph and (B) microphotograph (reflected, plane-polarized light) of silica and quartz-kaolinite altered breccia from Güneytepe (sample OD79899; ODD-210, 174.10–174.25 m). Pyrite occurs both in clasts and in fractures and vugs. C) Back-scattered electron (BSE) image of pyrite within an aggregate of tabular prismatic alunite crystals.

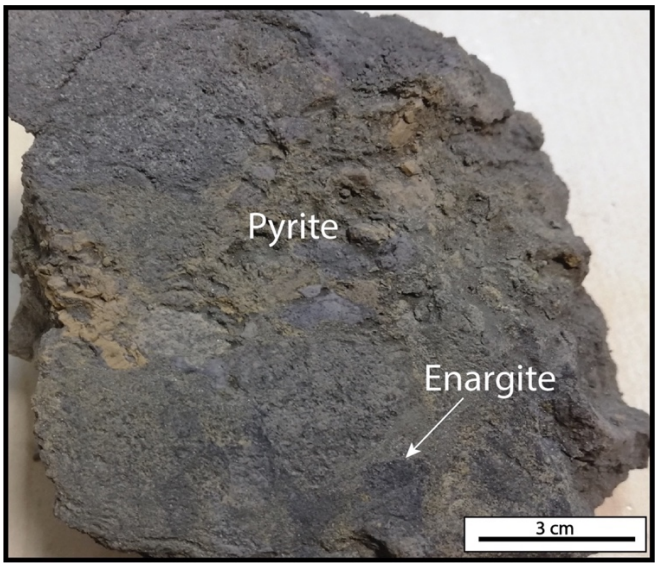


Figure 4.28. Drill core sample of quartz-alunite altered breccia with abundant pyrite and enargite from Keltepe (sample OD79845; ODD-316, 255.30–255.40 m, 0.53 g/t Au, 5.7 wt.% Cu, >1 wt.% As). Minor chalcocite has replaced primary Cu-sufides.

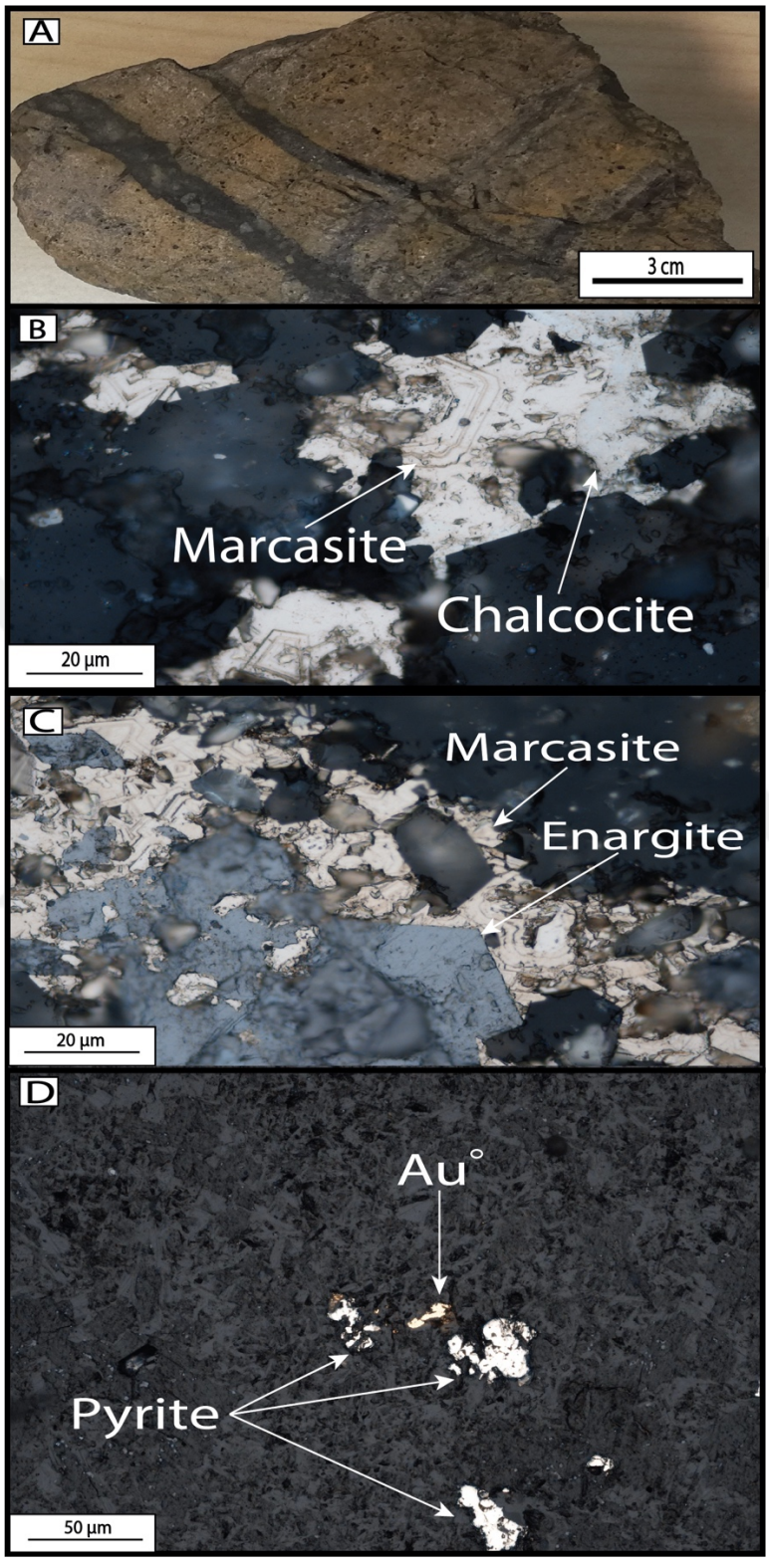


Figure 4.29 (A) Drill core photograph and (B and C) microphotographs (reflected, plane-polarized light) silica altered andesite porphyry cut by quartz-sulfide veins

porphyry from Keltepe (sample OD79948; ODD-316, 383.60–383.70 m, 0.2 wt.% Cu). Zoned, euhedral crystals of marcasite have been overgrown by enargite, which was in turn partially replaced by minor chalcocite. D) Reflected plane polarized light microphotographs (ODD-399, 33.49-33.64m, 30.5 g/t Au; 0.48 % wt. Cu), ~35µm size native gold and hypogene pyrite from Güneytepe.

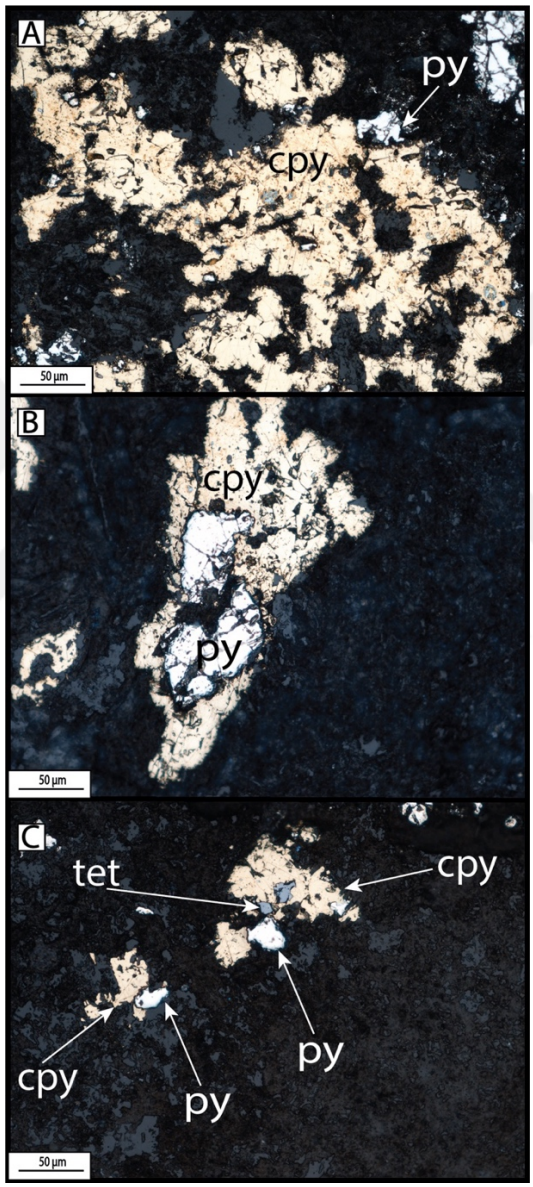


Figure 4.30. Microphotographs of hypogene sulfides (reflected, plane-polarized light) in sample OD79898 from Güneytepe (ODD-33, 132.30–132.50 m, 0.32 g/t Au, 5.74 wt.%. Cu). (A and B) Intergrown chalcopyrite and pyrite, (B) chalcopyrite-pyrite replacement, (C) disseminations of pyrite, chalcopyrite, and tetrahedrite. Abbreviations: py = pyrite, cpy = chalcopyrite, tet = tetrahedrite.

4.1.2.2.1 Pyrite chemistry

In general, the abundance of pyrite in quartz-alunite ± kaolinite alteration and gold grades are positively correlated at Öksüt. Nevertheless, microscopic gold was rarely observed in zones of primary mineralization, and also metallurgical tests yielded low gold recoveries. This was considered to be in relation to the possible refractory nature of gold in hypogene ores. Consequently, mineralogical characterization of pyrite was attempted through detailed LA-ICP-MS analyses (Appendices L–N).

LA-ICP-MS analyses were conducted on two samples obtained from gold mineralized drill hole intervals. Sample CTR2711 was collected from drill hole ODD-0399 (33.50 m; 30.5 g/t Au throughout this one-meter-long interval) from quartz-alunite-kaolinite alteration, and sample CTR2713 was collected from the same drill hole (36.30 m; 11.5 g/t Au throughout this one-meter-long interval).

Pyrites in sample CTR2711 range in size from ~0.1 up to 0.5 mm, are in anhedral spongy forms (Figure 4.31). These are found as disseminations throughout quartz-alunite altered andesite porphyry rock and they often lack inclusions. On the other hand, some of the pyrites are concentrated in fractures, and these are also anhedral and spongy. Inclusions in pyrite are generally non-opaque gangue mineral inclusions. Pyrites in sample CTR2713 have variable sizes; from minute grains with sizes of few microns to anhedral, coarser (~100–200 μm) crystals (Figure 4.32). Pyrites are irregularly disseminated through the sample, and in some places, they are ragged and abundant as patches. Chalcopyrite was intergrown with pyrite but has been mostly replaced by covellite (Figure 4.32).

During LA-ICP-MS analyses, measurements were taken from 20 different spots from each sample. A total of 26 different elements were measured including gold, titanium, copper, arsenic, tellurium, selenium, cobalt, nickel, mercury, bismuth, and lead from pyrite crystals. Only 5 pyrite spots from CTR2711 lack inclusions and as such these are regarded as clean pyrites (Figure 4.33A). The remaining 35 measured pyrites have inclusions (Figure 4.33B, C). Trace amounts of Au were measured from

most spots (avg. = 0.4 ppm) examined in clean pyrites with gold concentrations ranging from below detection limit (<0.1 ppm) to 0.7 ppm. On the other hand, pyrites with inclusions have elevated gold contents including two relatively high measurements of 461.98 ppm and 701.37 ppm. Overall, the average of 40 Au analyses is 40 ppm ranging from below detection limit (<0.1) to 701.4 ppm. This indicates that Au is hosted by pyrite both as native inclusions and in pyrite lattice with submicron size native gold inclusions (Figure 4.31 and 4.32). Elevated Bi and Pb results coherent with Au peaks indicate presence of a Au-Bi-Pb phase. Rather than Au, elevated Cu results are commented as chalcopyrite inclusions and K-Al peaks suggest clays/sericite/K-feldspar inclusions.

Pyrites in the analyzed samples have elevated copper contents ranging from below detection limit (~10 ppm) up to ~43 wt.%. Titanium abundance is generally very low in clean pyrites, but it reached to a maximum of ~5 wt.% in pyrite containing about 25 ppm Au. Arsenic is mostly low (<30 ppm), indicating that it was not a significant trace element of pyrite in Öksüt. Highest measured silver concentration is ~170 ppm in a sample which also has one of the highest measured Au concentrations (461.98 ppm) in all samples. However, silver abundance is generally <5 ppm and is also lower than Au. Selenium is mostly in a range of hundreds of ppm with few highly anomalous concentrations (~8800 ppm and ~1150 ppm), but tellurium is quite low in abundance (tens of ppm levels). Lead peaks with thousands of ppm where native gold inclusions present, and bismuth abundance increases to hundreds of ppm where Pb is high. Hg was not detected in any of the analysis.

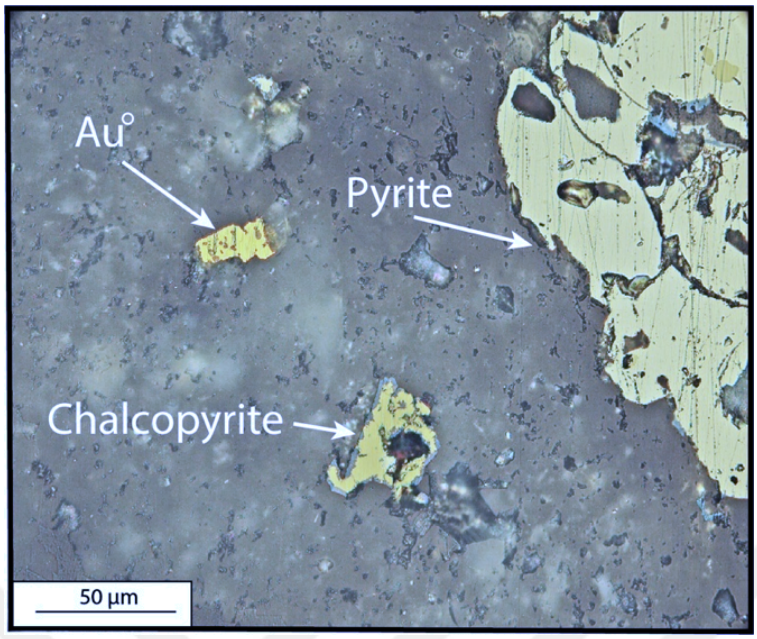


Figure 4.31. Microphotograph (reflected, plane-polarized light) of sample CTS2711 from Güneytepe showing an isolated native gold grain (~30 µm) with pyrite and chalcopyrite (ODD-399, 33.50-33.65 m; 30.5 g/t Au, 0.48 % wt. Cu).

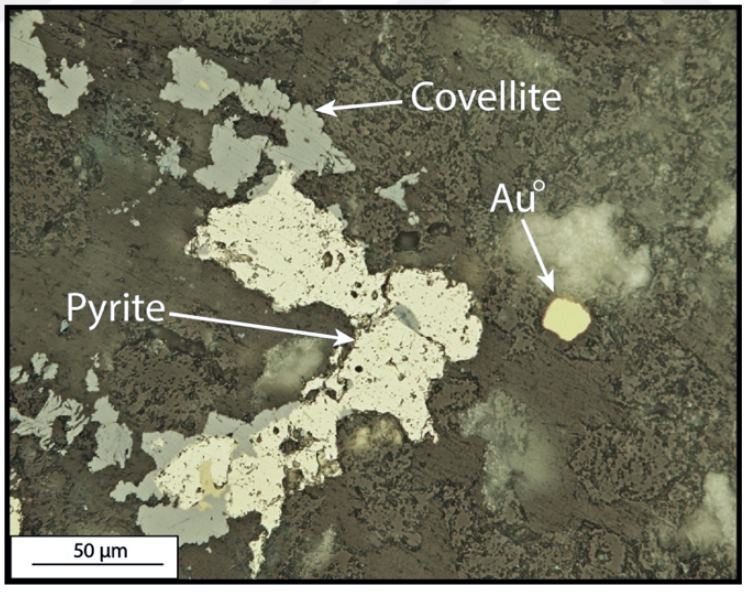


Figure 4.32. Microphotograph (reflected, plane-polarized light) of sample CTR2713 from Güneytepe showing an isolated native gold grain (~15 µm in size) alongside aggregates of pyrite and minor chalcopyrite. Chalcopyrite has mostly been replaced by covellite (ODD-399, 36.30–36.45 m, 11.5 g/t Au, 1.2 % wt. Cu).

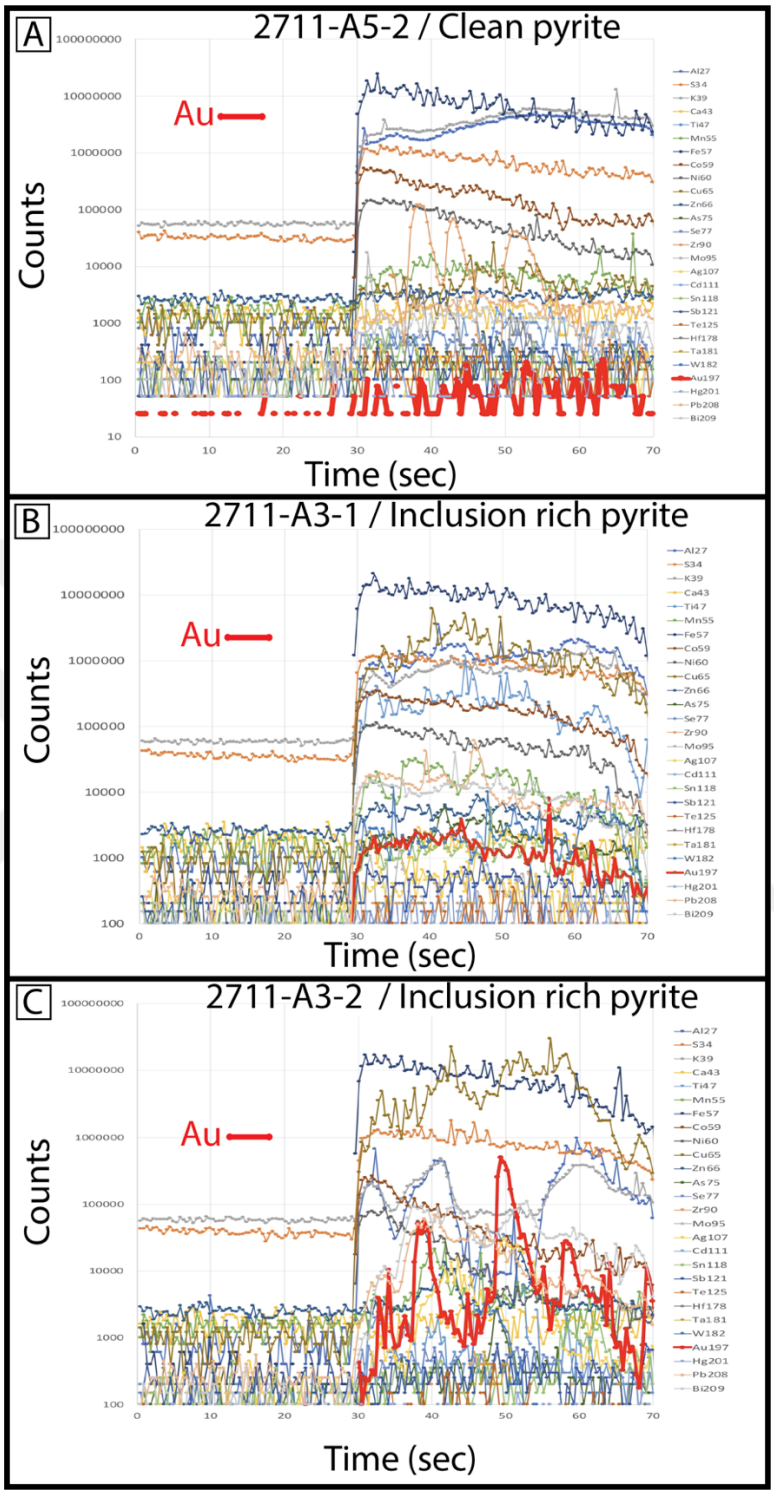


Figure 4.33. LA-ICP-MS trace of clean and inclusion rich pyrites in CTR2711-A5-2, CTR2711-A3-1 and CTR2711-A3-2 for selected trace elements. The diagram shows overall (A) low Au concentrations in clean pyrite and (B and C) high Au concentrations in inclusion rich pyrites.

4.1.2.3 Supergene mineralization

Deep supergene weathering and oxidation is a distinctive feature of the Öksüt deposit, and it likely enhanced overall low hypogene gold grades and recovery in both Güneytepe and Keltepe orebodies. Oxidation is most intense and has greater vertical extent down through the ledges. In Keltepe, oxidation reaches to depths of about 350 meters (Figure 4.19), whereas in Güneytepe it is limited to the top 100 meters from the surface (Figure 4.20).

Oxidation and weathering have resulted in strong zonation of gold and copper possibly due to contrasting behavior of these metals in the supergene environment. Silica-matrix breccias in ledges are completely devoid of sulfide minerals. In the supergene- oxidized zone, fine-grained gold (typically 5–10 μm) occurs within intensely oxidized, silica- or quartz-alunite±kaolinite altered, poorly-sorted polymict breccias containing abundant goethite and jarosite in the matrix (Figure 4.34A and B). The ubiquitous presence of these minerals indicates the former presence of abundant Fe-sulfides prior to supergene weathering and that gold was likely liberated after decomposition of pyrite during oxidation. The silicified cores of the breccia feeders return highest average gold grades of >2.5 g/t (up to 30 g/t Au), whereas quartz-alunite ± kaolinite-altered breccias in the oxidized zone have average gold grades of 1.2 g/t. Copper, however, has been completely leached and redeposited in the silica and quartz-alunite±kaolinite-altered breccias at the base of the oxidation zone (Figures 4.35A–C and 4.36A-B).

Supergene oxidized portions of the breccia feeders are underlain by an enrichment zone that hosts intervals of significant copper mineralization mainly in quartz-alunite ± kaolinite-altered breccias and andesites (4.36A-B). These comprise predominant chalcocite with subordinate malachite-covellite and sparse azurite, native copper, and cuprite (Figures 4.37A-C and 4.38A-B). Pyrite, marcasite and sparse enargite were also identified as relict hypogene sulfide phases (Figures 4.39A-B).

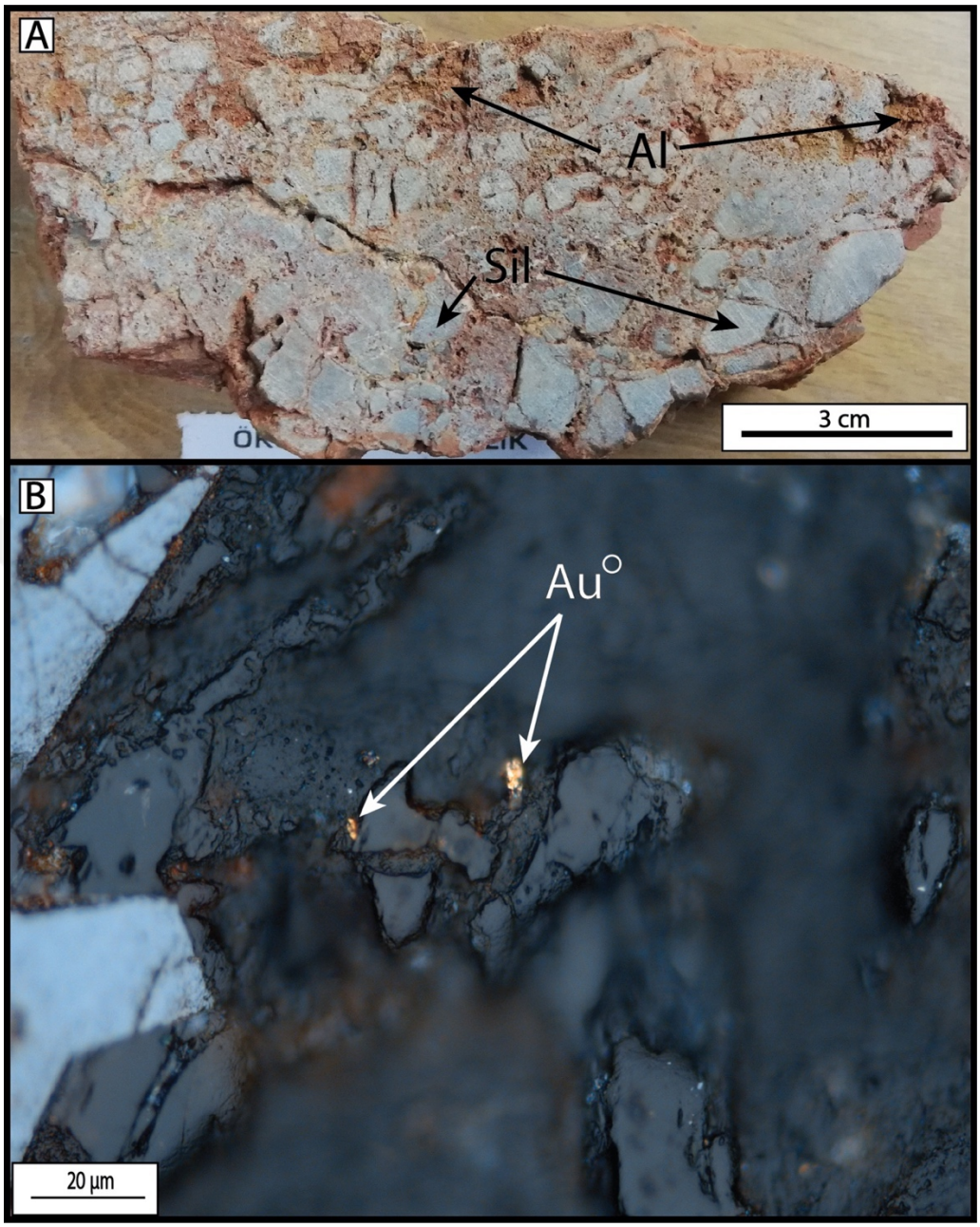


Figure 4.34. A) Drill core photograph and (B) microphotograph (reflected, plane-polarized light) sample OD79874 from Güneytepe (ODD-12, 53.20-53.27m, 3.39 g/t Au), A) strongly oxidized silica-alunite matrix and clasts dominant breccia, B) native gold around silica with Fe-oxides. Abbreviations: Al = alunite, Sil = silica.

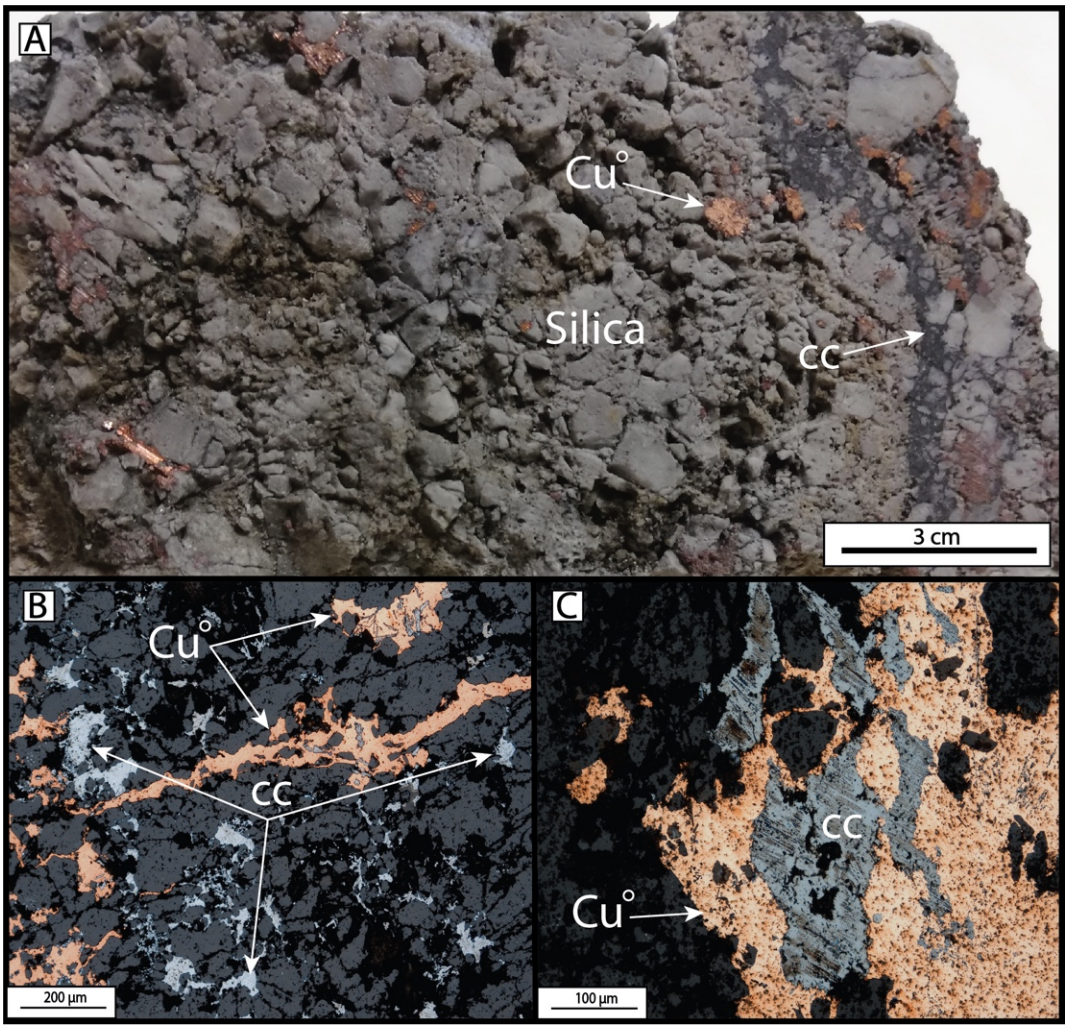


Figure 4.35. (A) Drill core photograph and (B-C) microphotographs (reflected, plane-polarized light) sample OD79849 from Keltepe N (ODD-333, 327.60-327.67m, 7.3% wt. Cu), (A) silica matrix breccia with vug and fracture filled native copper and chalcocite, (B) native copper and chalcocite intercalated with each other, (C) native copper replaced chalcocite. Abbreviations: cc = chalcocite.

Presence of relict enargite in the samples suggests that it was the main copper mineral prior to oxidation, and that leaching of this mineral phase should have resulted in removal of significant quantities of arsenic from the mineralized system (4.39A-B).

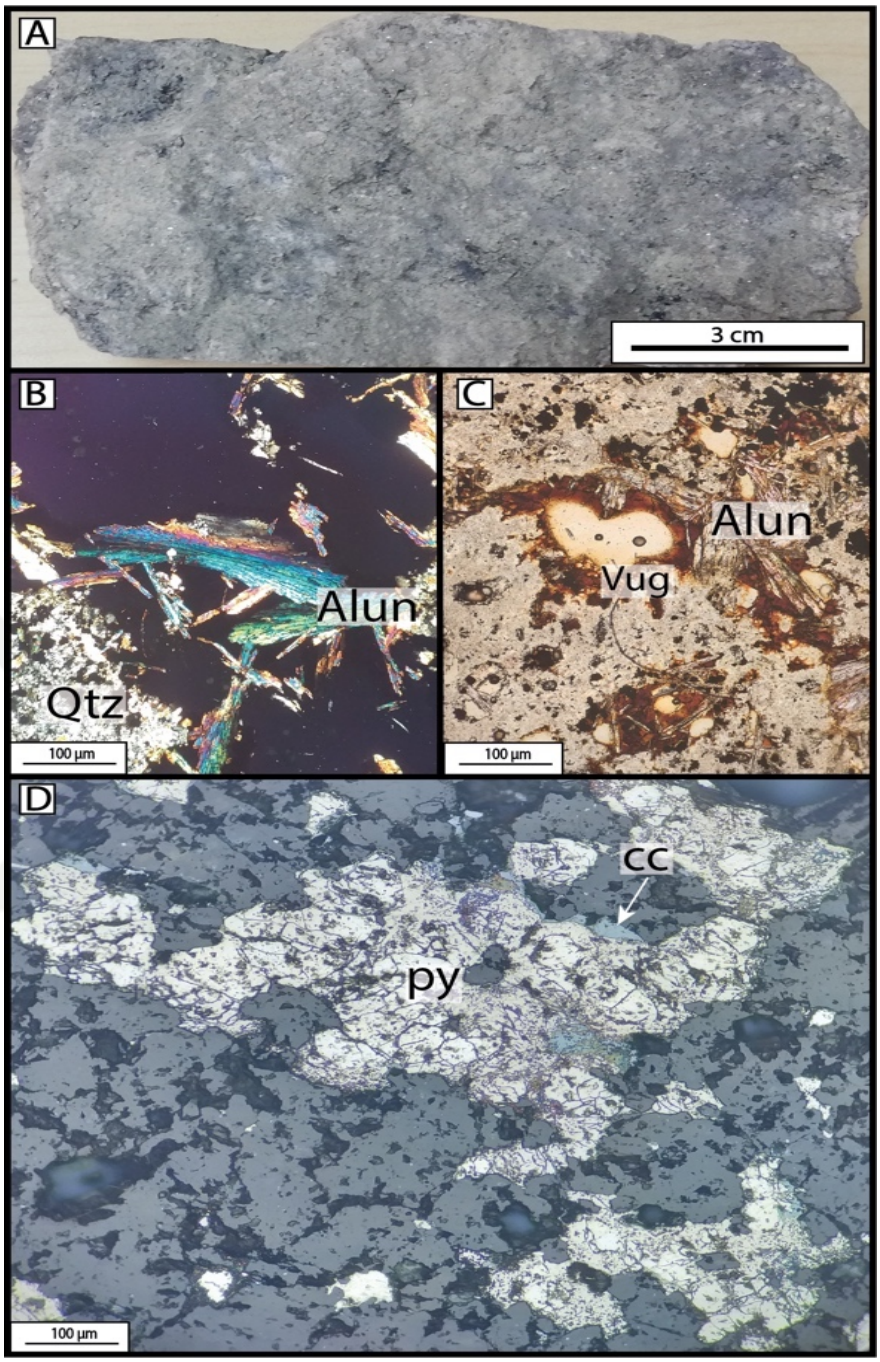


Figure 4.36. A) Drill core photograph, (B) microphotograph (transmitted, plane-polarized light), (C) microphotograph (transmitted, cross-polarized light), (D) microphotograph (reflected, plane-polarized light) sample OD79802 from Güneytepe (ODD-210, 182.00-182.10m, 0.24 g/t Au, 0.6% wt. Cu), A) well crystalline visible needle like fracture filled alunite, B) vug and fracture filled alunite with quartz, C) alunite around vugs, D) chalcocite replaced sooty pyrite. Abbreviations: Qtz = quartz, Alun = alunite, py = pyrite, cc = chalcocite

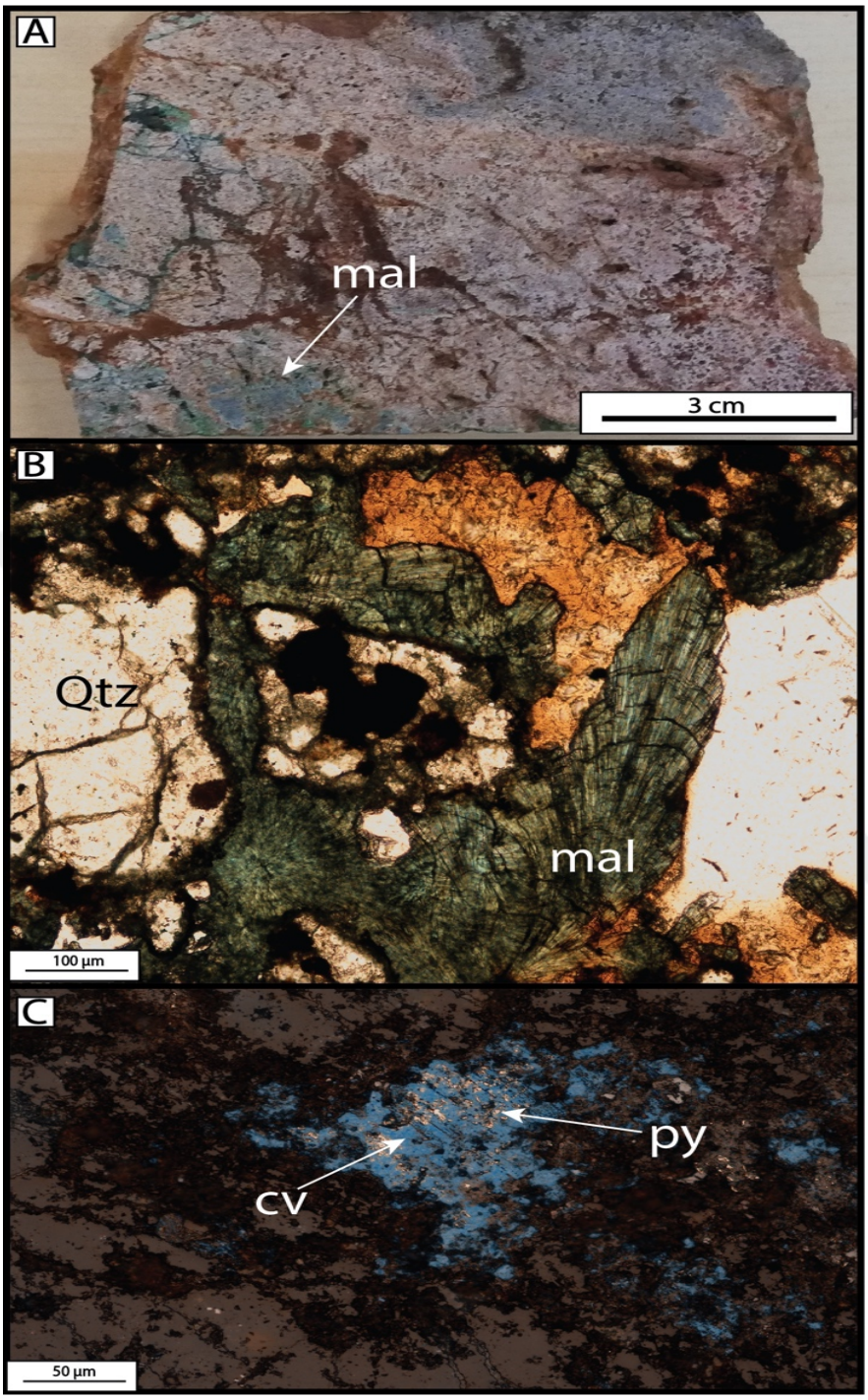


Figure 4.37. (A) Drill core photograph, (B) microphotograph (transmitted, plane-polarized light), (C) microphotograph (reflected, plane-polarized light), sample OD79965 from Keltepe (ODD-316, 180.90-181.00m, 1.33 g/t Au, 1% wt. Cu), (A) strongly silicified and fracture filled malachite, (B) fracture filled malachite around quartz, (C) pyrites are replaced by covellite. Abbreviations: mal = malachite, Qtz = quartz, py = pyrite, cv = covellite.

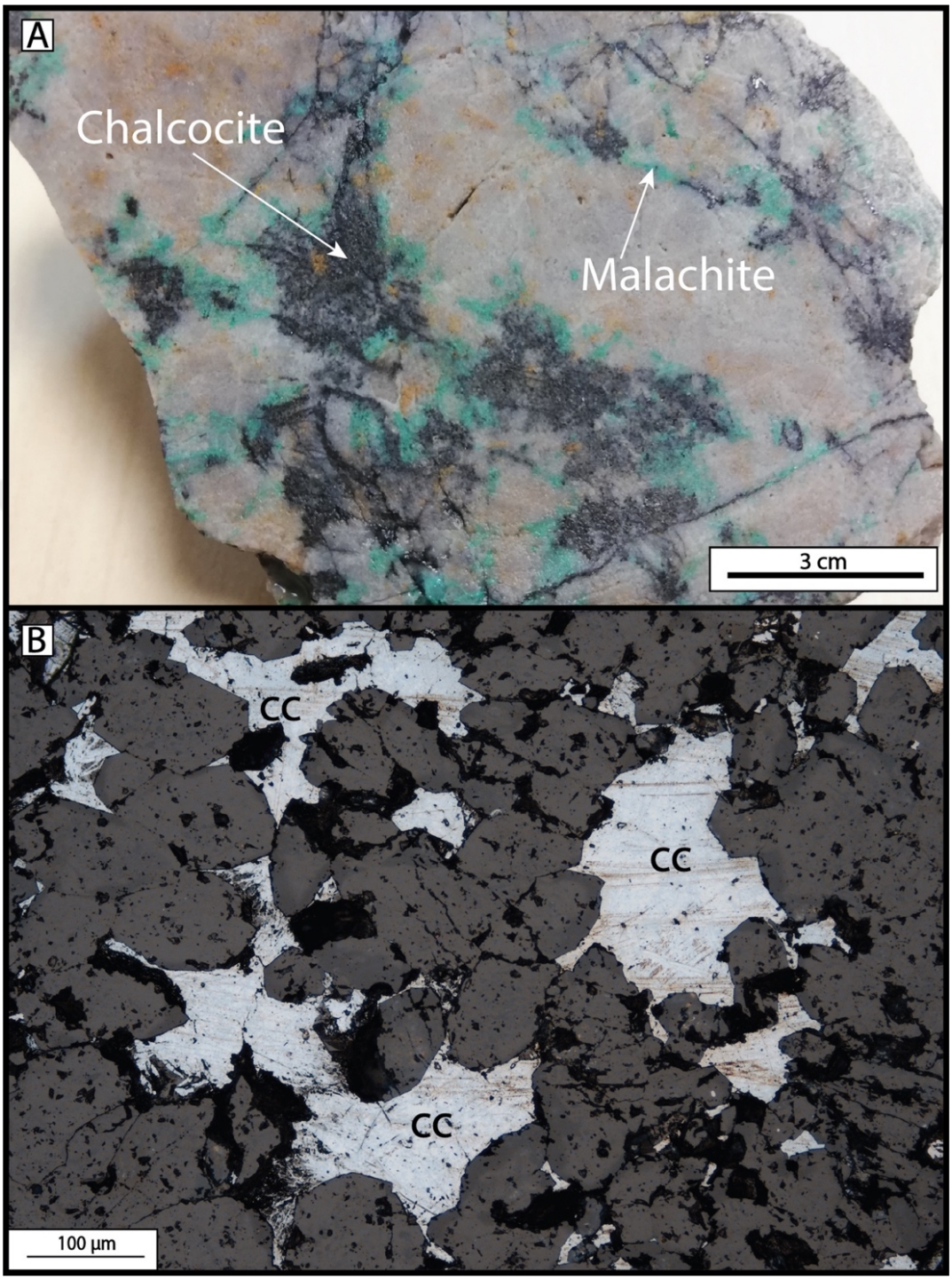


Figure 4.38. (A) Drill core photograph, (B) microphotograph (reflected, plane-polarized light), sample 78952 from Keltepe N (ODD-333, 315.00-315.22m, 3.4 % wt. Cu), (A) chalcocite-malachite replacement at the paleowater table level in supergene enrichment zone, (B) fracture filled chalcocite minerals. Abbreviations: cc = chalcocite.

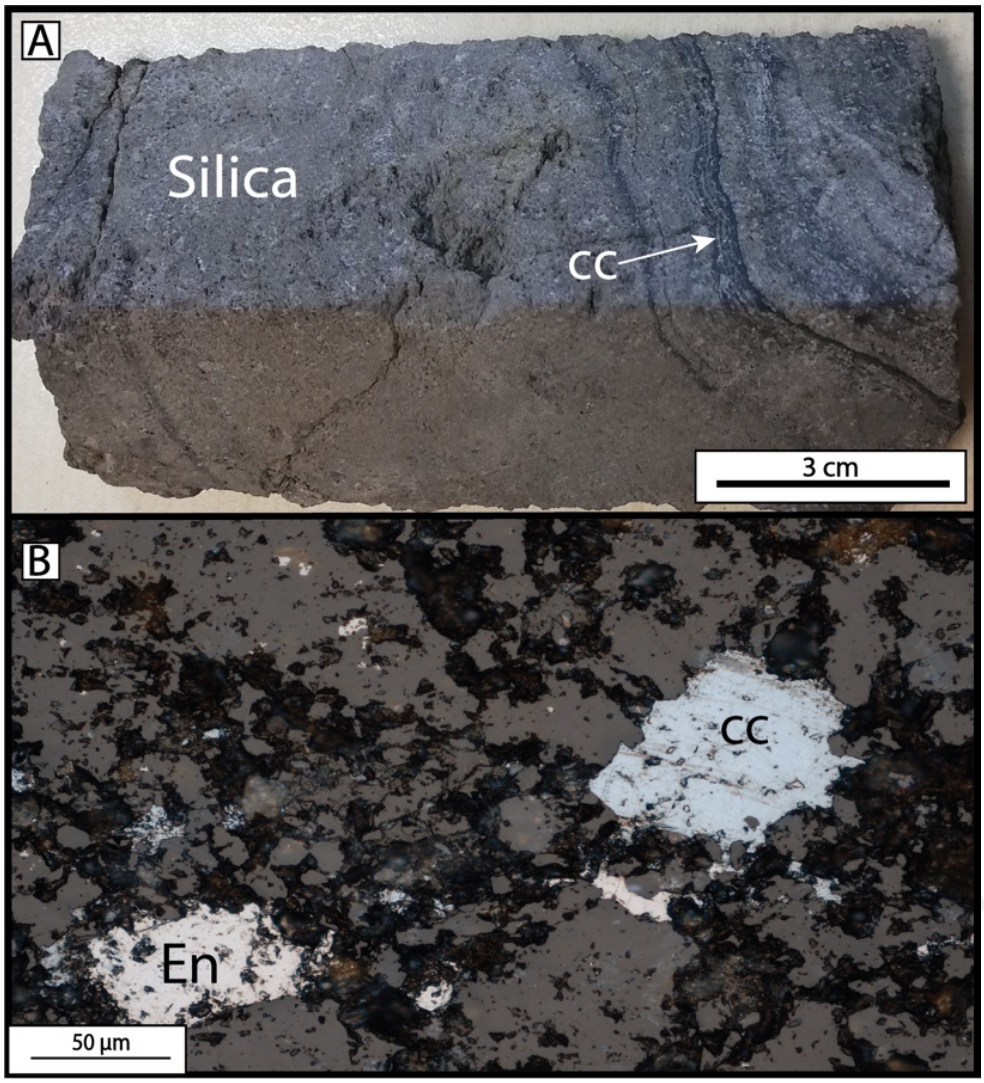


Figure 4.39. A) Drill core photograph, (B) microphotograph (reflected, plane-polarized light), sample OD78961 from Keltepe N (ODD-333, 332.10-332.20m, 4.5% wt. Cu), A) residual silica with chalcocite veinlets as bandings, B) hypogene enargite and supergene chalcocite minerals. Abbreviations: En = enargite, cc = chalcocite.

Chalcocite occurs as infill to irregular, hairline fractures, as matrix infill in breccia bodies, and locally as massive accumulations with pyrite (Figures 4.40A, B and 4.41A, B). It has been locally replaced by covellite and cuprite along narrow fractures. In the enriched zones, gold grades average around 0.5 g/t. (Figure 4.42A–C).

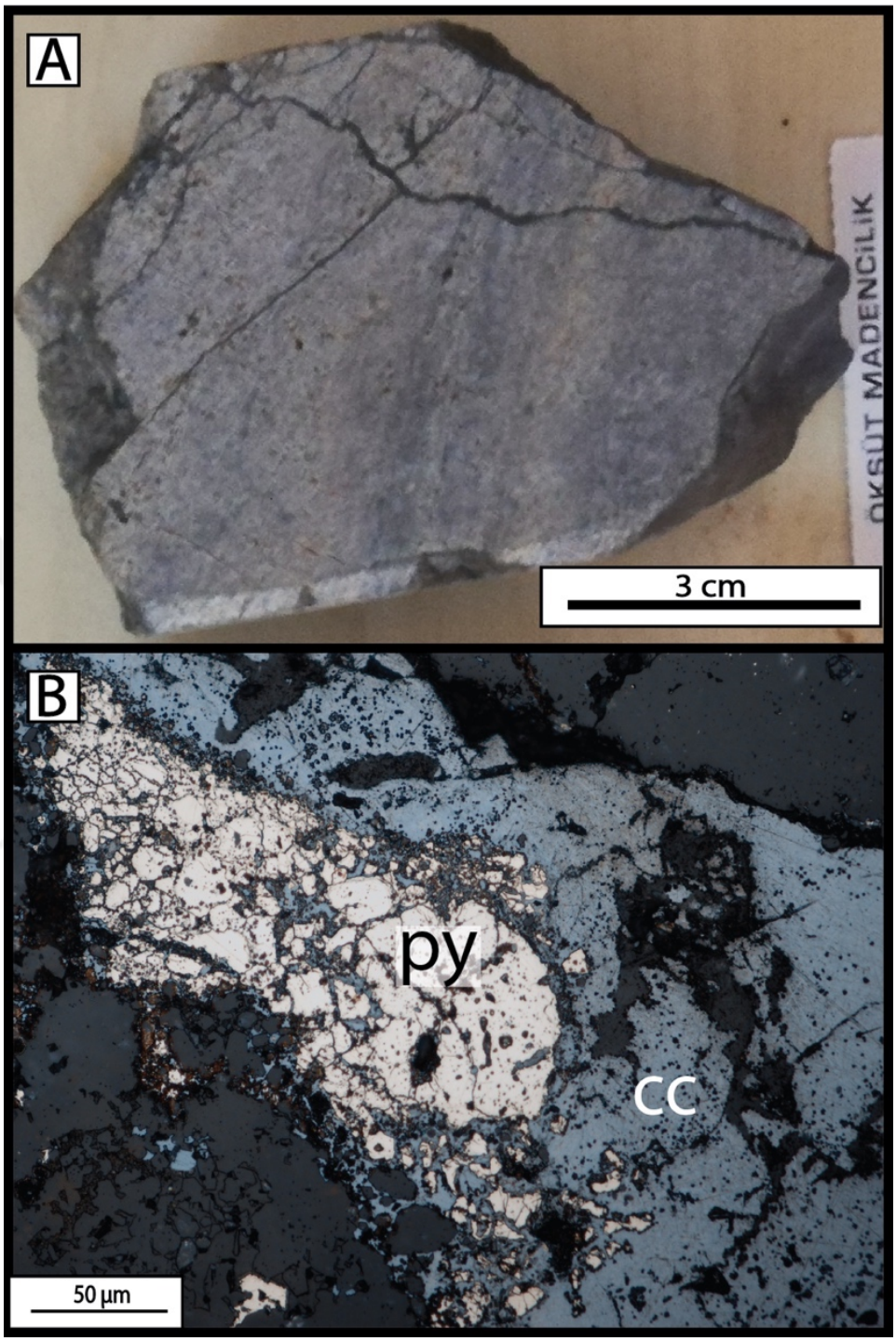


Figure 4.40. A) Drill core photograph, (B) microphotograph (reflected, plane-polarized light)**,** sample OD79838 from Keltepe (ODD-313, 235.00-235.10m, 2.81 g/t Au, 42.6 % wt. Cu), A) silica altered sheeted pyrite-chalcocite veinlets, B) chalcocite replaced pyrite. Abbreviations: py = pyrite, cc = chalcocite.

Enriched horizons are horizontal to sub-horizontal and developed irregularly throughout the district (Figure 4.43). Their thicknesses vary considerably, from 25 to 50 m in the root zones of breccia feeders to <5 m laterally away from the ledges. The chalcocite-pyrite contents may locally range up to over 40 vol.%, forming zones of semi-massive to massive sulfides. The most significant copper enrichment was encountered in drill hole ODD-333, where a ~50-m-thick interval of massive chalcocite-pyrite returned an average grade of 2.3 wt.% Cu.

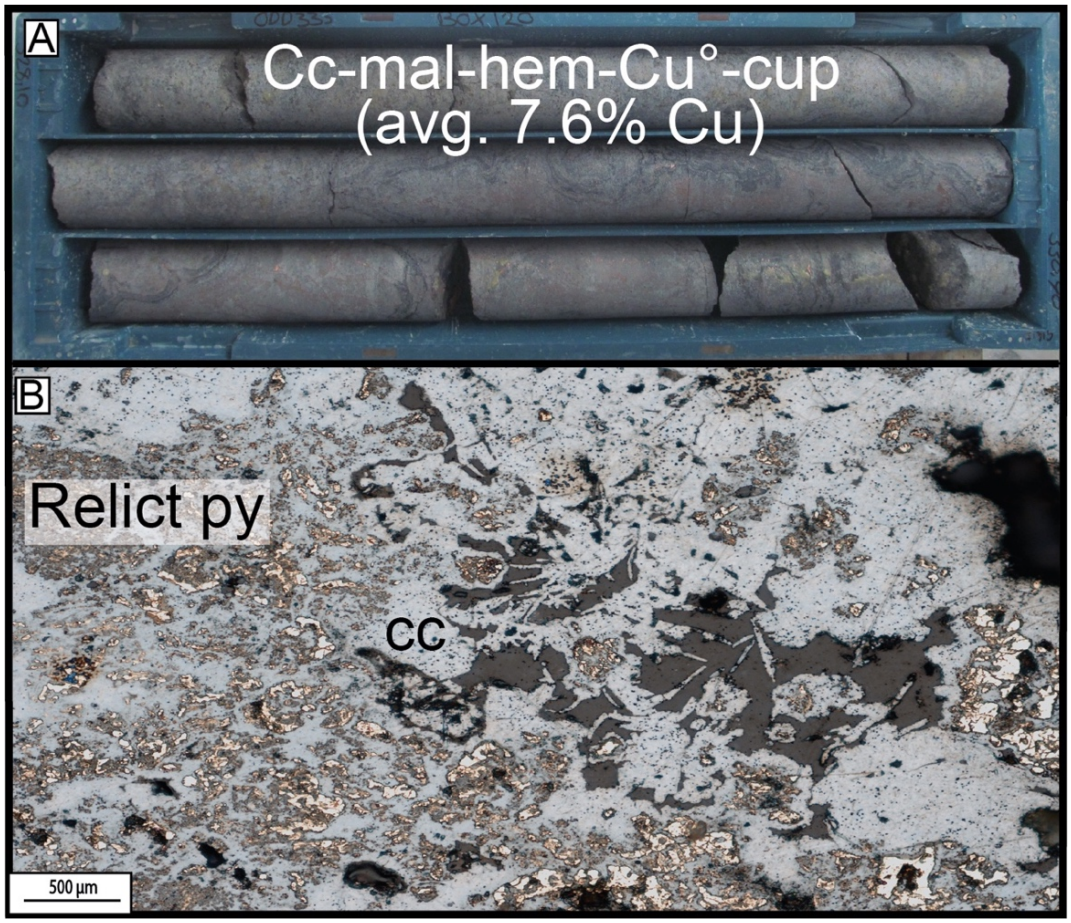


Figure 4.41. (A) Drill core interval with semi-massive sulfide chalcocite-rich zone with secondary Cu oxides, Cu hydroxy-carbonates and native copper in alunite-matrix breccia from Keltepe N (ODD-333, 328.10–330.90 m). (B) Microphotograph showing (reflected, plane-polarized light) of sample OD79838 (ODD-313, 235.00-235.10m, 2.8 g/t Au, 4.3 wt.% Cu), intense chalcocite replacement and relict pyrite. Abbreviations: cc = chalcocite, mal = malachite, hem = hematite, cup = cuprite, py = pyrite.

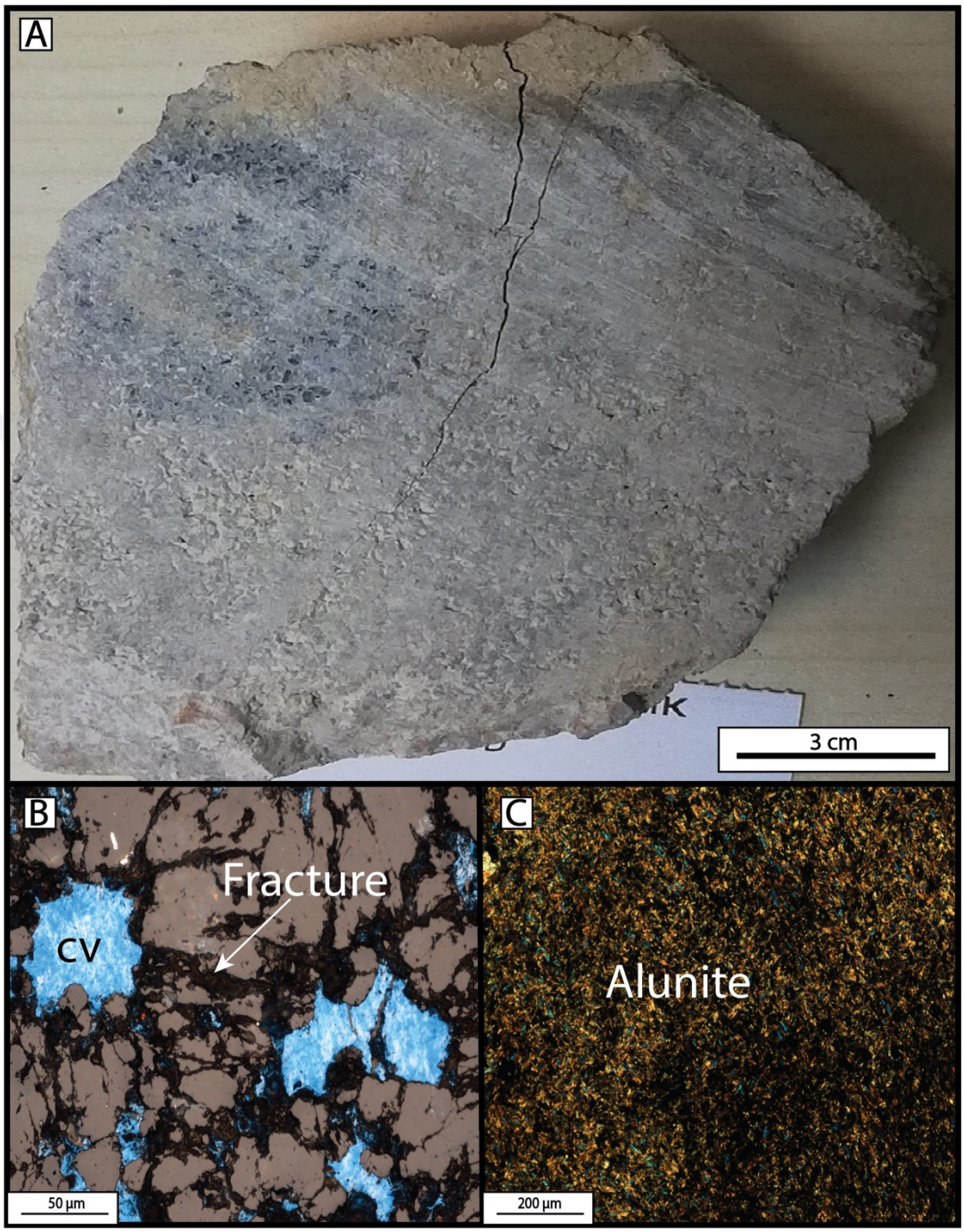


Figure 4.42. (A) Drill core photograph, (B) microphotograph (reflected, plane-polarized light), (C) microphotograph (transmitted, cross-polarized light) sample OD79952 from Keltepe (ODD-81, 293-293.10m, 0.31 g/t Au, 1.1% wt. Cu), (A) quartz-alunite altered andesitic rock with covellite patches, (B) fracture-filling covellite, (C) fine-grained alunite. Abbreviations: cv = covellite.

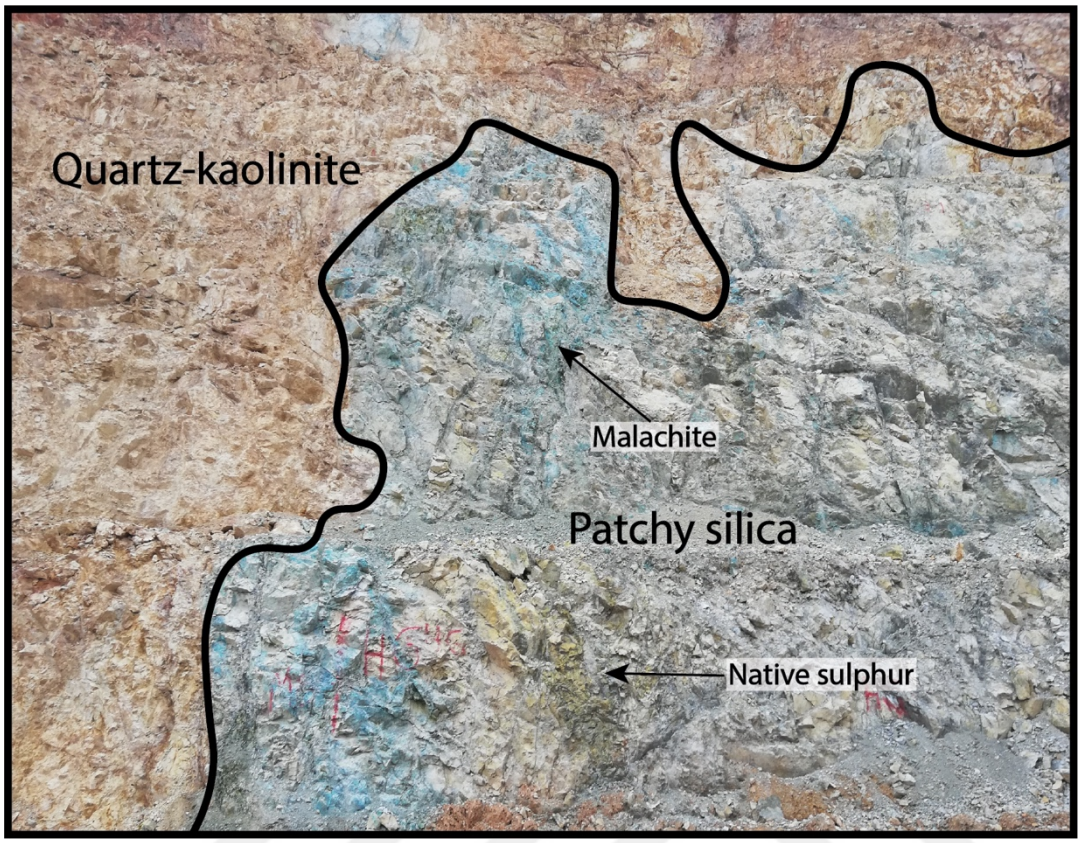


Figure 4.43. Güneytepe pit wall outcrops, quartz-kaolinite alteration patchy silica transition, also where oxide-sulfide boundary and supergene enrichment zone represented with malachite and native sulfur.

4.2 Geochronology

The age of hydrothermal activity related to Öksüt gold-copper mineralization was obtained with $^{40}Ar/^{39}Ar$ and U-Pb geochronology. $^{40}Ar/^{39}Ar$ geochronological analyses were performed on K-bearing minerals from epithermal- and porphyry-style alteration zones, whereas U-Pb geochronology was conducted on garnets obtained from calc-silicate alteration zones.

Two hypogene alunite, one illite, and one hydrothermal biotite separates, all obtained from drill core samples, were dated through $^{40}Ar/^{39}Ar$ step-heating method at the Nevada Isotope Geology Lab of the University of Nevada at Las Vegas, United States. Age uncertainties are reported at 2σ level. Detailed analytical procedures are

given in Appendix O, summary data is provided in Table 4.3, and age spectra are provided in Figure 4.44. Full geochronological data are also given in Appendix P for selected sample. All samples yielded disturbed and saddle-shaped spectra (Figure 4.44A-D).

Sample OD79802 was collected from drill hole ODD-210 from quartz-alunite-kaolinite alteration in Güneytepe and contains coarse (2.5 mm diameter), prismatic crystals of hypogene alunite together with quartz, kaolinite, pyrite, and chalcocite. This sample yielded a total gas age of 5.62 ± 0.06 Ma. A second alunite sample (OD79801) collected from an identical drill core interval in Güneytepe returned a total gas age of 7.59 ± 0.09 Ma. The saddle-shaped age spectrum (Figure 4.44B) with older early steps suggests the presence of excess argon. Although this sample did not yield a valid plateau age, ~77% of the 39Ar was released in two contiguous steps that have younger apparent ages (Figure 4.44B). The lowest step in the saddle with an age of 5.65 ± 0.14 Ma is interpreted to be a maximum age estimate for this sample. This date, which also correlates well with alunite sample OD79802, was taken as the preferred age of this sample.

Drill core sample OD78852 from the argillic zone to the northwest of Keltepe contains a mineral assemblage of illite, quartz, smectite, and pyrite. Illite from this sample returned a total gas age of 5.50 ± 0.34 Ma, correlating with the alunite ages. Steps 5 through 12 contained 69% of the ^{39}Ar released, returning a weighted mean age of 5.26 ± 0.33 Ma (Figure 4.44C). The hydrothermal biotite sample (OD78863) from deep biotite-magnetite ± K-feldspar ± anhydrite alteration zone immediately below the argillic alteration from northwest of Keltepe returned a total gas age of 7.41 ± 0.08 Ma, which is significantly older than the reported ages of least altered andesite porphyry and alteration minerals. This sample also did not produce a plateau. Saddle-shaped age spectra with a hump at moderate temperature steps (Figure 4.44) suggests the presence of excess argon. The lowest step with an age of 6.06 ± 0.05 Ma may hint at the maximum age of this sample, which seems reasonable when compared to other samples.

Although no plateau ages could be calculated for the samples, interpreted ages of the three samples obtained from shallow epithermal alteration agree within error (Table 4.3), and these ages (between 5.7 and 5.5 Ma) approximate the age of alteration associated with gold-copper mineralization. The 5.7 to 5.5 Ma timing also correlates well with the published U-Pb zircon ages of the host pyroxene andesite porphyry (5.7–5.4 Ma; Rabayrol et al., 2019; Aluç et al., 2020).

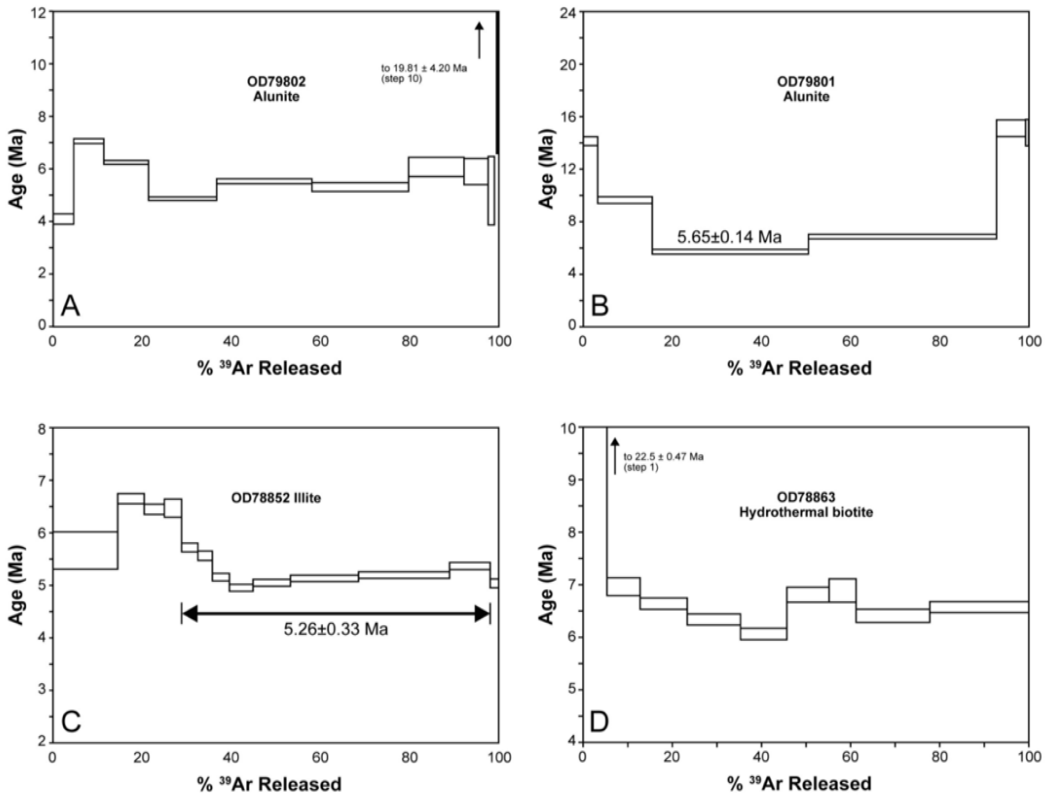


Figure 4.44. 40Ar/39Ar spectra of alunite, illite, and secondary biotite from Öksüt.

4.2.1 U-Pb garnet dating

Two garnet samples, OD78857 (Figure 4.45) and OD78859, from the Boztepe West prospect (Figure 3.5). Both samples were collected from drill-hole ODD-0337 and from shallow depths around 75 meters (Table 4.3). Garnets in these samples have been well-developed as coarse-grained, euhedral crystals of up to 1 cm. These occur

along fractures within pyroxene andesite porphyry, together with chlorite, epidote, carbonate, and pyrite.

U-Pb isotopic compositions of garnets were obtained using the TC-13 garnet as a reference material and QC-04 and DP-16 as monitoring garnet standards. A total of 70 analyses from sample OD78857 yielded U contents between 5.6 and 22.7 ppm. This sample produced a lower intercept age of 5.858±0.08 Ma (Figure 4.46A). From sample OD78859, a total of 80 analyses yielded U contents between 2.8 and 28.1 ppm. The lower intercept age for this sample is 5.35±0.22 Ma (Figure 4.46B).

The U-Pb garnet ages obtained from calc-silicate alteration from the western part of the DVC closely overlap with two alunite ages from the advanced argillic alteration zone in Öksüt, as well as with the age of illite sample from argillic alteration (Table 4.3). This indicates that different alteration styles related to magmatic-hydrothermal activity developed contemporaneously in different parts of the DVC, although these alteration styles are representing different levels of the magmatic-hydrothermal system at Öksüt.

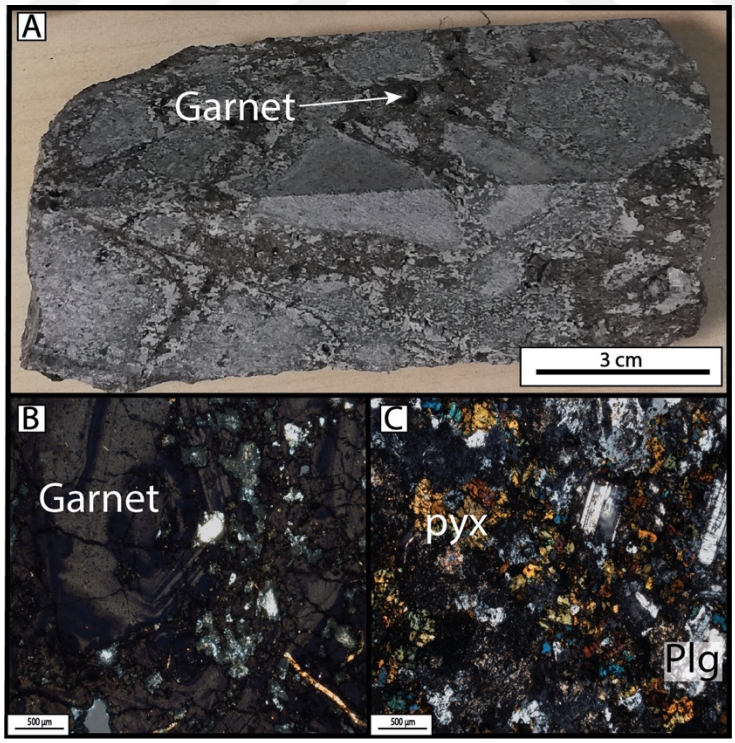


Figure 4.45. A) Drill core photograph, (B-C) microphotograph (transmitted, cross polarized light), sample OD78857 from Boztepe West (far west of Keltepe)- (ODD-337, 77.30-77.40m, 5.858 Ma), A) calc silicate altered brecciated rock with garnet veins, B) zoning in garnet and C) pyroxene-plagioclase dominant clasts and matrix. Abbreviations: pyx = pyroxene, Plg = plagioclase.

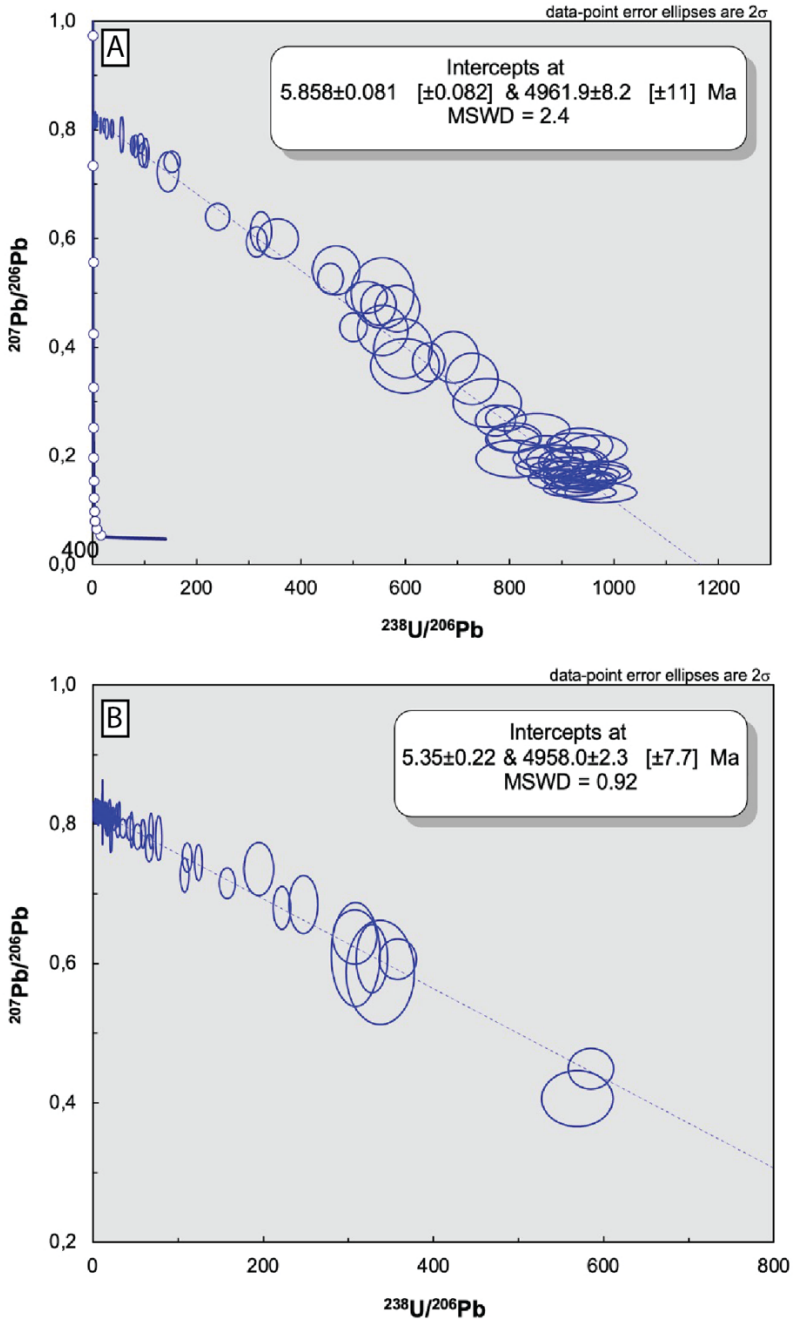


Figure 4.46. Terra-Wasserburg Concordia plots of garnet U-Pb data for samples (A) OD78857 and (B) OD78859 from Öksüt.

Table 4.3 Summary of Biotite, Alunite and Illite Minerals $^{40}Ar/^{39}Ar$ and Garnet Minerals U-Pb Geochronological Data from Hydrothermal Alteration Minerals.

Sample no.	Location; drill hole information	Mineral	Occurrence	Total gas age (Ma, 2σ)	Preferred age (Ma, 2σ)	Concordia age (Ma, 2σ)
OD78863	Keltepe West; ODD-337; 706.30-706.60m	Biotite	Biotite-magnetite-K-feldspar-altered pyroxene andesite porphyry	7.41 ± 0.08	-	-
OD79801	Güneytepe; ODD-210; 179.50-179.60m	Alunite	Quartz-alunite-kaolinite-altered pyroxene? andesite porphyry	7.59 ± 0.18	5.65 ± 0.14	-
OD79802	Güneytepe; ODD-210; 182.00-182.10m	Alunite	Quartz-alunite-kaolinite-altered pyroxene? andesite porphyry	5.62 ± 0.06	5.62 ± 0.06	-
OD79852	Keltepe West; ODD-337; 493.40-493.80m	Illite	Quartz-illite-smectite-kaolinite	5.50 ± 0.34	5.50 ± 0.34	-
OD78857	Keltepe West; ODD-337; 77.30-77.40m	Garnet	Calc-silicate altered pyroxene andesite	-	-	5.86 ± 0.08
OD78859	Keltepe West; ODD-337; 94.30-94.60m	Garnet	Calc-silicate altered pyroxene andesite	-	-	5.35 ± 0.22

CHAPTER 5

DISCUSSIONS AND CONCLUSIONS

5.1 Discussion

5.1.1 Constraints on formation of hypogene gold-copper mineralization

Öksüt is a typical, breccia-hosted epithermal gold-copper deposit emplaced along a dome-diatreme complex within the Develidağ Volcanic Complex (Yıldız et al., 2017; Figure 5.1). The host pyroxene andesite porphyry has been partly replaced by zoned alteration sequences characteristic of high-sulfidation epithermal systems. Within this environment, gold-copper mineralization most likely developed through exsolution, channeling and rapid escape of buoyant magmatic vapors along steep structures, some of which are associated with subvertical breccia bodies. As this magmatic vapor phase ascended to the volcanic levels, it evolved into low pH fluids due to condensation into a lower temperature meteoric aquifer (Heinrich, 2005; Hedenquist and Taran, 2013). Further acidification of magmatic vapors is promoted by condensation into local meteoric waters leading to pervasive zoned alteration (Hedenquist et al., 1998; Hedenquist and Taran, 2013). Oxygen and hydrogen isotope compositions of alunite and quartz as well as calculated fluid isotope compositions from Öksüt are consistent with such a mixed magmatic-meteoric, but predominantly magmatic, origin of the fluids (Aluç et al., 2020).

At this stage, the original andesitic wall rock had been completely replaced by massive and residual silica due to decreasing temperature and the low fluid pH, respectively. The outward zonation from central silica alteration through quartz-alunite ± kaolinite to illite-smectite ± chlorite assemblages reflect a decrease in fluid acidity and temperature (e.g., Stoffregen, 1987; Hedenquist et al., 1994; Hedenquist and Taran, 2013). The upward-flared form of the breccias is attributed to a

progressive approach to the paleosurface (Steven and Ratté, 1960; Hedenquist et al., 1994). Gold-copper mineralization was largely introduced subsequently into the same steep structures, with pyrite-enargite-gold overprinting the early residual vuggy and massive silica during the episodic phreatomagmatic brecciation.

The true nature of pyrite-enargite-gold mineralization (primary mineralogy, distribution, and mineral zonation) could not be well-constrained due to the widespread and intense supergene overprinting. Gold-copper mineralization is present in both Keltepe and Güneytepe, where steeply dipping breccias largely confine mineralization. Because highly permeable lithologies such as lacustrine sediments or volcaniclastic units are generally absent in the altered and mineralized stratigraphy, lateral migration of gold-copper mineralization from breccia feeders into enveloping pyroxene andesite porphyry was probably very limited. Thus, epithermal-style hydrothermal alteration and associated mineralization wane typically within just a few tens of meters of these conduits. At the base of the ledges, hypogene mineralization terminates in a zone of illite-smectite-kaolinite alteration and weakly to moderately developed quartz-pyrite-marcasite stockwork veinlets with argillic halos. This alteration assemblage is in turn transitional to a well-developed, albeit barren, potassic (biotite-magnetite ± K-feldspar ± anhydrite) alteration zone at depths greater than 400 m. Altered rocks at these levels contain abundant hydrothermal magnetite, both as disseminations and as M-type veinlets (Figure 4.17), a common feature of gold-rich porphyry systems (Sillitoe, 2000; Ulrich and Heinrich, 2002; Perelló et al., 2003). On the other hand, neither sulfide mineralization nor quartz veining, characteristic of porphyry deposits (Sillitoe, 2010), were identified in this zone, and associated gold and copper assays are identical to background values of the least altered rocks.

5.1.2 Geodynamic Setting of the Öksüt Au-Cu Deposit

In Anatolia, most porphyry and epithermal systems are associated with back-arc, syn- or postcollisional settings (e.g., İmer et al., 2013, 2015; Richards, 2015; Kuşçu

et al., 2019; Rabayrol et al., 2019). Our new $^{40}Ar/^{39}Ar$ alunite, illite and zircon U-Pb garnet ages (Table 4.3, Figures 4.44 and 4.46) from Keltepe, Güneytepe and Keltepe, combined with previously reported zircon U-Pb ages of Rabayrol et al. (2019) and Aluç et al. (2020) from the host pyroxene andesite porphyry, confirm the ~5.7 to 5.5 Ma age for formation of high-sulfidation epithermal mineralization at Öksüt. The timing of magmatism and epithermal-style alteration at Öksüt postdates the early to middle Miocene closure of the southern Neotethys Basin (Okay et al., 2010), which serves as unequivocal evidence for formation in a postsubduction setting. According to Aluç et al. (2020), epithermal-style mineralization at Öksüt is mainly hosted in the hornblende-phyric porphyry, and that the duration of mineralization was short-lived (<80 kyr) as constrained by the mean U-Pb zircon age of this unit (5.73 ± 0.06 Ma) and the youngest U-Pb zircon age (5.67 ± 0.07 Ma) of the overlying pyroxene andesite porphyry. However, our field, drill core, and petrographic observations, as well as interpreted $^{40}Ar/^{39}Ar$ ages, indicate that mineralization was rather coeval with the emplacement of pyroxene andesite porphyry and its timing likely extended at least to 5.5 Ma. Additonal U-Pb ages of two garnet samples (5.8 and 5.3 Ma) also indicate that relatively high temperature alteration styles may have developed contemporanously with shallow, low-temperature epithermal alteration.

Epithermal-style alteration and gold-copper mineralization developed coevally with andesitic volcanism at the Develidağ Volcanic Complex during regional-scale extension along the Ecemiş corridor (Figure 3.1; Koçyiğit and Erol, 2001; Jaffey et al., 2004). The ~5.7 to 5.5 Ma formation age also makes Öksüt the youngest major gold deposit in Anatolia, and possibly in the entire western Tethyan metallogenic belt. The older hydrothermal biotite total gas age of ~7.4 Ma (Table 4.3) from biotite-magnetite-K-feldspar-altered pyroxene andesite porphyry west of Keltepe does not agree with the U-Pb zircon age of the same unit (Rabayrol et al., 2019; Aluç et al., 2020), and is therefore considered unreliable. A pyroxene andesite porphyry unit with a slightly older U-Pb zircon age of 7.9 ± 0.14 Ma was reported from the Tekkedağ volcanic suite (Rabayrol et al., 2019), situated approximately 45 km to the northwest (Figure 3.1). Still, due to the absence of porphyry-altered/mineralized

clasts in phreatomagmatic breccias or evidence for late overprinting of biotite-magnetite ± K-feldspar±anhydrite alteration by epithermal assemblages, we tentatively infer that both epithermal and porphyry alter- ation styles at Öksüt developed contemporaneously as part of the same magmatic-hydrothermal event.

The late Miocene-early Pliocene magmatism at the Develidağ Volcanic Complex and throughout south-central Anatolia was a result of either postcollisional rollback of the Cyprian slab or delamination beneath central Anatolia (Rabayrol et al., 2019). Both scenarios involve remelting of previously modified subarc lithosphere to form calc-alkaline magmas that compositionally mimic those observed in continental arcs. Consequently, Richards (2009, 2011) suggested that such magmas may generate postsubduction Au-rich porphyry and epithermal systems through remobilization of sulfide phases normally retained in deep root sections of arcs.

Formation of porphyry deposits depends on a number of successive processes, from melt generation at depth through magma emplacement in mid- to upper-crustal levels, to ultimate ore deposition around shallowly emplaced intrusions. Unless these processes operate optimally, the chances of forming an economic porphyry system are likely to be low (e.g., Richards, 2003; Sillitoe, 2010). Source magmas of the late Miocene volcanic centers in south-central Anatolia are hydrous and oxidized and are therefore deemed to be potentially fertile for porphyry-style mineralization (Kuşçu et al., 2019; Rabayrol et al., 2019). In the presence of favorable magma compositions, evolution of upper-crustal magma chambers and style of magmatism play a vital role in later stages of fluid exsolution and sulfide precipitation. Transpressional or transtensional strain across arc segments or collisional to postcollisional settings are regarded as prerequisites for porphyry development (Tosdal and Richards, 2001), since such conditions promote efficient convective crystallization of magmas leading to volatile saturation and magmatic fluid exsolution (e.g., Shinohara and Hedenquist, 1997; Richards, 2003; Wilkinson, 2013). Notable exceptions to this are synextensional porphyry districts formed after crustal overthickening, as observed along the Miocene Gangdese belt in Tibet (Hou et al., 2009), the Cretaceous Zijinshan district in southeast China (Piquer et al.,

2017), the Eocene Biga Peninsula in northwest Anatolia (Sánchez et al., 2016), and probably also in the Kışladağ porphyry Au deposit in western Anatolia (Baker et al., 2016). Nevertheless, no major period of crustal thickening was recorded around the Ecemiş sector of the central Anatolian fault zone prior to the late Miocene, and thus, the prevalent extensional stress regime and explosive nature of Develidağ Volcanic Complex magmatism during Öksüt mineralization is hereby considered to be unfavorable for porphyry-style mineralization. This would explain the overall lack of quartz veining and sulfide precipitation in the biotite-magnetite ± K-feldspar ± anhydrite alteration zone, as well as the absence of phyllic alteration beneath both Keltepe and Güneytepe.

5.1.3 Regional Significance and Relation to Late Cenozoic Central Anatolian Tectonism

Late Cenozoic postsubduction magmatism along south-central and adjacent western Anatolian areas is considered to be highly productive in terms of gold mineralization. The latter region features some important gold±copperdeposits (e.g., Kışladağ; Figures 1.4 and 5.1, Table 5.1) and its mineralization potential has been

outlined through detailed exploration. In contrast, the extent of gold mineralization along the late Miocene-Pliocene volcanic belt in south-central Anatolia has not been constrained in detail, not least because this belt received little exploration until the work by Stratex during the last decade (Yıldız et al., 2017). Large areas of hydrothermally altered rock are present but apart from Öksüt, the only economically important systems recognized to date are the İnlice high-sulfidation (proven and probable reserves: 0.25 Moz) and Himmetdede low-sulfidation (proven and probable reserves plus inferred resource: 0.95 Moz) epithermal gold mineralizations.

Himmetdede, situated ~80 km to the northwest (Figure 1.4), is a metamorphic rock-hosted low-sulfidation Au deposit of unknown but probable late Cenozoic age (Table 5.1). Hypogene gold mineralization at Himmetdede is mainly contained in quartz-

dominant, sulfide-poor, pyritic breccias, and was likely sourced from a deep-seated intrusion laterally offset from the deposit. In these aspects, it differs significantly from the rest of the gold mineralized systems of the south-central Anatolian volcanic belt, and rather bears similarities to the low- temperature, breccia- and vein-hosted Sb-Hg-Ag deposits of the Niğde metamorphic massif (Figure 1.4), also associated with distal Miocene granitoids (Akçay, 1995).

İnlice is located approximately 300 km to the west of Öksüt and lies within the Konya volcanic district (Figure 1.4). It is, in most aspects, analogous to the Öksüt deposit. Mineralization is hosted by older (~9 Ma; Kuşcu et al., 2019; Rabayrol et al., 2019) calc- alkaline andesites and is confined to steeply dipping silica ledges with surrounding advanced argillic alteration (Hall et al., 2007). Supergene oxidation was only shallowly (<40 m) developed at İnlice and the overall system lacks copper mineralization and deeper porphyry-style alteration (Hall et al., 2007). The nearby Doğanbey porphyry Cu-Mo-Au prospect, situated about 16 km northwest of İnlice, is the only known porphyry occurrence throughout the entire extent of the Miocene-Pliocene belt in south-central Anatolia. Porphyry-style mineralization at Doğanbey occurs within potassic-altered pyroxene andesite porphyries (~10 Ma; Kuşcu et al., 2019; Rabayrol et al., 2019) concealed beneath a gold-mineralized lithocap (Hall et al., 2007). Both İnlice and Doğanbey were regionally controlled by the NW trending Akşehir fault zone (Figure 1.4), which according to Koçyiğit et al. (2000) accommodated a period of mild compression during the late Miocene, coincident with mineralization in these localities. This is in contrast to the predominantly extensional stress regime that prevailed during the late Miocene along the Ecemiş corridor. For the reasons explained above, the general tectonic setting of the Konya volcanic district may thus be more conducive for upper-crustal magma chamber development and porphyry-style mineralization.

Volcanism in the Melendiz area (Figure 1.4), on the other hand, is younger (5–3 Ma; Rabayrol et al., 2019) than that of Konya, Develidağ Volcanic Complex, and Tekkedağ areas. It contains few high-sulfidation epithermal prospects including Tepeköy, Boztepe, and Altunhisar (Figure 1.4). The Tepeköy prospect is hosted

within Miocene pyroxene-bearing andesite porphyries exposed in a stratovolcano setting. A K/Ar age of 4.2 ± 0.4 Ma was reported from Tepeköy (Türkecan et al., 2003), but the age of hydrothermal alteration is not known. The emplacement of the volcanic sequence at Tepeköy was controlled by the Tuz Gölü fault zone (Figure 1.4), which is conjugate to the Ecemiş¸ fault zone such that it similarly accommodated extension in the late Miocene (Koçyiğit and Beyhan, 1998).

Farther to the west, in western Anatolia, middle Miocene magmatism generated the world-class Kışladağ porphyry Au deposit and few important prospects, such as the AS Cu-Au and Pınarbaşı Cu-Mo porphyry systems (Figure 1.4 and 5.1; Table 5.1). These porphyry systems formed between 18 and 11 Ma (Baker et al., 2016; Delibaş¸ et al., 2017; Kuşcu et al., 2019; Rabayrol et al., 2019; Sönmez and Kuşcu, 2020), in relationship to post-subduction rollback of the Aegean slab and N-S-directed propagation of a slab tear to the west of the Konya volcanic district (Figure 5.2). Under such stress conditions, E-W- and NW-SE-trending grabens acted as the major foci of magmatism and porphyry-style mineralization (Figure 5.2; Table 5.1). Nature of Miocene magmatism in western Anatolia was mostly calc-alkaline, but the AS porphyry prospect is hosted within ~11 Ma alkaline intrusions developed on the western edge of the slab tear (Rabayrol et al., 2019; Sönmez and Kuşcu, 2020). No economic high-sulfidation epithermal system as in to Öksüt or İnlice has been discovered in this part of the belt so far, but this appears to be circumstantial and not directly related to regional tectonics or style of magmatism. Conversely, the south-central Anatolian tectonics during the late Miocene was controlled predominantly by transtensional or transpressional strike-slip fault systems (e.g., Ecemiş, Tuz Gölü and Akşehir fault zones; Figure 1.4) along which intermittent episodes of relaxation and extension led to development of high-sulfidation epithermal Au mineralization (Figure 5.2). Therefore, we consider the geodynamic conditions that led to formation of Öksüt to be considerably different in comparison to those responsible for the porphyry-style mineralization in western Anatolia.

5.1.4 Deep Oxidation of the Epithermal System

At Öksüt, supergene oxidation locally extends to depths of >300 m and it was fundamental to development of economic gold mineralization (Yıldız et al., 2017). Oxidation to similar or greater depths of >300 m has also been observed in some other important epithermal systems, particularly in the central Andes (Sillitoe, 2005). However, similar examples are not known in Turkey. As such, deep supergene oxidation is hereby regarded as a distinctive feature of the Öksüt high-sulfidation epithermal system among its Anatolian counterparts and appears to have resulted from a combination of both district- and regional-scale factors.

Major factors that contributed to deep oxidation of the Öksüt Au-Cu deposit are the sub-vertical, tabular, and permeable nature of the mineralized breccias, topographically prominent position of the Develidağ Volcanic Complex, and late Miocene to Recent >2-km uplift of the south-central Anatolian margin (Schildgen et al., 2012a,b; Yıldız et al., 2017). The first reason likely enhanced groundwater descent through breccia feeders, whereas the second two resulted in a deep-water table, enhancing sulfide enrichment by exposing zones of hypogene sulfides to oxidation. Consequently, refractory gold was liberated from sulfide minerals, making much of the gold-mineralized orebody amenable to cyanide leaching. In addition, copper was significantly redistributed and enriched into locally up to 50-m-thick but discontinuous chalcocitic zones, while arsenic was removed from the pyrite- enargite-gold ores.

5.2 Conclusions

The Öksüt gold-copper deposit formed at ~5.7 to 5.5 Ma during the emplacement of the Develidağ Volcanic Complex in south-central Anatolia. The close agreement between the ages of alteration minerals and that of the host andesite porphyry indicates contemporaneous development of late Miocene post-subduction volcanism and high-sulfidation epithermal Au-Cu mineralization. Öksüt formation was also

coincident with the onset of E-W-directed extension along the Ecemiş corridor, and that mineralization is closely associated with the vertical to sub-vertical faults developed in response to this extensional regime. Our reported ages confirm this largest known gold system in central Anatolia as the youngest epithermal deposit in the western Tethyan metallogenic belt.

Gold-copper mineralization is primarily hosted by structurally controlled breccia domains. These breccias are concentrated within the Keltepe and Güneytepe orebodies and show zoned alteration from a central silica through quartz- alunite-kaolinite to kaolinite-illite/smectite alteration at the peripheries. Gold is hosted in both of silica and quartz- alunite-kaolinite, where it is associated with a predominantly hypogene assemblage of pyrite, enargite, and marcasite. Deeper kaolinite-illite/smectite and locally developed biotite- magnetite ± K-feldspar ± anhydrite alteration zones, on the other hand, are devoid of any mineralization.

The gold potential at Öksüt is a result of the deeply oxidized nature of the hydrothermal system. This was interpreted to be a consequence of several factors, including significant surface uplift (>2 km) since the late Miocene, increased permeability of breccia zones for descending groundwaters, and deeply incised topography exposing parts of the hydro- thermal system to weathering. As a consequence, supergene weathering locally extended to depths of >300 m, generating gold-mineralized, silica and iron-hydroxide-rich breccias, and making Öksüt mineralization amenable to standard heap- leach methods. Copper, on the other hand, was largely redistributed in chalcocite zones beneath the oxidized gold ore.

Table 5.1. Summary Characteristics of Late Cenozoic Gold Systems in South Central and Western Anatolia. Abbreviations: azur = azurite, bn = bornite, bnnt = bournonite, cpy = chalcopyrite, cup = cuprite, FZ = fault zone, gn = galena, HS = high-sulfidation, LS = low-sulfidation, mag = magnetite, mal = malachite, mar = marcasite, moly = molybdenite, py = pyrite, sph = sphalerite, tet = tetrahedrite, ten = tennantite, VC = volcanic complex.

	Kayseri district		Konya district		Afyon-Uşak district	
	Öksüt	Himmetdede	Doğanbey	İnlice	AS	Kışladağ
Geologic setting	Remnant caldera	Concealed subvolcanic intrusion (dome?)	Volcanic dome	Volcanic dome	Intrusive stock	Stratovolcano
Basement	Tauride carbonate	Kırşehir massif	Tauride carbonate	Tauride carbonate	Menderes massif	Menderes massif
Formation	Develidağ VC	Bozçaldağ formation	Erenlerdağ VC	Erenlerdağ VC	Afyon volcanics	Beydağı stratovolcano
Host rock	Andesite porphyry, diatreme	Gneiss, schist, marble	Trachyte, tuff, ignimbrite (3)	Rhyolite, trachyte-latite porphyry	Monzonite, syenite	Monzonite, trachyte, latite
Stress regime	Extensional	Extensional	Extensional	Extensional	Extensional	Extensional
Regional structure	Ecemiş FZ	None recognized; local-scale normal and thrust faults	Akşehir-Afyon FZ	Akşehir- Afyon FZ	Sandıklı graben	Uşak-Güre Graben
Mineralization style	HS epithermal Au-Cu	LS epithermal Au	Porphyry Cu-Mo-Au	HS epithermal Au	Porphyry Cu-Au	Porphyry Au
Ore minerals	Au, Cu, cpy, py, mar, tet, en, cc, cov, mal, azur, cup, mag	Py, sph, gn, mar	Cpy, py, mol, mag	Au, Cu, cpy, py, en, sph, cc, cov, mal, bn	Py, tet, cpy, bn, moly, cov, mag, mal, azur	Au, py, sphy, mar, moly tet-ten, bnnt, cpy
Ore textures	Vuggy to massive quartz, breccia, disseminations	Breccia	Veinlets	Vuggy quartz, breccias, veins	Breccias, vein(let)s, disseminations	Stockwork veinlets, disseminations, breccias
Main alteration styles	Silicification, advance argillic, argillic, potassic	Silicification, argillic	Silicification, advance argillic, argillic	Silicification, advance argillic,argillic	Potassic, phyllic, advance argillic, propylitic	Potassic, phyllic, advance argillic
Alteration age	5.7-5.5 Ma	-	Micene	Miocene	11.2 Ma	14.5-13.8 Ma
Supergene oxidation	To 400 m depth	Deep (unreported)	-	~40 m	200 m	Shallow
Host rock age	5.7-5.4 Ma (2)	Middle to late Miocene?	Miocene	8.98 Ma	12.5 - 10.5 Ma	14.8-14.4 Ma
Data sources	1,2, this study		1, 3, 4	1, 3, 4	1, 3, 5	1, 6

Data sources: 1 = Rabayrol et al. (2019), 2 = Aluç et al. (2020), 3 = Kuşcu et al. (2019), 4 = Hall et al. (2007), 5 = Sönmez and Kuşcu (2020), 6 = Baker et al. (2016)

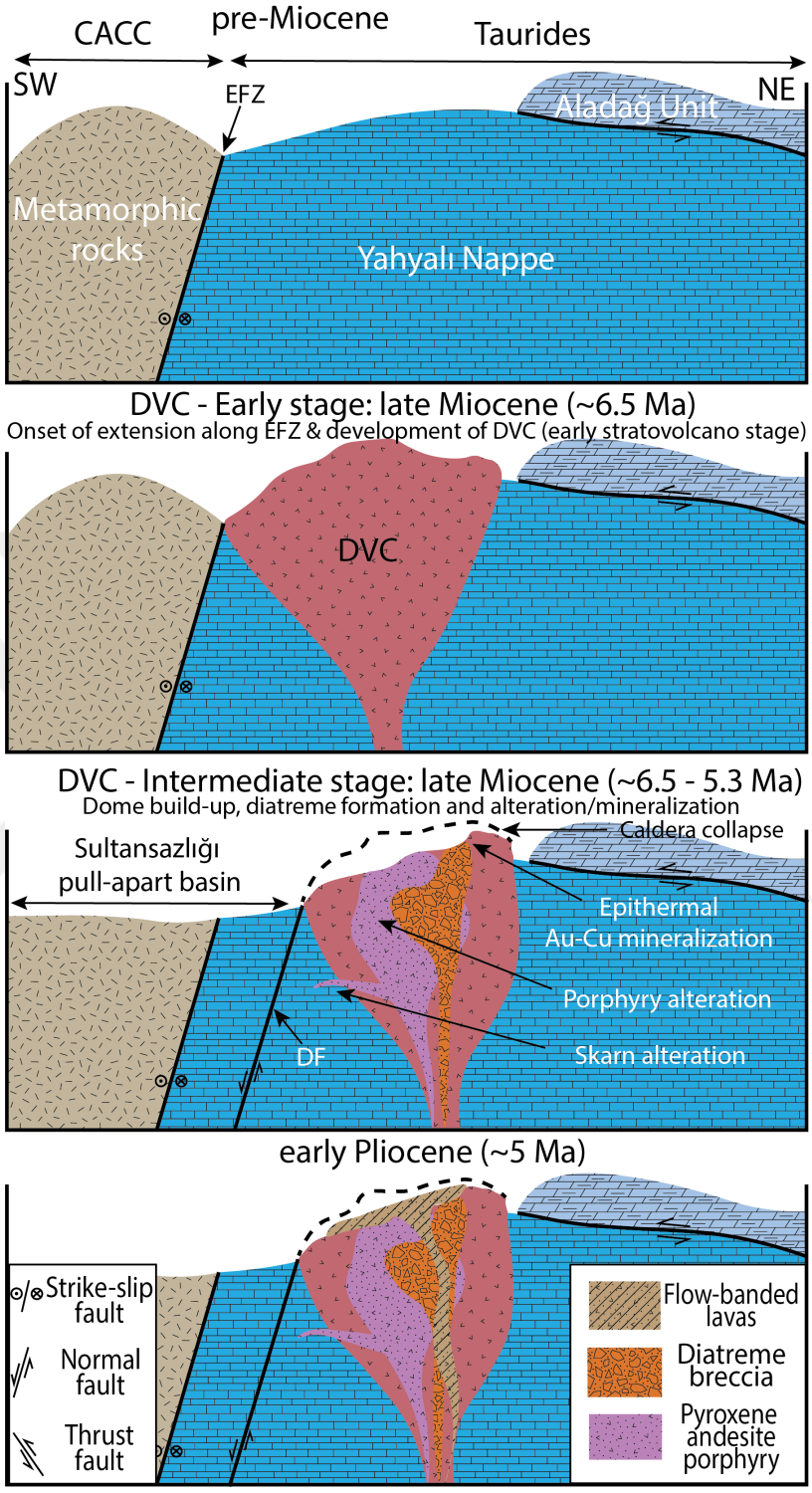


Figure 5.1. Cartoons showing simplified formation model of the Öksüt high-sulfidation epithermal deposit in relation to the DVC. Abbreviations: EFZ = Ecemiş Fault Zone, DF = Develi Fault.

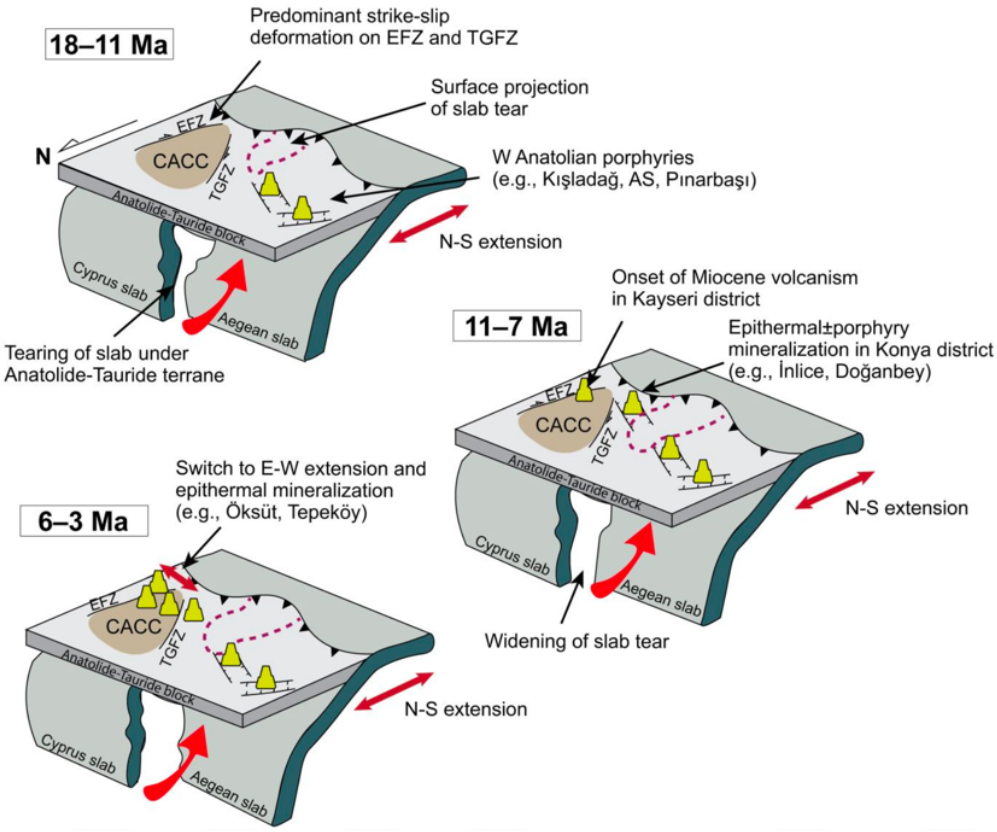


Figure 5.2. Cartoon illustrating the temporal evolution of late Cenozoic (middle to late Miocene-early Pliocene) gold-copper mineral districts in south central and western Anatolia in relationship to regional tectonics. Abbreviations: CACC = Central Anatolian Crystalline Complex, EFZ = Ecemiş fault zone, TGFZ = Tuz Gölü fault zone.

REFERENCES

Agostini, S., Doglioni, C., Innocenti, F., Manetti, P., Tonarini, S. (2010). On the geodynamics of the Aegean rift. Tectonophysics, 488, 7–21.

Akay, E. (2009). Geology and petrology of the Simav Magmatic Complex (NW Anatolia) and its comparison with the Oligo-Miocene granitoids in NW Anatolia: implications on Tertiary tectonic evolution of the region. International Journal of Earth Science, 98, 1655–1675.

Akçay, M. (1995). Geological and mineralogical investigation of the Gümüsler (Nig˘de) Sb ± Hg ± W occurences and implications on their gold potential: Geological Bulletin of Turkey, 38, 23–34.

Akçay, M., and Gündüz, Ö. (2004). Porphyry Cu–Au mineralisation associatedwith a multi-phase intrusion, and related replacement fronts inlimestones in an island arc setting near the Gümüşhane village(Artvin) in the Eastern Black Sea Province (Turkey). Chem Erde64(4):359–383

Akıman, O., Erler, A., Göncüoğlu, M.C., Güleç, N., Geven, A., Türeli, T.K., and Kadıoğlu, Y.K. (1993). Geochemical characteristics of granitoids along the western margin of the Central Anatolian Crystalline Complex and their tectonic implications: Geological Journal, 28, 371–382,

Albinson, T., Norman, D.I., Cole, D. and Chomiak, B. (2001). Controls on formation of low-sulfidation epithermal deposits in Mexico: Constraints from fluid inclusion and stable isotope data, Society of Economic Geologists Special Publication, 8, 1-32.

Aldanmaz, E., Pearce, J.A., Thirlwall, M.F., Mitchell, J.G. (2000). Petrogenetic evolution of late Cenozoic, post-collision volcanism in western Anatolia, Turkey. Journal of Volcanology and Geothermal Research, 102, 67–95.

Allen, M., Jackson, J. and Walker, R. (2004). Late Cenozoic reorganization of the Arabia-Eurasia collision and the comparison of short-term and long-term deformation rates. Tectonics, 23, 1-17.

Altan F., Atuk N. (1969). Kayseri–Sarımsaklı ovasının planlama Kademesinde hidrojeolojik etüd raporu, Devlet Su İşleri Genel Müdürlüğü Yeraltı Suları Dairesi Başkanlığı.

Altunkaynak, S., and Dilek, Y. (2006). Timing and nature of postcollisional volcanism in western Anatolia and geodynamic implications. In: Dilek, Y., Pavlides, S. (Eds.), Postcollisional Tectonics and Magmatism in the Mediterranean region and Asia: Geological Society of America Special Paper, 409, 321–351

Altunkaynak, S. (2007). Collision-driven slab breakoff magmatism in northwestern Anatolia, Turkey. Geological Journal, 115, 63–82.

Altunkaynak, Ş., Dilek, Y. (2013). Eocene mafic volcanism in northern Anatolia: its causes and mantle sources in the absence of active subduction. International Geology Review, 55, 1641–1659.

Aluç, A., Kuşcu, İ., Cihan, M., Serçe, D.C. and Bekarslan, S. (2017). Öksüt (Develi, Kayseri, Turkey) High Sulfidation Epithermal Gold Deposit Geology – Mineralogy - Timing and Genetic, 70. Turkey Geological Symposium Abstracts, 464–465.

Aluç, A., Kuşçu, İ., Peytcheva, I., Cihan, M., von Quadt, A. (2020). The late Miocene Öksüt high sulfidation epithermal Au-Cu deposit, central Anatolia, Turkey: Geology, geochronology, and geochemistry: Ore Geology Reviews, 126, no. 103795.

Arancibia, O., and Clark, A.H. (1996). Early magnetite-amphibole-plagioclase alteration-mineralization in the Island Copper porphyry copper-gold-molybdenum deposit, British Columbia: Economic Geology, 91, 402–438.

Arni, P. (1939). Tektonische Grundziige Ostanatoliens und benachbarter Gebiete. Veriiff. Inst. Lagerstöttenforsch. Tiirkei, Ser. B, 4: 90 pp.

Arribas, A., Cunningham, C.G., Rytuba, J.J., Rye, R.O., Kelly, W.C., Podwysocki, M.H., McKee, E.H. ve Tosdal, R.M., (1995). Geology, Geochronology, Fluid Inclusions and Isotope Geochemistry of the Rodalquilar Gold Alunite Deposit, Spain, Economic Geology, 90, 795-822.

Arribas, A.J., Hedenquist, J.W., Itaya, T., Okada, T., Concepción, R.A. and Garcia Jr, J.S. (1995). Contemporaneous formation of adjacent porphyry and epithermal Cu-Au deposits over 300 ka in northern Luzon, Philippines: Geology, 23, 337-340.

Arslan, M., Aslan, Z. (2006). Mineralogy, petrography and whole-rock geochemistry of the Tertiary granitic intrusions in the Eastern Pontides, Turkey. Journal of Asian Earth Science, 27, 177–193.

Arslan M, Temizel I, Abdioğlu E, Kolaylı H, Yücel C et al. (2013). 40Ar– 39Ar dating, whole-rock and Sr–Nd–Pb isotope geochemistry of post-collisional Eocene volcanic rocks in the southern part of the Eastern Pontides (NE Turkey): implications for magma evolution in extension-induced origin. Contributions to Mineralogy and Petrology 166: 113-142

Ashley, R.P., Silberman, M.L. (1976). Direct dating of mineralization at Goldfield, Nevada, by potassium-argon and fission-track methods. Economic Geology ; 71 (5)

Ashley, R. P. (1982). Occurence model for enargite-gold deposits: U.S. Geological Survey Open-File Report, 82(795), 144–147.

Aslan, Z., Arslan, M., Temizel, İ., Kaygusuz, A. (2014). K–Ar dating, whole-rock and Sr–Nd isotope geochemistry of calc-alkaline volcanic rocks around the Gümüşhane area: implications for post-collisional volcanism in the Eastern Pontides, Northeast Turkey. Mineralogy and Petrology, 108, 245–267.

Aydin, F., Karsli, O., Chen, B. (2008). Petrogenesis of the Neogene alkaline volcanics with implications for post-collisional lithospheric thinning of the Eastern Pontides, NE Turkey. Lithos 104, 249–266.

Baker, T., Bickford, D., Juras, S., Lewis, P., Oztas, Y., Ross, K., Tukac, A., Rabayrol, F., Miskovic, A., Friedman, R., Creaser, R.A. ve Spikings, R., (2016). The geology of the Kışladağ porphyry gold deposit, Turkey, Society of Economic Geologists Special Publication, 19, 57-83.

Ballhaus, C. (1993). Redox states of lithospheric and asthenospheric upper mantle. Contributions to Mineralogy and Petrology 114, 331–348.

Barrier, E. and Vrielynck, B. (2008). Palaeotectonic maps of the Middle East: scale 1:18,500,000.

Barton, P.B., Jr., and Skinner, B.J. (1979). Sulfide mineral stabilities, in Barnes, H.L., ed., Geochemistry of hydrothermal ore deposits, 2nd ed.: New York, Wiley-Interscience, 278–403.

Batum İ., (1978). Nevşehir güneybatısındaki Göllüdağ ve Acıgöl yöresi volkanitlerinin jeoloji ve petrografisi, Hacettepe University Earth Science, 4, 50–69.

Becker-Platen, J.D., Sickenberg, O., Sobien, H., Vertebrate. (1975). Lokalfaunen der Türkei und ihre Altersstellung, Geologisches Jahrbuch, 15

Bendezu, R., Fontbote, L., Cosca, M. (2003). Relative age of Cordilleran base metal lode and replacement deposits, and high sulfidation Au–(Ag) epithermal mineralization in the Colquijirca mining district, central Peru. Mineralium Deposita 38(6):683–694

Berger, B. R., and Henley, R. W. (1989). Advances in understanding of epithermal gold-silver deposits, with special reference to the western United States. Economic Geology Monograph, 6, 405–423.

Bertrand, G., Guillou-Frottier, L. and Loiselet, C. (2014). Distribution of porphyry copper deposits along the western Tethyan and Andean subduction zones: Insights from a paleotectonic approach: Ore Geology Reviews, 60, 174-190.

Bozkurt, E., Mittwede, S.K. (2001). Introduction to the geology of Turkey — a synthesis. International Geology Review, 43, 578–594.

Boztuğ, D., Erçin, I., Kuruçelik, M.K., Göç, D., Kömür, I., İskenderoğlu, A. (2006). Geochemical characteristics of the composite Kaçkar batholith generated in a Neo-Tethyan convergence system, Eastern Pontides, Turkey. Journal of Asian Earth Science, 27, 286–302.

Boztuğ, D. and Jonckheree, R.C. (2007). Apatite fission-track data from central-Anatolian granitoids (Turkey): constraints on Neo-Tethyan closure. Tectonics 26, TC3011.

Brandon, A.D., Draper, D.S. (1996). Constraints on the origin of the oxidation state of mantle overlying subduction zones: an example from Simcoe, Washington, USA. Geochimica et Cosmochimica Acta 60, 1739–1749.

Browne, P.R.L. (1971). Petrological logs of Broadlands drillholes BR1 to BR25: New Zealand Geological Survey Report 52, 86 p.

Browne, P.R.L. (1978). Hydrothermal alteration in active geothermal fields: Annual Review of Earth and Planetary Sciences, v. 6, p. 229–250.

Buchanan, L. J. (1981). Precious metal deposits associated with volcanic environments in the Southwest. Arizona Geological Society Digest, 14, 237–262.

Burke, K., and Şengör, A.M.C. (1986). Tectonic escape in the evolution of the continental crust. Reflect. Seismol. Cont. crust 14, 41–53

Burton, K.W., and O'Nions, R.K. (1992). The timing of mineral growth across a regional metamorphic sequence. Nature 357:235–238

Burton, K.W., Kohn, M.J., Cohen, A.S, O'Nions R.K. (1995). The relative diffusion of Pb, Nd, Sr and O in garnet. Earth Planet Science Letters, 133:199–211

Camus, F., and Dilles, J. (2001). A Special Issue Devoted to Porphyry Copper Deposits of Northern Chile. Economic Geology, 96 (2): 233–237

Chappell, B. W., and Stephens, W. E. (1988). Origin of infracrustal (I-type) granite magmas. Transactions of the Royal Society of Edinburgh: Earth Sciences 79, 71–86.

Chiaradia, M., Schaltegger, U., Spikings, R.A., Wotzlaw, J.F., Ovtcharova, M. (2013). How accurately can we date the duration of magmatic-hydrothermal events in porphyry systems? Economic Geologist, 108 (4), 565–584.

Cihan, M., Serçe, D.C., Bekarslan, S. (2016). Öksüt gold project; from grassroots to reserve and forward to mine development. SEG 2016 Conference Proceedings: Tethyan Tectonics and Metallogeny, September 25-28, 2016, Çeşme, İzmir, Turkey.

Clark, M., and Robertson, A. (2005). Uppermost Cretaceous–Lower Tertiary Ulukısla Basin, south-central Turkey: Sedimentary evolution of part of a unified basin complex within an evolv- ing Neotethyan suture zone: Sedimentary Geology, 173, 15–51

Cline, J.S., and Bodnar, R.J. (1991). Can economic porphyry copper mineralization be generated by a typical calc-alkaline melt? Journal of Geophysical Research 96, 8113–8126.

Cooke, D. R., and Simmons, S. F. (2000). Characteristics and genesis of epithermal gold deposits. Society of Economic Geologists Reviews, 13, 221–244.

Cosentino, D., Schildgen, T.F., Cipollari, P., Faranda, C., Gliozzi, E., Hudáčková, N., Lucifora, S. and Strecker, M.R. (2012). Late Miocene surface uplift of the

southern margin of the Central Anatolian Plateau, Central Taurides, Turkey: Geological Society of America Bulletin, 124, 133-145.

Crowe, D.E., Riciputi, L.R., Bezenek, S., Ignatiev, A. (2001). Oxygen isotope and trace element zoning in hydrothermal garnets: windows into large-scale fluid-flow behavior. Geology 29, 479–482.

Cox, D.P. and Singer, D.A. (1988). Distribution of gold in porphyry copper deposits: 23 p.

Çolakoğlu, A.R. and Arehart, G.B. (2010). The petrogenesis of Sarıçimen (Çaldıran-Van) quartz monzodiorite: Implication for initiation of magmatism (Late Medial Miocene) in the east Anatolian collision zone, Turkey: Lithos, 119, 607–620.

Çil, A., and İmer, A. (2021). Geologic Setting and Mineralization of Gicik Low-Sulfidation Epithermal Au Deposit (North-Central Anatolia): Society of Economic Geologists Annual Meeting, SEG100 Conference

Davidson, J.P. (1996). Deciphering mantle and crustal signatures in subduction zone magmatism. In: Bebout, G.E., Scholl, D.W., Kirby, S.H., Platt, J.P. (Eds.), Subduction: Top to bottom. : Geophysical Monograph, 96. American Geophysical Union, pp. 251–262.

Deen, J.A. (1990). Hydrothermal Ore Deposition Related to High-level Igneous Activity: A Stable- isotopic Study of the Julcani Afining District, Peru. Ph.D. thesis, University of Colorado, Boulder, Colorado.

Delibaş, O., Moritz, R., Chiaradia, M., Selby, D., Ulianov, A. and Revan, M.K. (2017). Post-collisional magmatism and ore-forming systems in the Menderes massif: new constraints from the Miocene porphyry Mo–Cu Pınarbaşı system, Gediz–Kütahya, western Turkey: Mineralium Deposita, 52, 1157-1178.

Delph, J.R., Abgarmi, B., Ward, K.M., Beck, S.L., Ozacar, A.A., Zandt, G., Sandvol, E., Turkelli, N., Kalafat, D. (2017). The effects of subduction termination on

the continental lithosphere: Linking volcanism, deformation, surface uplift, and slab tearing in central Anatolia: Geosphere, 13, 1–18.

Demirtaşlı, E. (1984). Stratigraphy and tectonics of the area between Silifke and Anamur, Central Taurus Mountains. In: Tekeli, O., Göncüoğlu, M.C. (Eds.), Proc. Int. Syrup. on the Geology of the Taurus Belt, 26-29 September, 1983, Ankara, 101-118.

de Hoog, J.C.M., Mason, P.R.D., van Bergen, M.J. (2001). Sulfur and chalcophile elements in subduction zones: constraints from a laser ablation ICP-MS study of melt inclusions from Galunggung Volcano, Indonesia. Geochimica et Cosmochimica Acta 65, 3147–3164.

D'Errico, M.E., Lackey, J.S., Surpless, B.E., Loewy, S.L., Wooden, J.L., Barnes, J.D., Strickland, A., Valley, J.W. (2012). A detailed record of shallow hydrothermal fluid flow in the Sierra Nevada magmatic arc from low-δ18O skarn garnets. Geology 40, 763–766.

Dewey, J.F., and Bird, J.M. (1970). Mountain belts and the new global tectonics. J. Geophys. Res. 75, 2625–2647

Dewey, J., Hempton, M., Kidd, W., Saroğlu, F. and Şengör, A. (1986). Shortening of continental lithosphere: the neotectonics of Eastern Anatolia—a young collision zone: Geological Society, London, Special Publications, 19, 1-36.

Dilek, Y., and Altunkaynak, Ş. (2009). lithospheric tearing in an orogenic belt western Turkey : mantle response to collision , slab breakoff , and Geochemical and temporal evolution of Cenozoic magmatism in Geological Society.

Dilek, Y. and Pavlides, S. (eds) Postcollisional tectonics and magmatism in the Medi- terranean region and Asia. Geological Society of America Special Paper, 409, 475–505.

Dirik, K., and Göncüoğlu, M. C. (1996). Neotectonic characteristics of central Anatolia. International Geology Review, 38(9), 807–817.

Eastoe, C.J. (1978). Fluid inclusion study of the Panguna porphyry copper deposit, Bougainville, Papua-New-Guinea: Economic Geology, 73, 721–748.

Einaudi, M.T., Hedenquist, J.W., and Inan, E.E. (2003). Sulfidation state of fluids in active and extinct hydrothermal systems: Transitions from porphyry to epithermal environments: Society of Economic Geologists Special Publication, 10, 285–313.

Emmons, W.H. (1917). The enrichment of ore deposits: U.S. Geological Survey Bulletin 625, 530 p.

Ercan T., Orta, (1986). Anadolu'daki Senozoyik volkanizması, Bulletin of the Mineral Research and Exploration. Turkey, 107, 119–140

Erdoğan, B., Uchman, A., Güngör, T., Özgül, N. (2004). Lithostratigraphy of the Lower Cambrian metaclastics and their age based on trace fossils in the Sandıklı region, southwestern Turkey. Geobios 37 (3), 346–360.

Espurt, N., Hippolyte, J.-C., Kaymakci, N., Sangu, E. (2014). Lithospheric structural control on inversion of the southern margin of the Black Sea Basin, Central Pontides, Turkey. Lithosphere 6, 26–34.

Fournier, R.O. (1999). Hydrothermal processes related to movement of fluid from plastic into brittle rock in the magmatic-epithermal environment: Economic Geology, 94, 1193–1211.

Georgatou, A.A. ve Chiaradia, M. (2020). Magmatic sulfides in high-potassium calc-alkaline to shoshonitic and alkaline rocks, Solid Earth, 11, 1–21.

Giggenbach, W.F. (1992). Magma degassing and mineral deposition in hydrothermal systems along convergent plate boundaries: Economic Geology, 87, 1927-1944.

Gökten, E., and Floyd, P.A. (1987). Geochemistry and tectonic environment of the Şarkışla area volcanic rocks in Central Anatolia, Turkey: Mineralogical Magazine, v. 51, 553–559

Gökten, E. (1993). Geology of the southern boundary of the Sivas Basin in the east of Ulaş (Sivas–Central Anatolia): Tectonic development related to the closure of inner Tauride Ocean: Turkish Association of Petroleum Geologists Bulletin, v. 5, no. 1, 35–55.

Göncüoğlu, M.C. (1977). Geologie des westlichen Niğde Massives, Diss., Rheinisch Friedrieh- Wilhelms-Univ., Bonn, 180 pp.

Göncüoğlu, M.C. (1982). Niğde Masifinde paragnayslarinda zirkon U/Pb yaşlari: Türkiye Jeoloji Kurumu Bülteni, 25, 61–66.

Göncüoğlu, M. C., Toprak, V., Kuşcu, İ., Erler, A., and Olgun, E. (1991). Geology of the western part of the Central Anatolian Massif. In Turkish Petroleum Corporation Report.

Göncüoğlu, M. C., Erler, A., Toprak, V., Olgun, E., Yalınız, K., Kuşçu, İ, Köksal, S. and Dirik, K. (1993). Geology of the Central part of the Central Anatolian Massif, Part 3: Geologic evolution of the Central Kõzõlõrmak Tertiary Basin. Turkish Petroleum Corporation (TPAO) Report No. 3313 (in Turkish).

Göncüoğlu, M.C. (2010). Introduction to the Geology of Turkey: Geodynamic evolution of the pre-Alpine and Alpine Terranes. MTA, 1-69.

Görür, N., Tüysüz, O., and Celal Şengör, A. M. (1998). Tectonic evolution of the central Anatolian basins. International Geology Review, 40(9), 831-850.

Gustafson, L. B., and Hunt, J.P. (1975). The porphyry copper deposit at El Salvador,Chile. Economic Geology 70, 857–912.

Güçtekin, A., and Köprübaşı, N. (2009). Geochemical characteristics of mafic and intermediate volcanic rocks from the Hasandağ and Erciyes volcanoes (Central Anatolia, Turkey). Turkish Journal of Earth Science, 18:1–27

Gül, M.A., Çuhadar, Ö., Özbaş, Y., Alkan, H., Efeçınar T. (1984). Bolkar-Belemedik yöresinin jeolojisi ve petrol olanakları. Türkiye Petrolleri Anonim Ortaklığı, Rapor 1972, 159 pp.

Gürsu, S., Göncuoğlu, C.M., Bayhan, H. (2004). Geology and geochemistry of the pre-Early Cambrian rocks in the Sandıklı area: implications for the Pan-African evolution of NW Gondwanaland. Gondwana Research 7 (4), 923–935.

Gürsu, S., and Göncüoğlu, C.M. (2006). Petrogenesis and tectonic setting of Cadomian felsic igneous rocks, Sandıklı area of the western Taurides, Turkey. International Journal of Earth Sciences 95, 741–757.

Güner Y., Emre Ö., Bas¸ H., (1984).Erciyes Yanardag˘ının Jeolojisi ve Jeomorfolojisi, Min. Res. Expl. Inst.Turkey Raport No 7570

Hall, D.J., Foster, R.P., Yildiz, B. and Redwood, S.D. (2007). The Inlice High-sulphidation Epithermal Gold Discovery: Defining a Potential New Gold Belt in Turkey: Proceedings of the Ninth Biennial SGA Meeting, Dublin, 113-116.

Hamlyn, P.R., Keays, R.R., Cameron, W.E., Crawford, A.J., Waldron, H.M. (1985). Precious metals in magnesian low-Ti lavas: implications for metallogenesis and sulfur saturation in primary magmas. Geochimica et Cosmochimica Acta 49, 1797–1811.

Hayba,D. O., Foley,N. K., and Heald-Wetlaufer,P. (1984). Characteristics that distinguish types of epithermal deposit slabs. I: Symposium on Exploration of Ore Deposits of the North American Cordillera, Reno, Nevada, March 25-28, 1984, Abstracts with Program, p. 21.

Heald, P, Foley, N.K., and Hayba, D.O. (1987). Comparative anatomy of volcanic-hosted epithermal deposits: Acid-sulfate and adularia-sericite types, Economic Geology, 82, l-26.

Hedenquist, J.W. (1986). Geothermal systems of the Taupo Volcanic Zone, New Zealand: Their characteristics and relation to volcanism and mineralization: Royal Society of New Zealand Bulletin, 23, 134–168.

Hedenquist, J.W. (1990). The thermal and geochemical structure of the Broadlands-Ohaaki geothermal system, New Zealand: Geothermics, 19, 151–185.

Hedenquist, J.W. (1991) Boiling and dilution in the shallow portion of the Waiotopu geo- thermal system, New Zealand: Geochimica et Cosmochimia Acta, 55, 2753–2765.

Hedenquist, J.W., Simmons, S.F., Giggenbach, W.F., Eldridge, C.S. (1993). White Island, New Zealand, volcanic–hydrothermal system represents the geochemical environ- ment of high-sulfidation Cu and Au ore deposition. Geology 21, 731–734.

Hedenquist, J.W., Aoki, M., and Shinohara, H. (1994). Flux of volatiles and ore-forming metals from the magmatic-hydrothermal system of Satsuma Iwojima volcano: Geology, 22, 585–588.

Hedenquist, J.W. and Lowenstern, J.B. (1994). The role of magmas in the formation of hydrothermal ore deposits: Nature, 370, 519-527.

Hedenquist, J.W., Izawa, E., Arribas, A., Jr., and White, N.C. (1996). Epithermal gold deposits: Styles, characteristics, and exploration: Poster and booklet, Resource Geology Special Publication 1, 17 p

Hedenquist, J.W., Arribas, A., and Reynolds, T.J. (1998). Evolution of an in- trusion-centered hydrothermal system: Far Southeast-Lepanto porphyry and epithermal Cu-Au deposits, Philippines: Economic Geology, 93, 373–404.

Hedenquist, J. W., Arribas, A., and Gonzalez-Urien, E. (2000). Exploration for epithermal gold deposits. Reviews in Economic Geology, 13(1), 245–277.

Hedenquist, J.W., and Taran, Y.A. (2013). Modeling the formation of advanced argillic lithocaps: volcanic vapor condensation above porphyry intrusions: Economic Geology, 108, 1523–1540.

Hedenquist, J. W., and Arribas, A. (2022). Exploration Implications of Multiple Formation Environments of Advanced Argillic Minerals, Economic Geology, 117, 3, 609–643

Heinrich, C.A., Ryan, C.G., Mernagh, T.P., and Eadington, P.J. (1992). Segregation of ore metals between magmatic brine and vapor—a fluid inclusion study using PIXE microanalysis: Economic Geology, 87, 1566–1583.

Heinrich, C.A., Günther, D., Audétat, A., Ulrich, T., Frischknecht, R. (1999). Metal fractionation between magmatic brine and vapor, determined by microanalysis of fluid inclusions: Geology, 27, 755–758.

Heinrich, C.A., Neubauer, F. (2002). Cu–Au–Pb–Zn–Ag metallogeny of the Alpine-Balkan-Carpathian-Dinaride geodynamic province. Mineralium Deposita, 37, 533–540.

Heinrich, C.A., Dreisner, T., Steffánson, A., Seward, T.M. (2004). Magmatic vapor contraction and the transport of gold from the porphyry environment to epithermal ore deposits. Geology 32, 761–764.

Heinrich, C.A. (2005). The physical and chemical evolution of low-salinity magmatic fluid at the porphyry to epithermal transition: A thermodynamic study: Mineralium Deposita, 39, 864−889.

Hempton, M.R. (1987). Constraints on Arabian plate motion and extensional history of the Red Sea. Tectonics 6, 687-705.

Henley, R.W., McNabb, A. (1978). Magmatic vapor plumes and ground–water interaction in porphyry copper emplacement. Economic Geology 73, 1–20.

Henley, R.W., and Ellis, A.J. (1983). Geothermal systems, ancient and modern: Earth Science Reviews, 19, l-50.

Higgins, M., L. M., Schoenbohm, G., Brocard, Kaymakci, N., Gosse, J. C., and Cosca, M. A. (2015). New kinematic and geochronologic evidence for the Quaternary evolution of the Central Anatolian fault zone (CAFZ), Tectonics, 34, 2118–2141,

Holwell, D.A., Fiorentini, M., McDonald, I., Lu, Y., Giuliani, A., Smith, D.J., Keith, M., Locmelis, M. (2019). A metasomatized lithospheric mantle control on the metallogenic signature of post-subduction magmatism. Nature Communications, 10:1–10

Hou, Z., Yang, Z., Qu, X., Meng, X., Li, Z., Beaudoin, G., Rui, Z., Gao, Y., Zaw, K. (2009). The Miocene Gangdese porphyry copper belt generated during post-collisional extension in the Tibetan Orogen. Ore Geology Reviews 36, 25–51.

Hou, Z., Yang, Z., Lu, Y., Kemp, A., Zheng, Y., Li, Q., Tang, J., Yang, Z. and Duan, L. (2015). A genetic linkage between subduction- and collision-related porphyry Cu deposits in continental collision zones: Geology, 43, 247-250.

Hüsing, S.K., Zachariasse, W.-J., van Hinsbergen, D.J., Krijgsman, W., Inceöz, M., Harzhauser, M., Mandic, O. and Kroh, A. (2009). Oligocene–Miocene basin evolution in SE Anatolia, Turkey: constraints on the closure of the eastern Tethys gateway: Geological Society, London, Special Publications, 311, 107-132.

Innocenti, F., Mazzuoili, G., Pasquare, F., Radi- Cati Di Brozola, F. and Villari, L. (1975). The Neogene calcalkaline volcanism of Central Anatolia: geochronological data on Kayseri-Nigde area. Geological Magazine, 112, 349–360.

Ilbeyli, N. (2004). Petrographic and geochemical charac- teristics of the Hamit Alkaline Intrusion in the Central Anatolian Crystalline Complex, Turkey. Turkish Journal of Earth Sciences, 13, 269–286.

Ishihara, S. (1981). The granitoid series and mineralization. Economic Geology 75th Anniversary Volume, 458–484.

Itaya, T., Arribas, A., Jr., and Okada, T. (1996). Argon release systematics of hypogene and supergene alunite based on progressive heating experi- ments from 100” to 1000°C: Geochimica et Cosmochimica Acta, 60, 4525-4535.

İmer, A., Richards, J. P., and Creaser, R. A. (2013). Age and tectonomagmatic setting of the Eocene Çöpler-Kabataş magmatic complex and porphyry-epithermal Au deposit, East Central Anatolia, Turkey. Mineralium Deposita, 48(5), 557–583.

İmer, A., Richards, J. P., Creaser, R. A., and Spell, T. L. (2015). The late Oligocene Cevizlidere Cu-Au-Mo deposit, Tunceli Province, eastern Turkey. Mineralium Deposita, 50(2), 245–263.

İmer, A., Richards, J. P., and Muehlenbachs, K. (2016). Hydrothermal evolution of the Çöpler porphyry-epithermal Au deposit, Erzincan Province, Central Eastern Turkey. Economic Geology, 111(7), 1619–1658.

Jaffey, N., and Robertson, A.H.F. (2001). New sedimentological and structural data from the Ecemis Fault Zone, southern Turkey: implications for its timing and offset and the Cenozoic tectonic escape of Anatolia: Journal of the Geological Society of London, 158, 367–378.

Jaffey, N., Robertson, A. and Pringle, M. (2004). Latest Miocene and Pleistocene ages of faulting, determined by $^{40}Ar/^{39}Ar$ single-crystal dating of airfall tuff and silicic extrusives of the Erciyes Basin, central Turkey: evidence for intraplate eformation related to the tectonic escape of Anatolia. Terra Nova, 16, 2, 45-53.

Jamtveit, B., Wogelius, R. A. and Fraser, D. G. (1993). Zonation patterns of skarn garnets: records of hydrothermal system evolution. Geology 21, 113–116.

Jung, S., and Mezger, K. (2003). U-Pb garnet chronometry in high-grade rocks—Case studies from the central Dama- ra orogen (Namibia) and implications for the interpreta- tion of Sm-Nd garnet ages and the role of high U-Th inclusions: Contributions to Mineralogy and Petrology, 146, 3, 382–396

Karig, D.E., and Kozlu, H. (1990). Late Paleogene-Neogene evolution of the triple junction region near Mara~, South-Central Turkey. J. Geol. Soc. London 147, 1023-1034.

Karslı, O., Dokuz, A., Uysal, İ., Aydın, F., Kandemir, R., and Wijbrans, J. (2010). Generation of the Early Cenozoic adakitic volcanism by partial melting of mafic lower crust, Eastern Turkey: Implications for crustal thickening to delamination. Lithos, 114, 109-120.

Kaygusuz, A., Siebel, W., Şen, C., Satir, M. (2008). Petrochemistry and petrology of I-type granitoids in an arc setting: the composite Torul pluton, Eastern Pontides, NE Turkey. International Journal of Earth Science. 97, 739–764.

Kaymakcı, N., Özçelik, Y., White, S.H., and Van Dijk, P.M. (2009). Tectono-stratigraphy of the Çankırı Basin: Late Cretaceous to early Miocene evolution of the Neotethyan suture zone in Turkey, in van Hinsbergen, D.J.J., Edwards, M.A., and Govers, R., eds., Collision and Collapse at the Africa-Ara- bia-Eurasia Subduction Zone: Geological Society of London Special Publication 311, 67–106

Kelley, S. (1995). Ar-Ar dating by laser microprobe. In: Potts, P.J., Bowles, J.F.W., Reed, S.J.B., Cave, M.R. (eds) Microprobe Techniques in the Earth Sciences. The Mineralogical Society Series, vol 6. Springer, Boston, MA

Kelley, K.A., and Cottrell, E. (2009). Water and the oxidation state of subduction zone magmas. Science 325, 605–607.

Kelling, G., Gökçen, S.L., Floyd, E.A., Gökçen A. (1987). Neogene tectonics and plate convergence in the eastern Mediterranean: New data from southern Turkey. Geology 15, 425-429

Ketin, I. (1955). Uber die Geologie der Gegend von Ovacuma iistlich Zonguldak. Rev. Fat. Sci. Univ. Istanbul, B, 20: 147-154.

Ketin, İ. (1966). Tectonic units of Anatolia. Maden Tetkik ve Arama Bulletin, 66, 23– 34.

Koçyiğit, A.D. (1983). Güneybatı Türkiye ve yakın dolayında levha içi yeni teknonik geilişim. Türkiye Jeoloji Kurumu Bülteni. 27, 1-16.

Koçyiğit, A., and Beyhan, A. (1998). A new intracontinental transcurrent structure: the Central Anatolian Fault Zone, Turkey: Tectonophysics, 284, 317-336.

Koçyiğit, A. and Erol, O. (2001). A tectonic escape structure: Erciyes pull-apart basin, Kayseri, central Anatolia, Turkey: Geodinamica Acta, 14, 133-145.

Kouzmanov, K., Ramboz, C., Lerouge, C., Deloule, E., Beaufort, D., Bogdanov, K. (2003). Stable isotopic constraints on the origin of epithermal Cu–Au and related porphyry copper mineralisations in the southern Pangyurishte district, Srednogorie zone, Bulgaria. In: Eliopoulos DG (ed) Mineral exploration and sus- tainable development. Millpress, Rotterdam, 1181–1184

Kuscu, I., and Erler, A. (1998). Mineralization events in a collision-related setting: The central anatolian crystalline complex, Turkey. International Geology Review, 40(6), 552–565.

Kuşcu İ., Tosdal R.M., Gençalioğlu-Kuşcu G. (2019). Porphyry-Cu Deposits of Turkey. In: Pirajno F., Ünlü T., Dönmez C., Şahin M. (eds) Mineral Resources of Turkey. Modern Approaches in Solid Earth Sciences, vol 16. Springer, Cham, Switzerland.

Kürkcüoğlu, B., Şen, E., Aydar, E., Gündoğdu, A., Gourgaud, M.N., (1998). Geochemical approach to magmatic evolution of Mt. Erciyes Stratovolcano, Central Anatolia, Turkey. Journal of Volcanology and Geothermal Research 473–494 (special issue).

Kürkcüoglu, B. (2010). Geochemistry and petrogenesis of basaltic rocks from the Develidağ volcanic complex, Central Anatolia, Turkey. Journal of Asian Earth Sciences, 37(1), 42–51.

Langton, J.M., and Williams, S.A. (1982). Structural, petrological, and mineralogical controls for the Dos Pobres orebody: Lone Star mining district, Graham County, Arizone, in Titley, S.R., ed., Advances of the porphyry copper deposits, Southwestern North America: Tucson, University of Arizona Press, 335-352.

Lefebvre, C., Meijers, M.J., Kaymakci, N., Peynircioğlu, A., Langereis, C.G., Van Hinsbergen, D.J. (2013). Reconstructing the geometry of central Anatolia during the late Cretaceous: Large-scale Cenozoic rotations and deformation between the Pontides and Taurides: Earth and Planetary Science Letters, 366, 83-98.

Leroux, G.M. (2016). Stratigraphic and petrographic characterization of HS epithermal Au- Ag mineralization at the TV Tower district, Biga Peninsula, NW Turkey: Unpublished M.Sc thesis, Vancouver, Canada, The University of British Columbia, 198 p.

Lindgren, W. (1922). A suggestion for the terminology of certain mineral deposits. Economic Geology, 17, 292–294.

Lindgren, W. (1933). Differentiation and ore deposition, Cordilleran region of the United States. Ore Deposits of the United States, Lindgren V, (170).

Lips, A.L. (2002). Correlating magmatic-hydrothermal ore deposit formation over time with geodynamic processes in SE Europe: Geological Society, London, Special Publications, 204, 69-79.

Longo, A.A., Dilles, J.H., Grunder, A.L., and Duncan, R. (2010). Evolution of calc-alkaline volcanism and associated hydrothermal gold deposits at Yana-cocha, Peru: Economic Geology, 105, 1191–1241.

Losada-Caldero`n, A.J., and McPhail D.C. (1996). Porphyry and high- sulfidation epithermal mineralization in the Nevados del Fam- atina mining district, Argentina. In: Camus F, Sillitoe RM, Peterson R (eds) Andean copper deposits: new discoveries, mineralization, styles and metallogeny. Society of Economic Geologist Special Publication, 5:91–118

Lowell, J.D. and Guilbert, J.M. (1970). Lateral and vertical alteration-mineralization zoning in porphyry ore deposits: Economic Geology, 65, 373-408.

Mair, J.L., Farmer, G.L., Groves, D.I., Hart, C.J. and Goldfarb, R.J. (2011). Petrogenesis of postcollisional magmatism at Scheelite Dome, Yukon, Canada: Evidence for a lithospheric mantle source for magmas associated with intrusion-related gold systems: Economic Geology, 106, 451-480.

Mancano, D.P., and Campbell, A.R. (1995). Microthermometry of enargite hosted fluid inclusions from the Lepanto, Philippines, high-sullidation Cu-Au deposit: Geochimica et Cosmochimica Acta, 59, 3909-3916.

McDougalL 1. and Harrison, T.M. (1988). Geochronology and Thermochrollology by the 40Ar/39Ar Method. Oxford University Press.

McKenzie, D. (1972). Active tectonics of the Mediterranean region: Geophysical Journal International, 30, 109-185.

Meijers, M.J., Kaymakci, N., Van Hinsbergen, D.J., Langereis, C.G., Stephenson, R.A. Hippolyte, J.C. (2010). Late Cretaceous to Paleocene oroclinal bending in the central Pontides (Turkey): Tectonics, 29, 1-21.

Meijers, M.J., Brocard, G.Y., Cosca, M.A., Lüdecke, T., Teyssier, C., Whitney, D.L., Mulch, A. (2018). Rapid late Miocene surface uplift of the central Anatolian Plateau margin: Earth and Planetary Science Letters, 497, 29–41

Mehnert, H. H., Lipman, P. W., and Steven, T. A. (1973). Age of mineralization at Summitville, Colorado, as indicated by K-Ar dating of alunite: Economic Geology , 68, 399-401.

Meinert, L.D. (1992). Skarns and skarn deposits. Geoscience Canada 19, 145–162.

Meinert, L.D. (2005). World skarn deposits: Economic Geology 100th Anniversary Volume, 299-336.

Menant, A., Jolivet, L., Tuduri, J., Loiselet, C., Bertrand, G., Guillou-Frottier, L. (2018). 3D subduction dynamics: A first-order parameter of the transition from copper-to gold-rich deposits in the eastern Mediterranean region: Ore Geology Reviews, 94, 118-135.

Meyer, C., and Hemley, J.J. (1967). Wall rock alteration, in Barnes, H.L., ed., Geochemistry of hydrothermal ore deposits: New York, Holt, Rinehart and Winston, 166-235.

Moix, P., Beccaletto, L., Kozur, H. W., Hochard, C., Rosselet, F., and Stampfli, G. M. (2008). A new classification of the Turkish terranes and sutures and its implication for the paleotectonic history of the region. Tectonophysics, 451(1– 4), 7–39.

Monod, O., Kozlu, H., Ghienne, J.-F., Dean, W.T., Günay, Y., Le Hérissé, A., Paris, F., Robardet, M. (2003). Late Ordovician glaciation in southern Turkey. Terra Nova 15, 249–257.

Moritz, R., Rezeau, H., Ovtcharova, M., Tayan, R., Melkonyan, R., Hovakimyan, S., Ramazanov, V., Selby, D., Ulianov, A., Chiaradia, M. (2016). Long-lived, stationary magmatism and pulsed porphyry systems during Tethyan subduction to post-collision evolution in the southernmost Lesser Caucasus, Armenia and Nakhitchevan: Gondwana Research, 37, 465-503.

Muntean, J., and Einaudi, M. (2001). Porphyry gold deposits of the Refugio district, Maricunga belt, northern Chile: Economic Geology, 95

MTA. (2002). Geological map of Turkey: Ankara, Turkey, Maden Tetkik ve Arama Genel Müdürlüğü (MTA), scale 1:500,000.

Noble D. C. and Silberman M. L. (1984). Evoluci6n volcfinica e hidrotermal y cronologia de K-Ar del distrito minero de Julcani, Society of Geologist Peru, Volume Jubilar, 60th Anniversar,. 5, 1-35.

Noll, P.D., Newsom, H.E., Leeman, W.P., Ryan, J.G. (1996). The role of hydrothermal fluids in the production of subduction zone magmas: evidence from siderophile and chalcophile trace elements and boron. Geochim. Cosmochim. Acta 60, 587–611.

Okay, A.İ., Şahintürk, Ö. (1997). Geology of the eastern Pontides. In: Robinson, A. (Ed.), Regional and Petroleum Geology of the Black sea and Surrounding Region. American Association of Petroleum Geologists Memoir, 68, 291–311.

Okay, A. I., and Tuysuz, O. (1999). Tethyan sutures of northern Turkey Major continental blocks of Turkey. The Mediterranean Basins: Tertiary Extension within the Alpine Orogen., 475–515.

Okay, A.I. (2008). Geology of Turkey: A synopsis. Anschnitt, 21, 19-42.

Okay, A.İ., Zattin, M. and Cavazza, W. (2010). Apatite fission-track data for the Miocene Arabia- Eurasia collision: Geology, 38, 35-38.

Oldaç Y.T., Saltık O., Türkmen M., Tezel H., (1970). Develi– Yeşilhisar ovası hidrojeolojik etüd raporu, Devlet Su İşleri Rapor No 1505/2-PK

Özgül, N. (1976). Toroslerin bazi temel jeoloji özellikleri. Türkiye Jeoloji Kurumu Bildileri, 19: 65-78.

Özgül N. (1984). Stratigraphy and tectonic evolution of the Central Taurides, International Symposium on the Geology of Taurus Belt, Ankara, O. Tekeli and M.C. Göncüoğlu (Eds.), 77-90.

Park, JW., Campbell, I.H., Chiaradia, M. et al. (2021). Crustal magmatic controls on the formation of porphyry copper deposits. Natural Reviews Earth and Environment, 2, 542–557.

Pasquare G. (1968). Geology of the Cenozoic volcanic area of Central Anatolia, Atti Accad. Naz. Lincei 9, 53–204.

Pearce, J. A., Bender, J. F., De Long, S. E., Kidd, W. S. F., Low, P. J., Güner, Y., Saroğlu, Y., Moorbath, S., Mitchell, J. G. (1990). Genesis of collision volcanism in Eastern Anatolia, Turkey. Journal of Volcanology and Geothermal Research, 44(1–2), 189–229.

Perello, J. (1994). Geology, porphyry Cu-Au, and epithermal Cu-Au-Ag mineralization of the Tombulilato district, North Sulawesi, Indonesia: Journal of Geochemical Exploration, 50, 221-256.

Perelló, J., Carlotto, V., Zárate, A., Ramos, P., Posso, H., Neyra, C., Caballero, A., Fuster, N., Muhr, R. (2003). Porphyry-style alteration and mineralization of the middle Eocene to early Oligocene Andahuaylas-Yauri Belt, Cuzco Region, Peru: Economic Geology, 98, 1575–1605

Pettke, T., Oberli, F. and Heinrich, C.A. (2010). The magma and metal source of giant porphyry- type ore deposits, based on lead isotope microanalysis of individual fluid inclusions: Earth and Planetary Science Letters, 296, 267-277.

Poisson, A.M., Akay, E., Dumont, J.F., Uysal, Ş. (1984). The Isparta Angle: a Mesozoic paleorift in the western Taurides. In: Tekeli, O., Göncüoğlu, M.C. (Eds.), Proc. Int. Symp. on the Geology of the Taurus belt, 26-29 September 1983, Ankara, 11-26.

Poisson, A.M., Guezou, J. C., Ozturk, A., Inan, S., Temiz, H., Gürsöy, H., Kavak, K. S., and Özden, S. (1996). Tectonic Setting and Evolution of the Sivas Basin, Central Anatolia, Turkey, International Geology Review, 38:9,838-853

Pourteau, A., Candan, O., and Oberhänsli, R. (2010). High pressure metasediments in central Turkey: Constraints on the Neotethyan closure history: Tectonics, v. 29, TC5004

Presnell, R.D. (1997). Structural controls on the plutonism and metallogeny in the Wasatch and Oquirrh Mountains, Utah: Society of Economic Geologist Guidebook Series, 29, 1-9.

Pudack, C., Halter, W.E., Heinrich, C.A., and Pettke, T. (2009). Evolution of magmatic vapor to gold-rich epithermal liquid: The porphyry to epithermal transition at Nevados de Famatina, Northwest Argentina: Economic Geology, 104, 449–477.

Rabayrol, F. (2018). Late cenozoic post subduction tectonic, magmatic and metallogenic evoluation of the Anatolide-Tauride orogenic belt, Turkey, PhD Thesis, Vancouver, 328p.

Rabayrol, F., Hart, C. J. R., and Thorkelson, D. J. (2019). Temporal, spatial and geochemical evolution of the late Cenozoic post-subduction magmatism in central and eastern Anatolia, Turkey. Lithos, 336-337, 67-69.

Rabayrol, F., and Hart, C.J.R. (2021). Petrogenetic and tectonic controls on magma fertility and the formation of post-subduction porphyry and epithermal mineralization along the late Cenozoic Anatolian Metallogenic Trend, Turkey. Miner Deposita 56, 279–306.

Redmond, P.B., Einaudi, M.T., Inan, E.E., Landtwing, M.R., and Heinrich, C.A. (2004). Copper deposition by fluid cooling in intrusion-centered sys- tems: New insights from the Bingham porphyry ore deposit, Utah: Geology, 32, 217–220.

Reed, M., Rusk, B., Palandri, J. (2013). The Butte Magmatic-Hydrothermal System: One Fluid Yields All Alteration and Veins. Economic Geology, 108 (6): 1379–1396.

Reid, G.D., Woodhouse, P., Stallman, M., Cihan, M., Landry, P., Hilkewich, T., Raponi, T.R., D'Souza, K., Sharpe, C. (2015). Technical NI 43-101 report on the Oksut gold project, Turkey: C.G. Inc., 271 p.

Reyes, A.G. (1990). Petrology of Philippine geothermal systems and the application of alteration mineralogy to their assessment: Journal of Volcanology and Geothermal Research, 43, 279–309.

Reynolds, T.J. and Bean, R.E. (1985). Evolution of Hydrothermal Fluid Characteristics at the Santa Rita, New Mexico, Porphyry Copper Deposit. Economic Geology, 80, 1328-1347

Richards, J.P. (2003). Tectono-magmatic precursors for porphyry Cu-(Mo-Au) deposit formation: Economic Geology, 98, 1515-1533.

Richards, J.P. (2005). Cumulative factors in the generation of giant calc-alkaline porphyry Cu deposits. In: Porter, T.M. (Ed.), Super Porphyry Copper and Gold Deposits: A Global Perspective vol. 1. Porter Geoscience Consulting Publishing, Linden Park, South Australia, 7–25.

Richards, J. P. (2009). Postsubduction porphyry Cu-Au and epithermal Au deposits: Products of remelting of subduction-modified lithosphere. Geology, 37 (3), 247- 250.

Richards, J.P. (2011). High Sr/Y arc magmas and porphyry Cu±Mo±Au deposits: just add water: Economic Geology, 106, 1075-1081.

Richards, J.P., Spell, T., Rameh, E., Razique, A., Fletcher, T. (2012). High Sr/Y magmas reflect arc maturity, high magmatic water content, and porphyry Cu ± Mo ± Au potential: examples from the Tethyan arcs of central and eastern Iran and western Pakistan. Economic Geology 107, 295–332.

Richards, J. P. (2015). Tectonic, magmatic, and metallogenic evolution of the Tethyan orogen: From subduction to collision. Ore Geology Reviews, 70, 323-345.

Robertson. A.H.F., and Grasso. M. (1995). Overview of the Late Tertiary-Recent tectonic and paleo-environmental develop ment of the Mediterranean region. Terra Nova 7, 114-127.

Robertson, A.H.F., and Mountrakis, D. (2006). Tectonic development of the Eastern Mediterranean region: an Introduction. Geological Society, London, Special Publications, 260, 1-9.

Robertson, A.H.F., Parlak, O., Rizaoğlu, T., Ünlügenç, Ü., İnan, N., Tasli, K. Ustaömer, T. (2007). Tectonic evolution of the South Tethyan ocean: evidence from the Eastern Taurus Mountains (Elaziğ region, SE Turkey): Geological Society, London, Special Publications, 272, 231-270.

Robertson, A., Parlak, O., Ustaömer, T. (2009). Melange genesis and ophiolite emplacement related to subduction of the northern margin of the Tauride–Anatolide continent, central and western Turkey. Geological Society of London Special Publications, 311, 966.

Rochrlach, B.D. (2002). Tectonic evolution, petrochemistry, geochronology and palaeohydrology of the Tampakan porphyry and high sulphidation epithermal Cu-Au deposit Mindanao, Phillipines. PhD, Australia National University, Canberra

Roedder, E., and Bodnar, R.J. (1971). Fluid inclusion studies on the porphyry-type ore deposits at Bingham, Utah, Butte, Montana, and Climax, Colorado. Economic Geology, 66, 98–120.

Rye, R.O. (1993). The evolution of magmatic fluids in the epithermal environment—the stable isotope perspective: Economic Geology, 88, 733–753.

Sarıfakıoğlu, E., Dilek, Y., Winchester, J.A. (2013). Late Cretaceous subduction initiation and Palaeocene–Eocene slab breakoff magmatism in South-Central Anatolia, Turkey. International Geology Reviews, 55, 66–87.

Sawkins, Frederick J. (1990). Integrated tectonic-genetic model for volcanic-hosted massive sulfide deposits. Geology, 18 (11), 1061 pp.

Sayit, K., Bedi, Y., Tekin, U.K., Göncüoglu, M.C., and Okuyucu, C. (2017). Middle Triassic back-arc basalts from the blocks in the Mersin Mélange, southern Turkey: Implications for the geodynamic evolution of the Northern Neotethys. Lithos, 268-271, 102-113.

Schildgen, T.F., Cosentino, D., Bookhagen, B., Niedermann, S., Yıldırım, C., Echtler, H., Wittmann, H. and Strecker, M.R. (2012a). Multi-phased uplift of the southern margin of the Central Anatolian plateau, Turkey: A record of tectonic and upper mantle processes: 268 Earth and Planetary Science Letters, 317, 85-95.

Schildgen, T.F., Cosentino, D., Caruso, A., Buchwaldt, R., Yıldırım, C., Bowring, S.A., Rojay, B., Echtler, H., and Strecker, M.R. (2012b). Surface expression of eastern Mediterranean slab dynam- ics: Neogene topographic and structural evolution of the southwest margin of the Central Anatolian Plateau, Turkey: Tectonics, v. 31, TC2005

Seedorff, E., Dilles, J.H., Proffett, J.M., Jr., Einaudi, M.T., Zurcher, L., Stavast, W.J.A., Johnson, D.A., and Barton, M.D. (2005). Porphyry deposits: Characteristics and origin of hypogene features: Economic Geology 100th Anniversary Volume, 251−298.

Seman, S., Stockli, D.F., and McLean, N. (2017). U-Pb geo- chronology of grossular-andradite garnet: Chemical Geology, 460, 106–116.

Seymen, Y. (1982). Kaman dolayinda Kirsehir Masifi- nin jeolojisi: Unpubl. habilitation thesis, I.T.U Maden Fakültesi, Istanbul, 164 p.

Shafiei, B., Haschke, M., Shahabpour, J. (2009). Recycling of orogenic arc crust triggers porphyry Cu mineralization in Kerman Cenozoic arc rocks, southeastern Iran. Miner. Deposita 44, 265–283.

Shanin, L. L., Iranov, I. B., and Shipulin, F. K. (1968). The possibleuse of alunite in K-Ar geochronometry:Geokhimiya, No. 1, 109-111

Sheppard, S.M.F., Nielsen, R.L., and Taylor, H.P.Jr. (1971). Hydrogen and oxygen isotope ratios in minerals from porphy copper deposits: Economic Geology, 66, 515-542.

Shinohara, H., and Hedenquist, J.W. (1997). Constraints on Magma Degassing beneath the Far Southeast Porphyry Cu–Au Deposit, Philippines. Journal of Petrology, 38, 1741-1752.

Silberman, M. L., and Ashley, R. P. (1970). Age of ore deposition at Goldfield, Nevada, from potassium-argon dating of alunite: Economic Geology, 65, 352-354.

Sillitoe, R.H. (1972). A plate tectonic model for the origin of porphyry copper deposits: Economic Geology, 67, 184−197.

Sillitoe, R.H., (1973). The tops and bottoms of porphyry copper deposits: Economic geology, 68, 799−815.

Sillitoe, R. H. (1977). Metallic mineralization affiliated to subaerial volcanism. Geological Society, London, Special Publications, 7, 99–116.

Sillitoe, R. H. (1993). Giant and bonanza gold deposits in the epithermal environment: Assessment of potential genetic factors. BH Whiting, CJ Hodgson and R. Mason. Society of Economic Geologists, Special Publication, (3), 125-156.

Sillitoe, R.H. (1994). Erosion and collapse of volcanoes: Causes of telescoping in intrusion-centered ore deposits: Geology, 22, 945-948.

Sillitoe, R.H. (1995). Exploration of porphyry copper lithocaps: Australasian Institute of Mining and Metallurgy Publication Series No. 9/95, 527-532.

Sillitoe, R. H. (1997). Characteristics and controls of the largest porphyry copper-gold and epithermal gold deposits in the circum-Pacific region. Australian Journal of Earth Sciences, 44(3), 373–388.

Sillitoe, R.H. (1998). Major regional factors favouring large size, high hypogene grade, elevated gold content and supergene oxidation and enrichment of porphyry copper deposits: Porphyry and Hydrothermal Copper and Gold Deposits—a global perspective: Perth, 49-60.

Sillitoe, R.H. (1999). Styles of high-sulphidation gold, silver, and copper mineralization in the porphyry and epithet-ma1 environments: Pacrim '99, Bali, Indonesia, l0-13 October, Proceedings, 29-44.

Sillitoe, R.H. (2000). Gold-Rich Porphyry Deposits: Descriptive and Genetic Models and Their Role in Exploration and Discovery, Gold in 2000. Reviews in Economic Geology, 13.

Sillitoe, R. H., and Hedenquist, J. W. (2003). Linkages between volcanotectonic settings, ore-fluid compositions, and epithermal precious-metal deposits. Society of Economic Geologists Special Publication, 10, 315–343.

Sillitoe, R.H. (2005). Supergene oxidized and enriched porphyry copper and related deposits: Economic Geology 100th Anniversary Volume, 723−768.

Sillitoe, R.H. (2010). Porphyry copper systems: Economic Geology, 105, 3-41.

Simmons, S.F. (1991) Hydrologic implications of alteration and fluid inclusion studies in the Fresnillo district, Mexico: Evidence for a brine reservoir and a descending water table during the formation of hydrothermal Ag-Pb-Zn orebodies: Economic Geology, 86, 1579–1601.

Simmons, S. F., White, N. C., and John, D. A. (2005). Geological characteristics of epithermal precious and base metal deposits. Economic Geology 100th Anniversary, 29(January 2005), 485–522.

Smith, M., William, T., Lepore, A., Incekaraoğlu, T., Shabestari, P., Boran, H., Raabe, K. (2014). Küçükdağ: A New, High Sulfidation Epithermal Au-Ag-Cu Deposit at the TV Tower Property in Western Turkey. Economic Geology, 109 (6): 1501–1511

Solomon, M. (1990). Subduction, arc reversal, and the origin of porphyry copper–gold deposits in island arcs. Geology 18, 630–633.

Sönmez, Ş. U., and Kuşçu, İ. (2020). Geology, geochemistry, geochronol- ogy and genesis of the late Miocene porphyry Cu-Au-Mo mineralization at Afyon-Sandıklı (AS) prospect, western Anatolia, Turkey: Ore Geology Reviews, 121, 103506.

Stampfli, G.M., Marcoux, J., Baud, A. (1991). Tethyan margins in space and time. In: Channell, J.E.T., Winterer, E.L., Jansa, L.F. (Eds.), Palaeogeography and paleoceanography of Tethys. Elsevier, Amsterdam, 373–409, Netherlands.

Stampfli, G.M. (2000). Tethyan oceans. In: Bozkurt, E., Winchester, J.A., Piper, J.D.A. (Eds.), Tectonics and Magmatism in Turkey and the Surrounding Area. Geological Society London, Special Publication No. 173, 1–23.

Stampfli, G.M., and Borel, G.D. (2002). A plate tectonic model for the Paleozoic and Mesozoic constrained by dynamic plate boundaries and restored synthetic oceanic isochrons, Earth and Planetary Science Letters, 196, Issues 1–2

Stampfli, G.M., Borel, G.D. (2004). The TRANSMED transects in space and time: con- straints on the paleotectonic evolution of the Mediterranean domain. In: Cavazza, W., Roure, F., Spakman, W., Stampfli, G.M., Ziegler, P. (Eds.), The TRANSMED Atlas: The Mediterranean Region from Crust to Mantle.Springer Verlag, Berlin, 53–80.

Steven, T.A., and Ratté, J.C. (1960). Geology of ore deposits of the Summitville district, San Juan Mountains, Colorado: U.S. Geological Survey Professional Paper 343, 70 p.

Stoffregen, R. (1987). Genesis of acid-sulfate Alteration and Au-Cu-Ag mineralization at Summitville, Colorado: Economic Geology, 82, 1575–1591.

Şengör, A.M.C., and Kidd, W.S.F. (1979). Post-collisional tectonics of the Turkish-Iranian plateau and a comparison with Tibet: Tectonophysics, 55, 361-376.

Şengör, A. M. C., and Yilmaz, Y. (1981). Tethyan evolution of Turkey: A plate tectonic approach. Tectonophysics, 75(3–4).

Şengör, A.M.C. (1982). The classical theories of orogenesis. In: Miyashiro, A., Aki, K., Şengör, A.M.C. (Eds.), Orogeny. John Wiley and sons, Chichester, 1–48.

Şengör, A.M.C. (1984). The Cimmeride Orogenic System and the Tectonics of Eurasia: Geological Society of America Special Paper 195, 82 p.

Sengor, A.M.C. (1987). Cross-faults and differential stretching of hanging walls in regions of low-angle normal faults: examples from western Turkey. In: Coward, M.P., Dewey, J.F., Hancock, P.L. (Eds.), Continental Extensional Tectonics. Geological Society Special Publication no.28, 575–689.

Tapponnier, P. (1977). Evolution tectonique du Systeme Alpin en Mediterranee: poincon- nement et ecrasement rigide-plastique. Bulletin de la Société Géologique de France, Ser. 7, 19: 437-460.

Taymaz, T., Yılmaz, Y., Dilek, Y. (2007). The geodynamics of the Aegean and Anatolia Introduction. In: Geol. Soc. London Spec. Publ. pp. 1–16.

Temizel, I., Arslan, M., Ruffet, G., Peucat, J.J. (2012). Petrochemistry, geochronology and Sr– Nd isotopic systematics of the Tertiary collisional and post-collisional volcanic rocks from the Ulubey (Ordu) area, eastern

Pontide, NE Turkey: implications for extension-related origin and mantle source characteristics. Lithos 128, 126–147.

Terzi, M.A. (2020). İnlice (Konya) Epitermal Altın Yatağının Jeolojisi, Jeokimyası ve Kökensel İncelenmesi, Aksaray, Turkey, PhD Thesis, 333 p.

Toksoy-Köksal, F. (2019). On the geodynamics of the Alpine collisional granitoids from Central Anatolia: petrology, age and isotopic characteristics of the granitoids of the Ekecikdag Igneous Association (Aksaray/Turkey), Geodinamica Acta, v.31, n.1, 1-26.

Toprak, V., and Göncüoğlu, M.C. (1993). Tectonic control on the development of the Neogene- Quaternary Central Anatolian Volcanic Province, Turkey: Geological Journal, 28, 357-369.

Toprak, V. (1994). Central Kizilirmak Fault Zone: Northern Margin of Central Anatolian Volcanics. TUBITAK, Doga, Turkish Journal of Earth Sciences, 3: 29–38.

Topuz, G., Okay, A.I., Altherr, R., Schwarz, W.H., Siebel, W., Zack, T., Satır, M., Şen, C. (2011). Post-collisional adakite-like magmatism in the Ağvanis Massif and implications for the evolution of the Eocene magmatism in the Eastern Pontides (NE Turkey). Lithos 125, 131–150.

Tosdal, R.M. and Richards, J.P. (2001). Magmatic and structural controls on the development of porphyry Cu±Mo±Au deposits: Reviews in Economic Geology, 14, 157-181.

Turner. G.. Miller. J.A. and Grasty, R.L. (1966). The thermal history of the Bruderheim meteorite. Earth Planetary Science Letters, 1, 155-7.

Türkecan, A., Akçay, A.E., Satır, M., Dönmez, M., Ercan, T. (2003). Melendiz Dağları (Niğde) volkanizması: 56th Geological Congress of Turkey, Extended abstracts, Ankara, Turkey, 16–17 (in Turkish with English abstract).

Ulrich, T., Günther, D., and Heinrich, C.A. (2001). Evolution of a porphyry Cu-Au deposit, based on LA-ICP-MS analysis of fluid inclusions, Bajo de la Alumbrera, Argentina: Economic geology, 96, 1743 (correctly reprinted in 2002, 97, 1888–1920).

Ulrich, T., and Heinrich, C.A. (2002). Geology and alteration geochemistry of the porphyry Cu-Au deposit at Bajo de la Alumbrera, Argentina: Economic Geology, 97, 1865–1888.

Umhoefer, P.J., Whitney, D.L., Teyssier, C., Fayon, A.K., Casale, G., Heizler, M.T. (2007). Yo-yo tectonics in a wrench zone, central Anatolia, in Till, A., Roeske, S., Sample, J., and Fos- ter, D., eds., Exhumation and Continental Strike-Slip Fault Systems: Geological Society of America Special Paper 434, 35–57.

Umhoefer, P.J., Thomson, S.N., Cosca, C.L.M.A., Teyssier, C., Whitney, D.L. (2020). Cenozoic tectonic evolution of the Ecemiş fault zone and adjacent basins, central Anatolia, Turkey, during the transition from Arabia-Eurasia collision to escape tectonics. Geosphere, 16 (6): 1358–1384.

Ustaömer, T., Robertson, A.F.H., (2010). Late Palaeozoic–Early Cenozoic tectonic development of the Eastern Pontides (Artvin area), Turkey: stages of closure of Tethys along the southern margin of Eurasia. Geological Society of London Special Publications, 340, 281–327

Vache, R. (1963). Akdagmadeni kontakt yataklari ve bunlarin Orta Anadolu Kristalinine karsi olan jeolojik cercevesi: M.T.A. Bulletin, 60, 22-36.

Vance, D., and Holland, T.J. (1993). A detailed isotopic and petrological study of a single garnet from the Gassetts Schist, Vermont. Contributions to Mineralogy and Petrology, 114, 101-118.

Vennemann, T.W., Muntean, J.L., Kesler, S.E., O'Neil, J.R., Valley, J.W., Russell, N. (1993). Stable isotope evidence for magmatic fluids in the Pueblo Viejo epithermal acid sulfate Au-Ag deposit, Dominican Republic. Economic Geology, 88 (1): 55–71

Vermeesch, P. (2018). IsoplotR: A free and open toolbox for geo- chronology: Geoscience Frontiers, 9, 1479–1493.

Wallace, P. J. (2003). Volatiles in subduction zone magmas: concentrations and fluxes based on melt inclusion and volcanic gas data: Journal of volcanology and geothermal research, 140, 217-240.

Wang, R., Richards, J.P., Hou, Z., Yang, Z. (2014). Extent of underthrusting of the Indian plate beneath Tibet controlled the distribution of Miocene porphyry Cu–Mo ± Au deposits. Mineralium Deposita 49, 165–173.

Webb, A.W., and McDougall N. (1968). The geochronology of the igneous rocks of Eastern Queensland:Australia Jour. Geol. Soc.,v. 15, pt. 2, 313-346

White, N.C., Leake, M.J., McCaughey, S.N., Parris, B.W. (1995). Epithermal deposits of the southwest Pacific: Journal of Geochemical Exploration, 54, 87-136.

Whitney, D., Teyssier, C., Dilek, Y., Fayon, A. (2001). Metamorphism of the Central Anatolian Crystalline Complex, Turkey: influence of orogen-normal collision vs. wrench-dominated tectonics on P–T–t paths: Journal of Metamorphic Geology, 19, 411-432.

Whitney, D.L., Teyssier, C., Fayon, A.K., Hamilton, M.A., Heizler, M. (2003). Tectonic controls on metamorphism, partial melting, and intrusion: timing and duration of regional metamorphism and magmatism in the Niğde Massif, Turkey: Tectonophysics, 376, 7-60.

Wilkinson, J.J. (2013). Triggers for the formation of porphyry ore deposits in magmatic arcs: Nature Geoscience, 6, 917–925.

Winter, J.D. (2001). An introduction to igneous and metamorphic petrology: U.S.R.P. Hall, 796 p.

Yalınız, M.K., Floyd, P.A. and Göncüoğlu, M.C., (1996). Supra-subduction zone ophiolites of Central Anatolia: geochemical evidence from the Sarıkaraman Ophiolite, Aksaray, Turkey: Mineralogical Magazine, 60, 697- 710.

Yalınız, K. and Göncüoğlu, M.C. (1998). General geological characteristics and distribution of Central Anatolian Ophiolites. Hacettepe Üniversitesi Yerbilimleri, 20, 19-30

Yaliniz, M. K., Floyd, P. A., and Göncüoglu, M. C. (2000). Geochemistry of volcanic rocks from the Çiçekdag ophiolite, central Anatolia, Turkey, and their inferred tectonic setting within the northern branch of Neotethyan ocean, in Bozkurt, E., Winchester, J. A., and Piper, J. D. A., eds., Tectonics and magmatism in Turkey and the surrounding area: Geological Society of London, Special Publication, no. 173, 203-218.

Yang, Z.M., Goldfarb R., Chang, Z.S. (2016). Generation of Postcollisional Porphyry Copper Deposits in Southern Tibet Triggered by Subduction of the Indian Continental Plate. In: Richards, Jeremy P., (ed.) Tectonics and Metallogeny of the Tethyan Orogenic Belt. Society of Economic Geologists Special Publication, 19. Society of Economic Geologists, Littleton, CO, USA, 279-300

Yao, Y., Chen, J., Lu, J., and Wang, R., Zhang, R. (2014). Geology and genesis of the Hehuaping magnesian skarn-type cassiterite-sulfide deposit, Hunan Province, Southern China. Ore Geology Reviews, 58, 163–184.

Yetiş, C. (1978). Geology of the (Tamardı-Nigde) region and the characteristics of the Ecemiş Fault Zone between Maden Boğazı and Kamışlı. lstanbul Univ. Fen Fak. Mecmuasi Ser. B 43, 41-61.

Yıldırım, C., Sarıkaya, M.A., and Çiner, A. (2016). Late Pleistocene intraplate extension of the Central Anatolian Plateau, Turkey: Inferences from cosmogenic exposure dating of alluvial fan, landslide and moraine surfaces along the Ecemiş Fault Zone: Tectonics, v. 35, no. 6, 1446–1464

Yıldız,B., Sillitoe, R.H., Foster, R., Hall, D., Stallman, M. (2016). Discovery of the Öksüt Million-Ounce High-Sulfidation Gold Deposit, Turkey. SEG2016 Conferance Tethyan Tecton Metallogeny. Society of Economic Geology.

Yıldız, B., Sillitoe, R.H., Foster, R., Hall, D., and Stallman, M. (2017). Öksüt: A high-sulphidation epithermal gold discovery in Turkey: NewGenGold 2017 Conference Proceedings, West Perth, Paydirt Media Pty Ltd., 273–287.

Yılmaz, Y. (1993). New evidence and model on the evolution of the southeast Anatolian orogen: Geological Society of America Bulletin, 105, 251-271.

Yılmaz, Y., Tüysüz, O., Yiğitbaş, E., Genç, S.C., and Şengör, A.M.C. (1997). Geology and tectonic evolution of the Pontides, in Robinson, A.G., ed., Regional and Petro- leum Geology of the Black Sea and Surrounding Region: American Association of Petroleum Geologists Memoir, 68, 183–266.

Yılmaz, Y., Genç, Ş.C., Karacık, Z., Altunkaynak, Ş. (2001). Two contrasting magmatic associations of NW Anatolia and their tectonic significance. Journal of Geodynamics, 31, 243–271.

Yigit, O. (2009). Mineral deposits of Turkey in relation to tethyan metallogeny: Implications for future mineral exploration. Economic Geology, 104(1), 19–51.

Yiğit, Ö. (2012). Discovered and undiscovered gold endowment of Turkey: a quantitative mineral resource assessment using GIS and rank statistical analysis, Mineralium Deposita, 47, 521–534.

Yurdakul, E., İmer, A., and Cihan, M. (2021). Timing and Nature of Mineralization and Associated Hydrothermal Alteration at the Öksüt High-Sulfidation Epithermal Au-Cu Deposit (Kayseri Province, Central Anatolia). Economic Geology Special Publication, No: 24, v.1, 49-68.

Zhai, D.G., Liu, J.J., Zhang, H.Y., Wang, J.P., Su, L., Yang, X.A., Wu, S.H. (2014). Origin of oscillatory zoned garnets from the Xieertala Fe–Zn skarn deposit, northern China: in situ LA–ICP-MS evidence. Lithos 190, 279–291.

APPENDICES

A. Collected and Studied Drillhole Samples.

Number	Sample Id	Hole Id	From	To	Deposit/Prospect
1	OD79951	ODD073	351,10	351,15	Keltepe
2	OD79952	ODD081	292,90	293,00	Keltepe
3	OD79953	ODD0316	209,95	210,00	Keltepe
4	OD79954	ODD0316	209,65	209,75	Keltepe
5	OD79955	ODD0316	211,60	211,70	Keltepe
6	OD79956	ODD0316	460,60	460,70	Keltepe
7	OD79957	ODD0178	152,10	152,15	Keltepe NW
8	OD79958	ODD0178A	261,90	261,98	Keltepe NW
9	OD79959	ODD0319	134,20	134,35	Yelibelen
10	OD79960	ODD0319	138,40	138,60	Yelibelen
11	OD79961	ODD0319	139,20	139,20	Yelibelen
12	OD79962	ODD0313	234,50	234,70	Keltepe
13	OD79963	ODD0313	235,80	235,85	Keltepe
14	OD79964	ODD0310	296,00	296,10	Keltepe
15	OD79965	ODD0316	180,90	181,00	Keltepe
16	OD79966	ODD0316	181,90	182,00	Keltepe
17	OD79967	ODD0316	211,50	211,60	Keltepe
18	OD79968	ODD0316	15,20	15,30	Keltepe

19	OD79969	ODD0316	27,00	27,10	Keltepe
20	OD79970	ODD0316	24,20	25,20	Keltepe
21	OD79971	ODD0316	31,50	31,60	Keltepe
22	OD79972	ODD0316	45,30	45,40	Keltepe
23	OD79973	ODD0316	60,10	60,20	Keltepe
24	OD79974	ODD0316	54,30	54,40	Keltepe
25	OD79975	ODD0316	69,60	69,80	Keltepe
26	OD79976	ODD0316	76,00	76,10	Keltepe
27	OD79977	ODD0316	85,75	85,85	Keltepe
28	OD79978	ODD0316	94,60	94,70	Keltepe
29	OD79979	ODD0316	93,50	93,60	Keltepe
30	OD79980	ODD0316	98,30	98,50	Keltepe
31	OD79981	ODD0316	97,70	97,80	Keltepe
32	OD79982	ODD0316	99,15	99,30	Keltepe
33	OD79983	ODD0316	104,80	104,90	Keltepe
34	OD79984	ODD0316	111,20	111,40	Keltepe
35	OD79985	ODD0316	116,40	116,45	Keltepe
36	OD79986	ODD0316	117,40	117,50	Keltepe
37	OD79987	ODD0316	117,60	117,70	Keltepe
38	OD79988	ODD0316	121,90	122,00	Keltepe
39	OD79989	ODD0316	131,90	132,15	Keltepe
40	OD79990	ODD0316	142,00	142,10	Keltepe

41	OD79991	ODD0316	143,50	143,60	Keltepe
42	OD79992	ODD0316	146,40	146,50	Keltepe
43	OD79993	ODD0316	150,00	150,10	Keltepe
44	OD79994	ODD0316	157,20	157,30	Keltepe
45	OD79995	ODD0316	159,70	159,80	Keltepe
46	OD79996	ODD0316	164,35	164,45	Keltepe
47	OD79997	ODD0316	165,10	165,30	Keltepe
48	OD79998	ODD0316	169,00	169,10	Keltepe
49	OD79999	ODD0316	169,70	169,80	Keltepe
50	OD80000	ODD0316	181,70	181,85	Keltepe
51	OD79901	ODD0316	182,15	182,25	Keltepe
52	OD79902	ODD0316	183,10	183,20	Keltepe
53	OD79903	ODD0316	188,70	188,80	Keltepe
54	OD79904	ODD0316	191,30	192,40	Keltepe
55	OD79905	ODD0316	205,25	205,30	Keltepe
56	OD79906	ODD0316	205,90	206,00	Keltepe
57	OD79907	ODD0316	211,55	211,60	Keltepe
58	OD79908	ODD0316	218,40	218,45	Keltepe
59	OD79909	ODD0316	233,90	233,95	Keltepe
60	OD79910	ODD0316	246,20	246,30	Keltepe
61	OD79911	ODD0316	250,50	250,60	Keltepe
62	OD79912	ODD0316	251,00	251,10	Keltepe

63	OD79913	ODD0316	254,15	254,25	Keltepe
64	OD79914	ODD0316	254,90	255,00	Keltepe
65	OD79915	ODD0316	258,60	258,80	Keltepe
66	OD79916	ODD0316	263,00	263,20	Keltepe
67	OD79917	ODD0316	267,40	267,50	Keltepe
68	OD79918	ODD0316	268,20	268,40	Keltepe
69	OD79919	ODD0316	272,05	272,20	Keltepe
70	OD79920	ODD0316	278,00	278,15	Keltepe
71	OD79921	ODD0316	289,70	289,80	Keltepe
72	OD79922	ODD0316	295,10	295,25	Keltepe
73	OD79923	ODD0316	296,65	296,75	Keltepe
74	OD79924	ODD0316	297,65	297,80	Keltepe
75	OD79925	ODD0316	306,25	306,40	Keltepe
76	OD79926	ODD0316	308,10	308,17	Keltepe
77	OD79927	ODD0316	312,40	312,50	Keltepe
78	OD79928	ODD0316	312,80	312,85	Keltepe
79	OD79929	ODD0316	316,90	317,05	Keltepe
80	OD79930	ODD0316	323,60	323,80	Keltepe
81	OD79931	ODD0316	326,40	326,60	Keltepe
82	OD79932	ODD0316	327,90	328,10	Keltepe
83	OD79933	ODD0316	328,20	328,40	Keltepe
84	OD79934	ODD0316	328,40	328,60	Keltepe

85	OD79935	ODD0316	333,50	333,65	Keltepe
86	OD79936	ODD0316	334,40	334,50	Keltepe
87	OD79937	ODD0316	353,60	353,70	Keltepe
88	OD79938	ODD0316	358,50	358,60	Keltepe
89	OD79939	ODD0316	359,25	359,35	Keltepe
90	OD79940	ODD0316	360,20	360,27	Keltepe
91	OD79941	ODD0316	363,20	363,25	Keltepe
92	OD79942	ODD0316	367,40	367,50	Keltepe
93	OD79943	ODD0316	371,40	371,48	Keltepe
94	OD79944	ODD0316	371,48	371,58	Keltepe
95	OD79945	ODD0316	373,90	374,00	Keltepe
96	OD79946	ODD0316	382,20	382,40	Keltepe
97	OD79947	ODD0316	382,90	383,00	Keltepe
98	OD79948	ODD0316	383,60	383,70	Keltepe
99	OD79949	ODD0316	386,40	386,55	Keltepe
100	OD79950	ODD0316	387,50	387,60	Keltepe
101	OD79851	ODD0316	394,00	394,25	Keltepe
102	OD79852	ODD0316	398,20	398,30	Keltepe
103	OD79853	ODD0316	399,80	399,90	Keltepe
104	OD79854	ODD0316	402,70	402,80	Keltepe
105	OD79855	ODD0316	407,30	407,50	Keltepe
106	OD79856	ODD0316	413,95	414,05	Keltepe

107	OD79857	ODD0316	416,95	417,00	Keltepe
108	OD79858	ODD0316	417,80	417,90	Keltepe
109	OD79859	ODD0316	420,20	420,30	Keltepe
110	OD79860	ODD0316	420,90	421,05	Keltepe
111	OD79861	ODD0316	430,70	430,80	Keltepe
112	OD79862	ODD0316	438,40	438,60	Keltepe
113	OD79863	ODD0316	445,15	445,25	Keltepe
114	OD79864	ODD0316	453,50	453,70	Keltepe
115	OD79865	ODD0316	457,20	457,30	Keltepe
116	OD79866	ODD0316	460,40	460,48	Keltepe
117	OD79867	ODD0316	214,00	214,05	Keltepe
118	OD79868	ODD0309	344,1	344,2	Keltepe
119	OD79869	ODD0309	344,9	345,00	Keltepe
120	OD79870	ODD0314	56,70	56,80	Keltepe NW
121	OD79871	ODD0315	313,10	313,20	Boztepe
122	OD79872	ODD0012	12,20	12,40	Güneytepe
123	OD79873	ODD0012	33,65	33,80	Güneytepe
124	OD79874	ODD0012	53,20	53,27	Güneytepe
125	OD79875	ODD0012	58,60	58,64	Güneytepe
126	OD79876	ODD0012	73,00	73,10	Güneytepe
127	OD79877	ODD0012	93,35	93,40	Güneytepe
128	OD79878	ODD0012	98,70	98,77	Güneytepe

129	OD79879	ODD0012	115,40	115,46	Güneytepe
130	OD79880	ODD0012	123,05	123,15	Güneytepe
131	OD79881	ODD0012	124,20	124,28	Güneytepe
132	OD79882	ODD0012	129,20	129,30	Güneytepe
133	OD79883	ODD0012	130,65	130,75	Güneytepe
134	OD79884	ODD0012	131,20	131,40	Güneytepe
135	OD79885	ODD0012	139,40	139,50	Güneytepe
136	OD79886	ODD0012	142,50	142,57	Güneytepe
137	OD79887	ODD0012	143,20	143,30	Güneytepe
138	OD79888	ODD0012	144,60	144,75	Güneytepe
139	OD79889	ODD0012	149,00	149,10	Güneytepe
140	OD79890	ODD0012	154,10	154,25	Güneytepe
141	OD79891	ODD0012	155,80	156,00	Güneytepe
142	OD79892	ODD0012	159,50	159,60	Güneytepe
143	OD79893	ODD0319	128,10	128,20	Yelibelen
144	OD79894	ODD0319	135,50	135,60	Yelibelen
145	OD79895	ODD0319	136,00	136,15	Yelibelen
146	OD79896	ODD0033	128,00	128,10	Güneytepe
147	OD79897	ODD0033	131,70	131,80	Güneytepe
148	OD79898	ODD0033	132,30	132,50	Güneytepe
149	OD79899	ODD0210	174,10	174,25	Güneytepe
150	OD79900	ODD0210	177,50	177,70	Güneytepe

151	OD79801	ODD0210	179,50	179,60	Güneytepe
152	OD79802	ODD0210	182,00	182,10	Güneytepe
153	OD79803	ODD0210	183,00	183,10	Güneytepe
154	OD79804	ODD0210	189,70	189,80	Güneytepe
155	OD79805	ODD0313	2,00	2,05	Keltepe
156	OD79806	ODD0313	7,80	7,90	Keltepe
157	OD79807	ODD0313	13,60	13,70	Keltepe
158	OD79808	ODD0313	16,70	16,80	Keltepe
159	OD79809	ODD0313	25,90	26,00	Keltepe
160	OD79810	ODD0313	31,20	31,30	Keltepe
161	OD79811	ODD0313	41,50	41,60	Keltepe
162	OD79812	ODD0313	51,10	51,20	Keltepe
163	OD79813	ODD0313	53,60	53,70	Keltepe
164	OD79814	ODD0313	57,40	57,45	Keltepe
165	OD79815	ODD0313	60,10	60,30	Keltepe
166	OD79816	ODD0313	63,40	63,50	Keltepe
167	OD79817	ODD0313	68,80	68,90	Keltepe
168	OD79818	ODD0313	80,70	80,80	Keltepe
169	OD79819	ODD0313	84,20	84,30	Keltepe
170	OD79820	ODD0313	93,10	93,15	Keltepe
171	OD79821	ODD0313	97,00	97,10	Keltepe
172	OD79822	ODD0313	102,70	102,80	Keltepe

173	OD79823	ODD0313	110,70	110,80	Keltepe
174	OD79824	ODD0313	112,40	112,45	Keltepe
175	OD79825	ODD0313	118,30	118,40	Keltepe
176	OD79826	ODD0313	128,00	128,10	Keltepe
177	OD79827	ODD0313	169,70	169,80	Keltepe
178	OD79828	ODD0313	182,50	182,60	Keltepe
179	OD79829	ODD0313	191,90	192,00	Keltepe
180	OD79830	ODD0313	194,50	194,60	Keltepe
181	OD79831	ODD0313	197,50	197,60	Keltepe
182	OD79832	ODD0313	197,65	197,70	Keltepe
183	OD79833	ODD0313	206,90	206,95	Keltepe
184	OD79834	ODD0313	210,80	210,90	Keltepe
185	OD79835	ODD0313	216,20	216,30	Keltepe
186	OD79836	ODD0313	219,90	220,00	Keltepe
187	OD79837	ODD0313	229,20	229,40	Keltepe
188	OD79838	ODD0313	235,00	235,10	Keltepe
189	OD79839	ODD0313	233,90	234,00	Keltepe
190	OD79840	ODD0313	239,60	239,70	Keltepe
191	OD79841	ODD0313	245,90	246,00	Keltepe
192	OD79842	ODD0313	250,20	250,30	Keltepe
193	OD79843	ODD0313	255,10	255,50	Keltepe
194	OD79844	ODD0313	258,20	259,20	Keltepe

195	OD79845	ODD0316	255,30	255,40	Keltepe
196	OD79846	ODD0333	314,67	314,75	Keltepe
197	OD79847	ODD0333	315,50	315,64	Keltepe
198	OD79848	ODD0333	319,80	319,95	Keltepe
199	OD79849	ODD0333	327,60	327,67	Keltepe
200	OD79850	ODD0333	332,10	332,20	Keltepe
201	OD78851	ODD0315	492,80	492,90	Boztepe
202	OD78852	ODD0315	493,40	493,80	Boztepe
203	OD78853	ODD0337	53,50	53,70	Boztepe West
204	OD78854	ODD0337	62,50	62,70	Boztepe West
205	OD78855	ODD0337	71,40	71,80	Boztepe West
206	OD78856	ODD0337	74,00	74,20	Boztepe West
207	OD78857	ODD0337	77,30	77,60	Boztepe West
208	OD78858	ODD0337	90,40	90,50	Boztepe West
209	OD78859	ODD0337	94,30	94,60	Boztepe West
210	OD78860	ODD0333	383,20	383,70	Keltepe N
211	OD78951	ODD0333	337,20	337,28	Keltepe N
212	OD78952	ODD0333	315,00	315,22	Keltepe N
213	OD78953	ODD0333	329,75	329,90	Keltepe N
214	OD78954	ODD0333	329,90	330,10	Keltepe N
215	OD78955	ODD0333	340,00	340,15	Keltepe N
216	OD78956	ODD0333	343,50	343,60	Keltepe N

217	OD78957	ODD0333	343,90	343,95	Keltepe N
218	OD78958	ODD0333	351,60	351,85	Keltepe N
219	OD78959	ODD0333	352,50	352,55	Keltepe N
220	OD78960	ODD0333	360,00	360,25	Keltepe N
221	OD78961	ODD0333	361,10	361,20	Keltepe N
222	OD78962	ODD0333	369,80	370,00	Keltepe N
223	OD78963	ODD0333	370,40	370,50	Keltepe N
224	OD78964	ODD0333	372,00	372,10	Keltepe N
225	OD78965	ODD0333	376,20	376,70	Keltepe N
226	OD78966	ODD0333	377,30	377,60	Keltepe N
227	OD78967	ODD0333	395,90	396,00	Keltepe N
228	OD78968	ODD0315	34,10	34,25	Boztepe
229	OD78969	ODD0315	42,60	42,80	Boztepe
230	OD78970	ODD0315	104,50	104,80	Boztepe
231	OD78971	ODD0315	106,50	106,60	Boztepe
232	OD78972	ODD0315	116,00	116,15	Boztepe
233	OD78973	ODD0315	116,35	116,45	Boztepe
234	OD78974	ODD0315	114,00	114,15	Boztepe
235	OD78975	ODD0315	117,00	117,20	Boztepe
236	OD78976	ODD0315	118,40	118,60	Boztepe
237	OD78977	ODD0315	134,50	134,60	Boztepe
238	OD78978	ODD0315	135,50	135,60	Boztepe

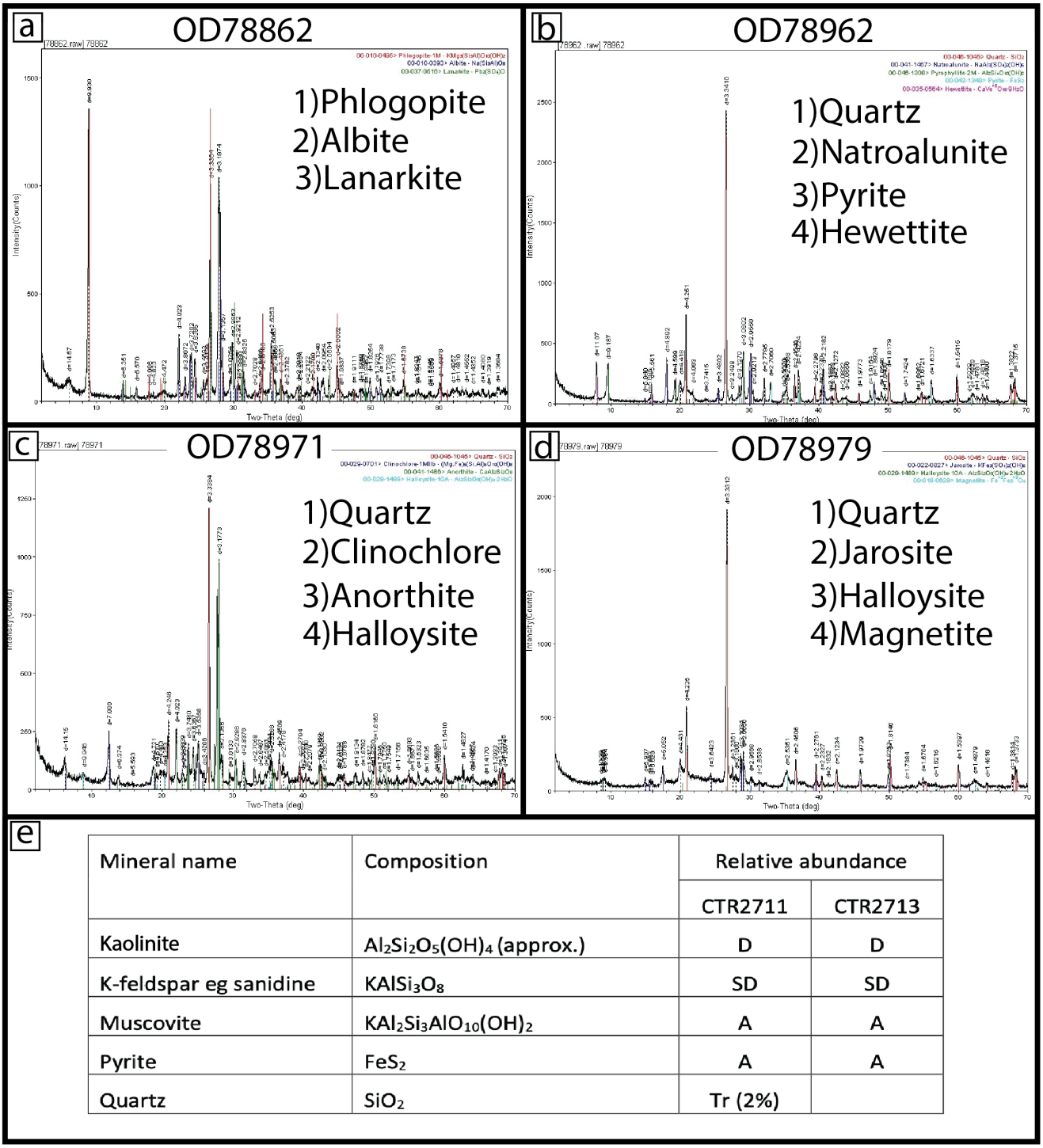
239	OD78979	ODD0315	139,90	140,20	Boztepe
240	OD78980	ODD0315	155,00	155,30	Boztepe
241	OD78981	ODD0315	157,20	157,50	Boztepe
242	OD78982	ODD0315	171,80	172,00	Boztepe
243	OD78983	ODD0315	171,50	171,60	Boztepe
244	OD78984	ODD0315	181,40	181,50	Boztepe
245	OD78985	ODD0315	221,00	221,10	Boztepe
246	OD78986	ODD0315	220,00	220,10	Boztepe
247	OD78987	ODD0315	253,20	253,40	Boztepe
248	OD78988	ODD0315	254,80	255,00	Boztepe
249	OD78989	ODD0315	255,60	255,80	Boztepe
250	OD78990	ODD0315	277,50	277,70	Boztepe
251	OD78991	ODD0315	277,70	277,80	Boztepe
252	OD78992	ODD0315	281,70	282,20	Boztepe
253	OD78993	ODD0315	289,90	290,10	Boztepe
254	OD78994	ODD0315	290,50	290,70	Boztepe
255	OD78995	ODD0315	290,20	290,30	Boztepe
256	OD78996	ODD0315	302,70	303,20	Boztepe
257	OD78997	ODD0315	309,80	309,90	Boztepe
258	OD78998	ODD0315	315,50	315,60	Boztepe
259	OD78999	ODD0315	355,40	355,65	Boztepe
260	OD79000	ODD0315	391,10	391,50	Boztepe

261	OD78861	ODD0337	703,00	703.60	Boztepe West
262	OD78862	ODD0337	708.40	709.80	Boztepe West
263	OD78863	ODD0337	706.30	706.60	Boztepe West
264	CTR2711	ODD0399	33.49	33.64	Güneytepe
265	CTR2713	ODD0399	36.29	36.44	Güneytepe

B. XRD Sample List

Sample ID	Hole Id	From	To	XRD Minerals
OD78862	ODD0337	708.40	709.80	Phologobite-albite-lanarkite-nacrite
OD78962	ODD0333	369.80	370.00	Quartz-natroalunite-pyrophyllite-pyrite-hecrettite
OD78971	ODD0315	106.50	106.60	Quartz-clinochlore-anorthite-hallosyte
OD78979	ODD0315	139.90	140.20	Quartz-jarosite-halloysite-magnetite
CTR2711	ODD0399	33.49	33.64	Kaolinite-K-feldspar-muscovite-pyrite-quartz
CTR2713	ODD0399	36.29	36.44	Kaolinite-K-feldspar-muscovite-pyrite-quartz

C. XRD Analysis Results



e

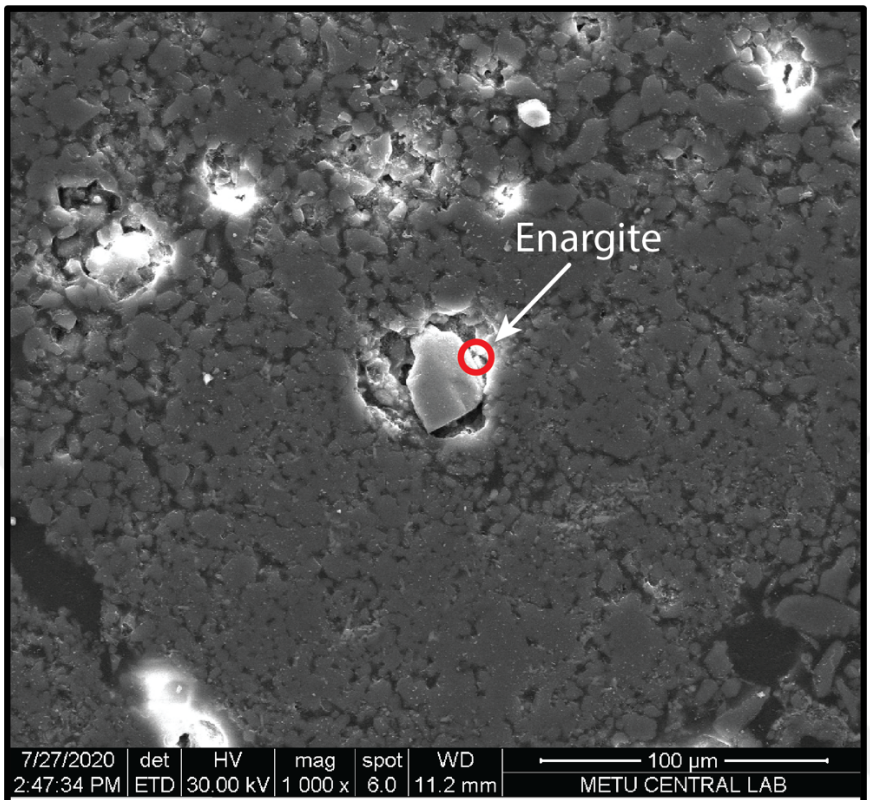
Mineral name	Composition	Relative abundance	
		CTR2711	CTR2713
Kaolinite	$Al_2Si_2O_5(OH)_4$ (approx.)	D	D
K-feldspar eg sanidine	$KAlSi_3O_8$	SD	SD
Muscovite	$KAl_2Si_3AlO_{10}(OH)_2$	A	A
Pyrite	FeS_2	A	A
Quartz	SiO_2	Tr (2%)	

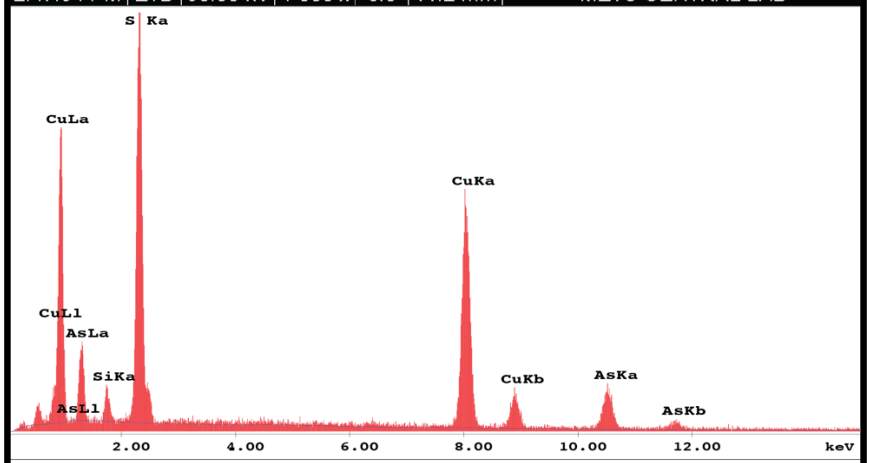
Numbered minerals are the most abundant ones in analysis in (a), (b), (c) and (d), and plots of two tetha(x axis) vs intensity(y axis) data of samples OD78862-78962-78971-78979, (e) analysis results of the samples CTR2711 and CTR2713. Abbreviations: D = Dominant, SD = Subdominant, A = Accessory, Tr = Trace.

D. Samples of SEM-EDX Analyzed Samples and Assay Results

SEM Id	Sample Id	Hole ID	Pit Location	From(m)	To(m)	Au gpt	Cu ppm	As ppm
1	79832	ODD0313	Keltepe	197,65	197,7	7,65	167	100
2	79899	ODD0210	Güneytepe	174,1	174,25	0,62	2826	230
3	79948	ODD0316	Keltepe	383,6	383,7	0,03	1502	510
4	79838	ODD0313	Keltepe	235	235,1	2,81	42600	865
5	79955	ODD0316	Keltepe	211,6	211,7	2,69	74900	2580
6	79845	ODD0316	Keltepe	255,3	255,4	0,53	57500	10001
7	79929	ODD0316	Keltepe	316,9	317,05	1,19	488	506

E. SEM and EDX Analysis Results of Sample OD79832



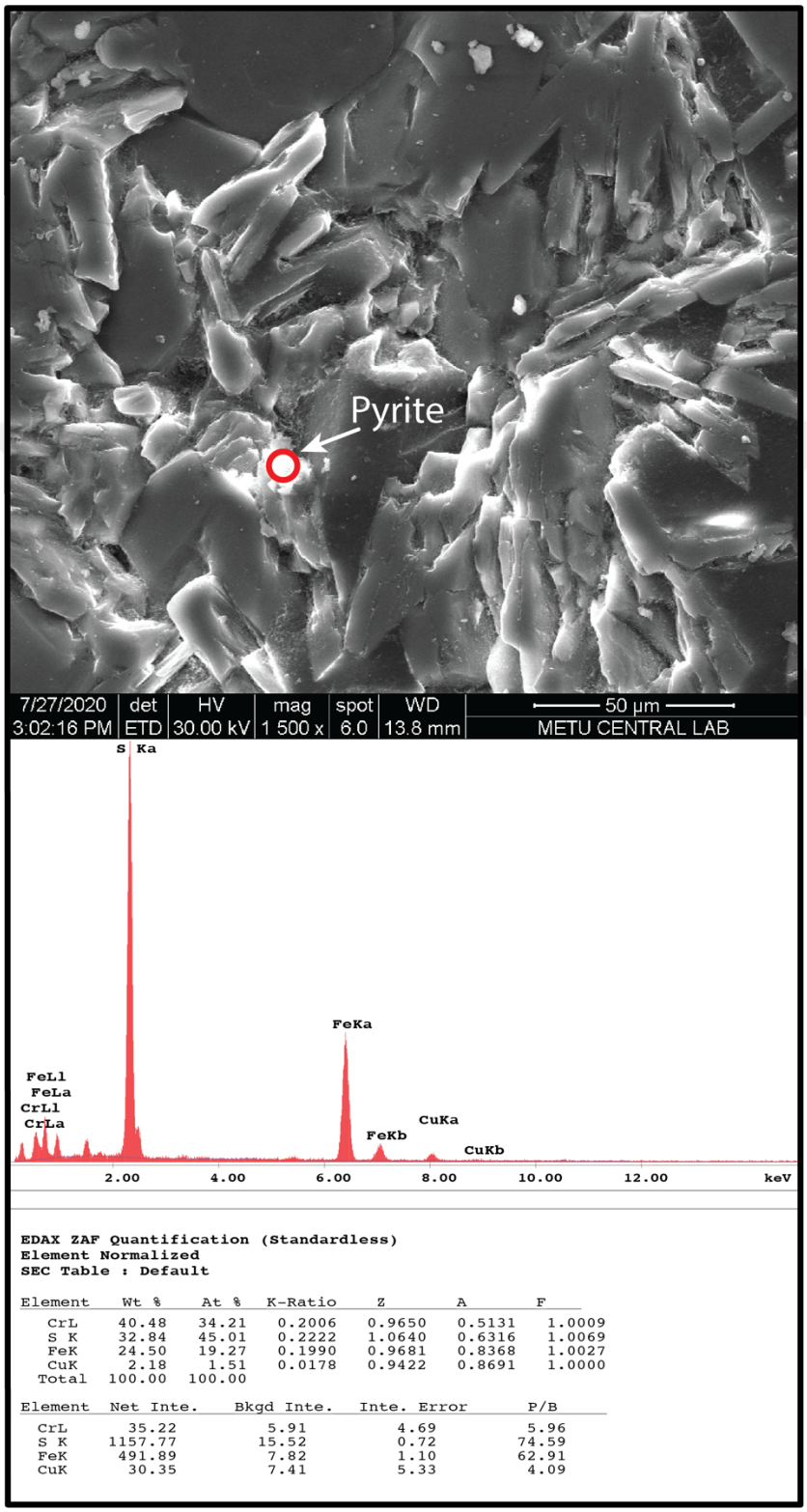


EDAX ZAF Quantification (Standardless)
Element Normalized
SEC Table : Default

Element	Wt %	At %	K-Ratio	Z	A	F
SiK	4.05	6.68	0.0122	1.0809	0.2769	1.0092
S K	35.52	51.28	0.1745	1.0737	0.4576	1.0000
CuK	42.51	30.97	0.4096	0.9527	0.9825	1.0295
AsK	17.92	11.07	0.1540	0.9099	0.9445	1.0000
Total	100.00	100.00				

Element	Net Inte.	Bkgd Inte.	Inte. Error	P/B
SiK	87.32	34.49	4.88	2.53
S K	1170.58	29.84	1.02	39.23
CuK	897.47	16.72	1.16	53.67
AsK	183.93	11.03	2.66	16.67

F. SEM and EDX Analysis Results of Sample OD79899

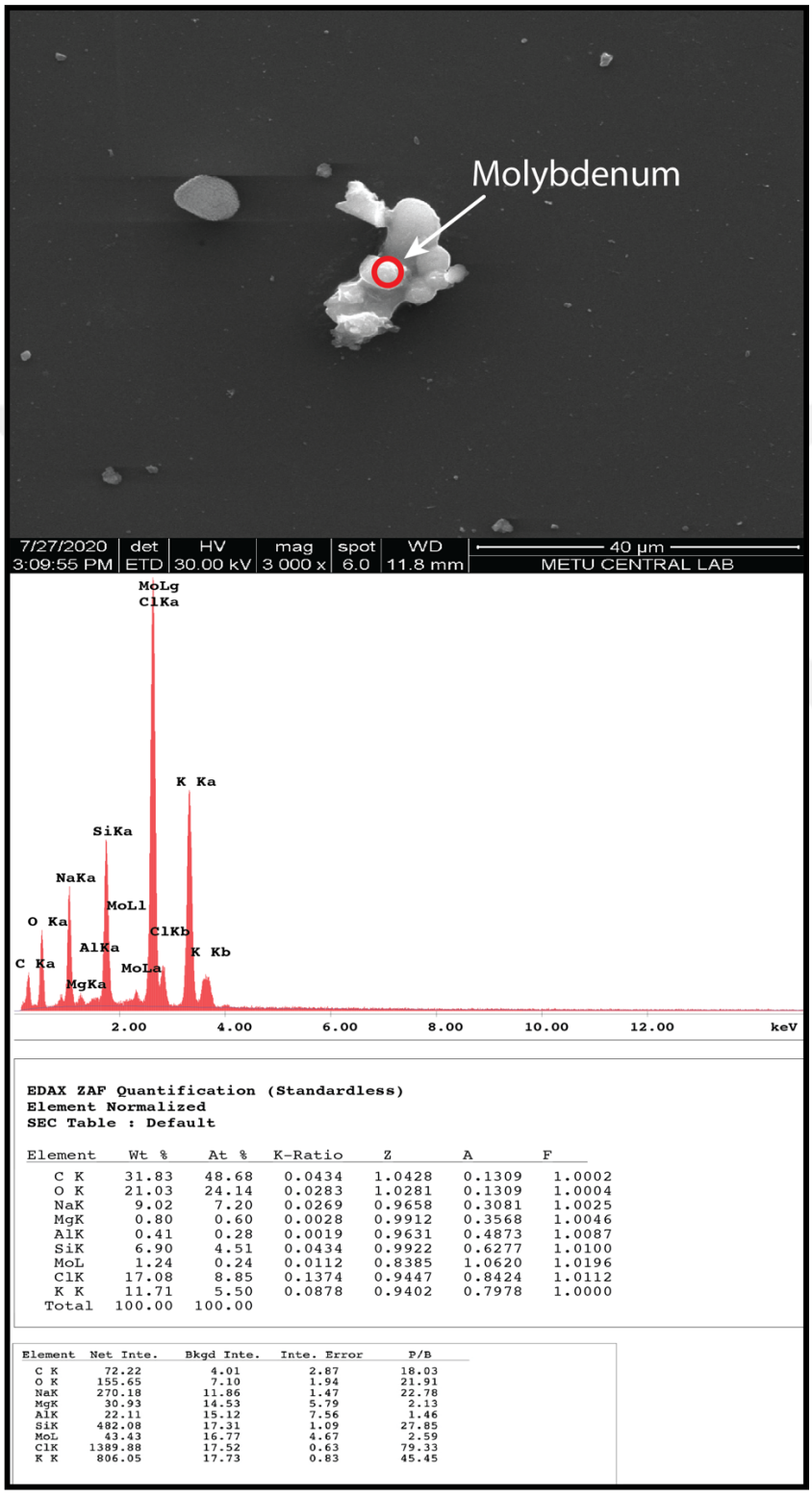


EDAX ZAF Quantification (Standardless)
Element Normalized
SEC Table : Default

Element	Wt %	At %	K-Ratio	Z	A	F
CrL	40.48	34.21	0.2006	0.9650	0.5131	1.0009
S K	32.84	45.01	0.2222	1.0640	0.6316	1.0069
FeK	24.50	19.27	0.1990	0.9681	0.8368	1.0027
CuK	2.18	1.51	0.0178	0.9422	0.8691	1.0000
Total	100.00	100.00				

Element	Net Inte.	Bkgd Inte.	Inte. Error	P/B
CrL	35.22	5.91	4.69	5.96
S K	1157.77	15.52	0.72	74.59
FeK	491.89	7.82	1.10	62.91
CuK	30.35	7.41	5.33	4.09

G. SEM and EDX Analysis Results of Sample OD79948

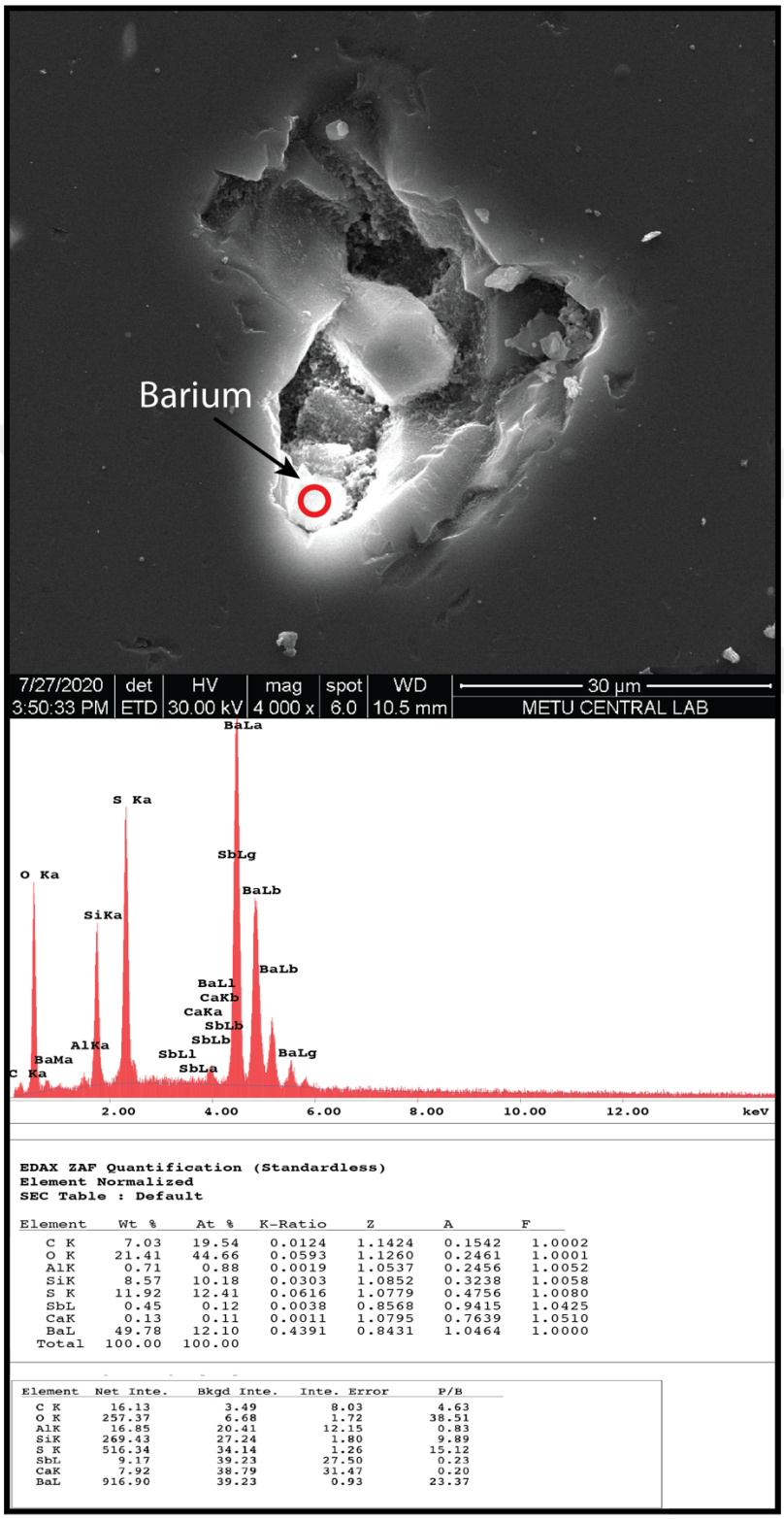


EDAX ZAF Quantification (Standardless)
Element Normalized
SEC Table : Default

Element	Wt %	At %	K-Ratio	Z	A	F
C K	31.83	48.68	0.0434	1.0428	0.1309	1.0002
O K	21.03	24.14	0.0283	1.0281	0.1309	1.0004
NaK	9.02	7.20	0.0269	0.9658	0.3081	1.0025
MgK	0.80	0.60	0.0028	0.9912	0.3568	1.0046
AlK	0.41	0.28	0.0019	0.9631	0.4873	1.0087
SiK	6.90	4.51	0.0434	0.9922	0.6277	1.0100
MoL	1.24	0.24	0.0112	0.8385	1.0620	1.0196
ClK	17.08	8.85	0.1374	0.9447	0.8424	1.0112
K K	11.71	5.50	0.0878	0.9402	0.7978	1.0000
Total	100.00	100.00				

Element	Net Inte.	Bkgd Inte.	Inte. Error	P/B
C K	72.22	4.01	2.87	18.03
O K	155.65	7.10	1.94	21.91
NaK	270.18	11.86	1.47	22.78
MgK	30.93	14.53	5.79	2.13
AlK	22.11	15.12	7.56	1.46
SiK	482.08	17.31	1.09	27.85
MoL	43.43	16.77	4.67	2.59
ClK	1389.88	17.52	0.63	79.33
K K	806.05	17.73	0.83	45.45

H. SEM and EDX Analysis Results of Sample OD79838

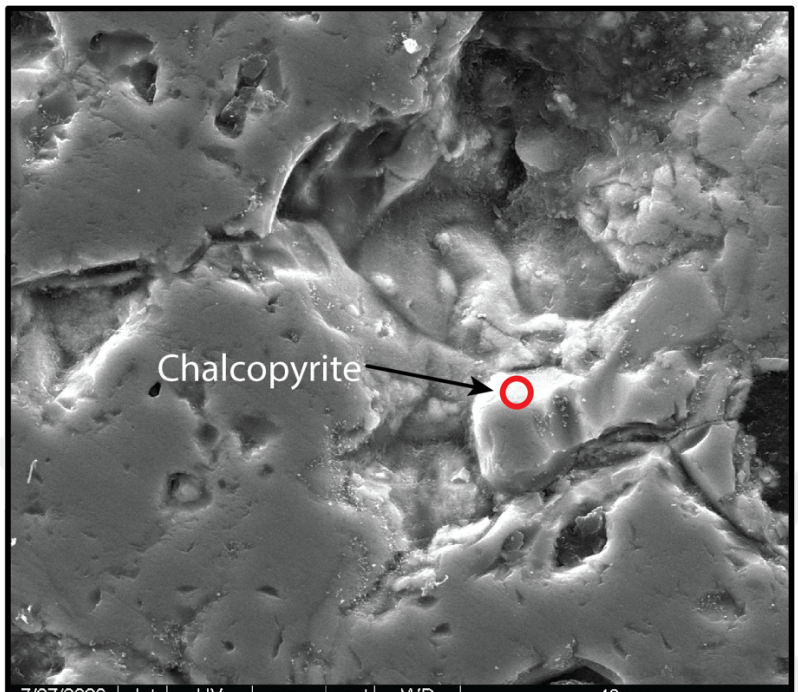


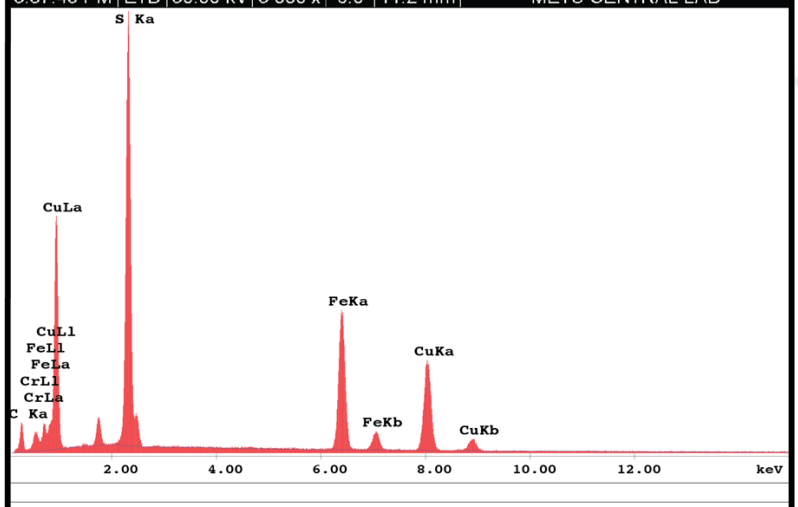
EDAX ZAF Quantification (Standardless)
Element Normalized
SEC Table : Default

Element	Wt %	At %	K-Ratio	Z	A	F
C K	7.03	19.54	0.0124	1.1424	0.1542	1.0002
O K	21.41	44.66	0.0593	1.1260	0.2461	1.0001
AlK	0.71	0.88	0.0019	1.0537	0.2456	1.0052
SiK	8.57	10.18	0.0303	1.0852	0.3238	1.0058
S K	11.92	12.41	0.0616	1.0779	0.4756	1.0080
SbL	0.45	0.12	0.0038	0.8568	0.9415	1.0425
CaK	0.13	0.11	0.0011	1.0795	0.7639	1.0510
BaL	49.78	12.10	0.4391	0.8431	1.0464	1.0000
Total	100.00	100.00				

Element	Net Inte.	Bkgd Inte.	Inte. Error	P/B
C K	16.13	3.49	8.03	4.63
O K	257.37	6.68	1.72	38.51
AlK	16.85	20.41	12.15	0.83
SiK	269.43	27.24	1.80	9.89
S K	516.34	34.14	1.26	15.12
SbL	9.17	39.23	27.50	0.23
CaK	7.92	38.79	31.47	0.20
BaL	916.90	39.23	0.93	23.37

I. SEM and EDX Analysis Results of Sample OD79955



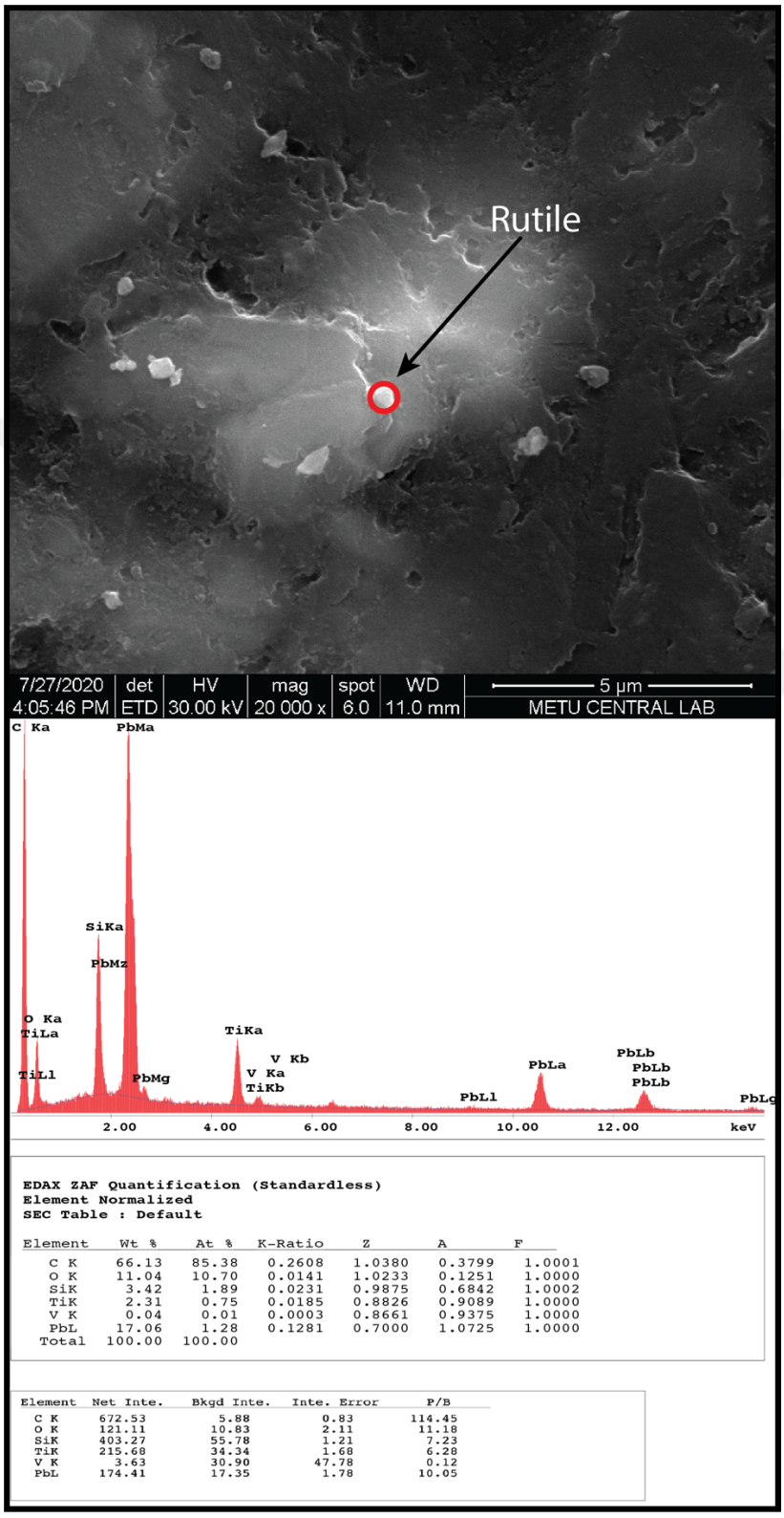


EDAX ZAF Quantification (Standardless)
Element Normalized
SEC Table : Default

Element	Wt %	At %	K-Ratio	Z	A	F
C K	26.33	58.18	0.0366	1.0947	0.1268	1.0002
CrL	23.85	12.17	0.0962	0.9372	0.4301	1.0009
S K	19.46	16.11	0.1307	1.0340	0.6462	1.0047
FeK	14.90	7.08	0.1303	0.9383	0.9082	1.0269
CuK	15.46	6.46	0.1310	0.9125	0.9284	1.0000
Total	100.00	100.00				

Element	Net Inte.	Bkgd Inte.	Inte. Error	P/B
C K	81.29	3.22	1.85	25.22
CrL	45.81	7.63	2.74	6.00
S K	1868.24	39.05	0.38	47.85
FeK	886.78	26.46	0.56	33.51
CuK	613.38	21.74	0.67	28.21

J. SEM and EDX Analysis Results of Sample OD79845

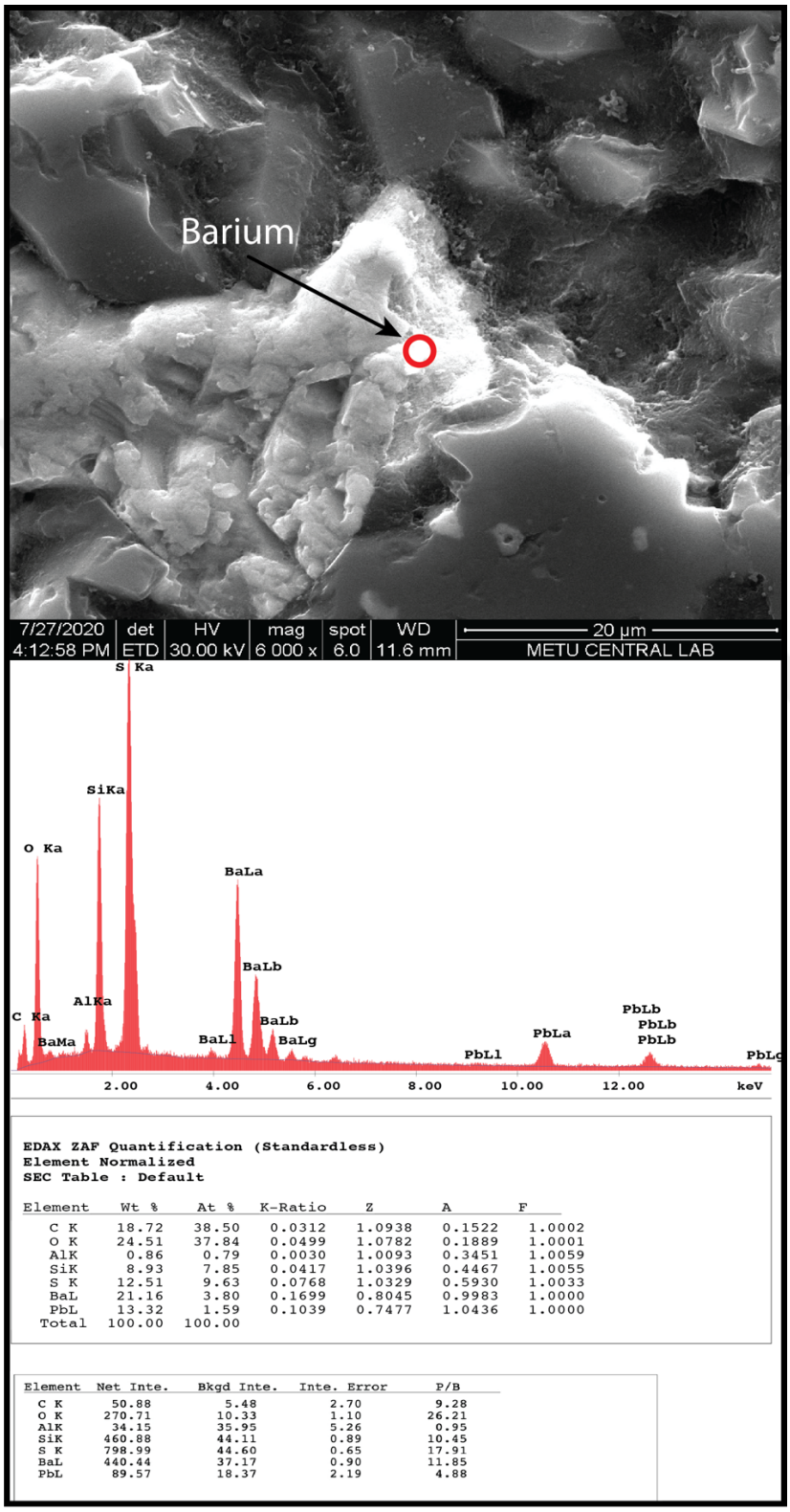


EDAX ZAF Quantification (Standardless)
Element Normalized
SEC Table : Default

Element	Wt %	At %	K-Ratio	Z	A	F
C K	66.13	85.38	0.2608	1.0380	0.3799	1.0001
O K	11.04	10.70	0.0141	1.0233	0.1251	1.0000
SiK	3.42	1.89	0.0231	0.9875	0.6842	1.0002
TiK	2.31	0.75	0.0185	0.8826	0.9089	1.0000
V K	0.04	0.01	0.0003	0.8661	0.9375	1.0000
PbL	17.06	1.28	0.1281	0.7000	1.0725	1.0000
Total	100.00	100.00				

Element	Net Inte.	Bkgd Inte.	Inte. Error	P/B
C K	672.53	5.88	0.83	114.45
O K	121.11	10.83	2.11	11.18
SiK	403.27	55.78	1.21	7.23
TiK	215.68	34.34	1.68	6.28
V K	3.63	30.90	47.78	0.12
PbL	174.41	17.35	1.78	10.05

K. SEM and EDX Analysis Results of Sample OD79929

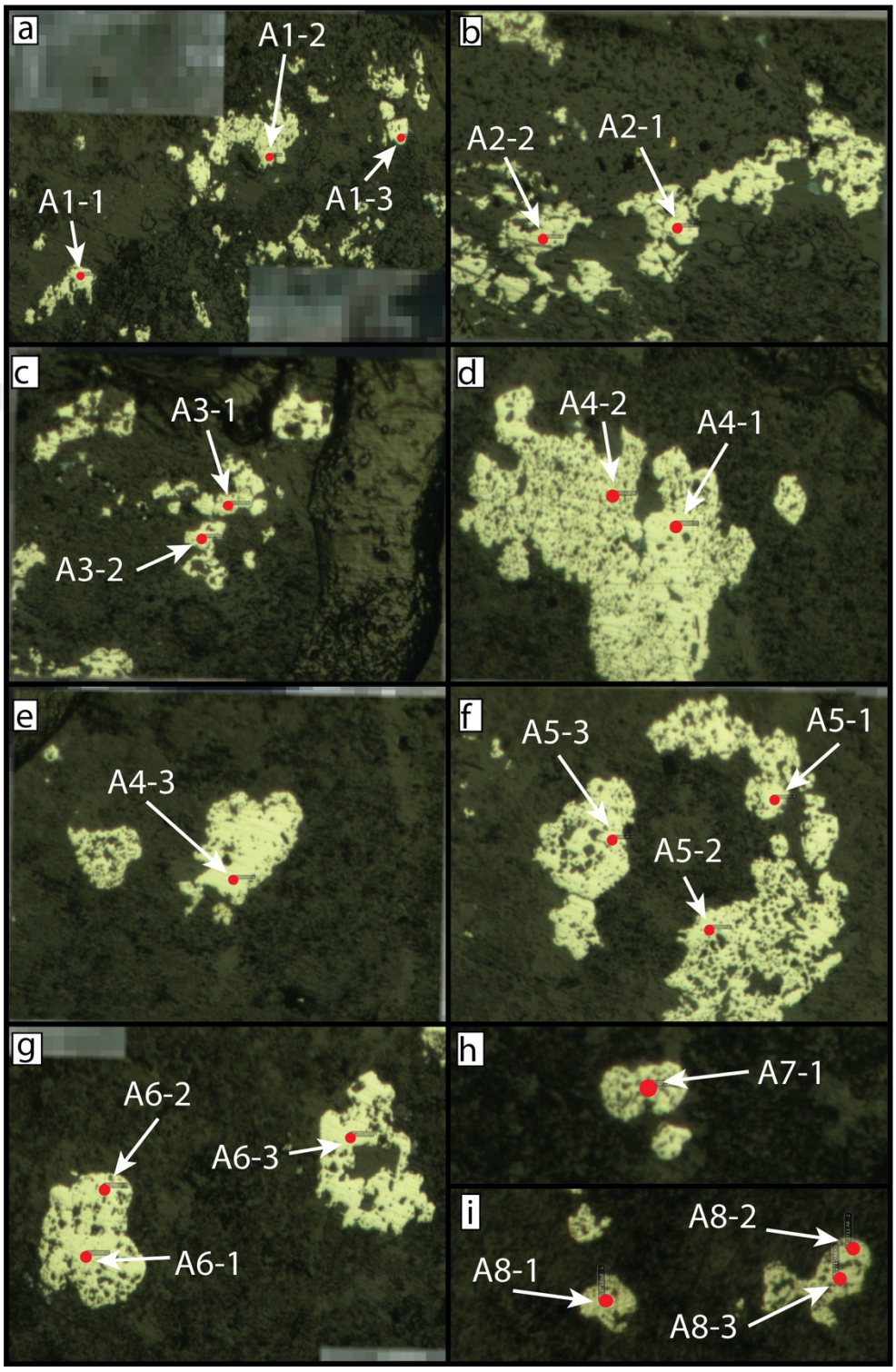


EDAX ZAF Quantification (Standardless)
Element Normalized
SEC Table : Default

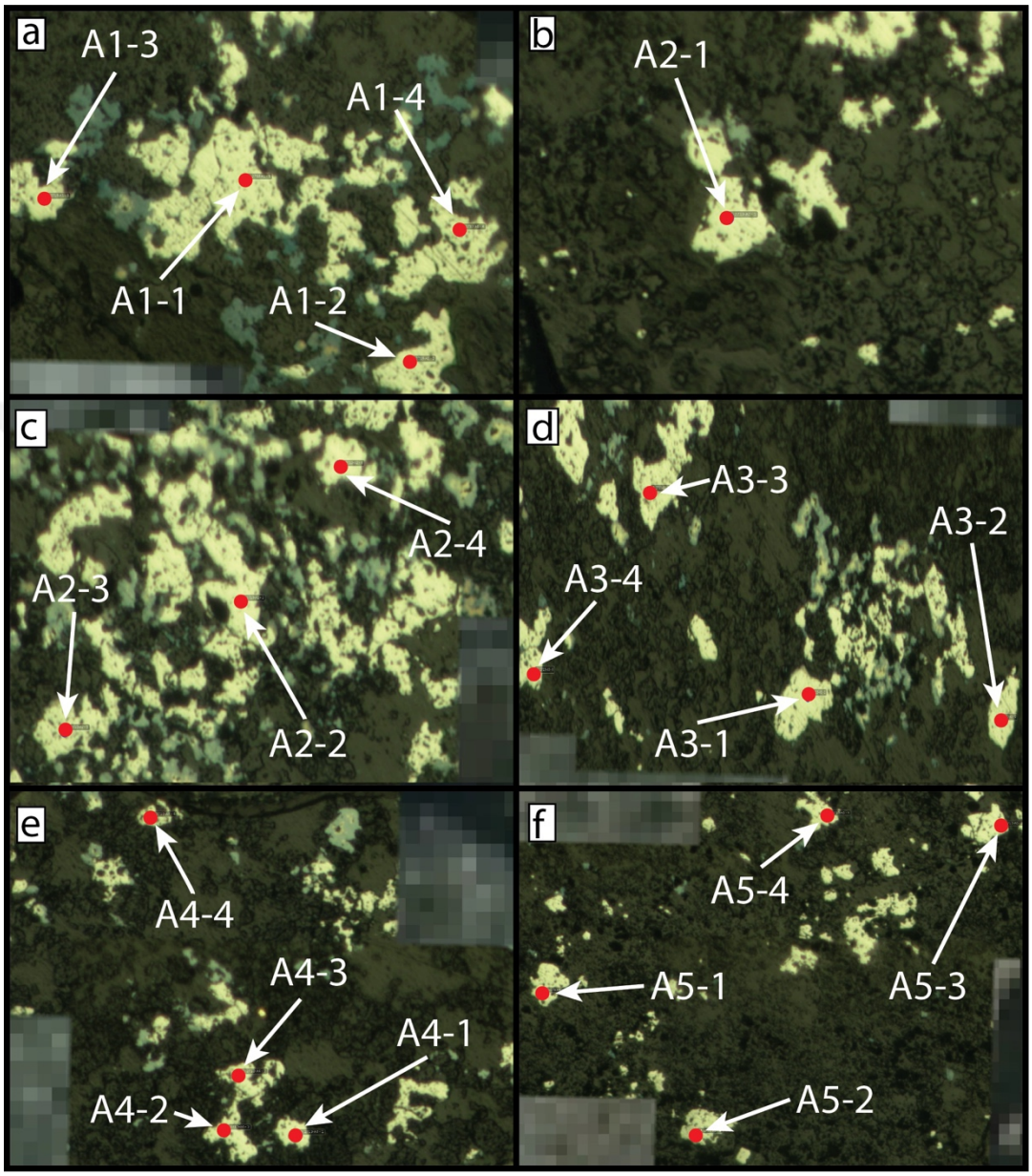
Element	Wt %	At %	K-Ratio	Z	A	F
C K	18.72	38.50	0.0312	1.0938	0.1522	1.0002
O K	24.51	37.84	0.0499	1.0782	0.1889	1.0001
AlK	0.86	0.79	0.0030	1.0093	0.3451	1.0059
SiK	8.93	7.85	0.0417	1.0396	0.4467	1.0055
S K	12.51	9.63	0.0768	1.0329	0.5930	1.0033
BaL	21.16	3.80	0.1699	0.8045	0.9983	1.0000
PbL	13.32	1.59	0.1039	0.7477	1.0436	1.0000
Total	100.00	100.00				

Element	Net Inte.	Bkgd Inte.	Inte. Error	P/B
C K	50.88	5.48	2.70	9.28
O K	270.71	10.33	1.10	26.21
AlK	34.15	35.95	5.26	0.95
SiK	460.88	44.11	0.89	10.45
S K	798.99	44.60	0.65	17.91
BaL	440.44	37.17	0.90	11.85
PbL	89.57	18.37	2.19	4.88

L. LA-ICP-MS Analysis Spots in Pyrites of Sample CTR2711



M. LA-ICP-MS Analysis Spots in Pyrites of Sample CTC2713



N. Samples CTR2711 and CTR2713 Pyrites LA-ICP-MS Analysis Results in PPM

Analysis	Comment	27Al	34S	39K	43Ca	47Ti	55Mn
2711-A1 - 1	small Au?	2913.70	5142523.69	952.34	<2063.639	25997.52	13.04
2711-A1 - 2	short, flat Au	356.66	4700081.67	356.66	<1971.512	2208.79	12.26
2711-A1 - 3	short	14643.02	5006431.38	6436.71	<2031.102	1997.46	17.88
2711-A2 - 1	clean	92.85	5460087.31	58.27	<1907.713	310.81	3.97
2711-A2 - 2	large Au inc	6555.57	4821274.97	3991.70	<1740.091	18426.33	100.26
2711-A3 - 1	flat Au	28132.85	5458754.75	11580.49	<2159.088	30302.43	140.02
2711-A3 - 2	large Au incs	3099.47	5892700.10	1598.41	<2231.779	1300.44	45.59
2711-A4 - 1	Bi-As-Pb-Au inc?	28003.30	4973989.63	13485.68	<1887.655	1133.23	43.99
2711-A4 - 2	small Au?	13420.74	4582746.82	5977.45	<1621.509	1738.14	55.40
2711-A4 - 3	Cu, clean	<3.082	4685211.36	<14.303	<1456.638	7.58	<1.711
2711-A5 - 1	clean	493.48	5188010.28	283.22	<1883.809	8.30	<2.314
2711-A5 - 2	clean	77792.68	5708810.39	68647.10	<2233.862	124.42	86.89
2711-A5 - 3	small Au?	108638.51	5614027.73	81199.88	4566.07	107.35	96.77
2711-A6 - 1	small Au incs, poss. zonation?	<3.494	5168911.62	<21.155	<1691.565	11.86	2.65
2711-A6 - 2	flat Au	61320.10	5486872.82	5900.80	5923.86	27.82	11.12
2711-A6 - 3	flat Au	20071.43	4966166.71	2860.34	<1866.902	139.43	8.85
2711-A7 - 1	small Au?	83178.37	4934614.62	22441.44	5719.26	4561.12	68.63
2711-A8 - 1	clean, short	909.77	5198100.05	864.34	<1647.572	62.23	11.66
2711-A8 - 2	short	357.38	5268138.13	39.37	440743.42	10.63	5.98
2711-A8 - 3	small Au	29196.35	5412779.14	22072.21	2017.12	3800.01	92.27
2713-A1 - 1	flat Au, poss. incs	1681.02	5596350.04	1074.16	<1687.139	22353.12	243.92
2713-A1 - 2	flat Au with incs	9275.29	5794829.79	4720.63	<1880.485	50583.85	61.16
2713-A1 - 3	Pb-Au incs?	1755.91	5449711.46	2079.29	<1446.066	372.19	24.51
2713-A1 - 4	Au incs	14859.52	5411611.95	12648.15	<1643.116	14.27	6.34
2713-A2 - 1		15624.18	5204559.88	3350.94	<1592.763	34.42	453.96
2713-A2 - 2	Au incs	27162.63	5500221.10	14699.23	<1537.437	225.53	30.72
2713-A2 - 3	Au incs	25461.24	5364951.91	12407.58	1903.51	22082.34	35.27
2713-A2 - 4	flat Au?	743.76	5433574.82	263.60	<1367.146	3679.51	17.16
2713-A3 - 1	flat Au & small incs	5321.35	5389594.25	1883.71	<1394.850	15642.06	32.73
2713-A3 - 2	flat Au, zonation?	118.90	5678240.15	37.60	<1401.144	196.98	41.80
2713-A3 - 3	Au incs	11135.02	6485147.76	5488.34	<1591.530	6376.05	12.05
2713-A3 - 4	Au incs	2641.49	5451367.03	1643.44	<1350.444	8301.76	41.39
2713-A4 - 1	short, Au incs	14133.44	4956086.25	10007.94	<1391.481	159.30	2.18
2713-A4 - 2	short, flat Au?	61815.57	4992330.31	32152.35	<1506.458	3028.67	34.83
2713-A4 - 3	short, Au incs, Au in Cu-phase	9179.64	4407544.75	920.94	<1187.839	781.81	6.03
2713-A4 - 4	short, Au incs, Au in Cu-phase	18921.37	5401835.87	4753.01	<1388.931	98.62	7.38
2713-A5 - 1	flat Au?	11542.03	4964920.77	7403.27	1351.80	39.90	214.68
2713-A5 - 2	flat Au?	42211.81	5546261.18	22568.86	<1493.420	35290.17	695.59
2713-A5 - 3	flat Au?	2129.45	4858910.68	1389.26	<1134.985	3377.69	77.14
2713-A5 - 4	flat Au	24386.80	5759902.21	11803.25	<1298.527	16634.86	166.60
	AVERAGE	20507.28	5282954.63	10527.42	66032.15	7038.73	79.54
	MINIMUM	92.85	4407544.75	37.60	1351.80	7.58	2.18
	MAXIMUM	108638.51	6485147.76	81199.88	440743.42	50583.85	695.59
	ST.DEV.	25952.22	402074.26	17250.09	165242.86	11831.65	134.52

cont...

Analysis	Comment	57Fe	59Co	60Ni	65Cu	66Zn	75As
2711-A1 - 1	small Au?	4650000.00	2064.82	2551.25	4893.44	<14.628	17.55
2711-A1 - 2	short, flat Au	4650000.00	1533.44	488.69	120.12	<14.251	35.13
2711-A1 - 3	short	4650000.00	331.83	345.19	600.95	15.58	9.46
2711-A2 - 1	clean	4650000.00	307.23	276.69	<9.358	<14.820	6.57
2711-A2 - 2	large Au inc	4650000.00	1183.79	800.72	10157.57	54.78	25.45
2711-A3 - 1	flat Au	4650000.00	2500.48	3510.15	79841.48	256.94	218.95
2711-A3 - 2	large Au incs	4650000.00	810.62	1139.56	430039.65	323.08	36.51
2711-A4 - 1	Bi-As-Pb-Au inc?	4650000.00	2267.42	1280.80	4933.85	48.89	1475.16
2711-A4 - 2	small Au?	4650000.00	2027.17	831.67	8065.31	35.42	20.11
2711-A4 - 3	Cu, clean	4650000.00	232.07	349.09	1780.23	<12.496	158.02
2711-A5 - 1	clean	4650000.00	616.24	518.76	505.78	36.53	8.77
2711-A5 - 2	clean	4650000.00	3267.96	5389.82	314.14	66.93	19.83
2711-A5 - 3	small Au?	4650000.00	3221.06	5187.04	21665.54	94.65	36.17
2711-A6 - 1	small Au incs, poss. zonation?	4650000.00	61.42	59.14	459.91	<17.102	6.94
2711-A6 - 2	flat Au	4650000.00	545.52	535.72	4573.38	32.99	30.22
2711-A6 - 3	flat Au	4650000.00	270.27	194.65	1300.69	<13.422	11.84
2711-A7 - 1	small Au?	4650000.00	2035.39	925.55	1648.48	26.78	375.92
2711-A8 - 1	clean, short	4650000.00	472.32	591.45	35.31	<19.745	4.76
2711-A8 - 2	short	4650000.00	1138.00	1289.96	4620.12	<24.634	23.74
2711-A8 - 3	small Au	4650000.00	68.58	46.15	188.44	<18.226	18.58
2713-A1 - 1	flat Au, poss. incs	4650000.00	9924.87	6037.61	25833.51	437.22	443.00
2713-A1 - 2	flat Au with incs	4650000.00	134.21	432.51	269911.84	81.60	52.25
2713-A1 - 3	Pb-Au incs?	4650000.00	35.44	179.88	33778.53	<15.585	16.07
2713-A1 - 4	Au incs	4650000.00	42.39	141.63	107107.29	46.09	9.49
2713-A2 - 1		4650000.00	125.68	41.43	407.16	62.10	9.73
2713-A2 - 2	Au incs	4650000.00	68.91	625.19	38569.77	41.77	9.52
2713-A2 - 3	Au incs	4650000.00	302.34	747.53	272134.78	29.85	309.21
2713-A2 - 4	flat Au?	4650000.00	3323.32	2636.89	1986.84	39.05	31.48
2713-A3 - 1	flat Au & small incs	4650000.00	1698.47	1288.53	24109.06	58.75	21.54
2713-A3 - 2	flat Au, zonation?	4650000.00	1372.38	2626.58	5260.98	32.35	17.84
2713-A3 - 3	Au incs	4650000.00	37.15	174.58	200046.23	39.85	32.95
2713-A3 - 4	Au incs	4650000.00	3827.13	5605.89	9649.90	37.91	129.73
2713-A4 - 1	short, Au incs	4650000.00	4262.36	3274.54	123565.01	<17.963	207.92
2713-A4 - 2	short, flat Au?	4650000.00	5333.21	3923.66	251176.38	<19.941	93.81
2713-A4 - 3	short, Au incs, Au in Cu-phase	4650000.00	68.69	70.08	95505.61	23.26	13.83
2713-A4 - 4	short, Au incs, Au in Cu-phase	4650000.00	155.66	198.33	154801.99	23.28	14.39
2713-A5 - 1	flat Au?	4650000.00	1454.59	346.45	406.80	71.03	134.71
2713-A5 - 2	flat Au?	4650000.00	3585.22	1719.72	4323.30	3110.45	114.06
2713-A5 - 3	flat Au?	4650000.00	1752.81	3559.02	793.19	21.33	17737.78
2713-A5 - 4	flat Au	4650000.00	3508.79	3288.40	4820.23	166.60	5196.99
	AVERAGE	4650000.00	1649.23	1580.76	56408.53	189.82	678.40
	MINIMUM	4650000.00	35.44	41.43	35.31	15.58	4.76
	MAXIMUM	4650000.00	9924.87	6037.61	430039.65	3110.45	17737.78
	ST.DEV.	0.00	1955.93	1757.50	100241.61	580.86	2891.30

cont...

Analysis	Comment	77Se	90Zr	95Mo	107Ag	111Cd	118Sn	121Sb
2711-A1 - 1	small Au?	178.95	2.08	9.08	<0.803	<0.352	25.78	1.17
2711-A1 - 2	short, flat Au	324.61	0.15	1.03	<0.667	0.34	4.34	1.24
2711-A1 - 3	short	141.98	0.15	1.98	<0.755	<0.518	6.57	<0.990
2711-A2 - 1	clean	201.15	<0.041	0.14	<0.723	<0.414	1.07	<0.879
2711-A2 - 2	large Au inc	215.65	1.95	5.67	3.42	0.37	20.96	1.46
2711-A3 - 1	flat Au	86.78	1.53	11.31	4.83	20.46	32.88	6.76
2711-A3 - 2	large Au incs	377.29	1.02	0.23	170.95	2.79	5.26	2.27
2711-A4 - 1	Bi-As-Pb-Au inc?	235.95	0.03	1.86	<0.746	<0.483	0.94	<0.911
2711-A4 - 2	small Au?	105.47	0.48	2.72	<0.703	<0.405	1.49	1.30
2711-A4 - 3	Cu, clean	181.48	<0.018	0.39	<0.615	<0.306	<0.794	<0.784
2711-A5 - 1	clean	459.30	<0.007	0.62	<0.821	0.77	<1.064	1.41
2711-A5 - 2	clean	382.23	408.60	3.64	<1.056	0.55	<1.386	1.79
2711-A5 - 3	small Au?	342.97	111.52	23.63	<1.205	<0.831	<1.398	<1.082
2711-A6 - 1	small Au incs, poss. zonation?	179.88	<0.006	<0.073	0.81	<0.551	<0.943	<0.825
2711-A6 - 2	flat Au	154.59	0.05	0.72	1.52	<0.308	3.34	2.31
2711-A6 - 3	flat Au	209.29	5530.56	1.09	<0.748	1.90	<0.853	<0.858
2711-A7 - 1	small Au?	117.09	1.14	1.28	1.04	0.61	2.65	1.10
2711-A8 - 1	clean, short	158.18	0.17	0.05	<0.752	<0.307	<1.077	<0.919
2711-A8 - 2	short	383.69	0.06	<0.018	2.48	1.02	1.53	<1.093
2711-A8 - 3	small Au	167.45	0.25	<0.100	<0.826	<0.650	3.03	<0.912
2713-A1 - 1	flat Au, poss. incs	497.86	1.15	9.38	5.10	3.26	21.44	2.02
2713-A1 - 2	flat Au with incs	908.50	3.57	9.21	6.51	<0.544	51.17	3.78
2713-A1 - 3	Pb-Au incs?	832.72	14.15	<0.059	<0.688	0.40	<0.856	1.85
2713-A1 - 4	Au incs	743.77	0.78	0.28	4.39	0.79	3.36	<0.766
2713-A2 - 1		<24.333	<0.024	1.97	<0.707	1.46	<0.935	<0.676
2713-A2 - 2	Au incs	729.02	<0.185	0.45	0.89	<0.564	<0.931	1.15
2713-A2 - 3	Au incs	734.87	0.38	1.49	5.64	5.06	18.34	2.03
2713-A2 - 4	flat Au?	594.95	0.31	1.66	<0.750	0.32	6.12	0.84
2713-A3 - 1	flat Au & small incs	795.26	0.39	3.17	1.39	1.38	23.46	<0.772
2713-A3 - 2	flat Au, zonation?	8801.66	<0.062	0.32	4.66	0.38	<0.911	<0.804
2713-A3 - 3	Au incs	1149.50	0.18	0.49	3.32	3.64	30.88	1.79
2713-A3 - 4	Au incs	693.74	0.15	4.67	<0.848	0.94	9.67	<0.842
2713-A4 - 1	short, Au incs	969.29	<0.005	1.58	2.19	7.76	<1.082	<0.819
2713-A4 - 2	short, flat Au?	537.52	0.50	4.39	2.08	1.55	1.63	<0.907
2713-A4 - 3	short, Au incs, Au in Cu-phase	750.60	<0.043	17.36	2.43	2.17	1.58	<0.735
2713-A4 - 4	short, Au incs, Au in Cu-phase	769.81	0.07	10.61	2.78	1.16	1.31	1.01
2713-A5 - 1	flat Au?	115.42	<0.079	2.72	1.36	<0.161	<0.971	<0.845
2713-A5 - 2	flat Au?	96.10	3.33	9.21	4.96	2.54	32.95	2.49
2713-A5 - 3	flat Au?	95.92	0.31	6.53	2.42	0.45	3.37	31.64
2713-A5 - 4	flat Au	265.51	4.60	4.75	3.78	<0.618	21.31	19.21
	AVERAGE	632.97	202.99	4.32	10.39	2.48	12.46	4.22
	MINIMUM	86.78	0.03	0.05	0.81	0.32	0.94	0.84
	MAXIMUM	8801.66	5530.56	23.63	170.95	20.46	51.17	31.64
	ST.DEV.	1374.52	1009.11	5.26	35.04	4.13	13.49	7.43

cont...

Analysis	Comment	125Te	178Hf	181Ta	182W	197Au	208Pb	209Bi
2711-A1 - 1	small Au?	6.68	0.14	0.07	81.31	0.31	1.55	15.99
2711-A1 - 2	short, flat Au	23.19	0.05	<0.013	6.72	1.79	3.33	69.46
2711-A1 - 3	short	<4.875	<0.023	0.06	10.93	0.10	2.36	15.32
2711-A2 - 1	clean	4.24	<0.006	<0.003	2.60	<0.081	<0.422	2.29
2711-A2 - 2	large Au inc	18.80	0.23	0.15	244.79	701.37	13.07	11.01
2711-A3 - 1	flat Au	45.72	0.07	0.12	48.64	17.89	115.94	62.66
2711-A3 - 2	large Au incs	33.81	<0.007	0.26	9.89	461.98	231.97	375.08
2711-A4 - 1	Bi-As-Pb-Au inc?	17.71	<0.006	0.01	3.95	3.18	26.57	121.47
2711-A4 - 2	small Au?	11.04	<0.006	0.11	3.88	0.70	37.25	14.90
2711-A4 - 3	Cu, clean	5.54	<0.049	<0.022	<0.053	<0.080	<0.316	0.17
2711-A5 - 1	clean	<4.606	0.14	<0.005	<0.040	0.10	0.97	0.34
2711-A5 - 2	clean	76.95	9.33	<0.006	0.89	0.70	21.76	8.90
2711-A5 - 3	small Au?	150.57	4.27	<0.010	1.59	1.94	37.22	20.28
2711-A6 - 1	small Au incs, poss. zonation?	5.79	<0.005	<0.003	<0.057	1.08	3.06	2.13
2711-A6 - 2	flat Au	58.80	0.05	0.03	<0.093	2.88	34.34	14.98
2711-A6 - 3	flat Au	13.25	150.20	0.08	0.63	0.74	5.36	2.20
2711-A7 - 1	small Au?	37.91	<0.006	0.36	11.74	0.68	13.13	30.09
2711-A8 - 1	clean, short	5.49	<0.023	0.05	<0.046	<0.086	<0.490	0.55
2711-A8 - 2	short	43.54	<0.020	<0.037	<0.075	0.22	9.85	4.64
2711-A8 - 3	small Au	39.39	0.11	0.16	2.08	0.31	6.92	3.16
2713-A1 - 1	flat Au, poss. incs	63.75	0.11	0.51	133.63	10.85	654.32	306.86
2713-A1 - 2	flat Au with incs	72.16	0.44	2.41	1144.36	25.25	122.49	25.76
2713-A1 - 3	Pb-Au incs?	37.19	0.72	0.09	0.05	6.71	114.27	1.51
2713-A1 - 4	Au incs	50.86	<0.009	<0.022	0.08	9.88	86.47	16.06
2713-A2 - 1		<5.181	<0.008	0.02	0.18	0.25	457.49	6.68
2713-A2 - 2	Au incs	77.42	0.03	<0.005	0.21	14.26	139.09	76.17
2713-A2 - 3	Au incs	68.78	<0.046	0.28	393.53	23.50	103.24	85.37
2713-A2 - 4	flat Au?	20.25	<0.043	0.02	198.34	1.53	327.85	231.53
2713-A3 - 1	flat Au & small incs	24.43	0.07	0.97	97.15	5.88	489.68	92.82
2713-A3 - 2	flat Au, zonation?	144.20	<0.022	<0.003	1.33	7.81	3165.33	635.80
2713-A3 - 3	Au incs	132.95	0.13	0.04	57.21	28.57	212.06	5.59
2713-A3 - 4	Au incs	36.13	0.15	0.82	62.69	3.16	60.30	17.69
2713-A4 - 1	short, Au incs	73.79	<0.023	0.02	0.37	15.25	76.26	20.21
2713-A4 - 2	short, flat Au?	57.27	<0.029	1.39	2.65	18.68	97.37	14.75
2713-A4 - 3	short, Au incs, Au in Cu-phase	17.54	<0.066	0.03	0.60	12.93	22.71	4.26
2713-A4 - 4	short, Au incs, Au in Cu-phase	42.19	<0.023	<0.002	0.38	82.02	97.22	4.46
2713-A5 - 1	flat Au?	21.58	0.09	<0.002	0.27	1.26	1347.33	47.14
2713-A5 - 2	flat Au?	51.57	0.11	0.87	207.89	4.65	3458.73	74.78
2713-A5 - 3	flat Au?	17.14	<0.039	0.07	20.61	6.63	2503.56	58.62
2713-A5 - 4	flat Au	69.23	0.43	1.11	492.31	7.33	3354.29	80.67
	AVERAGE	45.32	8.34	0.37	95.40	40.06	471.75	64.56
	MINIMUM	4.24	0.03	0.01	0.05	0.10	0.97	0.17
	MAXIMUM	150.57	150.20	2.41	1144.36	701.37	3458.73	635.80
	ST.DEV.	37.12	33.46	0.56	219.10	135.04	975.81	123.35

O. $^{40}Ar/^{39}Ar$ Analyses - Description and Procedures

Samples analyzed by the $^{40}Ar/^{39}Ar$ method at the University of Nevada Las Vegas were wrapped in Al foil and stacked in 6 mm inside diameter sealed fused silica tubes. Individual packets averaged 2 mm thick and neutron fluence monitors (FC-2, Fish Canyon Tuff sanidine) were placed every 5-10 mm along the tube. Synthetic K-glass and optical grade CaF_2 were included in the irradiation packages to monitor neutron induced argon interferences from K and Ca. Loaded tubes were packed in an Al container for irradiation. Samples irradiated at the Oregon State TRIGA Reactor, Corvallis, OR were in-core for 9.1 hours in the F-12 position, In-Core Irradiation Tube (ICIT) of the 1 MW TRIGA type reactor. Correction factors for interfering neutron reactions on K and Ca were determined by repeated analysis of K-glass and CaF_2 fragments. Measured $(^{40}Ar/^{39}Ar)_K$ values were 1.55 (± 2.67%) x 10^{-1}. Ca correction factors were $(^{36}Ar/^{37}Ar)_{Ca}$ = 1.66 (± 0.76%) x 10^{-4} and $(^{39}Ar/^{37}Ar)_{Ca}$ = 6.51 (± 0.28%) x 10^{-4}. J factors were determined by fusion of 6-10 individual crystals of neutron fluence monitors which gave reproducibility's of 0.09% to 0.11% at each standard position. Variation in neutron fluence along the 100 mm length of the irradiation tubes was <4%. Matlab curve fit was used to determine J and uncertainty in J at each standard position. No significant neutron fluence gradients were present within individual packets of crystals as indicated by the excellent reproducibility of the single crystal fluence monitor fusions.

Irradiated FC-2 sanidine standards together with CaF_2 and K-glass fragments were placed in a Cu sample tray in a high vacuum extraction line and were fused using a 20 W CO_2 laser. Sample viewing during laser fusion was by a video camera system and positioning was via a motorized sample stage. Samples analyzed by the furnace step heating method utilized a double vacuum resistance furnace similar to the Staudacher et al. (1978) design. Reactive gases were removed by three GP-50 SAES getters prior to being admitted to a MAP 215-50 mass spectrometer by expansion. The relative volumes of the extraction line and mass spectrometer allow 80% of the gas to be admitted to the mass spectrometer for laser fusion analyses and

76% for furnace heating analyses. Peak intensities were measured using a Balzers electron multiplier by peak hopping through 7 cycles; initial peak heights were determined by linear regression to the time of gas admission. Mass spectrometer discrimination and sensitivity was monitored by repeated analysis of atmospheric argon aliquots from an on-line pipette system. Measured $^{40}Ar/^{36}Ar$ ratios were 345.79 ± 0.10% during this work, thus a discrimination correction of 0.8546 (4 AMU) was applied to measured isotope ratios. The sensitivity of the mass spectrometer was ~6 x 10^{-17} mol mV^{-1} with the multiplier operated at a gain of 36 over the Faraday. Line blanks averaged 4.33 mV for mass 40 and 0.01 mV for mass 36 for laser fusion analyses and 23.66 mV for mass 40 and 0.07 mV for mass 36 for furnace heating analyses. Discrimination, sensitivity, and blanks were relatively constant over the period of data collection. Computer automated operation of the sample stage, laser, extraction line and mass spectrometer as well as final data reduction and age calculations were done using LabSPEC software written by B. Idleman (Lehigh University). An age of 28.02 Ma (Renne et al., 1998) was used for the Fish Canyon Tuff sanidine fluence monitor in calculating ages for samples.

For $^{40}Ar/^{39}Ar$ analyses a plateau segment consists of 3 or more contiguous gas fractions having analytically indistinguishable ages (i.e. all plateau steps overlap in age at ± 2σ analytical error) and comprising a significant portion of the total gas released (typically >50%). Total gas (integrated) ages are calculated by weighting by the amount of ^{39}Ar released, whereas plateau ages are weighted by the inverse of the variance. For each sample inverse isochron diagrams are examined to check for the effects of excess argon. Reliable isochrons are based on the MSWD criteria of Wendt and Carl (1991) and, as for plateaus, must comprise contiguous steps and a significant fraction of the total gas released. All analytical data are reported at the confidence level of 1σ (standard deviation).

Renne, P.R., Swisher, C.C, Deino, A.L., Karner, D.B., Owens, T.L., DePaolo, D.J., (1998). Intercalibration of standards, absolute ages and uncertainties in $^{40}Ar/^{39}Ar$ dating, Chemical Geology, 145, 117-152.

Staudacher, T.H., Jessberger, E.K., Dorflinger, D., and Kiko, J., (1978). A refined ultrahigh-vacuum furnace for rare gas analysis, J. Phys. E: Sci. Instrum., 11, 781-784.

Wendt, I., and Carl, C., (1991). The statistical distribution of the mean squared weighted deviation, Chemical Geology, 86, 275-285.

P. $^{40}Ar/^{39}Ar$ Analyses Data

OD79802, Alunite, 54.28 mg, J = 0.001768 ± 0.40%													
4 amu discrimination = 0.8546 ± 0.10%, 40/39K = 0.155 ± 2.67%, 36/37Ca = 0.000166 ± 0.76%, 39/37Ca = 0.000651 ± 0.28%													
Step	**T (ºC)**	**t (min.)**	**^{36}Ar**	**^{37}Ar**	**^{38}Ar**	**^{39}Ar**	**^{40}Ar**	**%^{40}Ar***	**% ^{39}Ar rlsd**	**Ca/K**	**40Ar*/39ArK**	**Age (Ma)**	**1σ**
1	500	12	1,409	0,554	0,958	52,938	566,269	12,9	4,6	0,054509953	1,282487	4,09	0,10
2	510	12	0,941	0,823	1,191	79,102	520,333	36,3	6,8	0,054193338	2,211794	7,04	0,04
3	520	12	1,120	1,218	1,705	115,750	642,161	37,8	10,0	0,054810012	1,959426	6,24	0,03
4	530	12	1,488	2,054	2,580	179,097	827,954	35,1	15,4	0,059737404	1,526067	4,86	0,03
5	540	12	1,408	3,097	3,401	249,477	976,716	46,9	21,5	0,064661461	1,730125	5,51	0,05
6	550	12	1,221	3,705	3,393	252,364	900,257	49,6	21,7	0,076471055	1,663775	5,30	0,09
7	560	12	0,724	2,545	1,977	144,432	559,783	52,8	12,4	0,091783056	1,902485	6,06	0,18
8	570	12	0,612	1,268	0,963	63,334	343,524	37,4	5,5	0,104285043	1,846494	5,88	0,25
9	580	12	0,697	0,562	0,450	20,768	279,179	13,4	1,8	0,140956737	1,617554	5,15	0,66
10	600	12	1,210	0,240	0,356	4,777	449,861	7,1	0,4	0,26170682	6,244701	19,81	4,20
							Cumulative %^{39}Ar rlsd =		100,0		Total gas age =	5,62	0,03

Q. U-Pb Data of Garnets in Samples CTC78859 and CTC78857

Source file Sample ID#Spot	DC207_235	DC206_238	DC207_206	DC208_232	DC208_206	DCAge207_235	DCAge206_238	DCAge208_232	DCAge207_206
	DC= Data Corrected Isotope Proportion, DCAge=Data Corrected Ma Ages								
78859#01	15,1	0,129	0,817	0,213	2,011	2846	784	3920	5000
78859#02	1,903	0,018	0,797	0,021	1,985	1082	112,5	416	4955
78859#03	0,473	0,005	0,674	0,005	1,92	393	32,8	95,4	4678
78859#03	0,376	0,004	0,741	0,004	1,88	324	26,4	70,6	4829
78859#04	0,675	0,006	0,75	0,01	1,891	524	41,4	208,5	4849
78859#05	1,163	0,01	0,785	0,013	1,83	786	66,3	257	4929
78859#06	41,1	0,359	0,825	0,21	2,049	3797	1977	3850	5019
78859#07	3,84	0,034	0,817	0,031	2,057	1605	215	615	5000
78859#08	29,45	0,258	0,829	0,178	2,043	3478	1477	3310	5026,4
78859#09	30,4	0,267	0,82	0,715	2,04	3510	1524	11150	5006,1
78859#10	5,84	0,052	0,818	0,025	2,07	1953	328	493	5003
78859#11	27,8	0,247	0,826	0,163	2,055	3413	1430	3050	5020,5
78859#12	34,5	0,302	0,829	0,208	2,053	3627	1702	3820	5027,3
78859#13	99,5	0,881	0,823	0,704	2,045	4681	4080	10780	5013
78859#14	0,209	0,002	0,611	0,001	1,33	193	15,74	28,1	4570
78859#15	43,9	0,366	0,825	0,306	2,038	3860	2070	5550	5018,8
78859#16	0,264	0,002	0,591	0,003	1,5	241	15,3	52,9	4490
78859#17	0,75	0,007	0,732	0,017	1,855	568	47,8	340	4808
78859#18	0,0734	0,001	0,408	8E-04	1,48	72,1	9,07	16,8	4000
78859#19	0,321	0,003	0,69	0,002	1,73	282	20,8	45,1	4714
78859#20	71,3	0,624	0,817	0,282	2,039	4349	3126	5020	5000,6
78859#21	12,98	0,116	0,82	0,166	2,036	2678	704	3110	5006,2

78859#22	9,3	0,083	0,82	0,057	2,036	2372	514	1124	5008
78859#23	2,99	0,028	0,801	0,014	2,012	1404	175	285	4965
78859#24	3,2	0,029	0,817	0,014	1,992	1459	182,8	289	5001
78859#25	5,59	0,049	0,814	0,04	1,983	1920	307	790	4993
78859#26	11,69	0,104	0,824	0,069	2,059	2585	638	1345	5017
78859#27	24,7	0,216	0,821	0,129	2,079	3295	1262	2450	5010
78859#28	4,16	0,038	0,79	0,032	1,887	1666	238	628	4939
78859#29	0,0782	0,001	0,452	0,002	1,2	76,7	8,84	44,1	4126
78859#30	39,9	0,346	0,826	0,826	2,047	3786	1917	12170	5022
78859#31	1,65	0,015	0,787	0,023	1,982	1001	98	450	4933
78859#32	0,342	0,004	0,684	0,019	1,549	299	23,3	386	4701
78859#33	4,232	0,038	0,808	0,028	1,992	1683	239,1	559	4979
78859#34	0,211	0,003	0,642	0,002	1,78	195	16,8	40,8	4606
78859#35	27,7	0,248	0,817	0,504	2,045	3408	1429	8250	5000,3
78859#36	1,291	0,012	0,795	0,016	1,942	843	75,4	314	4951
78859#37	10,27	0,09	0,821	0,101	2,042	2460	554	1951	5009
78859#38	17,9	0,161	0,829	0,1	2,056	2986	962	1930	5027
78859#39	3,974	0,035	0,813	0,012	2,065	1632	221,9	245,1	4992
78859#40	25,6	0,228	0,825	0,131	2,069	3330	1320	2480	5017,3
78859#41	20,43	0,175	0,821	0,112	2,043	3114	1039	2148	5010
78859#42	85	0,739	0,825	0,72	2,055	4520	3570	1,10E+04	5019
78859#43	8,28	0,073	0,833	0,073	2,103	2262	452	1419	5036
78859#43	8,61	0,073	0,823	0,053	2,04	2298	455	1038	5013
78859#44	3,67	0,033	0,811	1,408	1,997	1566	207	17770	4987
78859#45	1,96	0,018	0,799	0,369	1,971	1113	117,7	6460	4961
78859#46	16,97	0,15	0,827	1,206	2,032	2935	901	15990	5024
78859#47	5,73	0,051	0,817	0,079	2,001	1936	318	1531	5000

78859#48	22,93	0,202	0,821	0,46	2,054	3224	1187	7650	5009
78859#49	2,4	0,023	0,799	0,155	1,965	1242	145	2920	4960
78859#50	1,314	0,012	0,77	0,033	1,908	852	78	660	4895
78859#51	141,9	1,269	0,827	4,067	2,06	5047	5304	32890	5023,3
78859#52	58	0,511	0,825	0,576	2,064	4140	2661	9200	5018
78859#53	0,786	0,007	0,756	0,007	1,864	589	46,9	145,3	4864
78859#54	2,956	0,026	0,819	0,015	2,082	1396	167,4	309	5005
78859#54	1,461	0,014	0,791	0,007	1,984	914	87,6	146,2	4941
78859#55	7,8	0,069	0,82	0,023	2,062	2317	433	454	5006
78859#56	5,73	0,051	0,809	0,019	1,984	1937	322	388	4982
78859#56	12,89	0,113	0,828	0,048	2,069	2672	689	954	5024
78859#57	12,1	0,107	0,819	0,056	2,089	2616	656	1100	5005
78859#58	15,25	0,132	0,823	0,135	2,038	2855	797	2570	5014
78859#59	0,218	0,003	0,617	0,001	1,55	200	16,9	24	4550
78859#60	0,507	0,005	0,72	0,045	1,787	417	32,9	888	4782
78859#61	6,61	0,058	0,824	0,279	2,06	2065	362	4970	5016
78859#62	4,86	0,044	0,815	0,342	2,018	1796	277	5950	4995
78859#63	26,9	0,238	0,823	0,594	2,054	3381	1376	9420	5014
78859#64	0,19	0,002	0,609	0,006	1,42	177	14,54	120	4531
78859#65	7,5	0,067	0,815	0,253	1,996	2170	416	4550	4997
78859#66	6,49	0,059	0,821	0,256	2,021	2045	368	4610	5010
78859#67	6,24	0,057	0,819	0,054	2,053	2011	357	1063	5004
78859#68	10,21	0,089	0,824	0,055	2,077	2454	549	1073	5017
78859#69	5,11	0,044	0,817	0,016	2,071	1842	277	326,4	4999
78859#70	5,3	0,046	0,817	0,022	2,036	1868	291	441	5001
78859#71	17,75	0,156	0,821	0,092	2,048	2976	934	1780	5010
78859#72	4,998	0,046	0,806	0,042	2,059	1819	291	826	4975

78859#73	6,36	0,058	0,813	0,034	2,022	2026	363	684	4991
78859#74	4,71	0,042	0,823	0,03	2,051	1772	264	596	5013
78859#75	33,6	0,299	0,83	0,139	2,062	3606	1687	2622	5029
78859#76	5,87	0,054	0,815	0,041	2,092	1957	335,9	805	4996
78857#01	39,8	0,346	0,818	0,165	2,037	3768	1925	3090	5002
78857#02	0,0969	0,001	0,481	6E-04	2	94	9,52	11,65	4205
78857#03	0,904	0,008	0,758	0,004	2,096	654	54,3	74,4	4871
78857#04	235	2,05	0,823	1,057	2,054	5551	7230	14600	5014,8
78857#05	0,358	0,004	0,697	0,002	2,029	311	22,67	35,5	4731
78857#06	1,115	0,011	0,775	0,004	2,021	764	67,4	86,9	4907
78857#07	0,094	0,001	0,503	7E-04	1,83	94	9,39	13,9	4290
78857#08	0,212	0,003	0,617	0,002	1,78	196	16,18	31,3	4551
78857#09	3,42	0,03	0,806	0,02	1,983	1508	189	393	4977
78857#10	0,497	0,005	0,745	0,002	2,029	418	34,2	46,7	4840
78857#11	0,106	0,002	0,495	7E-04	2,04	105	9,94	13,4	4241
78857#12	0,0387	0,001	0,266	4E-04	2,08	38,9	6,77	8,08	3340
78857#13	0,0276	9E-04	0,225	4E-04	1,59	27,6	5,68	7,69	3030
78857#14	0,0238	1E-03	0,179	5E-04	0,95	23,9	6,13	11	2690
78857#15	0,0206	9E-04	0,167	8E-04	0,43	20,7	5,71	16,3	2720
78857#16	0,098	0,001	0,433	0,003	1,13	95	9,4	69	4140
78857#17	2,49	0,022	0,807	0,01	2,042	1270	141	199,6	4977
78857#18	0,0647	0,001	0,375	5E-04	1,98	63,7	8,12	10,37	3810
78857#19	0,0322	0,001	0,232	4E-04	2	32,2	6,5	7,39	3090
78857#20	0,0184	9E-04	0,159	3E-04	2,17	18,5	5,51	7,02	2520
78857#21	0,0187	8E-04	0,167	3E-04	2,18	18,8	5,37	6,76	2690
78857#22	0,0203	8E-04	0,174	5E-04	0,95	20,4	5,38	9,65	2630
78857#23	0,121	0,002	0,545	0,003	1,3	123	11,19	69,2	4422

78857#24	0,094	0,001	0,4	0,002	0,9	91	8,83	41	3950
78857#25	0,0208	9E-04	0,16	4E-04	1,76	20,9	5,78	7,35	2610
78857#26	0,0212	9E-04	0,167	3E-04	1,85	21,3	5,73	7,05	2610
78857#27	0,0178	9E-04	0,143	3E-04	1,88	17,9	5,67	6,68	2380
78857#28	0,0212	9E-04	0,176	3E-04	2,18	21,3	5,96	7,02	2690
78857#29	0,0984	0,002	0,439	6E-04	1,97	95,3	10,47	11,45	4061
78857#30	0,282	0,003	0,643	0,003	1,8	254	21,9	61,3	4608
78857#31	0,61	0,006	0,728	0,016	1,75	483	36,3	325	4822
78857#32	0,0523	0,001	0,384	5E-04	1,88	52,3	7,58	10,85	3860
78857#33	0,0307	0,001	0,235	4E-04	1,89	30,7	6,49	7,66	3150
78857#34	0,225	0,003	0,598	0,001	1,932	209	16,66	21,9	4508
78857#35	0,0184	9E-04	0,157	3E-04	2	18,5	5,59	6,91	2450
78857#36	0,0185	9E-04	0,154	3E-04	2,27	18,6	5,61	6,98	2420
78857#37	0,0244	9E-04	0,194	6E-04	0,86	24,5	5,74	11,2	2890
78857#38	0,0711	0,001	0,368	0,002	0,77	69,8	8,75	32,3	3810
78857#39	0,0244	9E-04	0,196	4E-04	1,13	24,6	6,1	7,31	2830
78857#40	0,0364	0,001	0,271	4E-04	1,75	36,6	6,63	7,48	3330
78857#41	0,0186	9E-04	0,154	3E-04	1,85	18,8	5,52	6,56	2400
78857#42	0,0222	9E-04	0,18	3E-04	1,81	22,3	5,78	6,57	2730
78857#43	0,849	0,008	0,761	0,003	2,12	624	51,8	57,7	4874
78857#43	0,0214	0,001	0,196	4E-04	2,36	21,5	6,51	8,08	2810
78857#44	0,0371	0,001	0,3	7E-04	0,6	36,9	6,94	13,9	3510
78857#45	0,0484	0,001	0,344	0,002	0,86	48,8	7,22	30,2	3770
78857#46	1,02	0,01	0,774	0,005	1,985	719	63,6	100,9	4904
78857#46	0,136	0,002	0,488	9E-04	1,6	130	13,9	19	4200
78857#47	0,0201	9E-04	0,167	4E-04	2	20,2	5,48	7,29	2580
78857#48	0,0175	9E-04	0,14	4E-04	2,29	17,6	5,73	7,21	2260

78857#49	0,016	9E-04	0,133	3E-04	1,29	16,2	5,56	7,03	2200
78857#50	0,0249	8E-04	0,214	6E-04	0,86	25	5,45	12,4	3010
78857#51	0,03	1E-03	0,25	0,001	0,706	30	6,18	24,5	3320
78857#52	0,0221	9E-04	0,187	4E-04	0,5	22,2	5,68	7,6	2870
78857#53	6,12	0,054	0,813	0,068	2,032	1997	341,1	1324	4990
78857#54	0,929	0,009	0,78	0,004	2,085	667	57	78,9	4916
78857#55	0,0191	9E-04	0,159	3E-04	2,09	19,2	6	6,99	2520
78857#56	0,198	0,002	0,603	0,002	1,656	185	14,8	36,9	4559
78857#57	0,0264	9E-04	0,221	5E-04	0,67	26,4	5,63	10,2	3000
78857#58	0,0232	9E-04	0,192	8E-04	0,5	23,5	5,94	16,2	2830
78857#59	0,015	8E-04	0,133	5E-04	0,545	15,1	5,41	10,9	2200
78857#60	0,0762	0,001	0,474	0,001	1,16	74,6	9,02	29,8	4160
78857#61	1,703	0,015	0,795	0,016	2,01	1010	94,4	327	4951
78857#62	0,0285	9E-04	0,208	4E-04	0,91	28,5	6,07	8,05	2940
78857#63	0,126	0,002	0,529	0,001	1,56	120,5	11,56	23,3	4338
78857#64	0,0226	9E-04	0,189	5E-04	0,73	22,7	5,78	10,3	2870
78857#65	16,39	0,145	0,818	0,326	2,033	2900	872	5700	5003
78857#66	4,06	0,036	0,813	0,094	2,017	1670	230	1880	4991
78857#67	17,14	0,152	0,827	0,288	2,034	2942	911	5110	5024
78857#68	10,9	0,097	0,821	0,375	2,04	2515	594	6440	5010